

博士論文

**Analysis of turbulent structures around building
via spectral proper orthogonal decomposition
and its applications to outdoor wind environment**

(SPOD による建物周りの乱流構造解析
及び屋外風環境分析への応用)

張 秉超

Abstract

Understanding the main turbulent structures is of vital importance for pedestrian-level wind or outdoor air ventilation control. However, the turbulence still has not been fully understood in physics, and continuing inability to understand the turbulence limits reliable predictions and further technological advancement. Modal analysis methods are the potential solutions, and the technique called spectral proper orthogonal decomposition (SPOD) is one of them. SPOD is a decomposition method combining the spatial decomposition of proper orthogonal decomposition (POD) and temporal analysis of the Fourier series.

This study pioneers the applications of SPOD in wind environment fields. The applications in the following two classical cases were introduced: the flow field around a single square-section building model and a two-dimensional street canyon flow. The effectivity of SPOD in the identification of characteristic flow structures was well proved, even for the cases with very high Reynolds numbers. In addition, mathematical tools for evaluating the pedestrian-level wind environment and outdoor air exchanging are also developed in this study.

First, SPOD analysis was performed on the flow field around a square-section building model calculated by large-eddy simulation (LES) to identify the three-dimensional main flow features within the sampling field. The identified features, including the low-frequency modes related to the fluctuation of the incoming flow, primary wake vortex shedding (Kármán-type vortex shedding), tip and base vortices, and primary side vortex shedding (flow separation), were extracted from the single case at once. The primary frequency and the intensity of these features were revealed by studying the typical SPOD modes and estimating the energy percentage. In addition, the local-space SPOD spectrum was also defined to analyse the composition of the kinetic energy within some local parts of the sampling domain.

The identified flow features and their details are summarised as follows: first, two energetic modes at low frequency were chosen as the typical modes to depict the symmetric and antisymmetric fluctuations around the building. They were found to be

directly related to the inflow fluctuation by the local-space SPOD spectrum. The primary wake vortex shedding was depicted using a complex mode at the Strouhal frequency, which exhibited periodic vortex shedding. The tip and base vortex pair on one side of the building appeared in one SPOD mode, which indicated their correlation. The mode also showed an arch structure by which the tip and base vortices were connected. The same structure was found on the roof of the building illustrated by another mode, which showed the other kind of development of the tip vortices. The primary side vortex shedding caused by the strong shear force and separation appeared on both the roof and sides of the building. However, the vortices at different heights on the sides were not synchronised. Finally, the local-space SPOD spectrum precisely showed the different compositions of the fluctuation patterns on the front, side, and back of the prism. In general, the SPOD spectrum provided a comprehensive view of the turbulent structures in this flow field, which was an integration of all the above flow features. Unlike previous studies, where different flow features were studied by different physical quantities, this study revealed the primary frequency and intensity for all features, using a single mathematical process.

Subsequently, the target was focused on the pedestrian-level wind of the same case. The SPOD results for two simulation cases were compared, where the only difference was the existence of fluctuation at the inflow boundary, to show how the inflow fluctuation influenced the turbulent structures around the building. The results showed that the input of the inflow fluctuation on the inlet boundary had a significant influence on the turbulent structures at a low frequency because the modes and energy significantly differed. In both cases, the strongest modes corresponded to the Kármán-type vortex shedding, while the frequency was slightly larger when no fluctuation was input at the inflow boundary. The difference in the shapes of the Kármán-type vortex shedding was considered related to the difference in the mean velocity and TKE fields of the two cases. At a high frequency, flow separation phenomenon occurred on both sides of the building. In the case where no fluctuation was input at the inflow boundary, this phenomenon exhibited a peak on the distribution of energy, while it was not quite significant in the other case. A method was developed to decompose the TKE at a certain point and display the extent to which the fluctuating wind speed at the point is influenced by each mode. This is considered useful in the finding the main reason of large fluctuation and improvement of pedestrian-level wind.

In the other application, the SPOD technique was applied to decompose the velocity field of a two-dimensional street canyon. The SPOD modes, depicting the large-scale coherent structures and Kelvin–Helmholtz instabilities, were well extracted and visualised. The

SPOD modes depicted the Kelvin–Helmholtz instabilities as a series of vortices, which are generated at the roof level, and enter the canyon following the principal recirculation, while the fluctuation caused by the external large-scale coherent structures directly strengthens or weakens the principal recirculation. In addition, the ejection events and pollutant removal were quantitatively analysed using the newly defined SPOD co-spectra to understand their relationships with the turbulent fluctuation patterns. The results showed that both Kelvin–Helmholtz instabilities and large-scale coherent structures can cause ejection and sweep events at the roof level, thus contributing to pollutant removal. However, the former contributed to stronger ejection and sweep events with stronger vertical components. The Kelvin–Helmholtz instabilities accounted for a small percentage of TKE, but they contributed most to the vertical turbulent mass flux at the roof level. In contrast, the large-scale coherent structures occupied a large proportion of the TKE, while they contributed less towards vertical turbulent mass flux. The intermittent concentration fluctuation fit better with the time scale of the Kelvin–Helmholtz instabilities.

The spanwise performance and nonlinear interactions of the turbulent structures were investigated by modifying the original SPOD to the one combining two-dimensional Fourier transform (2DFT). The SPOD co-spectrum defined in our previous study was also modified to a 2DFT version. As the result, the modes extracted by SPOD with 2DFT showed clearer shapes of turbulent structures than the previous study because of the increase of the flow realisations. These turbulent structures were depicted by periodic fluctuation patterns detected along both the time and spanwise direction with specific frequencies and wavenumbers. The nondimensional time scales were found approximately 1–5 times of the nondimensional spanwise length scales for both large- and small-scale structures, although the mechanisms of these structures differ. This can be explained by the self-similarity of the high-Reynolds-number turbulence, i.e., a constant aspect ratio of the length scale is maintained. The SPOD co-spectra showed that the sweep and ejection events at the roof level mainly occurred at the spanwise nondimensional wavenumber of 1–4 and frequency of 0.2–0.8. This range coincided with that of the small-scale structures caused by the Kelvin–Helmholtz instabilities at the roof level. The same range of wavenumber and frequency were found for pollutant removal. Although the large-scale structures contributed less to the pollutant removal than the small-scale structures, they still had a good chance to enhance the pollutant removal indirectly by amplifying the small-scale structures. The amplitude of the small-scale structures showed a weak but non-negligible correlation with the state of the large-scale structures. The joint probability distribution indicated that the high- and low-momentum fluids passing through the canyon were related to the amplifying and suppressing of the

small-scale structures. This phenomenon appeared stochastically along both the time and spanwise direction.

In summary, as SPOD has shown its effectiveness and efficiency in turbulent structure analysis for high-Reynolds-number turbulence, it has the potential to become another useful tool for further research or design in the field of wind environment. Techniques developed in this study are also considered of great application value in broad application prospects.

Contents

Abstract	i
Contents	v
List of figures	ix
List of tables	xii
Nomenclature	xv
Chapter 1 Introduction	1
1.1 Backgrounds	1
1.1.1 Urban wind environment.....	1
1.1.2 CFD simulation for outdoor wind environment	2
1.1.3 Coherent turbulent structures	3
1.1.4 POD based analysis methods	5
1.1.5 Other modal analysis methods: Koopman analysis and DMD.....	6
1.1.6 Method comparison for time series analysis.....	7
1.2 Research objectives	9
1.3 Thesis structure.....	10
Reference	12
Chapter 2 CFD simulation for urban wind environment	17
2.1 Overview	17
2.2 Governing equations.....	17
2.3 Numerical methods.....	18
2.3.1 Spatial discretisation.....	18
2.3.2 Time matching method.....	19
2.3.3 Discretisation of the convective term	21
2.3.4 Discretisation of the pressure term	25
2.3.5 Discretisation of the diffusion term	25
2.3.6 PISO algorithm.....	26
2.4 Large-eddy simulation.....	28
2.4.1 Turbulent modelling	28
2.4.2 Filtered governing equations	28
2.4.3 Subgrid-scale modelling.....	29
2.4.4 Wall modelling	30

2.5	Summary	32
	Reference	32
Chapter 3 Basic theory and algorithm of SPOD.....		35
3.1	Overview	35
3.2	Basic theory	35
3.2.1	Function space and inner product	35
3.2.2	POD.....	36
3.2.3	Extension to SPOD	37
3.3	Algorithm.....	39
3.3.1	Eigenvalue problem in the matrix form.....	39
3.3.2	Snapshot POD algorithm	40
3.3.3	DFT and Welch's method.....	41
3.3.4	Algorithm of SPOD	42
3.4	Summary and application guide.....	44
	Reference	44
Chapter 4 Identification of three-dimensional flow features around a square-section building model		47
4.1	Introduction.....	47
4.2	Analysis methods	49
4.2.1	Similarity between inter-frequency modes	49
4.2.2	Local-space spectrum.....	50
4.3	Outline of simulation of the flow field	51
4.4	SPOD analysis of the velocity field.....	55
4.4.1	Performing SPOD	55
4.4.2	SPOD spectrum.....	56
4.4.3	Low-frequency modes	66
4.4.4	Primary wake vortex shedding.....	67
4.4.5	Tip and base vortices	67
4.4.6	Primary side vortex shedding.....	69
4.4.7	Local-space spectrum.....	69
4.5	Summary.....	71
	Reference	72
Chapter 5 Analysis of the pedestrian-level wind around a square-section building model: the effect of inflow fluctuation on turbulent structures.....		77
5.1	Introduction.....	77
5.2	Outline of the simulation of the flow field.....	78
5.3	Analysis results	80
5.3.1	Analysis results for the whole flow field at the pedestrian level	80

5.3.2	Comparison of results with POD.....	87
5.3.3	Energy distribution at a certain point	90
5.4	Summary	93
	Reference	94
Chapter 6 Spectral analysis of turbulent flow in a two-dimensional street canyon and its role in pollutant removal.....		97
6.1	Introduction	97
6.2	Large-eddy simulation.....	100
6.2.1	Physical Models and Equations	100
6.2.2	Simulation design	100
6.2.3	Statistics and validation.....	102
6.3	Definition of SPOD co-spectrum	106
6.4	Decomposition of the velocity field	108
6.4.1	Performing SPOD.....	108
6.4.2	SPOD spectrum and turbulent fluctuation patterns	109
6.4.3	Ejection and sweep events at the roof level.....	115
6.5	Spectral analysis for the pollutant removal	118
6.6	Summary	122
	Reference	124
Chapter 7 Analysis of a two-dimensional street canyon flow passing and mechanism of pollutant removal via SPOD with 2DFT		127
7.1	Introduction	127
7.2	Large-eddy simulation.....	129
7.2.1	Physical models and simulation design	129
7.2.2	Statistics and validation.....	131
7.3	SPOD with 2DFT	134
7.3.1	Theory.....	134
7.3.2	Algorithm	136
7.3.3	SPOD co-spectrum	137
7.4	Results and discussion.....	138
7.4.1	Performing SPOD with 2DFT on the velocity field.....	138
7.4.2	SPOD spectrum and turbulent fluctuation patterns	139
7.4.3	Results of SPOD co-spectrum.....	153
7.5	Nonlinear interactions between large- and small-scale structures	158
7.5.1	Definition of the mode state	158
7.5.2	Correlation analysis between the states of large- and small-scale structures	159
7.6	Summary	163

Reference	164
Chapter 8 Conclusions and prospective.....	167
8.1 Conclusions.....	167
8.2 Prospective for further work	170
Reference	171
Publications	173
Acknowledgements	175

List of figures

Chapter 1

Figure 1.1 Thesis structure and theme of each chapter.....	12
--	----

Chapter 2

Figure 2.1 Geometry of an element on the x direction	21
Figure 2.2 Second-order TVD region.....	25
Figure 2.3 Experimental measurements and the law-of-the-wall.....	31

Chapter 4

Figure 4.1 Simulation domain	53
Figure 4.2 Mean velocity within the sampling domain	54
Figure 4.3 TKE within the sampling domain	54
Figure 4.4 Comparison of the results between the LES and experiment.....	55
Figure 4.5 SPOD spectrum.....	57
Figure 4.6 Mode ($fb/U_H = 0.0169, n = 1$)	58
Figure 4.7 Mode ($fb/U_H = 0.0169, n = 2$)	59
Figure 4.8 Mode ($fb/U_H = 0.0845, n = 1$)	60
Figure 4.9 Mode ($fb/U_H = 0.2281, n = 1$)	61
Figure 4.10 Mode ($fb/U_H = 0.2281, n = 2$)	62
Figure 4.11 Mode ($fb/U_H = 0.4562, n = 1$)	63
Figure 4.12 Mode ($fb/U_H = 0.8786, n = 1$)	64
Figure 4.13 Mode ($fb/U_H = 0.8870, n = 2$)	65
Figure 4.14 Local-space SPOD spectrum for the inlet face of the sampling domain	70
Figure 4.15 Local-space SPOD spectra for the front, side, and the back of the prism	71

Chapter 5

Figure 5.1 Comparison of mean velocity and RMS velocity fluctuation in the x, y, z directions between LES (Case 2) and the WTE database provided by AIJ	79
---	----

Figure 5.2 Mean velocity and TKE on $z = 0.125b$ plane (Case 1).....	80
Figure 5.3 Mean velocity and TKE on $z = 0.125b$ plane (Case 2).....	80
Figure 5.4 Result of the SPOD eigenvalues (Case 1)	81
Figure 5.5 Result of the SPOD eigenvalues (Case 2)	81
Figure 5.6 Eigenfunctions corresponding to the SPOD modes at some specific frequencies	82–84
Figure 5.7 POD modes (Case 1)	89
Figure 5.8 Power spectral density functions of the POD mode coefficients (Case 1)	90
Figure 5.9 Result of $s_{f,n}(\mathbf{x})$ at observation point $\mathbf{x}_A = (0, 0.6b)$ in Case 2.....	92
Figure 5.10 Result of $s_{f,n}(\mathbf{x})$ at observation point $\mathbf{x}_B = (0.7b, 0.6b)$ in Case 2	92

Chapter 6

Figure 6.1 Simulation domain.....	101
Figure 6.2 Profiles of the mean streamwise velocity at $x/H = 0.25, 0.5$ and 0.75	103
Figure 6.3 Profiles of the root mean square of the streamwise fluctuating velocity at $x/H = 0.25, 0.5$ and 0.75	103
Figure 6.4 Profiles of the mean concentration at $x/H = 0.25, 0.5$ and 0.75	104
Figure 6.5 Cross-sections of mean velocity with streamlines on the x - z plane, TKE and mean concentration.....	105
Figure 6.6 Streamwise distributions of advective, turbulent and total vertical mass fluxes at $z/H = 1$	106
Figure 6.7 SPOD spectrum (single-sided)	110
Figure 6.8 Eigenfunctions for the seven selected modes	110–112
Figure 6.9 Lissajous curves between the streamwise and vertical components of the seven selected modes at the roof-height centre point.....	116
Figure 6.10 SPOD co-spectrum (single-sided) between the streamwise and vertical fluctuation velocity at the roof-height centre point and SPOD co-spectrum integrated spatially along the roof-height line	117
Figure 6.11 SPOD co-spectrum (single-sided) between the vertical fluctuating velocity and concentration at the roof-height centre point and SPOD co- spectrum integrated spatially along the roof-height line.....	119
Figure 6.12 Spatial-temporal variation in normalised concentration, vertical component of mode A, B2, D1, and D2 on the roof-height line from nondimensional time $tU_{\text{ref}}/H = 0$ –48.....	121

Figure 6.13 Spatial variation of the SPOD co-spectrum values for the seven selected modes along the roof-height line	121
Chapter 7	
Figure 7.1 Simulation domain	130
Figure 7.2 Profiles of the mean streamwise velocity at $x/H = 0.25, 0.5$ and 0.75	132
Figure 7.3 Profiles of the root mean square of the streamwise fluctuating velocity at $x/H = 0.25, 0.5$ and 0.75	132
Figure 7.4 Profiles of the mean concentration at $x/H = 0.25, 0.5$ and 0.75	133
Figure 7.5 Cross-sections of mean velocity with streamlines on the x - z plane, TKE and mean concentration	133
Figure 7.6 SPOD spectrum showing the largest nondimensional eigenvalues plotted versus the nondimensional frequency and wavenumber	141
Figure 7.7 SPOD spectrum showing the second largest nondimensional eigenvalues plotted versus the nondimensional frequency and wavenumber	142
Figure 7.8 Eigenfunctions for the eight selected modes.....	143–150
Figure 7.9 Schematic of the manner by which SPOD spectrum shows multiple physical structures	151
Figure 7.10 SPOD co-spectrum between the streamwise and vertical fluctuation velocity integrated spatially along the line at the roof level line	155
Figure 7.11 SPOD co-spectrum between the vertical fluctuating velocity and concentration integrated spatially along the line at the roof level line	156
Figure 7.12 Spatial variation of the SPOD co-spectrum values for the seven selected modes along the line at the roof level line	158
Figure 7.13 Probability density functions of the fluctuation states	160
Figure 7.14 Probability density functions of the correlation coefficient over the time and spanwise direction.....	163

List of tables

Chapter 4

Table 4.1 CFD simulation conditions	53
Table 4.2 Basic flow features and the corresponding typical SPOD modes	57

Chapter 5

Table 5.1 Parameters used when performing SPOD	81
Table 5.2 Corresponding relations between POD modes and SPOD modes	88

Chapter 6

Table 6.1 CFD simulation conditions	101
Table 6.2 Parameters used when performing SPOD according to the algorithm proposed by Towne et al. (2018)	109
Table 6.3 Percentage of vertical turbulent mass flux at the roof level and whole-field TKE.....	120

Chapter 7

Table 7.1 CFD simulation conditions	130
Table 7.2 Parameters used in the energy and mode estimation when performing SPOD with 2DFT	138
Table 7.3 Zone division and percentages of whole-field TKE and vertical turbulent mass flux at the roof level within the zones	140
Table 7.4 Correlation coefficients between the state of the large-scale structure and the amplitude of the small-scale structure when choosing various modes as the large- and small-scale structure.	161

Nomenclature

Variables

a	mode coefficient
b	building width
c	concentration
\mathbf{C}	two-point correlation
C_{ref}	reference concentration
C_s	Smagorinsky constant
f	frequency
F	volume flux
G	filter function in LES
H	height of building or canyon
k	turbulent kinetic energy
L_y	length of line source, spanwise length of canyon
n	mode index
\mathbf{n}	normal direction vector of surface
N	number of the elements in CFD
N_b	number of blocks in Welch's method
N_F	number of discretisation in DFT
N_o	overlap length in Welch's method
N_s	number of sampling points
N_t	number of snapshots
p	pressure
P	estimated energy percentage accounted for by a certain coherent motion
P_c	source term of the tracer gas
Q	total emission rate
R	correlation coefficient
s	local-space SPOD spectrum
S	area of surface (in Chapter 2)
	spectrum, cross-spectrum, co-spectrum (in other chapters)
S_{ij}	strain-rate tensor
Sc	Schmidt number

Sc_T	sub-grid scale turbulence Schmidt number
t	time
T	length of time series
u	streamwise velocity
\mathbf{u}	velocity vector, $[u, v, w]^T$
u^+	nondimensional velocity
u_τ	friction velocity
U_H	mean inlet velocity at building height
U_{ref}	reference velocity
v	spanwise velocity
V	volume
w	vertical velocity
\mathbf{W}	weight due to the nonuniformity of grid
x	streamwise spatial coordinate
\mathbf{x}	spatial coordinate vector, $[x, y, z]^T$
y	spanwise spatial coordinate
y^+	nondimensional wall distance
z	vertical spatial coordinate
γ	spatial similarity coefficient between SPOD modes
Γ	local space of interest (defined differently in each chapter)
δ	Kronecker delta
ζ_X	state of a fluctuation pattern defined by mode X
ζ_L	state of a fluctuation pattern caused by large-scale structures
ζ_S	state of a fluctuation pattern caused by small-scale structures
η	wavenumber in the spanwise direction
Δ	filter width in LES
τ	time lag
τ_{ij}	SGS stress tensor in LES
λ	mode energy, eigenvalue, SPOD spectrum
ν	kinematic viscosity
ν_T	eddy viscosity
ρ	density
ϕ	general scalar quantity
Φ	general vector or matrix quantity
Ψ	mode, eigenfunction
ω	nodal value of window function in Welch's method
ϖ	element of DFT matrix
Ω	spatial interval

All the bold characters in the thesis denote a vector, a matrix, or a tensor.

Constants

e	Euler's number, base of natural logarithm
E	wall roughness parameter
i	imaginary unit, $\sqrt{-1}$
κ	von Kármán constant
π	circular constant

Acronyms, abbreviations

AIJ	Architectural Institute of Japan
CD	central differencing
CFD	computational fluid dynamics
COST	European Cooperation in the Field of Scientific and Technical Research
DFT	discrete Fourier transform
DNS	direct numerical simulation
DMD	dynamic mode decomposition
EDMD	extended dynamic mode decomposition
EMD	empirical mode decomposition
HHT	Hilbert-Huang transform
IMF	intrinsic mode function
LES	large-eddy simulation
LUD	linear upwind differencing
mPOD	multi-scale proper orthogonal decomposition
PISO	pressure-implicit splitting of operators
POD	proper orthogonal decomposition
QUICK	Quadratic upstream interpolation for convective kinematics
RANS	Reynolds-averaged Navier-Stokes
RMS	root mean square
SGS	subgrid-scale
SIMPLE	semi-implicit method for pressure linked equations
SPOD	spectral proper orthogonal decomposition
TKE	turbulent kinetic energy
TV	total variation
TVD	total variation diminishing
UD	upwind differencing
WTE	wind tunnel experiment
2DFT	two-dimensional Fourier transformation

Operators

$\nabla\Phi$	gradient
$\nabla\cdot\Phi$	divergence
$\nabla^2\Phi$	Laplacian
$[\Phi]$	matrix consisting of Φ from all the elements
$ \Phi $	complex modulus
$\ \Phi\ $	vector norm
Φ'	fluctuation part, $\Phi - E(\Phi)$
Φ''	sub-filter part in LES, $\Phi - \overline{\Phi}$
Φ^T	matrix transpose
Φ^*	complex conjugate
Φ^\dagger	Hermitian transpose
$\hat{\Phi}$	Fourier transform
$\overline{\Phi}$	spatial filtering in LES
	spatial average (in other chapters)
$E(\Phi)$	expectation
$\text{Re}(\Phi)$	real part of complex number
$\text{Im}(\Phi)$	imaginary part of complex number
$\Phi_1 \cdot \Phi_2$	inner product (between vectors, matrices, or tensors)
$\langle \Phi_1, \Phi_2 \rangle$	inner product (between functions)

Chapter 1

Introduction

1.1 Backgrounds

1.1.1 Urban wind environment

The construction of buildings in urban area brings inevitable change to the microclimate. The air flow depends highly on the shape and size of a single building it passes, as well as the interaction of the multiple buildings. The change of the air flow can further change the transport of heat and air pollution. These changes can be either favourable or unfavourable, depending on how they affect the comfort and health of the human beings living in urban area.

On the one hand, the dense and higher-rise buildings in the metropolitan area can block the flow of fresh air into the urban area and deteriorated the ventilation performance inside. The urbanization results in the concentration of pollutants and heat emitted from transportation and residential/industrial facilities, while the weak airflow results in a weak air circulation, making the urban area a thermally uncomfortable space and causing the air pollution problems. From this perspective, it seems that strong winds are preferred.

On the other hand, the local strong winds around high-rise buildings can cause discomfort or even danger to the pedestrian. Since the first report of a human fatal accident due to a gust around a building (Lawson and Penwarden, 1975), the research on the pedestrian-level wind has been more and more conducted. Wind comfort and wind danger criteria has been made in many countries to prevent such wind nuisance by making restrictions to urban design.

The urban design depends on the precise evaluation of the wind environment, and the latter requires effective methods for accurately understanding of the complex flow field.

1.1.2 CFD simulation for outdoor wind environment

Wind tunnel experiment (WTEs) and computational Fluid Dynamics (CFD) simulation are the two main methods for studying the outdoor wind environment. The latter becomes more and more popular today due to the rapid development of the computational technology. Large-eddy simulation (LES) and Reynolds-averaged Navier-Stokes simulations (RANS) are the two most widely used approaches. In RANS, the Navier–Stokes equations are averaged to solve the mean flow. However, the velocity fluctuations still appear in the RANS equations due to the nonlinearity of the Navier–Stokes equations, which is known as the Reynolds stress. To close the equations, Reynolds stress is modelled by known (averaged) quantities. In LES, the velocity fluctuations are resolved, but in large length scales, while the fluctuations in the scale smaller than the filter are modelled. Due to the low computational cost, the applications of RANS in the wind environment, (e.g. Blocken et al., 2012; Liu et al., 2017; Peng et al., 2018) are much more than those of LES (e.g. Adamek et al., 2017; Gousseau et al., 2011). However, the limitation of RANS is its incapability to model the transient features of the flow field such as separation and recirculation downstream of windward edges and vortex shedding in the wake (Blocken, 2018). In general, LES gives more accurate results than RANS (Tominaga and Stathopoulos, 2011)

In the early years, applying CFD to the outdoor wind environment was quite challenging due to the following four main difficulties, summarised by Murakami (1998): (1) the high Reynolds numbers requiring fine grid resolution and accurate wall functions; (2) the highly three-dimensional and complex flow field characterized by impinging, separation, vortex shedding; (3) the numerical problems related to the sharp edges of bluff body; (4) the treatment of the inflow boundary condition, especially in LES. Although the situation has changed a lot with the development of new models and the enhancement of computation ability, these potential problems remain our great concern in the application of CFD.

Compared to the full-scale field measurement or WTE, the main advantages of CFD are that it can provide detailed information of the flow variables in the whole flow field (Blocken, 2018). However, the accuracy and reliability of CFD are concerned, since the simulation is sensitive to many numerical conditions set by the user, including the setting of the computational geometry and grid, turbulent models, boundary conditions, discretisation schemes, wall treatment methods, etc. Therefore, it always requires validation after simulation, in which the results of CFD should be compared to the measurement results.

This stimulates the development of practice guidelines for CFD applications. The most detailed and systematic guidelines for wind environment simulation is provided by Architectural Institute of Japan (AIJ) (Tominaga et al., 2008; Yoshie et al., 2007) and European Cooperation in the Field of Scientific and Technical Research (COST) (Franke et al., 2007). These efforts mainly focus on the instructions towards reliable RANS simulation, but provide little hints for LES application. The AIJ is currently establishing appropriate LES guidelines for the pedestrian wind environment in built-up areas (Okaze et al., 2017).

1.1.3 Coherent turbulent structures

Turbulent flows are a regime in fluid dynamics where the velocity varies irregularly in both space and time. They consist of multi-scale and chaotic motions which can be divided into elementary components, termed as coherent turbulent structures. The notion of “coherence” refers to the property that a turbulent structure must keep its shape for a relatively long time, or appear periodically and intermittently. Therefore, turbulent structures are usually observed and studied by statistical methods.

One of the most typical and basic turbulent structures is the hairpin vortices, which have been suggested to be the main sustaining flow pattern in turbulent boundary layer (Perry and Chong, 1982). Hairpin vortices are usually described as the simplest structures in wall turbulence, through which the momentum is transport and the turbulent kinetic energy is produced (Adrian, 2007). Please refer to the review of Alfonsi (2006) for more of the coherent structures developing in wall-bounded flows.

In building engineering, building structures are usually modelled as three-dimensional finite-length cylinder mounted on the wall (floor), located within an atmospheric boundary layer. The end effect and boundary layer cause the flow field to become complex and strongly three-dimensional (Kawamura et al., 1984; Sumner et al., 2004; Wang et al., 2009). Wang et al. (2004) provided a simplified model for the complex flow structures around a wall-mounted finite-length cylinder with a square cross-section. The four main flow features include the horseshoe vortices, located at the front base of the cylinder; base vortices, developing from the base on the two sides; primary vortex shedding (or Kármán vortex street), along the cylinder sides; and tip vortices, emitting from the free end of the cylinder. The interrelationship between these vortices are further studied by Wang and Zhou (2009), who assumed an integrated model for these vortices.

No doubt that an urban area, consisting of multiple buildings with various shapes, can

produce more complex combination of turbulent structures, or may even generate new type of turbulent structures. As a simplified case study, the turbulent structures produced by a uniform two-dimensional street canyon are studied in many literatures. The turbulent structures in this case can be abstracted by one type of large-scale structures carrying the low- and high- momentum fluids passing through the canyon (Inagaki and Kanda, 2010; Kanda, 2006; Michioka et al., 2011; Michioka and Sato, 2012), and another type of small-scale structures mainly occurring at the roof level of the canyon (Cui et al., 2004; Letzel et al., 2008; Louka et al., 2000). Both were shown to be related to the pollutant removal from the canyon. Blackman and Perret (2016) indicated a non-linear interactions between these two types of structures, that the amplitude of the small-scale structures have a low but unneglectable correlation with the low- and high- momentum fluids of the large-scale structures.

Previous methods for investigating these turbulent structures varied, and were primarily based on quantitative flow visualisation. Both CFD simulations and WTEs provide detailed flow field data for examining flow structures. However, when the target is in the boundary layer flow with a high Reynolds number, which is usually true in studies of building engineering (Uehara et al., 2003), the turbulent motion and the strong perturbation caused by the approaching flow can be obstacles to obtaining a clear visualisation of the featured flow structures. Direct observation of the instantaneous flow field will not provide a clearly recognisable flow structure, while the time-average field will lose the information of chronological vortex development. Moreover, measuring the frequency or the intensity for a certain flow feature can also be a difficult task because the flow field is mixed by the features of all the time scales. Because flow features are controlled by different physical mechanisms that require various physical quantities to describe them, previous research tended to observe these different physical quantities. However, this makes it difficult to compare or study the correlation between features. Similar problems also exist in the design work regarding a turbulent fluid field. For example, due to the lack of quantitatively analysing the turbulent structures around buildings, empirical explanations are usually preferred when assessing and improving the wind environment for an urban area. Understanding the main flow patterns from the turbulence is of vital importance for pedestrian-level wind control or wind pressure assessment on a building surface. The continuing inability to understand the turbulence limits reliable predictions. Thus, this further limits technological advancement in many aspects (Cantwell, 1981).

1.1.4 *POD based analysis methods*

Almost 50 years ago, a technique called proper orthogonal decomposition (POD) was first applied by Lumley (1970, 1967), and has become one of the widely used methods for extracting coherent structures from turbulent flow data. POD is a technique used to obtain a linear basis according to the spatial linear correlation of the data, which allows it to decompose data most efficiently. In subsequent developments, POD has been known as a new analysis tool in wind engineering (Bienkiewicz, 1996). Tamura et al. (1999) reviewed the application of POD in random wind pressure fields and further used it to predict the responses to wind forces acting on buildings. Additionally, Solari et al. (2007) and Carassale et al. (2007) summarized some theoretical aspects and cutting-edge studies on POD with special regard to applications in wind engineering. Recent applications of POD include Kikitsu et al. (2008), who decomposed the wind velocity field in the wake region behind a vibrating three-dimensional square prism and demonstrated systematic structures; Kawai et al. (2012), who investigated the near wake structure behind a 3D square prism and discussed the motion of the arch-type vortex; Wang et al. (2019a), who identified extreme wake patterns of turbulent wind fields around three different rectangular building models measured using particle image velocimetry; Wang et al. (2019b) and Wang and Lam (2019) extracted the symmetric and antisymmetric fluctuating wake characteristics by performing POD on the symmetric or antisymmetric part of the velocity field on several horizontal planes in the near wake.

However, only spatial correlation is considered in the original theory of POD, and because flow is a time-dependent phenomenon in most scenarios, the temporal correlation is also unneglectable to capture the coherent structure with the strongest correlation. A possible solution can be treating the time as the fourth direction in addition to the three spatial coordinates. In such way, four-dimensional modes will be provided in POD. Theoretically, if the flow field is homogeneous in one or more directions, the spectrum of the eigenvalues becomes continuous and the eigenfunctions become Fourier modes (Aubry et al., 1988). Therefore, combining Fourier transformation with POD is a better application. The fluctuations along the inhomogeneous directions can be analysed by POD, and the fluctuations along the homogeneous directions are decomposed by Fourier analysis.

Following this idea, spectral POD (SPOD) was developed (Picard and Delville, 2000), which treats the fluctuation along time as homogeneous. This makes SPOD as an advanced technique of performing POD analysis in the frequency domain via discrete Fourier transform (DFT). This approach is expected to be an effective method in elucidating the spatiotemporal structures of flows (Towne et al., 2018). SPOD has been

applied to a variety of flows. Recent applications include boundary layers (Tutkun and George, 2017), the wake of a wind turbine (Araya et al., 2017), turbulent jets (Schmidt et al., 2017), and the flow around an airfoil (Abreu et al., 2017). However, the applications are still few, and no reports have been found in the field of wind environments.

In addition to the SPOD, other DFT-POD hybrid approaches were also developed recently. The decomposition proposed by Sieber et al. (2016), which was also called SPOD, applied a low-pass filter along the diagonals of POD correlation matrix to force POD to resemble DFT. The multi-scale proper orthogonal decomposition (mPOD) proposed by Mendez et al. (2019) combined the ideas from Sieber's SPOD and the SPOD in Towne et al. (2018) to integrate their advantages. However, none of the aforementioned methods preserve the orthogonality property. Thus, the spatial modes are not mutually orthogonal. The orthogonality property of POD or SPOD makes it easy to compute the mode energy and provides comprehensible physical meaning to mode energy. It directly connects mode energy to turbulent kinetic energy (TKE), or root mean square (RMS) velocity fluctuation, which is considered convenient in the applications of wind engineering and wind environment assessment.

1.1.5 Other modal analysis methods: Koopman analysis and DMD

In addition to POD, there exist other modal analysis methods developed for elucidate the physically important features of the flow. In this section, the series of methods based on the Koopman analysis and dynamic mode decomposition (DMD) are briefly reviewed, while other methods, mainly applied in turbulence control, are not included in the review of this section. For a complete introduction of modal analysis methods in fluid mechanics, please refer to Taira et al. (2017).

The Koopman operator is an infinite dimensional linear operator for describing a nonlinear dynamical system by describe the evolution of observables with infinite numbers (Koopman, 1931). The observables are related to the states of the system, and thus are described mathematically as the functions of states. To fully capture the nonlinear dynamics, one may need to observe on an infinite number of such functions, while this is impossible in application. The idea of Mezić (2005) is to decompose the infinite dimensional Koopman operator into dynamically relevant modes based on the eigenfunctions. Then, a truncation can be made, and the infinite dimensional Koopman operator can be approximated by the combination of the modes with a finite number. Each mode describes a spatial motion of the fluid, multiplied by a time-dependent

function, $\exp(\lambda t)$, where λ is a complex-valued eigenvalue describing the oscillation characteristics of such a motion. The methods based on the Koopman operator decomposition are applied in the analysis the flow past a circular cylinder (Bagheri, 2013), neural data (Brunton et al., 2016), and power system (Susuki et al., 2016), and were proved useful.

In most applications, the explicit form of the dynamical system is unknown, and only the snapshot data at the timesteps within an infinite time period are available. In these cases, data-driven methods are preferred. The first of such approach was DMD (Schmid, 2010), which implicitly uses the linear combination of the states as the dictionary of the observables. Rowley et al. (2009) demonstrated that DMD modes constitute a subset of Koopman modes. Chen et al. (2012) proved that DMD will reduce essentially to the discrete Fourier transform if the mean of snapshots is subtracted. After the development of DMD, many modifications have been developed aiming for making the decomposition results closer to Koopman operator decomposition. Extended DMD (EDMD), developed by Williams et al. (2015a), applied a more complicate dictionary (e.g. high-order polynomials) of the observable functions so that it is more powerful when applied to nonlinear systems. However, this rich dictionary can easily reach the boundary that the algorithm is invalid to perform. The solution is provided by Williams et al. (2015b), where the kernel trick is applied. This medicated approach is call kernel DMD. However, the careful choice of the dictionary is needed, since it largely affects the decomposition results which should be converge to the Koopman modes. This issue is addressed by Li et al. (2017), where they employed ideas from machine learning to improve EDMD. The limitation of this approach is the low computational speed, so it is considered unpracticable in urban wind environment where extremely high dimensional nonlinear systems are dealing with.

1.1.6 Method comparison for time series analysis

The flow fields are usually spatiotemporal data, which requires the modal analysis methods to deal with the fluctuations along multiple directions (i.e., the spatial directions and time). The methods applied for different directions can be either the same or different. One can apply the same methods for multiple directions, which results in a multi-dimensional version of the method. Alternatively, one can also apply the multiple methods for multiple directions, which results in a combined method. For better comparison, this section discusses the methods applied to the fluctuation along a single direction—time. The time series analysis methods are listed as follows.

(1) *Fourier transform*. Fourier transform is the most frequently used transform that decomposes functions depending on time into sinusoid basis functions depending on temporal frequency. The Fourier transform of a function is a complex-valued function of frequency, whose magnitude represents the amount of that frequency present in the original function, and whose argument is the phase offset of the basic sinusoid in that frequency.

(2) *Karhunen–Loève transform*. If POD is performed on a single stochastic process, it reduces to Karhunen–Loève transform. Similar to the description of POD, Karhunen–Loève transform represents a stochastic process as a linear combination of orthogonal functions, i.e., a function basis (Ghanem and Spanos, 1991). For a homogeneous process, the Karhunen–Loève basis is then a Fourier basis (Aubry et al., 1988).

(3) *Koopman analysis and DMD*. Although Koopman analysis treats the spatial and temporal fluctuations differently, it is a systematic method where the spatial and temporal processes cannot be separated. Here, we only inspect how it treats the temporal fluctuation. In Koopman analysis, each mode describes a spatial motion of the fluid, multiplied by a time-dependent function in the form of $\exp(\lambda t)$ (Mezić, 2013). As a subset of Koopman modes, DMD modes will reduce to DFT modes if the mean of snapshots is subtracted (Chen et al., 2012).

(4) *Hilbert transform*. Hilbert transform is a linear operator that produces a 90° phase shift in a signal. It is useful for analysing nonstationary signals by expressing frequency as a rate of change in phase, so that the frequency can vary with time. Combining the original signal and its Hilbert transform, the instantaneous frequency can be obtained. However, multiple time-varying frequencies coexist typically in raw recordings. Therefore, decomposing the time signal before computing the instantaneous frequency is suggested, which results in the following methods.

(5) *Empirical mode decomposition (EMD) and Hilbert-Huang transform (HHT)*. EMD is a method of breaking down a signal without leaving the time domain. It decomposes a signal into so-called intrinsic mode functions (IMFs) which form a complete and nearly orthogonal basis for the original signal. HHT (Huang et al., 1998) further applies the Hilbert transform to the IMFs to obtain instantaneous frequency data. EMD and HHT are designed to work well for data that is nonstationary and nonlinear. In contrast to other common transforms like the Fourier transform, EMD and HHT are more like an algorithm (an empirical approach) that can be applied to a data set, rather than a theoretical tool.

(6) *Wavelet transform*. A wavelet is a wave-like oscillation with an amplitude that begins at zero, increases, and then decreases back to zero. Wavelet transform decomposes a function into a set of wavelets with various scales and locations. By using wavelet transform, one can extract local spectral and temporal information simultaneously. While a major disadvantage of the Fourier transform is it only captures global frequency information.

The flow around the buildings is usually considered as homogenous and, sometimes even, stationary temporal stochastic process in many researches and designs. Therefore, expect for the long-lasting regular or periodic fluctuations lying in the field, other stochastic or transient temporal variation is inconsequential in the study. A combination of POD and Fourier analysis is considered sufficient for the analysis.

1.2 Research objectives

The limitations of previous studies with regard to a turbulent flow around buildings are mainly caused by the lack of methods for quantitatively and concretely analysing the turbulent structures, while modal analysis methods are considered to be the potential solutions. In this study, SPOD is chosen to be the tool for decomposing the turbulent flow and elucidating the turbulent structures. As a start of applying SPOD in wind environment, the research targets are chosen to be the two most fundamental and classical cases: (1) the flow field around single square-section building model and (2) the two-dimensional street canyon flow. The effectivity of SPOD when applied on the cases with high Reynolds numbers is investigated. In addition to the turbulent structure identification, this study also focusses on the developing mathematical tools for evaluating the pedestrian-level wind environment and outdoor air exchanging. The questions to be addressed in the present study are listed as follow.

- (1) For the case of single square-section building model:
 - a. What are the main turbulent structures around this single building? How do they move in space over time?
 - b. How much is primary frequency and intensity of each turbulent structure? Especially, how to evaluate these quantities quantitatively?
 - c. How to evaluate and identify the main turbulent structures which determine the dynamics within a local space of interest?
 - d. How do these turbulent structures influence the pedestrian-level wind? How to identify the main cause of a too-large fluctuation wind velocity at a certain point of interest?

e. How does the inflow fluctuation influence the turbulent structures around the building, and further influence the pedestrian-level wind?

(2) For the case of two-dimensional street canyon:

a. What are the main turbulent structures within the two-dimensional street canyon flow?

We have known that these turbulent structures were described as large- and small-scale structures by the statistics performed in the previous studies, but what do they exactly look like? How do they move in space over time?

b. Which of these turbulent structures relate to ejection and sweep events at the roof level?

How much do they contribute to the pollutant removal at the roof level, quantitatively?

c. How do these turbulent structures perform on the spanwise direction? And again, how do these characteristics on the spanwise direction relate to ejection and sweep events and pollutant removal at the roof level?

d. What is nonlinear interactions between the large- and small-scale structures? How much are the small-scale structures amplified or suppressed by the large-scale structures?

1.3 Thesis structure

The structure of this thesis is illustrated in Figure 1.1, which also provides the theme of each chapter. The thesis is divided into five parts and eight chapters:

(1) The first part, i.e., Chapter 1, introduces the research background and clarifies the research purpose.

(2) All the fundamental theories applied in this study are introduced in the second parts. The basic theories and algorithms of CFD and SPOD are briefly explained.

(3) In third part, we start to apply SPOD on the flow around a square-section building model. In Chapter 4, the analysis is performed on the three-dimensional velocity field obtained by LES. We present a comprehensive view of the three-dimensional turbulent structures in this flow, which is an integration of almost all the flow features. The identified flow features are visualised to examine the details, and then compared to previous studies. Based on the SPOD theory, new quantities are defined to quantitatively reveal the primary frequency and relative intensity of these flow features. In addition, the local-space spectrum was proposed to observe the detailed energy composition within a local space, to show which flow features directly related to the fluctuation within this local space. In Chapter 5, the target is focused on the pedestrian-level wind of the same

case. The turbulent structures that have large influence on the pedestrian-level wind is examined. The SPOD results for two simulation cases are compared, where the only difference is the existence of fluctuation at the inflow boundary, to show how the inflow fluctuation influenced the turbulent structures around the building. Finally, a mathematical tool is developed to pinpoint the main cause of a too-large wind fluctuation at a certain point of interest, which is considered useful in attempting to improve pedestrian wind comfort.

(4) SPOD is also applied on the two-dimensional canyon flow in the fourth part. In Chapter 6, this study begins by reproducing the LES for a two-dimensional street canyon with reference to the simulation and wind tunnel experiment conducted by Michioka et al. (2011). SPOD technique is applied to decompose the velocity field. The SPOD modes, depicting the large-scale coherent structures and Kelvin–Helmholtz instabilities, are well extracted and visualised. The ejection events and pollutant removal are quantitatively analysed using the newly defined SPOD co-spectra to understand their relationships with the turbulent fluctuation patterns. Chapter 7 continues the study, but the spanwise performance of the structures are mainly focused on. This is done by modifying the original SPOD to the one combining 2DFT. The SPOD co-spectrum defined in our previous study is also modified to a 2DFT version. These tools are applied to the street canyon case as the post-processing methods to further study on the turbulent structures and pollutant removal mechanism. Finally, based on these results, the nonlinear interactions between the large- and small-scale structures are discussed.

(5) The final part, i.e., Chapter 8, closes the thesis, summarises the findings obtained of this study, and prospects future studies.

Introduction

Chapter 1: Backgrounds and reseach objectives

Fundamental theories

Chapter 2: CFD
Chapter 3: SPOD

Flow around a single building

Chapter 4: Turbulent structure identification
Chapter 5: Influence on pedestrain-level wind

Street canyon flow

Chapter 6: Turbulent structures and pollutant removal mechanism
Chapter 7: Spanwise performance and nonlinear interactions

Close

Chapter 8: Conclusions and prospective

Figure 1.1 Thesis structure and theme of each chapter.

Reference

- Abreu, L.I., Cavalieri, A.V.G., Wolf, W.R., 2017. Coherent hydrodynamic waves and trailing-edge noise, in: 23rd AIAA/CEAS Aeroacoustics Conference, 2017. American Institute of Aeronautics and Astronautics Inc, AIAA. <https://doi.org/10.2514/6.2017-3173>
- Adamek, K., Vasan, N., Elshaer, A., English, E., Bitsuamlak, G., 2017. Pedestrian level wind assessment through city development: A study of the financial district in Toronto. *Sustain. Cities Soc.* 35, 178–190. <https://doi.org/10.1016/J.SCS.2017.06.004>
- Adrian, R.J., 2007. Hairpin vortex organization in wall turbulence. *Phys. Fluids* 19, 41301. <https://doi.org/10.1063/1.2717527>
- Alfonsi, G., 2006. Coherent structures of turbulence: Methods of eduction and results. *Appl. Mech. Rev.* 59, 307–323. <https://doi.org/10.1115/1.2345370>
- Araya, D.B., Colonius, T., Dabiri, J.O., 2017. Transition to bluff-body dynamics in the wake of vertical-axis wind turbines. *J. Fluid Mech.* 813, 346–381. <https://doi.org/10.1017/jfm.2016.862>
- Aubry, N., Holmestil, P., John, L., Stone, E., 1988. The dynamics of coherent structures in the wall region of a turbulent boundary layer. *J. Fluid Mech.* 192, 115–173. <https://doi.org/10.1017/S0022112088001818>
- Bagheri, S., 2013. Koopman-mode decomposition of the cylinder wake. *J. Fluid Mech.* 726, 596–623. <https://doi.org/10.1017/jfm.2013.249>
- Bienkiewicz, B., 1996. New tools in wind engineering. *J. Wind Eng. Ind. Aerodyn.* 65, 279–300. [https://doi.org/10.1016/S0167-6105\(97\)00047-0](https://doi.org/10.1016/S0167-6105(97)00047-0)
- Blackman, K., Perret, L., 2016. Non-linear interactions in a boundary layer developing over an array of cubes using stochastic estimation. *Phys. Fluids* 28, 095108. <https://doi.org/10.1063/1.4962938>
- Blocken, B., 2018. LES over RANS in building simulation for outdoor and indoor applications: A foregone conclusion? *Build. Simul.* 11, 821–870. <https://doi.org/10.1007/s12273-018-0459-3>
- Blocken, B., Janssen, W.D., van Hooff, T., 2012. CFD simulation for pedestrian wind

- comfort and wind safety in urban areas: General decision framework and case study for the Eindhoven University campus. *Environ. Model. Softw.* 30, 15–34. <https://doi.org/10.1016/J.ENVSOFT.2011.11.009>
- Brunton, B.W., Johnson, L.A., Ojemann, J.G., Kutz, J.N., 2016. Extracting spatial-temporal coherent patterns in large-scale neural recordings using dynamic mode decomposition. *J. Neurosci. Methods* 258, 1–15. <https://doi.org/10.1016/j.jneumeth.2015.10.010>
- Cantwell, B.J., 1981. Organized Motion in Turbulent Flow. *Annu. Rev. Fluid Mech.* 13, 457–515. <https://doi.org/10.1146/annurev.fl.13.010181.002325>
- Chen, K.K., Tu, J.H., Rowley, C.W., 2012. Variants of dynamic mode decomposition: Boundary condition, Koopman, and fourier analyses. *J. Nonlinear Sci.* 22, 887–915. <https://doi.org/10.1007/s00332-012-9130-9>
- Cui, Z., Cai, X., J. Baker, C., 2004. Large-eddy simulation of turbulent flow in a street canyon. *Q. J. R. Meteorol. Soc.* 130, 1373–1394. <https://doi.org/10.1256/qj.02.150>
- Franke, J., Hellsten, A., Schlünzen, H., Carissimo, B., 2007. Best Practice Guideline for the CFD Simulation of Flows in the Urban Environment. COST Office, Brussels.
- Ghanem, R.G., Spanos, P.D., 1991. Stochastic Finite Elements: A Spectral Approach, Stochastic Finite Elements: A Spectral Approach. Springer New York. <https://doi.org/10.1007/978-1-4612-3094-6>
- Gousseau, P., Blocken, B., Stathopoulos, T., van Heijst, G.J.F., 2011. CFD simulation of near-field pollutant dispersion on a high-resolution grid: A case study by LES and RANS for a building group in downtown Montreal. *Atmos. Environ.* 45, 428–438. <https://doi.org/10.1016/j.atmosenv.2010.09.065>
- Huang, N.E., Shen, Z., Long, S.R., Wu, M.C., Snin, H.H., Zheng, Q., Yen, N.C., Tung, C.C., Liu, H.H., 1998. The empirical mode decomposition and the Hubert spectrum for nonlinear and non-stationary time series analysis. *Proc. R. Soc. A Math. Phys. Eng. Sci.* 454, 903–995. <https://doi.org/10.1098/rspa.1998.0193>
- Inagaki, A., Kanda, M., 2010. Organized structure of active turbulence over an array of cubes within the logarithmic layer of atmospheric flow. *Boundary-Layer Meteorol.* 135, 209–228. <https://doi.org/10.1007/s10546-010-9477-0>
- Kanda, M., 2006. Large-eddy simulations on the effects of surface geometry of building arrays on turbulent organized structures. *Boundary-Layer Meteorol.* 118, 151–168. <https://doi.org/10.1007/s10546-005-5294-2>
- Kawai, H., Okuda, Y., Ohashi, M., 2012. Near wake structure behind a 3D square prism with the aspect ratio of 2.7 in a shallow boundary layer flow. *J. Wind Eng. Ind. Aerodyn.* 104–106, 196–202. <https://doi.org/10.1016/j.jweia.2012.04.019>
- Kawamura, T., Hiwada, M., Hibino, T., Mabuchi, I., Kumada, M., 1984. Flow around a Finite Circular Cylinder on a Flat Plate : Cylinder height greater than turbulent boundary layer thickness. *Bull. JSME* 27, 2142–2151. <https://doi.org/10.1299/jsme1958.27.2142>
- Kikitsu, H., Okuda, Y., Ohashi, M., Kanda, J., 2008. POD analysis of wind velocity field in the wake region behind vibrating three-dimensional square prism. *J. Wind Eng. Ind. Aerodyn.* 96, 2093–2103. <https://doi.org/10.1016/J.JWEIA.2008.02.057>
- Koopman, B.O., 1931. Hamiltonian Systems and Transformation in Hilbert Space. *Proc. Natl. Acad. Sci.* 17, 315–318. <https://doi.org/10.1073/pnas.17.5.315>
- Lawson, T. V, Penwarden, A.D., 1975. The effects of wind on people in the vicinity of buildings., in: *Proceedings of the Fourth International Conference on Wind Effects on Buildings and Structures*. Cambridge University Press, Heathrow, pp. 605–622.
- Letzel, M.O., Krane, M., Raasch, S., 2008. High resolution urban large-eddy simulation studies from street canyon to neighbourhood scale. *Atmos. Environ.* 42, 8770–8784. <https://doi.org/10.1016/j.atmosenv.2008.08.001>
- Li, Q., Dietrich, F., Bollt, E.M., Kevrekidis, I.G., 2017. Extended dynamic mode decomposition with dictionary learning: A data-driven adaptive spectral decomposition of the koopman operator. *Chaos* 27, 103111. <https://doi.org/10.1063/1.4993854>
- Liu, S., Pan, W., Zhang, H., Cheng, X., Long, Z., Chen, Q., 2017. CFD simulations of wind distribution in an urban community with a full-scale geometrical model. *Build. Environ.* 117, 11–23. <https://doi.org/10.1016/j.buildenv.2017.02.021>

- Louka, P., Belcher, S.E., Harrison, R.G., 2000. Coupling between air flow in streets and the well-developed boundary layer aloft. *Atmos. Environ.* 34, 2613–2621. [https://doi.org/10.1016/S1352-2310\(99\)00477-X](https://doi.org/10.1016/S1352-2310(99)00477-X)
- Lumley, J.L., 1970. *Stochastic Tools in Turbulence*. Academic Press.
- Lumley, J.L., 1967. The structure of inhomogeneous turbulent flows. *Atmos. Turbul. wave Propag.* 166–178.
- Mendez, M.A., Balabane, M., Buchlin, J.M., 2019. Multi-scale proper orthogonal decomposition of complex fluid flows. *J. Fluid Mech.* 870, 988–1036. <https://doi.org/10.1017/jfm.2019.212>
- Mezić, I., 2013. Analysis of Fluid Flows via Spectral Properties of the Koopman Operator. *Annu. Rev. Fluid Mech.* 45, 357–378. <https://doi.org/10.1146/annurev-fluid-011212-140652>
- Mezić, I., 2005. Spectral properties of dynamical systems, model reduction and decompositions. *Nonlinear Dyn.* 41, 309–325. <https://doi.org/10.1007/s11071-005-2824-x>
- Michioka, T., Sato, A., 2012. Effect of Incoming Turbulent Structure on Pollutant Removal from Two-Dimensional Street Canyon. *Boundary-Layer Meteorol.* 145, 469–484. <https://doi.org/10.1007/s10546-012-9733-6>
- Michioka, T., Sato, A., Takimoto, H., Kanda, M., 2011. Large-Eddy Simulation for the Mechanism of Pollutant Removal from a Two-Dimensional Street Canyon. *Boundary-Layer Meteorol.* 138, 195–213. <https://doi.org/10.1007/s10546-010-9556-2>
- Murakami, S., 1998. Overview of turbulence models applied in CWE-1997. *J. Wind Eng. Ind. Aerodyn.* 74–76, 1–24. [https://doi.org/10.1016/S0167-6105\(98\)00004-X](https://doi.org/10.1016/S0167-6105(98)00004-X)
- Okaze, T., Kikumoto, H., Ono, H., Imano, M., Hasama, T., Kishida, T., Nakao, K., Ikegaya, N., Tabata, Y., Tominaga, Y., 2017. Large-eddy simulations of flow around a high-rise building: validation and sensitivity analysis on turbulent statistics, in: *7th European and African Conference on Wind Engineering*. Liege, Belgium.
- Peng, L., Liu, J.P., Wang, Y., Chan, P. wai, Lee, T. cheung, Peng, F., Wong, M. sing, Li, Y., 2018. Wind weakening in a dense high-rise city due to over nearly five decades of urbanization. *Build. Environ.* 138, 207–220. <https://doi.org/10.1016/j.buildenv.2018.04.037>
- Perry, A.E., Chong, M.S., 1982. On the mechanism of wall turbulence. *J. Fluid Mech.* 119, 173–217. <https://doi.org/10.1017/S0022112082001311>
- Picard, C., Delville, J., 2000. Pressure velocity coupling in a subsonic round jet, in: *International Journal of Heat and Fluid Flow*. Elsevier Science Inc, pp. 359–364. [https://doi.org/10.1016/S0142-727X\(00\)00021-7](https://doi.org/10.1016/S0142-727X(00)00021-7)
- Rowley, C.W., Mezi, I., Bagheri, S., Schlatter, P., Henningson, D.S., 2009. Spectral analysis of nonlinear flows. *J. Fluid Mech.* 641, 115–127. <https://doi.org/10.1017/S0022112009992059>
- Schmid, P.J., 2010. Dynamic mode decomposition of numerical and experimental data. *J. Fluid Mech.* 656, 5–28. <https://doi.org/10.1017/S0022112010001217>
- Schmidt, O.T., Towne, A., Colonius, T., Cavalieri, A.V.G., Jordan, P., Brès, G.A., 2017. Wavepackets and trapped acoustic modes in a turbulent jet: Coherent structure eduction and global stability. *J. Fluid Mech.* 825, 1153–1181. <https://doi.org/10.1017/jfm.2017.407>
- Sieber, M., Paschereit, C.O., Oberleithner, K., 2016. Spectral proper orthogonal decomposition. *J. Fluid Mech.* 792, 798–828. <https://doi.org/10.1017/jfm.2016.103>
- Solari, G., Carassale, L., Tubino, F., 2007. Proper orthogonal decomposition in wind engineering - Part 1: A state-of-the-art and some prospects. *Wind Struct.* 10, 153–176. <https://doi.org/10.12989/was.2007.10.2.153>
- Sumner, D., Heseltine, J.L., Dansereau, O.J.P., 2004. Wake structure of a finite circular cylinder of small aspect ratio. *Exp. Fluids* 37, 720–730. <https://doi.org/10.1007/s00348-004-0862-7>
- Susuki, Y., Mezi, I., Raak, F., Hikiyara, T., 2016. Applied Koopman operator theory for power systems technology. *Nonlinear Theory Its Appl. IEICE* 7, 430–459.

- <https://doi.org/10.1587/nolta.7.430>
- Taira, K., Brunton, S.L., Dawson, S.T.M., Rowley, C.W., Colonius, T., McKeon, B.J., Schmidt, O.T., Gordeyev, S., Theofilis, V., Ukeiley, L.S., 2017. Modal Analysis of Fluid Flows: An Overview. *AIAA J.* 55, 4013–4041. <https://doi.org/10.2514/1.J056060>
- Tamura, Y., Suganuma, S., Kikuchi, H., Hibi, K., 1999. Proper orthogonal decomposition of random wind pressure field. *J. Fluids Struct.* 13, 1069–1095. <https://doi.org/10.1006/jfls.1999.0242>
- Tominaga, Y., Mochida, A., Yoshie, R., Kataoka, H., Nozu, T., Yoshikawa, M., Shirasawa, T., 2008. AIJ guidelines for practical applications of CFD to pedestrian wind environment around buildings. *J. Wind Eng. Ind. Aerodyn.* 96, 1749–1761. <https://doi.org/10.1016/J.JWEIA.2008.02.058>
- Tominaga, Y., Stathopoulos, T., 2011. CFD modeling of pollution dispersion in a street canyon: Comparison between LES and RANS. *J. Wind Eng. Ind. Aerodyn.* 99, 340–348. <https://doi.org/10.1016/j.jweia.2010.12.005>
- Towne, A., Schmidt, O.T., Colonius, T., 2018. Spectral proper orthogonal decomposition and its relationship to dynamic mode decomposition and resolvent analysis. *J. Fluid Mech.* 847, 821–867. <https://doi.org/10.1017/jfm.2018.283>
- Tutkun, M., George, W.K., 2017. Lumley decomposition of turbulent boundary layer at high Reynolds numbers. *Phys. Fluids* 29. <https://doi.org/10.1063/1.4974746>
- Uehara, K., Wakamatsu, S., Ooka, R., 2003. Studies on critical Reynolds number indices for wind-tunnel experiments on flow within urban areas. *Boundary-Layer Meteorol.* 107, 353–370. <https://doi.org/10.1023/A:1022162807729>
- Wang, F., Cheng, L., Lam, K.M., 2019a. POD characterisation of extreme wake patterns of turbulent wind fields past rectangular buildings. *Environ. Fluid Mech.* 1–31. <https://doi.org/10.1007/s10652-019-09683-z>
- Wang, F., Lam, K.M., 2019. Geometry effects on mean wake topology and large-scale coherent structures of wall-mounted prisms. *Phys. Fluids* 31, 125109. <https://doi.org/10.1063/1.5126045>
- Wang, F., Lam, K.M., Zu, G.B., Cheng, L., 2019b. Coherent structures and wind force generation of square-section building model. *J. Wind Eng. Ind. Aerodyn.* 188, 175–193. <https://doi.org/10.1016/j.jweia.2019.02.019>
- Wang, H., Zhou, Y., Chan, C., Zhou, T., 2009. Momentum and heat transport in a finite-length cylinder wake. *Exp. Fluids* 46, 1173–1185. <https://doi.org/10.1007/s00348-009-0620-y>
- Wang, H.F., Zhou, Y., 2009. The finite-length square cylinder near wake. *J. Fluid Mech.* 638, 453–490. <https://doi.org/10.1017/S0022112009990693>
- Wang, H.F., Zhou, Y., Chan, C.K., Wong, W.O., Lam, K.S., 2004. Flow Structure Around A Finite-Length Square Prism, in: 15th Australasian Fluid Mechanics Conference . Sydney, Australia.
- Williams, M.O., Kevrekidis, I.G., Rowley, C.W., 2015a. A Data-Driven Approximation of the Koopman Operator: Extending Dynamic Mode Decomposition. *J. Nonlinear Sci.* 25, 1307–1346. <https://doi.org/10.1007/s00332-015-9258-5>
- Williams, M.O., Rowley, C.W., Kevrekidis, I.G., 2015b. A kernel-based method for data-driven Koopman spectral analysis. *J. Comput. Dyn.* 2, 247–265. <https://doi.org/10.3934/jcd.2015005>
- Yoshie, R., Mochida, A., Tominaga, Y., Kataoka, H., Harimoto, K., Nozu, T., Shirasawa, T., 2007. Cooperative project for CFD prediction of pedestrian wind environment in the Architectural Institute of Japan. *J. Wind Eng. Ind. Aerodyn.* 95, 1551–1578. <https://doi.org/10.1016/J.JWEIA.2007.02.023>

Chapter 2

CFD simulation for urban wind environment

2.1 Overview

This chapter briefly summarise the CFD techniques used in the simulation of urban wind environment. The wind flow in urban areas is usually simulated as incompressible fluids governed by incompressible Navier-Stokes equations, which is provided in Section 2.2. Section 2.3 briefly introduced the numerical methods used in solving the equation, including the spatial and temporal discretisation and solving algorithm. To avoid enormous and unfordable calculation, the turbulence is modelled by either RANS or LES in practice. The latter is introduced in Section 2.4 and applied in the studies in the subsequent chapters.

2.2 Governing equations

The wind flow in urban areas is turbulent flow, whose motion is described by the governing equations of the fluid in general. The governing equations are derived from the conservation laws of mass and momentum. For meteorological problems, both the equations expressing the state of the air and the laws of thermodynamics are naturally required. However, considering that the thermal influence on the urban flow during the strong winds is relatively small, the simulation target is simplified to an isothermal flow field. In the simulation, the velocity vector $\mathbf{u} = [u, v, w]^T$ and pressure p of the air are expressed as the functions of time t and position $\mathbf{x} = [x, y, z]^T$.

First, the conservation of mass is considered. Since the flow speed is far lower than the sonic speed, the fluid is considered incompressible, that is, the density is constant. The conservation of mass indicates that, for an arbitrary control volume in the domain, the volume of the fluid flowing in is equal to the volume flowing out. Mathematically, it is expressed as

$$\nabla \cdot \mathbf{u} = 0. \tag{2.1}$$

Then, the equation for the conservation of momentum can be written as

$$\underbrace{\frac{\partial \mathbf{u}}{\partial t}}_{\text{transient term}} + \underbrace{\nabla \cdot (\mathbf{u}\mathbf{u}^\top)}_{\text{convective term}} = - \underbrace{\frac{1}{\rho} \nabla p}_{\text{pressure term}} + \underbrace{\nu \nabla^2 \mathbf{u}}_{\text{diffusion term}}, \quad (2.2)$$

where ρ and ν are the density and kinematic viscosity of air, respectively, which are considered constant. Eq. (2.2), usually called Navier-Stokes equation, indicates that the temporal variation of the momentum of the fluid per mass is caused by the pressure and frictional force. When dealing with the atmospheric boundary layer, the Coriolis force caused by the rotation of the earth and the buoyancy caused by the temperature difference should also be considered, and added to the right side of Eq. (2.2) as the source term. The governing equations can also be written in the tensor form as

$$\frac{\partial u_i}{\partial x_i} = 0, \quad (2.3)$$

$$\frac{\partial u_i}{\partial t} + \frac{\partial (u_i u_j)}{\partial x_j} = - \frac{1}{\rho} \frac{\partial p}{\partial x_i} + \nu \frac{\partial^2 u_i}{\partial x_j \partial x_j}. \quad (2.4)$$

2.3 Numerical methods

2.3.1 Spatial discretisation

For the first step, the space where the flow is to be computed is divided into a large number of geometrical elements called grid cells. As the requirements, there should be no holes between the grid cells, and the grid cells do not overlap. In addition, the grid cells should be as regular as possible with no abrupt changes in the volume or in the stretching ratio.

Subsequently, as the calculation domain has been divided into small elements, the governing equations are discretised by the finite volume method. The governing equation (2.2) is integrated over the J th element Ω_J as

$$\int_{\Omega_J} \frac{\partial \mathbf{u}}{\partial t} d\mathbf{x} + \int_{\Omega_J} \nabla \cdot (\mathbf{u}\mathbf{u}^\top) d\mathbf{x} = \int_{\Omega_J} \left(-\frac{1}{\rho} \nabla p \right) d\mathbf{x} + \int_{\Omega_J} \nu \nabla^2 \mathbf{u} d\mathbf{x}, \quad J = 1, 2, \dots, N. \quad (2.5)$$

N is the total number of the elements. The transient and the pressure terms are usually considered constant in the small element. The equation is further divided by the element volume V_J , we get

$$\left(\frac{\partial \mathbf{u}}{\partial t} \right)_J + \underbrace{\frac{1}{V_J} \int_{\Omega_J} \nabla \cdot (\mathbf{u}\mathbf{u}^\top) d\mathbf{x}}_{\text{Con}_J} = \underbrace{\frac{1}{V_J} \int_{\Omega_J} \left(-\frac{1}{\rho} \nabla p \right) d\mathbf{x}}_{\text{Pre}_J} + \underbrace{\frac{1}{V_J} \int_{\Omega_J} \nu \nabla^2 \mathbf{u} d\mathbf{x}}_{\text{Dif}_J}, \quad J = 1, 2, \dots, N, \quad (2.6)$$

where the quantities with the subscript J denotes their values within the J th element. For brevity, the vector consisting of the values from all the elements is represented by the quantity within square brackets. For instance, the velocity within the J th element is represented by \mathbf{u}_J , and the vector consisting of the velocities in all the elements is represented by $[\mathbf{u}]$, that is,

$$[\mathbf{u}] = \begin{bmatrix} \vdots \\ \mathbf{u}_J \\ \vdots \end{bmatrix}. \quad (2.7)$$

Now Eq. (2.6) is written in the matrix form as

$$\frac{\partial [\mathbf{u}]}{\partial t} + [Con] = [Pre] + [Dif]. \quad (2.8)$$

The goal at this point is to express all these terms in Eq. (2.8) as the linear combinations of the velocity and pressure values at the cell centroids. If it is done, the momentum equation (2.8) can be written into the algebraic form as

$$[A][\mathbf{u}] = [B][p] + [C], \quad (2.9)$$

where $[A]$, $[B]$, and $[C]$ are the already-known coefficient matrices, whose sizes are $3N \times 3N$, $3N \times N$, and $3N \times 1$, respectively. The continuity equation (2.1) is discretised as

$$\nabla \cdot [\mathbf{u}] = 0, \quad (2.10)$$

where the operator on the aggregated vector is defined as $\nabla \cdot [\mathbf{u}] \equiv [\nabla \cdot \mathbf{u}]$, which converts a $3N \times 1$ vector to a $N \times 1$ vector. The velocity-pressure coupling problem indicated by Eq. (2.9) with the restriction of Eq. (2.10) can be solved by numerical procedures. The widely used ones are the semi-implicit method for pressure linked equations (SIMPLE) algorithm (Patankar and Spalding, 1972) and the pressure-implicit splitting of operators (PISO) algorithm (Issa, 1986).

The following subsections will be arranged as follows: The discretisation methods of the transient, convective, pressure and diffusion terms are introduced in Subsection 2.3.2 to 2.3.5, respectively. The PISO algorithm is introduced in Subsection 2.3.6 to solve the velocity-pressure coupling problem indicated by Eqs. (2.9) and (2.10).

2.3.2 Time matching method

The transient term in Eq. (2.8) is discretised by the time matching methods. the time matching methods provide the link between the already-known flow state at time t and the unknown flow state at time $t + \Delta t$. By solving the state step-by-step, the whole time

series of the state can be obtained. There are two types of time matching methods: the explicit methods and the implicit methods. In the explicit methods, the unknown state is expressed only by the known flow states, so that the solution be simply calculated the substitution. Although the calculation time per step is short, the time step needs to be small enough to avoid the instability. In the implicit methods, linear equations need to be solved to obtain the unknown state. Therefore, the calculation time per step increases, but the stability is easier to control.

In this subsection, Eq. (2.8) is briefly written as

$$\frac{\partial[\mathbf{u}]}{\partial t} = f([\mathbf{u}]), \quad (2.11)$$

where $f([\mathbf{u}])$ denotes all other terms in Eq. (2.8). The following time matching methods are the typical ones, where $[\mathbf{u}]^n$ denotes the state of the velocity at the n th time-step which is already known, $[\mathbf{u}]^{n+1}$ denotes the state at the $(n+1)$ th time-step which we want to solve. The known states should be sorted into the coefficient matrix $[C]$ in Eq. (2.9).

(1) Explicit Euler method:

$$[\mathbf{u}]^{n+1} = [\mathbf{u}]^n + f([\mathbf{u}]^n)\Delta t. \quad (2.12)$$

(2) Adams–Bashforth methods (explicit):

The first-order Adams–Bashforth method is equivalent to the explicit Euler method. The second- and third-order Adams–Bashforth methods are as follow

$$[\mathbf{u}]^{n+1} = [\mathbf{u}]^n + \left(\frac{3}{2}f([\mathbf{u}]^n) - \frac{1}{2}f([\mathbf{u}]^{n-1}) \right) \Delta t. \quad (2.13)$$

$$[\mathbf{u}]^{n+1} = [\mathbf{u}]^n + \left(\frac{23}{12}f([\mathbf{u}]^n) - \frac{16}{12}f([\mathbf{u}]^{n-1}) + \frac{5}{12}f([\mathbf{u}]^{n-2}) \right) \Delta t. \quad (2.14)$$

(3) Implicit Euler method:

$$[\mathbf{u}]^{n+1} = [\mathbf{u}]^n + f([\mathbf{u}]^{n+1})\Delta t. \quad (2.15)$$

(4) Crank–Nicolson method (implicit):

$$[\mathbf{u}]^{n+1} = [\mathbf{u}]^n + \left(\frac{1}{2}f([\mathbf{u}]^{n+1}) + \frac{1}{2}f([\mathbf{u}]^n) \right) \Delta t. \quad (2.16)$$

2.3.3 Discretisation of the convective term

The volume integral of the convective term is first replaced by the surface integral using the divergence theorem, that is

$$Cov_J = \frac{1}{V_J} \int_{\Omega_J} \nabla \cdot (\mathbf{u}\mathbf{u}^T) d\mathbf{x} = \frac{1}{V_J} \int_{\partial\Omega_J} \mathbf{u}(\mathbf{u} \cdot \mathbf{n}) dS, \quad J = 1, 2, \dots, N, \quad (2.17)$$

where $\partial\Omega_J$ denotes the surface of the element Ω_J , and \mathbf{n} denotes the normal direction vector of the surface. If the element is a polyhedron and values are assumed constant over each face, the convective term can be further written as

$$Cov_J = \frac{1}{V_J} \sum_m \mathbf{u}_{J,m} \underbrace{(\mathbf{u}_{J,m} \cdot \mathbf{n}_{J,m})}_{F_{J,m}} S_{J,m} = \sum_m \frac{F_{J,m}}{V_J} \mathbf{u}_{J,m}, \quad J = 1, 2, \dots, N, \quad (2.18)$$

where S is the area of the surface, and the face-values are indexed by the subscript J,m denoting the m th surface of the J th element. Here, the velocity $\mathbf{u}_{J,m}$ needs to be interpolated by the velocity values at the centroids. Note that in the linear solver, the velocity in the brackets in Eq. (2.18) is regarded as already known, which takes the values obtained in the last iteration or given in the initial guess in the first iteration. In Eq. (2.18), the known parts can be substituted by $F_{J,m}$, which denotes the volume flux across the m th surface of the J th element. This volume flux is constant in each time-step, and should be sorted into the coefficient matrix $[A]$ in Eq. (2.9).

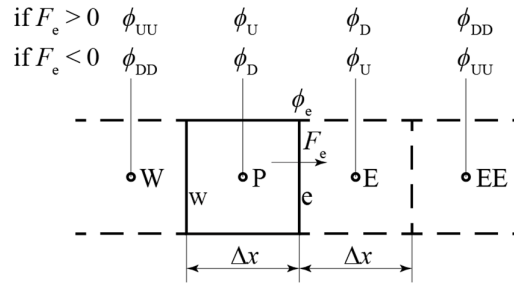


Figure 2.1 Geometry of an element on the x direction.

The target now is to provide the interpolation for the face-value $\mathbf{u}_{J,m}$. For simplicity, an element in a Cartesian grid in Figure 2.1 is considered. The target element, with the centroid of P, is surrounded by the elements with the centroids named as E and W in the x direction, and the surfaces of the target element adjacent to the other elements are named as e and w correspondingly, whose normal direction is pointing in the positive x direction. We use the general scalar quantity ϕ to denote the x -, y -, or z -directional velocity. ϕ_e denotes the velocity on face e, which is the face-value we want to find. The volume flux on face e is denoted by F_e . The velocity values at the centroids distinguished by the subscripts U and D, which the upstream and downstream of face e, respectively. Our target is to approximate face-value ϕ_e by the linear combination of ϕ_{UU} , ϕ_U , ϕ_D , and

ϕ_{DD} . The most typical schemes for this purpose are as follows:

(1) Upwind differencing (UD) scheme:

$$\phi_e \approx \tilde{\phi}_e = \phi_U. \quad (2.19)$$

The face-value is approximated by the value at the first node upstream of the face. To evaluate the scheme, ϕ_U is expanded by the Taylor series at face e as

$$F_e \phi_U = F_e \phi_e - \sum_{n=1,3,5,\dots} \frac{1}{2^n n!} |F_e| \left(\frac{\partial^n \phi}{\partial x^n} \right)_e (\Delta x)^n + \sum_{n=2,4,6,\dots} \frac{1}{2^n n!} F_e \left(\frac{\partial^n \phi}{\partial x^n} \right)_e (\Delta x)^n. \quad (2.20)$$

The error of the current scheme is

$$F_e \tilde{\phi}_e - F_e \phi_e = - \sum_{n=1,3,5,\dots} \frac{1}{2^n n!} |F_e| \left(\frac{\partial^n \phi}{\partial x^n} \right)_e (\Delta x)^n + \sum_{n=2,4,6,\dots} \frac{1}{2^n n!} F_e \left(\frac{\partial^n \phi}{\partial x^n} \right)_e (\Delta x)^n. \quad (2.21)$$

Note that none of the terms on the right side equal to zero, so the UD scheme is a first-order scheme. Specifically, the $n = 1$ term relates to the dissipation error, which is dominated by $(\partial \phi / \partial x)_e$, same form with the diffusion term (see Subsection 2.3.5), and thus causes the artificial viscosity (numerical viscosity). The artificial viscosity has a positive effect on numerical stabilisation. However, the numerical viscosity can sometimes reach the same level of the molecular and eddy viscosity, and may cause large errors. On the other hand, the $n = 2$ term relates to the dispersion error, which can cause spatial numerical vibration in the region where discontinuities or shocks occur and the gradient is large.

(2) Central differencing (CD) scheme:

$$\phi_e \approx \tilde{\phi}_e = \frac{\phi_U + \phi_D}{2}. \quad (2.22)$$

The central differencing scheme provides a linear interpolation between two neighbouring values. The above approximation is valid under the condition that the mesh is regular, i.e., Δx is constant for all the grid cells. If it is not the case, the above interpolation should be weighted by the distance from the target face to the neighbouring centroids. To evaluate the scheme, ϕ_U is expanded by the Taylor series at face e in Eq. (2.20), and ϕ_D is expanded as

$$F_e \phi_D = F_e \phi_e + \sum_{n=1,3,5,\dots} \frac{1}{2^n n!} |F_e| \left(\frac{\partial^n \phi}{\partial x^n} \right)_e (\Delta x)^n + \sum_{n=2,4,6,\dots} \frac{1}{2^n n!} F_e \left(\frac{\partial^n \phi}{\partial x^n} \right)_e (\Delta x)^n. \quad (2.23)$$

The error of the current scheme is

$$F_e \tilde{\phi}_e - F_e \phi_e = \sum_{n=2,4,6,\dots} \frac{1}{2^n n!} F_e \left(\frac{\partial^n \phi}{\partial x^n} \right)_e (\Delta x)^n, \quad (2.24)$$

Note that note that the first nonzero terms on the right side is ordered by 2, so the CD scheme is a second-order scheme with no dissipation error. However, the existence of the dispersion error implies that the numerical vibration is likely to happen.

(3) Linear upwind differencing (LUD) scheme (second-order):

$$\phi_e \approx \tilde{\phi}_e = \frac{3}{2}\phi_U - \frac{1}{2}\phi_{UU}, \quad (2.25)$$

under the assumption a regular mesh with constant Δx . To evaluate the scheme, ϕ_U is expanded by the Taylor series at face e in Eq. (2.20), and ϕ_{UU} is expanded as

$$F_e \phi_{UU} = F_e \phi_e - \sum_{n=1,3,5,\dots} \frac{3^n}{2^n n!} |F_e| \left(\frac{\partial^n \phi}{\partial x^n} \right)_e (\Delta x)^n + \sum_{n=2,4,6,\dots} \frac{3^n}{2^n n!} F_e \left(\frac{\partial^n \phi}{\partial x^n} \right)_e (\Delta x)^n. \quad (2.26)$$

The error of the current scheme is

$$\begin{aligned} F_e \tilde{\phi}_e - F_e \phi_e = & - \sum_{n=1,3,5,\dots} \left(\frac{3}{2} - \frac{3^n}{2} \right) \frac{1}{2^n n!} |F_e| \left(\frac{\partial^n \phi}{\partial x^n} \right)_e (\Delta x)^n \\ & + \sum_{n=2,4,6,\dots} \left(\frac{3}{2} - \frac{3^n}{2} \right) \frac{1}{2^n n!} F_e \left(\frac{\partial^n \phi}{\partial x^n} \right)_e (\Delta x)^n, \end{aligned} \quad (2.27)$$

Note that note that the first nonzero terms on the right side is ordered by 2, so the LUD scheme is a second-order scheme.

(4) Quadratic upstream interpolation for convective kinematics (QUICK) scheme (third-order):

$$\phi_e \approx \tilde{\phi}_e = \frac{3}{8}\phi_D + \frac{3}{4}\phi_U - \frac{1}{8}\phi_{UU}, \quad (2.28)$$

under the assumption a regular mesh with constant Δx . To evaluate the scheme, ϕ_U , ϕ_D , and ϕ_{UU} are expanded by the Taylor series at face e in Eqs. (2.20), (2.23), and (2.27). The error of the current scheme is

$$\begin{aligned} F_e \tilde{\phi}_e - F_e \phi_e = & \sum_{n=1,3,5,\dots} \left(-\frac{3}{8} + \frac{3^n}{8} \right) \frac{1}{2^n n!} |F_e| \left(\frac{\partial^n \phi}{\partial x^n} \right)_e (\Delta x)^n \\ & + \sum_{n=2,4,6,\dots} \left(\frac{9}{8} - \frac{3^n}{8} \right) \frac{1}{2^n n!} F_e \left(\frac{\partial^n \phi}{\partial x^n} \right)_e (\Delta x)^n, \end{aligned} \quad (2.29)$$

Note that note that the first nonzero terms on the right side is ordered by 3, so the LUD scheme is a third-order scheme.

Before introducing the next schemes, a general form for the four schemes above can be given as

$$\phi_e = \phi_D + \frac{1}{2}(\phi_D - \phi_U)\xi(r), \quad (2.30)$$

where

$$r = \frac{\phi_U - \phi_{UU}}{\phi_D - \phi_U}, \quad (2.31)$$

and ξ is a limiter function of r . The ξ function is unique for each of the four schemes:

UD: $\xi(r) = 0$;

CD: $\xi(r) = 1$;

LUD: $\xi(r) = r$;

QUICK: $\xi(r) = (3+r)/4$.

(5) Total variation diminishing (TVD) schemes:

The concept of TVD is proposed by Harten (1983). First, the total variation (TV) is defined as

$$TV(\phi^n) = \sum_J |\phi_{J+1}^n - \phi_J^n|, \quad (2.32)$$

to measure the spatial variation of the quantity. A numerical method is said to be TVD if,

$$TV(\phi^{n+1}) \leq TV(\phi^n), \quad (2.33)$$

which implies that the spatial variation decreases with the time-step. Godunov's theorem proves that monotonicity-preserving linear schemes are at most only first order accurate. Higher order linear schemes, although more accurate for smooth solutions, are not TVD and tend to introduce spurious oscillations where discontinuities or shocks arise. Sweby (1984) indicated that the second-order TVD schemes should have the limiter function in the range shown in Figure 2.2. Three classical TVD schemes (Roe, 1986) are as follow

MIN_MOD: $\xi(r) = \max[0, \min(1, r)]$;

Van Leer: $\xi(r) = (r + |r|)/(1 + r)$;

SUPERBEE: $\xi(r) = \max[0, \min(1, 2r), \min(2, r)]$.

The MIN_MOD and SUPERBEE are the lowest and highest boundaries of the second order TVD region, respectively. Generally, the higher the limiter function is located, the higher accuracy it can achieve in capturing discontinuities or shocks.

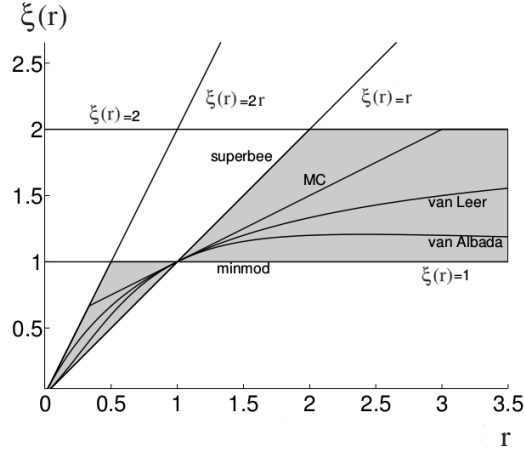


Figure 2.2 Second-order TVD region.

2.3.4 Discretisation of the pressure term

Similar to the convective term, the volume integral of the pressure term is replaced by the surface integral, then converted to the sum of the face-values multiplied by the surface areas, which takes the form

$$\begin{aligned}
 Pre_J &= \frac{1}{V_J} \int_{\Omega_J} \left(-\frac{1}{\rho} \nabla p \right) d\mathbf{x} = \frac{1}{V_J} \int_{\partial\Omega_J} \left(-\frac{p}{\rho} \right) \mathbf{n} dS \\
 &= \frac{1}{V_J} \sum_m \left(-\frac{p_{J,m}}{\rho} \right) S_{J,m} \mathbf{n}_{J,m} = \sum_m \left(-\frac{S_{J,m} \mathbf{n}_{J,m}}{V_J \rho} \right) p_{J,m}, \quad J = 1, 2, \dots, N.
 \end{aligned} \tag{2.34}$$

We only need to provide the interpolation for the face-value $p_{J,m}$, since other quantities are already known. This is usually be done by the CD scheme, whose process is the same as introduced in the last subsection, where the general scalar quantity ϕ can also denote the pressure field. The coefficients are sorted into the coefficient matrix $[B]$ in Eq. (2.9)

2.3.5 Discretisation of the diffusion term

Again, the volume integral of the diffusion term is replaced by the surface integral, then converted to the sum of the face-values multiplied by the surface areas, which takes the form

$$\begin{aligned}
 Dif_J &\approx \frac{1}{V_J} \int_{\Omega_J} v \nabla^2 \mathbf{u} d\mathbf{x} = \frac{1}{V_J} \int_{\partial\Omega_J} v (\mathbf{n} \cdot \nabla \mathbf{u}) dS \\
 &= \frac{1}{V_J} \sum_m v (\mathbf{n} \cdot \nabla \mathbf{u})_{J,m} S_{J,m} = \sum_m \left(\frac{v S_{J,m}}{V_J} \right) (\mathbf{n} \cdot \nabla \mathbf{u})_{J,m}, \quad J = 1, 2, \dots, N,
 \end{aligned} \tag{2.35}$$

where

$$(\mathbf{n} \cdot \nabla \mathbf{u})_{J,m} = \begin{bmatrix} \frac{\partial u}{\partial x} n_x + \frac{\partial u}{\partial y} n_y + \frac{\partial u}{\partial z} n_z \\ \frac{\partial v}{\partial x} n_x + \frac{\partial v}{\partial y} n_y + \frac{\partial v}{\partial z} n_z \\ \frac{\partial w}{\partial x} n_x + \frac{\partial w}{\partial y} n_y + \frac{\partial w}{\partial z} n_z \end{bmatrix}_{J,m} \cdot \quad (2.36)$$

For simplicity, an element in a Cartesian grid in Figure 2.1 is again considered. We focus on approximating the value on face e, where normal direction of the face is pointing in the positive x direction. Again, we use the general scalar quantity ϕ to denote the x -, y -, or z -directional velocity. Our target is to approximate face-value $(\partial\phi/\partial x)_e$ by the linear combination of ϕ_P , and ϕ_E , which denoting the values at the centroids of P and W, respectively. This can usually be done by the central differencing scheme as

$$\left(\frac{\partial \phi}{\partial x} \right)_e = \frac{\phi_P - \phi_E}{\Delta x}, \quad (2.37)$$

under the assumption a regular mesh with constant Δx . If the mesh is not regular, ϕ_P , and ϕ_E should be weighted by the distance. The discretisation on the y and z direction can be performed in the same manner.

2.3.6 PISO algorithm

The main problem in solving the velocity-pressure coupling problem indicated by Eqs. (2.9) and (2.10) is that, Eq. (2.10) is just a restriction to the momentum equation, and no equation is available for the pressure. Therefore, the velocity field solved directly from the momentum equation will not satisfy the continuity equation, and needs to be corrected by iteration, which is done by the SIMPLE algorithm. The PISO algorithm modified the iteration process of the SIMPLE algorithm so that the solution can converge faster.

The PISO algorithm utilises the splitting of operations in the solution of the discretised momentum and pressure equations. First, the coefficient matrix $[A]$ in Eq. (2.9) is splatted into diagonal part and off-diagonal part, so that

$$[A][\mathbf{u}] - [B][p] - [C] = [A_p][\mathbf{u}] - [B][p] + [H] = 0, \quad (2.38)$$

where $[A_p]$ is the diagonal matrix consisting of the diagonal elements of $[A]$, and

$$[H] = [A][\mathbf{u}] - [A_p][\mathbf{u}] - [C], \quad (2.39)$$

The inverse matrix of the diagonal matrix is easy to found. Therefore, it gives an explicit expression for the velocity field that

$$[\mathbf{u}] = [A_p]^{-1} ([B][p] - [H]). \quad (2.40)$$

The divergence operator is imposed on both side of Eq. (2.40), the Poisson equation for pressure is obtained as

$$\nabla \cdot [\mathbf{u}] = \nabla \cdot ([A_p]^{-1} [B][p]) - \nabla \cdot [A_p]^{-1} [H] = 0, \quad (2.41)$$

The pressure field is updated by solving the pressure field from this equation. The velocity field calculated by Eq. (2.40) with this pressure field will satisfy the continuity equation, but this explicit process brings errors so that this new velocity field will be slightly off the momentum equation, because the $[H]$ vector also depends on the velocity field. Therefore, the fields should be corrected by iteration.

The iteration process of the PISO algorithm is as follow:

Step 1: The velocity field $[\mathbf{u}]^\oplus$ is solved by the original equation

$$[A][\mathbf{u}]^\oplus = [B][p]^n + [C], \quad (2.42)$$

using the pressure field $[p]^n$ solved in the last time-step. Note that this velocity field does not satisfy the continuity equation, so it needs to be corrected.

Step 2: The $[H]^\oplus$ vector corresponding by the current velocity field $[\mathbf{u}]^\oplus$ is calculated by

$$[H]^\oplus = [A][\mathbf{u}]^\oplus - [A_p][\mathbf{u}]^\oplus - [C]. \quad (2.43)$$

Step 3: The updated pressure field $[p]^\oplus$ is solved by the following equation

$$\nabla \cdot ([A_p]^{-1} [B][p]^\oplus) = \nabla \cdot ([A_p]^{-1} [H]^\oplus). \quad (2.44)$$

Step 4: The updated velocity field $[\mathbf{u}]^{\oplus\oplus}$ calculated by

$$[\mathbf{u}]^{\oplus\oplus} = [A_p]^{-1} ([B][p]^\oplus - [H]^\oplus). \quad (2.45)$$

This new velocity field satisfies the continuity equation, but does not satisfy the momentum equation.

Step 5: Go back to Step 2 to update the $[H]$ vector using the new velocity field. Step 2 to 4 is iterated until a low residual is obtained. Finally, we get the velocity field $[\mathbf{u}]^{n+1}$ and the pressure field $[p]^{n+1}$ for the next time-step.

2.4 Large-eddy simulation

2.4.1 Turbulent modelling

In urban wind environment problems usually with a very large Reynolds number, the turbulence to be dealt with contains the fluctuation of various scales. Ideally, the basic governing equations are solved by direct numerical simulation (DNS) to obtain the vortices of all scales. However, a sufficiently fine calculation grid is required to resolve the vortices of all the scales, and thus the required amount of calculation is enormous. Such approach can be difficult in practical application.

To solve this problem, only the vortices of the scales larger than a threshold are simulated, and the fluctuations of the scales smaller than that threshold are expressed by a simpler model. Such approaches can be roughly classified into two types. One type of approaches takes the ensemble mean or the time average for the governing equations, so that only the averaged fields are simulated. The ensemble mean refers to the mean weighted by the probability of the occurrence of all possible states of the system. During the averaging, the fluctuation components are expressed by models. This kind of models are called the RANS turbulence models. The other type of approaches coarse-grains the governing equations by applying an appropriate spatial filter, and simulates only the flow of a scale larger than the scale corresponding to the filter width. The variable components of the scale below that filter width are expressed by models. This kind of approach is called LES. The models used in both types of approaches are collectively called turbulence models.

In the current study, since the analysis of the turbulent fluctuation is aimed for, the time signal data of the instantaneous field is required. The RANS approach is considered not suitable for this study. Although the obtained turbulence is spatially filtered on a small scale by LES so that it is not exactly equivalent to the real instantaneous field, the turbulent flow features to be identified are on a much larger scale compared to the filter scale. Therefore, LES is performed for each case in this study. The filtered governing equations and models in LES are introduced in the next section.

2.4.2 Filtered governing equations

LES is based on the spatial filtering operation, which decomposed the variable ϕ into the filtered (grid scale, resolved) part $\bar{\phi}$ and the sub-filter (subgrid scale, unresolved) part ϕ'' , that is

$$\phi(\mathbf{x}, t) = \bar{\phi}(\mathbf{x}, t) + \phi''(\mathbf{x}, t). \quad (2.46)$$

The filtered variable is defined as

$$\bar{\phi}(\mathbf{x}, t) = \int_{\Omega} G(\mathbf{x}, \tilde{\mathbf{x}}, \Delta) \phi(\tilde{\mathbf{x}}, t) d\tilde{\mathbf{x}}, \quad (2.47)$$

where Ω is the simulation domain, and G is the filter function. The filtered function depends on the difference $\mathbf{x} - \tilde{\mathbf{x}}$ and on the filter width Δ . The following filter functions are the most frequently used ones:

(1) Gaussian filter:

$$G(\mathbf{x}, \tilde{\mathbf{x}}, \Delta) = \left(\frac{6}{\pi \Delta^2} \right)^{\frac{3}{2}} \exp \left(-\frac{6 \|\mathbf{x} - \tilde{\mathbf{x}}\|^2}{\Delta^2} \right). \quad (2.48)$$

(2) Top-hat filter:

$$G(\mathbf{x}, \tilde{\mathbf{x}}, \Delta) = \begin{cases} \frac{1}{\Delta^3}, & \|\mathbf{x} - \tilde{\mathbf{x}}\| \leq \frac{\Delta}{2} \\ 0, & \|\mathbf{x} - \tilde{\mathbf{x}}\| > \frac{\Delta}{2} \end{cases}. \quad (2.49)$$

For three-dimensional computations with the filter widths in three directions Δx , Δy , and Δz , the filter width in the filter functions is often taken as to be $\Delta = \sqrt[3]{\Delta x \Delta y \Delta z}$.

Subsequently, the spatial filtering is applied to the Navier-Stokes equations to remove the small-scale turbulence. For the incompressible flow, the governing equations (2.3) and (2.4) are filtered on both sides and take the form as

$$\frac{\partial \bar{u}_i}{\partial x_i} = 0, \quad (2.50)$$

$$\frac{\partial \bar{u}_i}{\partial t} + \frac{\partial (\bar{u}_i \bar{u}_j)}{\partial x_j} = -\frac{1}{\rho} \frac{\partial \bar{p}}{\partial x_i} + \nu \frac{\partial^2 \bar{u}_i}{\partial x_j \partial x_j} - \frac{\partial \tau_{ij}}{\partial x_j}, \quad (2.51)$$

where $\tau_{ij} = \overline{u_i u_j} - \bar{u}_i \bar{u}_j$ is called the subgrid-scale (SGS) stress tensor. The SGS stress tensor describes the influence of the unresolved-scale turbulence on the resolved-scale motions, which is unknown in the equations and needs to be modelled to close the equations.

2.4.3 Subgrid-scale modelling

On the average, the turbulent energy is transported from the large scales to the small scales. Therefore, the main task of a SGS model is to simulate the energy transfer and to provide the means of energy dissipation. The standard Smagorinsky model, which is the most representative SGS model, is introduced below.

In standard Smagorinsky model (Smagorinsky, 1963), the SGS stress tensor is taken to be proportional to the strain rate of the resolved flow, that is

$$\tau_{ij} - \frac{1}{3} \delta_{ij} \tau_{kk} = -2\nu_T \bar{S}_{ij}, \quad (2.52)$$

where ν_T is the eddy viscosity, and

$$\bar{S}_{ij} = \frac{1}{2} \left(\frac{\partial \bar{u}_i}{\partial x_j} + \frac{\partial \bar{u}_j}{\partial x_i} \right), \quad (2.53)$$

is the strain-rate tensor of the filtered velocity. Subsequently, the eddy viscosity ν_T is estimated by the SGS length scale Δ and the velocity scale $\sqrt{2\bar{S}_{ij}\bar{S}_{ij}}$ that

$$\nu_T = (C_s \Delta)^2 \sqrt{2\bar{S}_{ij}\bar{S}_{ij}}, \quad (2.54)$$

where C_s is the Smagorinsky constant. Although Lilly (1967) found the theoretical value for the Smagorinsky constant to be 0.18, it still depends on the effect of the mean flow strain or shear in various flow types. Moreover, the eddy viscosity is nonzero at the wall boundaries, which is contrary to the notion that there is no turbulence near walls. To reduce the eddy viscosity near walls, the model is modified by the Van Driest damping (Van Driest, 1956) as

$$\nu_T = \left(C_s \Delta \left(1 - e^{-y^+/25} \right) \right)^2 \sqrt{2\bar{S}_{ij}\bar{S}_{ij}}, \quad (2.55)$$

where y^+ is the dimensionless wall distance. For the calculation of the dimensionless wall distance, please see the next section. In OpenFOAM (The OpenFOAM Foundation Ltd, 2020), the Van Driest damping is applied in the region up to y^+ of 500.

2.4.4 Wall modelling

The gradient of the velocity field near the wall varies greatly, and the accurate calculation of the gradient near the wall is crucial to the calculation of the shear force. For example, in the case the no-slip boundary condition is imposed on the wall, the velocity on the wall is zero. As the distance from the wall increases, the velocity gradually increases to the mainstream velocity. In this near-wall region, the closer to the wall, the greater the gradient of speed change, so a dense grid is needed to resolve these gradients. However, a poor convergence may occur if the thickness of the grid near the wall is extremely thin, which results in high aspect-ratio cells. At the same time, the number of grids increases sharply, and the solution time increases accordingly. Alternatively, the wall models may be used in LES. In this case, the grid is not fine enough to resolve the gradients near the wall, but the transition between the wall velocity and outer flow (the velocity at the first grid point) and the shear force should be modelled.

Figure 2.3 provides the experiments measurements showing the relation of the nondimensional velocity u^+ and wall distance y^+ defined by

$$u^+ = \frac{u}{u_\tau}, \quad (2.56)$$

$$y^+ = \frac{y_p u_\tau}{\nu}, \quad (2.57)$$

where u_τ is the friction velocity, and y_p is the normal distance to the wall surface. The near-wall region is usually divided into three regions, namely the viscous sub-layer region ($0 < y^+ < 5$), buffer layer region ($5 < y^+ < 30$), and log-law region ($30 < y^+ < 200$). The standard wall functions for the viscous sub-layer and log-law region can be written as

$$u^+ = y^+, \quad 0 < y^+ < 5, \quad (2.58)$$

$$u^+ = \frac{1}{\kappa} \ln(Ey^+), \quad 30 < y^+ < 200, \quad (2.59)$$

where κ and E are von Kármán constant and wall roughness parameter which are approximately 0.4187 and 9.793, respectively.

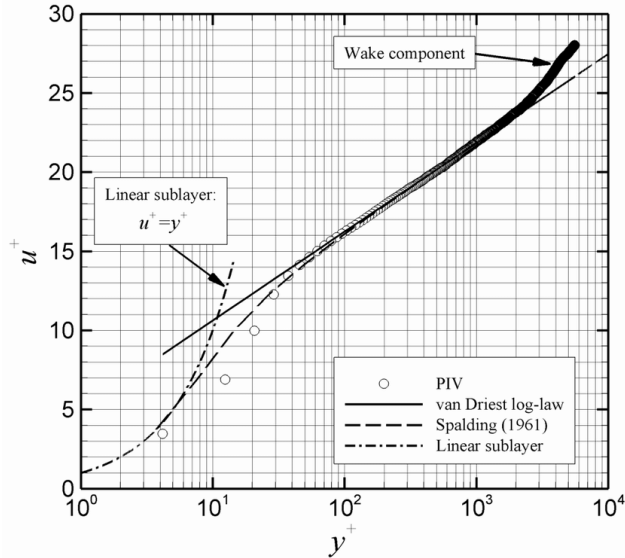


Figure 2.3 Experimental measurements and the law-of-the-wall (Humble et al., 2006).

One can simply use piecewise functions to model the relation in the whole near-wall region. Alternatively, one can also choose to use a single and smooth function, the Spalding's wall function (Spalding, 1962):

$$y^+ = u^+ + \frac{1}{E} \left(e^{\kappa u^+} - 1 - \kappa u^+ - \frac{1}{2} (\kappa u^+)^2 - \frac{1}{6} (\kappa u^+)^3 \right). \quad (2.60)$$

This wall function can be applied in the cases that one cannot guarantee that the position of first cell centroid is always located in the viscous sub-layer or log-law region.

In OpenFOAM, this wall function is realised by manipulating the eddy viscosity ν_T . The friction velocity u_τ is calculated from the following equation

$$f(u_\tau) = -y^+ + u^+ + \frac{1}{E} \left(e^{\kappa u^+} - 1 - \kappa u^+ - \frac{1}{2} (\kappa u^+)^2 - \frac{1}{6} (\kappa u^+)^3 \right) = 0. \quad (2.61)$$

Since the velocity and normal distance at the first grid is known (given by the last iteration), the only unknown variable u_τ can be calculated by Newton-Raphson method, where the iteration is

$$u_\tau^{\text{new}} = u_\tau^{\text{old}} - \frac{f(u_\tau^{\text{old}})}{\left(\frac{df}{du_\tau} \right) \Big|_{u_\tau^{\text{old}}}}. \quad (2.62)$$

Subsequently, the eddy viscosity ν_T at the first cell is calculated by

$$\nu_T = \frac{u_\tau^2}{\|d\mathbf{u}/d\mathbf{n}\|} - \nu, \quad (2.63)$$

where $\|d\mathbf{u}/d\mathbf{n}\|$ is the magnitude of the velocity gradient along the wall normal.

2.5 Summary

In this chapter, the CFD techniques is briefly introduced, including the governing equations, numerical methods, and LES. In the studies described in the subsequent chapters, LES is applied to obtain the turbulence data for further analysis.

Reference

- Harten, A., 1983. High resolution schemes for hyperbolic conservation laws. *J. Comput. Phys.* 49, 357–393. [https://doi.org/10.1016/0021-9991\(83\)90136-5](https://doi.org/10.1016/0021-9991(83)90136-5)
- Humble, R.A., Scarano, F., Van Oudheusden, B.W., Tuinstra, M., 2006. PIV Measurements of a Shock Wave/Turbulent Boundary Layer Interaction.
- Issa, R.I., 1986. Solution of the implicitly discretised fluid flow equations by operator-splitting. *J. Comput. Phys.* 62, 40–65. [https://doi.org/10.1016/0021-9991\(86\)90099-9](https://doi.org/10.1016/0021-9991(86)90099-9)
- Lilly, D.K., 1967. The representation of small-scale turbulence in numerical simulation experiments, in: *Proceedings of the IBM Scientific Computing Symposium on Environmental Science*. <https://doi.org/http://dx.doi.org/10.5065/D62R3PMM>
- Patankar, S. V., Spalding, D.B., 1972. A calculation procedure for heat, mass and momentum transfer in three-dimensional parabolic flows. *Int. J. Heat Mass Transf.*

- 15, 1787–1806. [https://doi.org/10.1016/0017-9310\(72\)90054-3](https://doi.org/10.1016/0017-9310(72)90054-3)
- Roe, P.L., 1986. Characteristic-Based Schemes for the Euler Equations. *Annu. Rev. Fluid Mech.* 18, 337–365. <https://doi.org/10.1146/annurev.fl.18.010186.002005>
- Smagorinsky, J., 1963. General circulation experiments with the primitive equations. *Mon. Weather Rev.* 91, 99–164. [https://doi.org/10.1175/1520-0493\(1963\)091<0099:gcewtp>2.3.co;2](https://doi.org/10.1175/1520-0493(1963)091<0099:gcewtp>2.3.co;2)
- Spalding, D.B., 1962. A new analytical expression for the drag of a flat plate valid for both the turbulent and laminar regimes. *Int. J. Heat Mass Transf.* 5, 1133–1138. [https://doi.org/10.1016/0017-9310\(62\)90189-8](https://doi.org/10.1016/0017-9310(62)90189-8)
- Sweby, P.K., 1984. High Resolution Schemes Using Flux Limiters for Hyperbolic Conservation Laws. *SIAM J. Numer. Anal.* 21, 995–1011. <https://doi.org/10.1137/0721062>
- The OpenFOAM Foundation Ltd, 2020. OpenFOAM | Free CFD Software | The OpenFOAM Foundation [WWW Document]. URL <https://openfoam.org/> (accessed 1.16.21).
- Van Driest, E.R., 1956. On Turbulent Flow Near a Wall. *J. Aeronaut. Sci.* 23, 1007–1011. <https://doi.org/10.2514/8.3713>

Chapter 3

Basic theory and algorithm of SPOD

3.1 Overview

In this chapter, the basic theory of POD and SPOD is introduced in Section 3.2, followed by their algorithms in Section 3.3. This chapter only provide the theory relating to the application of wind velocity field, which is low-speed incompressible flow. For more general introduction and details of SPOD, please refer to Towne et al. (2018) and Schmidt and Colonius (2020).

3.2 Basic theory

3.2.1 Function space and inner product

Let $\mathbf{u}(\mathbf{x}, t) = [u(\mathbf{x}, t), v(\mathbf{x}, t), w(\mathbf{x}, t)]^\top$ denotes the vector field of velocity, where $\mathbf{x} = [x, y, z]^\top \in \Omega$, that is, a spatial location within an interval Ω , and $0 < t \leq T$ is time. The superscript \cdot^\top denotes the transpose of the matrix. The research target is the fluctuation velocity field $\mathbf{u}'(\mathbf{x}, t) = \mathbf{u}(\mathbf{x}, t) - E(\mathbf{u}(\mathbf{x}, t))$, where $E(\cdot)$ denotes the expectation.

In POD, the vector field is described as a (sometimes complex-valued) vector function defined on Ω . The problem is restricted to the space of square-integrable functions, L^2 functions, which implies that the fields should have finite kinetic energy. In such space, the definition of the inner product is needed for measuring distance and correlation, which is chosen to be the following form in this study

$$\langle \mathbf{f}(\mathbf{x}), \mathbf{g}(\mathbf{x}) \rangle = \frac{1}{V} \int_{\Omega} \mathbf{g}^\dagger(\mathbf{x}) \mathbf{f}(\mathbf{x}) d\mathbf{x}, \quad (3.1)$$

where $V = \int_{\Omega} d\mathbf{x}$ is the total volume of the field, \mathbf{f} and \mathbf{g} are two functions, \mathbf{g}^\dagger denotes the Hermitian transpose of \mathbf{g} , which is taking the transpose and then taking the complex conjugate. This integral is divided by a volume V to normalise the inner product value

to the spatial average. Then, the norm of the function \mathbf{f} is $\langle \mathbf{f}(\mathbf{x}), \mathbf{f}(\mathbf{x}) \rangle$, which denotes the spatial average kinetic energy in physics.

3.2.2 POD

The target of POD is seeking a deterministic function among all the functions in the space, which is most similar to the stochastic function \mathbf{u}' on average. Mathematically, the notion of “most similar” corresponds to seeking a function $\boldsymbol{\psi}(\mathbf{x})$ which will maximise the following the quantity

$$\lambda = \frac{E\left(\langle \mathbf{u}'(\mathbf{x}, t), \boldsymbol{\psi}(\mathbf{x}) \rangle^2\right)}{\langle \boldsymbol{\psi}(\mathbf{x}), \boldsymbol{\psi}(\mathbf{x}) \rangle}. \quad (3.2)$$

This means that the function is found to maximise the inner product to the fluctuation field, so it most closely resembles to the fluctuation. A necessary condition for this maximisation problem is that $\boldsymbol{\psi}$ is the eigenfunction of the two-point correlation tensor. This results in a Fredholm eigenvalue problem (Fredholm, 1903)

$$\frac{1}{V} \int_{\Omega} \mathbf{C}(\mathbf{x}, \tilde{\mathbf{x}}) \boldsymbol{\psi}(\tilde{\mathbf{x}}) d\tilde{\mathbf{x}} = \lambda \boldsymbol{\psi}(\mathbf{x}), \quad (3.3)$$

where

$$\mathbf{C}(\mathbf{x}_1, \mathbf{x}_2) = E\left(\mathbf{u}'(\mathbf{x}, t) \mathbf{u}'^\dagger(\tilde{\mathbf{x}}, t)\right), \quad (3.4)$$

is the space correlation tensor between the two points, \mathbf{x} and $\tilde{\mathbf{x}}$. According to the Hilbert-Schmidt theory (Pipkin, 1991), a finite set of eigenvalues λ_n and eigenfunctions $\boldsymbol{\psi}_n(\mathbf{x})$ exist, which can be ranked by the eigenvalues $\lambda_1 \geq \lambda_2 \geq \dots \geq 0$. The largest eigenvalue λ_1 and the its corresponding eigenfunction $\boldsymbol{\psi}_1$ is the solution to the aforementioned maximisation problem.

All the eigenfunctions are normalised, and they are orthogonal with each other as follows:

$$\langle \boldsymbol{\psi}_n(\mathbf{x}), \boldsymbol{\psi}_m(\mathbf{x}) \rangle = \delta_{nm} = \begin{cases} 0, & n \neq m \\ 1, & n = m \end{cases}. \quad (3.5)$$

Therefore, they can serve as a complete linear basis for $\mathbf{u}'(\mathbf{x}, t)$. The fluctuating velocity can be represented by a modal decomposition in the eigenfunctions:

$$\mathbf{u}'(\mathbf{x}, t) = \sum_n a_n(t) \boldsymbol{\psi}_n(\mathbf{x}), \quad (3.6)$$

where

$$a_n(t) = \langle \mathbf{u}'(\mathbf{x}, t), \boldsymbol{\psi}_n(\mathbf{x}) \rangle, \quad (3.7)$$

is a set of linearly uncorrelated time series, with the property

$$\mathbb{E}(a_n(t)a_m^*(t)) = \lambda_n \delta_{nm}, \quad (3.8)$$

where a_m^* denotes the conjugate of a_m . In most applications, $\boldsymbol{\psi}_n(\mathbf{x})$ is called the mode which represents the fluctuation pattern of the flow field, and λ_n measures the intensity of the corresponding mode, called the mode energy.

Furthermore, taking use of Eqs. (3.6) and (3.8), the correlation tensor can be represented by eigenfunctions as

$$\mathbf{C}(\mathbf{x}, \tilde{\mathbf{x}}) = \sum_n \lambda_n \boldsymbol{\psi}_n(\mathbf{x}) \boldsymbol{\psi}_n^\dagger(\tilde{\mathbf{x}}). \quad (3.9)$$

Moreover, the TKE can be represented by the summation of the eigenvalues,

$$\begin{aligned} 2\bar{k} &= \frac{1}{V} \int_{\Omega} 2k(\mathbf{x}) d\mathbf{x} = \frac{1}{V} \mathbb{E}(\mathbf{u}'^\dagger(\mathbf{x}, t) \mathbf{u}'(\mathbf{x}, t)) \\ &= \sum_n \mathbb{E}(a_n(t)a_n^*(t)) \langle \boldsymbol{\psi}_n(\mathbf{x}), \boldsymbol{\psi}_n(\mathbf{x}) \rangle = \sum_n \lambda_n. \end{aligned} \quad (3.10)$$

where $k(\mathbf{x})$ is the TKE at the point \mathbf{x} , and \bar{k} denotes the spatial average TKE. From Eq. (3.10), one can know that the mode energy λ_n , which depicts the intensity of the corresponding mode $\boldsymbol{\psi}_n(\mathbf{x})$, is also a part of the TKE of the flow field. The fluctuation velocity has been decomposed into a set of spatial mode, $\boldsymbol{\psi}_n(\mathbf{x})$, stochastically vibrating with time with the intensity λ_n .

3.2.3 Extension to SPOD

The space-time correlation tensor is considered in SPOD:

$$\mathbf{C}(\mathbf{x}, \tilde{\mathbf{x}}, t, \tilde{t}) = \mathbb{E}(\mathbf{u}'(\mathbf{x}, t) \mathbf{u}'^\dagger(\tilde{\mathbf{x}}, \tilde{t})). \quad (3.11)$$

On the condition that the wind speed time series is a stationary stochastic process, the space-time correlation tensor depends only on the time lag $\tau = t - \tilde{t}$. Subsequently, the cross-spectrum tensor is represented by the Fourier transform of the correlation tensor as

$$\mathbf{S}(\mathbf{x}, \tilde{\mathbf{x}}, f) = \int_{-\infty}^{+\infty} \mathbf{C}(\mathbf{x}, \tilde{\mathbf{x}}, \tau) e^{-i2\pi f\tau} d\tau. \quad (3.12)$$

where $i = \sqrt{-1}$, and f is the frequency. The cross-spectrum tensor can also be written as

$$\mathbf{S}(\mathbf{x}, \tilde{\mathbf{x}}, f) = \frac{1}{T} \mathbb{E}(\hat{\mathbf{u}}'(\mathbf{x}, f) \hat{\mathbf{u}}'^\dagger(\tilde{\mathbf{x}}, f)) = \frac{1}{T} \hat{\mathbf{u}}'(\mathbf{x}, f) \hat{\mathbf{u}}'^\dagger(\tilde{\mathbf{x}}, f), \quad (3.13)$$

where $\hat{\mathbf{u}}'$ denotes the Fourier transformation of \mathbf{u}' .

For a given frequency f , the eigenvalue problem becomes

$$\frac{1}{V} \int_{\Omega} \mathbf{S}(\mathbf{x}, \tilde{\mathbf{x}}, f) \boldsymbol{\Psi}_f(\tilde{\mathbf{x}}) d\tilde{\mathbf{x}} = \lambda_f \boldsymbol{\Psi}_f(\tilde{\mathbf{x}}). \quad (3.14)$$

Similar as in POD, the equation above defines a finite set of eigenvalues $\lambda_{f,n}$ and eigenfunctions $\boldsymbol{\Psi}_{f,n}(\mathbf{x})$ where the eigenfunctions are normalised and orthogonal to each other as

$$\langle \boldsymbol{\Psi}_{f,n}(\mathbf{x}), \boldsymbol{\Psi}_{f,m}(\mathbf{x}) \rangle = \delta_{nm}. \quad (3.15)$$

Subsequently, the Fourier transformation of the fluctuation velocity will be expanded as

$$\hat{\mathbf{u}}'(\mathbf{x}, f) = \sum_n a_{f,n} \boldsymbol{\Psi}_{f,n}(\mathbf{x}). \quad (3.16)$$

where $a_{f,n}$ is the mode coefficient which can be calculated by

$$a_{f,n} = \langle \hat{\mathbf{u}}'(\mathbf{x}, f), \boldsymbol{\Psi}_{f,n}(\mathbf{x}) \rangle. \quad (3.17)$$

The mode coefficients also have the property

$$\frac{1}{T} \text{E}(a_{f,n} a_{f,m}^*) = \frac{1}{T} a_{f,n} a_{f,m}^* = \lambda_{f,n} \delta_{nm}. \quad (3.18)$$

If the unitary Fourier transformation is performed on both sides of Eq. (3.16), we get

$$\mathbf{u}'(\mathbf{x}, t) = \int_{-\infty}^{+\infty} \sum_n a_{f,n} \boldsymbol{\Psi}_{f,n}(\mathbf{x}, t) e^{i2\pi f t} df. \quad (3.19)$$

which is the decomposition form of SPOD, and is a hybrid of the Fourier transformation and POD. In Eq. (3.19), if this part $\boldsymbol{\Psi}_{f,n}(\mathbf{x}) e^{i2\pi f t}$ is seen as a whole, it becomes a period function showing a harmonic fluctuation pattern. Creating an animation of its real part

$$\text{Re}(\boldsymbol{\Psi}_{f,n}(\mathbf{x}) e^{i2\pi f t}) = \text{Re}(\boldsymbol{\Psi}_{f,n}(\mathbf{x})) \cos(2\pi f t) - \text{Im}(\boldsymbol{\Psi}_{f,n}(\mathbf{x})) \sin(2\pi f t) \quad (3.20)$$

is considered an excellent way of flow visualisation. If one uses the imaginary part to make the animation, the same harmonic fluctuation will show, but it will have a $\pi/2$ phase difference with respect to the real part.

Furthermore, taking use of Eqs. (3.13), (3.16), and (3.18), the cross-spectrum tensor can be represented by the eigenfunctions as

$$\mathbf{S}(\mathbf{x}, \tilde{\mathbf{x}}, f) = \sum_n \lambda_{f,n} \boldsymbol{\Psi}_{f,n}(\mathbf{x}) \boldsymbol{\Psi}_{f,n}^\dagger(\tilde{\mathbf{x}}) \quad (3.21)$$

Moreover, an important property of SPOD is the relationship between the mode energy and the TKE, which is deduced as follows:

$$2\bar{k} = \frac{1}{V} \int_{\Omega} \left(\frac{1}{T} \int_0^T \mathbf{u}'^{\dagger}(\mathbf{x}, t) \mathbf{u}'(\mathbf{x}, t) dt \right) d\mathbf{x} = \frac{1}{V} \int_{\Omega} \left(\frac{1}{T} \int_{-\infty}^{+\infty} \hat{\mathbf{u}}'^{\dagger}(\mathbf{x}, f) \hat{\mathbf{u}}'(\mathbf{x}, f) df \right) d\mathbf{x}$$

$$= \int_{-\infty}^{+\infty} \sum_n \left(\frac{1}{T} a_{f,n} a_{f,n}^* \right) \langle \boldsymbol{\psi}_{f,n}(\mathbf{x}), \boldsymbol{\psi}_{f,n}(\mathbf{x}) \rangle df = \int_{-\infty}^{+\infty} \sum_n \lambda_{f,n} df. \quad (3.22)$$

The second equation in Eq. (3.22) is an application of Parseval's theorem, and the third used the decomposition form, Eq. (3.16), along with the orthogonality properties, Eqs. (3.15) and (3.18). This property shows that the mode energies are parts of the TKE, and they make up the TKE of the whole flow field when they are integrated over all the frequencies f and summed over all the mode numbers n .

3.3 Algorithm

3.3.1 Eigenvalue problem in the matrix form

A common way for calculating the POD modes from the data is to directly convert the eigenvalue problem Eq. (3.3) to the matrix form. Usually, the interval Ω is discretised by cells, and the vector field is described by the values at the cell centroids. Denote the coordinates of the cell centroids by $\mathbf{x}_1, \mathbf{x}_2, \dots, \mathbf{x}_{N_s}$, and the discrete time by t_1, t_2, \dots, t_{N_t} . The whole data of the fluctuation velocity vector field will be included in the following $3N_s \times N_t$ matrix

$$[\mathbf{u}'] = \begin{bmatrix} \mathbf{u}'(\mathbf{x}_1, t_1) & \cdots & \mathbf{u}'(\mathbf{x}_1, t_{N_t}) \\ \vdots & \ddots & \vdots \\ \mathbf{u}'(\mathbf{x}_{N_s}, t_1) & \cdots & \mathbf{u}'(\mathbf{x}_{N_s}, t_{N_t}) \end{bmatrix}. \quad (3.23)$$

The correlation matrix can be written as

$$[\mathbf{C}] = \frac{1}{N_t} [\mathbf{u}'] [\mathbf{u}']^\dagger, \quad (3.24)$$

which is a $3N_s \times 3N_s$ matrix. The matrix form of the eigenvalue problem of Eq. (3.3) becomes

$$[\mathbf{C}][\mathbf{W}][\boldsymbol{\psi}] = \lambda[\boldsymbol{\psi}], \quad (3.25)$$

where

$$[\boldsymbol{\psi}] = \begin{bmatrix} \boldsymbol{\psi}(\mathbf{x}_1) \\ \vdots \\ \boldsymbol{\psi}(\mathbf{x}_{N_s}) \end{bmatrix} \quad (3.26)$$

is the vector form of the eigenfunction in the size of $3N_s \times 1$, and

$$[\mathbf{W}] = \text{diag} \left(\frac{\Delta V_1}{V}, \frac{\Delta V_1}{V}, \frac{\Delta V_1}{V}, \frac{\Delta V_2}{V}, \frac{\Delta V_2}{V}, \frac{\Delta V_2}{V}, \dots, \frac{\Delta V_{N_s}}{V}, \frac{\Delta V_{N_s}}{V}, \frac{\Delta V_{N_s}}{V} \right) \quad (3.27)$$

is the diagonal weight matrix whose elements consist of the cell volume ΔV_j of the j th

cell. Note that the spatial grids are typically not uniform, if they are inherited directly from CFD simulation. Therefore, the weight matrix is necessary in this case, if a correct TKE is aimed for when performing the reconstruction.

The eigenvalue problem indicated in Eq. (3.25) can be solved by a computer algebra system program, such as Matlab (2020) or Octave (2020), or by a linear algebra library of a programming language, such as NumPy on Python (2020) or LINPACK on FORTRAN (1982). However, this algorithm might be too costly to perform, because the cell number N_s may be exceedingly large to obtain a satisfying spatial resolution for three-dimensional field visualisation. In such a situation, computing the eigenvalues for a $3N_s \times 3N_s$ matrix is usually unpractical.

3.3.2 Snapshot POD algorithm

If the cell number largely exceeds the snapshot number, i.e., $N_s \gg N_t$, which is usually true for the data directly obtained from CFD simulation, then the snapshot POD algorithm (Sirovich, 1987) is preferred in this case. Without losing the spatial resolution, the snapshot POD algorithm greatly reduces the amount of calculation by sacrificing the number of the available modes.

The algorithm starts by constructing the matrix

$$[\underline{\mathbf{C}}] = \frac{1}{N_t} [\mathbf{u}']^\dagger [\mathbf{W}] [\mathbf{u}']. \quad (3.28)$$

Note that the size of $[\underline{\mathbf{C}}]$ is $N_t \times N_t$, which is much smaller than the correlation matrix $[\mathbf{C}]$, but the following eigenvalue problem

$$[\underline{\mathbf{C}}][\underline{\boldsymbol{\Psi}}] = \lambda [\underline{\boldsymbol{\Psi}}], \quad (3.29)$$

shares the same non-zero eigenvalues with Eq. (3.25), and the eigenvectors of these two eigenvalue problems can be related to each other. This can be easily proved by the singular value decomposition. With the n th eigenvectors $[\underline{\boldsymbol{\Psi}}]_n$ solving from the above smaller eigenvalue problem, the eigenvectors corresponding to the POD modes can be recovered by

$$[\boldsymbol{\Psi}]_n = \frac{1}{\sqrt{\lambda_n}} [\mathbf{u}'] [\underline{\boldsymbol{\Psi}}]_n, \quad n = 1, 2, \dots, N_t. \quad (3.30)$$

Due to the great reduction of the computation amount and memory resources, the snapshot POD algorithm has been used in fluid mechanics to computing POD modes from high-dimensional data.

3.3.3 DFT and Welch's method

Before introducing the algorithm of SPOD, the algorithms for estimating the Fourier spectrum should be introduced first.

For simplicity, a one-dimensional stochastic time series $u(t)$ is considered in this subsection with the sampling frequency f_s . The time series is discretised and written into a row as

$$[u] = [u(t_1) \quad u(t_2) \quad \cdots \quad u(t_{N_t})]. \quad (3.31)$$

The DFT for this time series can be performed by

$$[\hat{u}] = [u][\varpi], \quad (3.32)$$

where $[\varpi]$ is the well-known DFT matrix (Frigo and Johnson, 1998) defined as

$$[\varpi] = \begin{bmatrix} 1 & 1 & 1 & \cdots & 1 \\ 1 & \varpi & \varpi^2 & \cdots & \varpi^{N_F-1} \\ 1 & \varpi^2 & \varpi^4 & \cdots & \varpi^{2(N_F-1)} \\ \vdots & \vdots & \vdots & \ddots & \vdots \\ 1 & \varpi^{N_F-1} & \varpi^{2(N_F-1)} & \cdots & \varpi^{(N_F-1)^2} \end{bmatrix}, \quad (3.33)$$

where $\varpi = e^{-i2\pi/N_F}$, and N_F is the number of discretisation in DFT, which equals to N_t in this case. Now the j th element of $[\hat{u}]$ is the Fourier component $\hat{u}(f_j)$ at the discrete frequency

$$f_j = \begin{cases} \frac{j-1}{N_t} f_s, & j \leq \frac{N_F}{2} \\ \frac{j-1-N_F}{N_t} f_s, & j > \frac{N_F}{2} \end{cases}. \quad (3.34)$$

Subsequently, the spectrum of $u(t)$ can be naively estimated by

$$S(f_j) = \frac{1}{f_s N_F} \hat{u}(f_j) \hat{u}^*(f_j), \quad j = 1, 2, \dots, N_F, \quad (3.35)$$

and the cross-spectrum of $u(t)$ and another stochastic time series, e.g., $v(t)$, can be naively estimated by

$$S(f_j) = \frac{1}{f_s N_F} \hat{u}(f_j) \hat{v}^*(f_j), \quad j = 1, 2, \dots, N_F, \quad (3.36)$$

where the DFT of $v(t)$ is calculated in the same manner. However, the spectrum estimated in this way do not converge as N_t increases (Bartlett, 1948), and the uncertainty of the estimation is unacceptable. This problem can be solved by averaging the spectra over multiple realizations of the stochastic time series.

To this end, the Welch's method (Welch, 1967) is preferred and has become the most widely used approach for spectral density estimation. It is carried out by dividing the time signal into blocks, forming the periodogram for each block, and averaging. First, $[u]$ is divided into a set of overlapping blocks with the block length N_F . The m th block $[u]_m$ is represented as

$$[u]_m = \left[u(t_{(m-1)(N_F-N_o)+1}) \quad u(t_{(m-1)(N_F-N_o)+2}) \quad \cdots \quad u(t_{(m-1)(N_F-N_o)+N_F}) \right], \quad m = 1, 2, \dots, N_b, \quad (3.37)$$

where N_o is the number of the elements by which the blocks overlap (usually equals to $N_F/2$), and N_b is the number of the blocks. In this case, N_F is the number of elements which no longer equals to N_t . After that, the DFT is performed to each block as

$$[\hat{u}]_m = [u]_m [\omega][\varpi], \quad m = 1, 2, \dots, N_b, \quad (3.38)$$

where

$$[\omega] = \text{diag}(\omega_1, \omega_2, \dots, \omega_{N_F}), \quad (3.39)$$

is the weight matrix consisting of the nodal values of a window function. The window function is imposed to reduce the spectral leakage (Harris, 1978) due to the truncation in at the both sides of each block. Now the spectrum of $u(t)$ can be estimated by averaging the DFTs of all the blocks as

$$S(f_j) = \frac{1}{\mathcal{G}N_b} \sum_{m=1}^{N_b} \hat{u}_m(f_j) \hat{u}_m^*(f_j), \quad j = 1, 2, \dots, N_F, \quad (3.40)$$

where $\hat{u}_m(f_j)$ is the j th element of $[\hat{u}]_m$, and

$$\mathcal{G} = f_s N_F \sum_{p=1}^{N_F} w_p^2. \quad (3.41)$$

The cross-spectrum of $u(t)$ and another stochastic time series $v(t)$ is estimated by

$$S(f_j) = \frac{1}{\kappa N_b} \sum_{m=1}^{N_b} \hat{u}_m(f_j) \hat{v}_m^*(f_j), \quad j = 1, 2, \dots, N_F, \quad (3.42)$$

where $v(t)$ is also divided into blocks, and the DFT of each block is performed in the same manner.

3.3.4 Algorithm of SPOD

Combining the advantages of the snapshot POD algorithm (Sirovich, 1987) and Welch's method (Welch, 1967), Towne et al. (2018) proposed an efficient algorithm for calculating only a few of the SPOD modes with the highest fluctuation energy, which is

introduced in this subsection.

Same as the Welch's method, the data in Eq. (3.23) is first divided into blocks. The m th block is represented by

$$[\mathbf{u}']_m = \begin{bmatrix} \mathbf{u}'(\mathbf{x}_1, t_{(m-1)(N_F-N_o)+1}) & \cdots & \mathbf{u}'(\mathbf{x}_1, t_{(m-1)(N_F-N_o)+N_F}) \\ \vdots & \ddots & \vdots \\ \mathbf{u}'(\mathbf{x}_{N_s}, t_{(m-1)(N_F-N_o)+1}) & \cdots & \mathbf{u}'(\mathbf{x}_{N_s}, t_{(m-1)(N_F-N_o)+N_F}) \end{bmatrix}, \quad m = 1, 2, \dots, N_b. \quad (3.43)$$

The DFT of the m th block is calculated by

$$[\hat{\mathbf{u}}']_m = [\mathbf{u}']_m [\omega][\varpi], \quad m = 1, 2, \dots, N_b. \quad (3.44)$$

The j th column of $[\hat{\mathbf{u}}']_m$, denoted by $[\hat{\mathbf{u}}']_m^{(j)}$, is the Fourier component at the discrete frequency f_j given by Eq. (3.34). Now we construct a new matrix consisting of the j th columns extracted from all the blocks as

$$[\hat{\mathbf{U}}]_{f_j} = \begin{bmatrix} [\hat{\mathbf{u}}']_1^{(j)} & [\hat{\mathbf{u}}']_2^{(j)} & \cdots & [\hat{\mathbf{u}}']_m^{(j)} & \cdots & [\hat{\mathbf{u}}']_{N_b}^{(j)} \end{bmatrix}, \quad j = 1, 2, \dots, N_F. \quad (3.45)$$

Subsequently, the cross-spectrum matrix for the discrete frequency f_j is estimated by

$$[\mathbf{S}]_{f_j} = \frac{1}{\mathcal{G}N_b} [\hat{\mathbf{U}}]_{f_j} [\hat{\mathbf{U}}]_{f_j}^\dagger, \quad j = 1, 2, \dots, N_F, \quad (3.46)$$

where the coefficient \mathcal{G} is given in Eq. (3.41). The matrix form of the eigenvalue problem in Eq. (3.14) is represented as

$$[\mathbf{S}]_{f_j} [\mathbf{W}][\boldsymbol{\Psi}]_{f_j} = \lambda_{f_j} [\boldsymbol{\Psi}]_{f_j}, \quad j = 1, 2, \dots, N_F, \quad (3.47)$$

where $[\mathbf{W}]$ is the weight matrix given by Eq. (3.27). Note that the size of $[\hat{\mathbf{U}}]_{f_j}$ is $N_F \times N_b$ and $N_F \gg N_b$, the idea of the snapshot POD can be applied here to reduce the required computation. The matrix in size $N_b \times N_b$ can be constructed by

$$[\underline{\mathbf{S}}]_{f_j} = \frac{1}{\kappa N_b} [\hat{\mathbf{U}}]_{f_j}^\dagger [\mathbf{W}][\hat{\mathbf{U}}]_{f_j}, \quad j = 1, 2, \dots, N_F. \quad (3.48)$$

The eigenvalue problem to be solved becomes

$$[\underline{\mathbf{S}}]_{f_j} [\underline{\boldsymbol{\Psi}}]_{f_j} = \lambda_{f_j} [\underline{\boldsymbol{\Psi}}]_{f_j}, \quad j = 1, 2, \dots, N_F. \quad (3.49)$$

The eigenvalue problem in Eq. (3.49) shares the same non-zero with that in Eq. (3.47). With the n th eigenvectors $[\underline{\boldsymbol{\Psi}}]_{f_j, n}$ solving from Eq. (3.49), the eigenvectors corresponding to the SPOD modes can be recovered by

$$[\boldsymbol{\Psi}]_{f_j, n} = \frac{1}{\sqrt{\lambda_{f_j, n}}} [\hat{\mathbf{U}}]_{f_j} [\underline{\boldsymbol{\Psi}}]_{f_j, n}, \quad j = 1, 2, \dots, N_F, \quad n = 1, 2, \dots, N_b. \quad (3.50)$$

The obtained eigenvectors are the discrete form of the eigenfunctions, as shown in Eq.

(3.26).

As suggested by Schmidt and Colonius (2020), a proper number of snapshots within each block needs to be chosen to strike a balance between the resolvable frequency range and the uncertainty. In Welch's method, if the number of snapshots within each block is too small, the frequency resolution will be low, and aliasing errors will occur. If it is too large, the number of blocks will be insufficient because of the invariant amount of data, which will cause uncertainty in the energy estimation. In practice, the resolvable frequency range should cover the lowest frequency of interest, and the number of blocks should be sufficient to obtain a relatively precise result. For the time series which is not long enough, the above two requirements can be mutually exclusive. Collecting more data to get more realisations of the Fourier transform might be the only valid solution for this problem.

3.4 Summary and application guide

In this chapter, the basic theory and algorithms of POD and SPOD is briefly introduced. The general POD theory is first introduced, then extended to SPOD by combining it with the Fourier decomposition on time. Consequently, the algorithm of SPOD is established as a combination of the snapshot POD algorithm and Welch's method with DFT.

As a simple application guide of SPOD, for each specific set of (f, n) , the complex mode $\boldsymbol{\psi}_{f,n}(\mathbf{x})$ depicts a harmonic fluctuation pattern decomposed from the flow fluctuation. Animating the time-periodic function $\boldsymbol{\psi}_{f,n}(\mathbf{x})e^{i2\pi ft}$ is considered an excellent method for turbulent visualisation. In addition, the intensity of this fluctuation pattern can be measured quantitatively using the value of the mode energy $\lambda_{f,n}$. Similar to the Fourier spectrum, the SPOD spectrum can be obtained by plotting the mode energy versus frequency to show the energy distribution. The phase information of each mode was also obtained from the mode coefficient $a_{f,n}$. All these are considered to have the potential to facilitate understanding the turbulent flow to a great extent.

Reference

- Bartlett, M.S., 1948. Smoothing periodograms from time-series with continuous spectra. *Nature*. <https://doi.org/10.1038/161686a0>
- Dongarra, J., Bunch, J., Moler, C., Stewart, P., 1982. LINPACK [WWW Document]. URL <http://www.netlib.org/linpack/> (accessed 1.25.21).
- Eaton, J.W., 2020. GNU Octave [WWW Document]. URL <https://www.gnu.org/software/octave/index> (accessed 1.25.21).
- Fredholm, I., 1903. Sur une classe d'équations fonctionnelles. *Acta Math.* 27, 365–390. <https://doi.org/10.1007/BF02421317>

- Frigo, M., Johnson, S.G., 1998. FFTW: An adaptive software architecture for the FFT, in: ICASSP, IEEE International Conference on Acoustics, Speech and Signal Processing - Proceedings. pp. 1381–1384. <https://doi.org/10.1109/ICASSP.1998.681704>
- Harris, F.J., 1978. On the Use of Windows for Harmonic Analysis with the Discrete Fourier Transform. *Proc. IEEE* 66, 51–83. <https://doi.org/10.1109/PROC.1978.10837>
- NumPy, 2020. NumPy [WWW Document]. URL <https://numpy.org/> (accessed 1.25.21).
- Pipkin, A.C., 1991. Hilbert—Schmidt Theory, in: *A Course on Integral Equations*. Springer, New York, pp. 44–71. https://doi.org/10.1007/978-1-4612-4446-2_3
- Schmidt, O.T., Colonius, T., 2020. Guide to Spectral Proper Orthogonal Decomposition. *AIAA J.* 58, 1023–1033. <https://doi.org/10.2514/1.J058809>
- Sirovich, L., 1987. Turbulence and the dynamics of coherent structures. I. Coherent structures. *Q. Appl. Math.* 45, 561–571.
- The MathWorks Inc., 2020. MATLAB - MathWorks - MATLAB & Simulink [WWW Document]. URL <https://www.mathworks.com/products/matlab.html> (accessed 1.25.21).
- Towne, A., Schmidt, O.T., Colonius, T., 2018. Spectral proper orthogonal decomposition and its relationship to dynamic mode decomposition and resolvent analysis. *J. Fluid Mech.* 847, 821–867. <https://doi.org/10.1017/jfm.2018.283>
- Welch, P.D., 1967. The Use of Fast Fourier Transform for the Estimation of Power Spectra: A Method Based on Time Averaging Over Short, Modified Periodograms. *IEEE Trans. Audio Electroacoust.* 15, 70–73. <https://doi.org/10.1109/TAU.1967.1161901>

Chapter 4

Identification of three-dimensional flow features around a square-section building model

4.1 Introduction

Most man-made architectural structures present bluff forms to the wind (Irwin, 2008). The effects of wind flow indicate the unique nature of the problems that can be encountered by building structures. Therefore, an understanding of bluff body aerodynamics is pivotal to make progress in our understanding of wind engineering (Flay, 2013).

Inspired by classical studies in the aeronautical field, flow around infinite cylinders has been well studied, and an enormous amount of research has been published (Matsumoto, 1999; Williamson, 1996; Zdravkovich, 1990). However, the practical demand in engineering impelled the study of the flow around a finite-length cylinder. In the field of wind environment, or wind engineering, building structures are usually represented by three-dimensional prisms with free ends located in the atmospheric boundary layer flow.

The end effect and boundary layer cause the flow field to become strongly three-dimensional, which differs from the two-dimensional flow around infinite cylinders (Kawamura et al., 1984; Sumner et al., 2004; Wang et al., 2009). Wang et al. (2004) provided a simplified model for the complex flow around a wall-mounted finite-length cylinder with a square cross-section. The four main flow features include the horseshoe vortices, located at the front base of the cylinder; base vortices, developing from the base on the two sides; primary vortex shedding (or Kármán vortex street), along the cylinder sides; and tip vortices, emitting from the free end of the cylinder.

Previous methods for investigating these flow features varied, and were primarily based on quantitative flow visualisation. Both CFD simulations and WTEs provide detailed

flow field data for examining flow features (Uffinger et al., 2013). However, when the finite-length cylinder is in the boundary layer flow with a high Reynolds number, the turbulent motion and the strong perturbation caused by the approaching flow can be obstacles to obtaining a clear visualisation of the featured flow structures. Direct observation of the instantaneous flow field will not provide a clearly recognisable flow structure, while the time-average field will lose the information of chronological vortex development. Moreover, measuring the frequency or the intensity for a certain flow feature can also be a difficult task because the flow field is mixed by the features of all the time scales. Because flow features are controlled by different physical mechanisms that require various physical quantities to describe them, previous research on bluff body aerodynamics tended to observe these different physical quantities. However, this makes it difficult to compare or study the correlation between features. Similar problems also exist in the design work regarding a turbulent fluid field. For example, due to the lack of quantitatively analysing the turbulent structures around buildings, empirical explanations are usually preferred when assessing and improving the wind environment for an urban area (Zhang et al., 2020).

To solve this problem, we seek a single mathematical procedure to identify and extract the various flow features. The modal decomposition methods (Taira et al., 2017) were considered as potential solutions. On this point, POD and SPOD is considered good tools for extracting coherent structures from turbulent flow data. Recent applications of POD or SPOD for identifying coherent structures around three-dimensional bluff bodies placed in the boundary layer are limited. Wang et al.(2019) and Wang and Lam (2019) extracted the symmetric and antisymmetric fluctuating wake characteristics by performing POD on the symmetric or antisymmetric part of the velocity field on several horizontal planes in the near wake. Nevertheless, the influence of the three-dimensional flow structures was not well illustrated by the two-dimensional flow field in these studies.

This study identified the three-dimensional main flow features around a square-section building model using SPOD analysis. The analysis was performed on the three-dimensional velocity field obtained by LES. Using this single technique, we presented a comprehensive view of the turbulent structures around the square-section cylinder, which is an integration of almost all the flow features. The identified three-dimensional flow features were visualised in multimedia views to examine the details, and then compared to previous studies. Based on the SPOD theory, new quantities were defined to quantitatively reveal the primary frequency and relative intensity of these flow features. In addition, the local-space spectrum was proposed to observe the detailed energy composition within a local space, to show which flow features directly related to the

fluctuation within this local space.

This chapter is organised as follows. The analysis methods based on SPOD technique is first introduced in Section 4.2. Section 4.3 introduces the simulation of the flow field. Section 4.4 provides the SPOD analysis results. Wherein, the typical modes for each of the flow features are displayed, studied in detail, and compared to the observations of the former studies. Section 4.5 provides the summaries and conclusion.

4.2 Analysis methods

4.2.1 Similarity between inter-frequency modes

After performing SPOD to the data, spatial similarity can usually be observed between the modes from different frequencies, especially when the frequency values are close. Sometimes, the most energetic modes within a range of frequencies can resemble each other, depicting almost the same vortex motion, with only a slight difference in the vortex size or some other details. Typically, the SPOD modes change continuously with the frequency, as is the case for circular functions in the Fourier transformation. To quantitatively measure this similarity of the modes, we define the spatial similarity coefficient γ between mode (f_1, n_1) and mode (f_2, n_2) as follows:

$$\gamma_{(f_1, n_1), (f_2, n_2)} = \left| \left\langle \Psi_{f_1, n_1}(\mathbf{x}), \Psi_{f_2, n_2}(\mathbf{x}) \right\rangle \right|, \quad (4.1)$$

where $|\cdot|$ denotes the modulus of a complex number. Note that γ has a range of $0 \leq \gamma \leq 1$, given by the Cauchy–Schwarz inequality, and the values 0 or 1 are taken when $f_1 = f_2$. This coefficient can also be understood as:

$$\gamma_{(f_1, n_1), (f_2, n_2)} = \sqrt{\frac{\left\langle \Psi_{f_1, n_1}(\mathbf{x}), \Psi_{f_2, n_2}(\mathbf{x}) \right\rangle \left\langle \Psi_{f_1, n_1}(\mathbf{x}), \Psi_{f_2, n_2}(\mathbf{x}) \right\rangle^*}{\left\langle \Psi_{f_1, n_1}(\mathbf{x}), \Psi_{f_1, n_1}(\mathbf{x}) \right\rangle \left\langle \Psi_{f_2, n_2}(\mathbf{x}), \Psi_{f_2, n_2}(\mathbf{x}) \right\rangle^*}}, \quad (4.2)$$

Because the denominator equals 1, Eq. (4.2) is equivalent to Eq. (4.1). Note that Eq. (4.2) is analogous to the definition of the correlation coefficient between two random variables.

Furthermore, it can be interesting and sometimes significant to calculate the percentage of the total energy that a certain coherent motion accounts for. Because a strict physical definition of the coherent structure is still not quantitatively given (Träumner et al., 2015), this paper offers an intuitive estimation. First, we select a typical periodic fluctuation pattern $\Psi_{f_1, n_1}(\mathbf{x})$ defined by an SPOD mode, which is considered best for depicting the coherent motion of interest. Then, the estimated percentage value is calculated by:

$$P_{f_1, n_1} = \frac{1}{2\bar{k}} \int_{-\infty}^{+\infty} \sum_n \gamma_{(f,n),(f_1,n_1)}^2 \lambda_{f,n} df \times 100\%. \quad (4.3)$$

Here, the γ^2 value can be understood as a weight, so that the more similar the mode (f, n) is to the selected typical mode (f_1, n_1), the more energy is counted. The derivation is provided below.

The procedure of determining the energy of a certain spatial fluctuation pattern is similar to that of the classical POD technique (Lumley, 1970, 1967). One can assume that $\boldsymbol{\psi}_{f_1, n_1}(\mathbf{x})$ is one of the POD modes of this dataset, and then try to find its energy. Note that $\boldsymbol{\psi}_{f_1, n_1}(\mathbf{x})$ is typically not one of the POD modes, but our purpose is the same. First, the wind velocity data are projected onto the spatial pattern $\boldsymbol{\psi}_{f_1, n_1}(\mathbf{x})$:

$$a_{f_1, n_1}^{\text{POD}}(t) = \langle \mathbf{u}'(\mathbf{x}, t), \boldsymbol{\psi}_{f_1, n_1}(\mathbf{x}) \rangle = \int_{-\infty}^{+\infty} \sum_n a_{f,n} \langle \boldsymbol{\psi}_{f,n}(\mathbf{x}), \boldsymbol{\psi}_{f_1, n_1}(\mathbf{x}) \rangle e^{i2\pi ft} df. \quad (4.4)$$

where $a_{f_1, n_1}^{\text{POD}}(t)$ denotes the temporal fluctuation under this pattern. The Fourier transformation of it can be easily obtained as

$$\hat{a}_{f_1, n_1}^{\text{POD}}(f) = \sum_n a_{f,n} \langle \boldsymbol{\psi}_{f,n}(\mathbf{x}), \boldsymbol{\psi}_{f_1, n_1}(\mathbf{x}) \rangle. \quad (4.5)$$

Subsequently, the energy $\lambda_{f_1, n_1}^{\text{POD}}$ is defined as the variance of this complex time series, which can be deduced as:

$$\begin{aligned} \lambda_{f_1, n_1}^{\text{POD}} &= \frac{1}{T} \int_0^T a_{f_1, n_1}^{\text{POD}}(t) a_{f_1, n_1}^{\text{POD}}(t) dt = \frac{1}{T} \int_{-\infty}^{+\infty} \hat{a}_{f_1, n_1}^{\text{POD}}(f) \hat{a}_{f_1, n_1}^{\text{POD}}(f) df \\ &= \int_{-\infty}^{+\infty} \sum_n \left(\frac{1}{T} a_{f,n}^* a_{f,n} \right) \cdot \left| \langle \boldsymbol{\psi}_{f,n}(\mathbf{x}), \boldsymbol{\psi}_{f_1, n_1}(\mathbf{x}) \rangle \right|^2 df = \int_{-\infty}^{+\infty} \sum_n \gamma_{(f,n),(f_1,n_1)}^2 \lambda_{f,n} df. \end{aligned} \quad (4.6)$$

The second equation is an application of Parseval's theorem, and the third equation uses the orthogonality property of $a_{f,n}$. Finally, the resulting energy value is divided by the total energy $2\bar{k}$, and Eq. (4.3) can be obtained.

4.2.2 Local-space spectrum

The kinetic energy in POD-based methods is usually calculated as the sum (or average) in the entire flow field. However, some small-scale flow features are concentrated within a local space and can be easily overlooked because of their low kinetic energy. In some applications, we are interested in how much a certain global flow feature influences the velocity within an interested local space. One optional solution is to directly perform the POD-based methods on this local space, but the correlation information between the local space and other fields will be sacrificed. Recognising the mechanism of the flow features within such a small space could be a difficult task. This section aims to provide an

alternative solution.

Suppose $\Gamma \subset \Omega$ is the local space of interest. The local-space SPOD spectrum $s_{f,n}$ is defined as:

$$s_{f,n} = \frac{\lambda_{f,n}}{V_\Gamma} \int_\Gamma \boldsymbol{\psi}_{f,n}^\dagger(\mathbf{x}) \boldsymbol{\psi}_{f,n}(\mathbf{x}) d\mathbf{x}, \quad (4.7)$$

where V_Γ is the volume of the local space Γ , $\boldsymbol{\psi}_{f,n}(\mathbf{x})$ and $\lambda_{f,n}$ are the mode and mode energy calculated from the whole field Ω , respectively. The average kinetic energy within the field Γ , $2\overline{k_\Gamma}$, is decomposed into local-space mode energy $s_{f,n}$ corresponding to mode (f, n) , which can be derived as follows:

$$\begin{aligned} 2\overline{k_\Gamma} &= \frac{2}{V_\Gamma} \int_\Gamma \left(\frac{1}{2T} \int_0^T \mathbf{u}'^\dagger(\mathbf{x}, t) \mathbf{u}'(\mathbf{x}, t) dt \right) d\mathbf{x} = \frac{1}{V_\Gamma} \int_\Gamma \left(\frac{1}{T} \int_{-\infty}^{+\infty} \hat{\mathbf{u}}'^\dagger(\mathbf{x}, f) \hat{\mathbf{u}}'(\mathbf{x}, f) df \right) d\mathbf{x} \\ &= \int_{-\infty}^{+\infty} \sum_n \left(\frac{1}{T} \mathbf{a}_{f,n}^* \mathbf{a}_{f,n} \right) \left(\frac{1}{V_\Gamma} \int_\Gamma \boldsymbol{\psi}_{f,n}^\dagger(\mathbf{x}) \boldsymbol{\psi}_{f,n}(\mathbf{x}) d\mathbf{x} \right) df = \int_{-\infty}^{+\infty} \sum_n s_{f,n} df. \end{aligned} \quad (4.8)$$

This technique can be applied to analyse the composition of the kinetic energy for a certain local part of the sampling field, and to provide information about which modes (or flow features) are directly related to the kinetic energy in this local space.

4.3 Outline of simulation of the flow field

The flow field around a single building model (1:1:2 prism) (Figure 4.1) was calculated via LES using open source CFD software, OpenFOAM, with reference to the guidebook proposed by the AIJ (Architectural Institute of Japan, 2016). This simulation reproduced the results of the WTE for the same building model (Meng and Hibi, 1998).

This case was chosen because it is a typical bluff body representing a common building type in the real world, around which the flow structures illustrated in Wang et al. (2004) occur. As a typical case for studying the accuracy of CFD, AIJ has provided the WTE database, which can serve as the exact values, and several CFD guidelines were developed based on this case study (Okaze et al., 2017; Tominaga et al., 2008; Yoshie et al., 2007). Therefore, the accuracy of this simulation can be easily guaranteed.

The data were not directly obtained by performing a WTE because it is still not a popular technique to obtain the three-dimensional velocity for the whole three-dimensional field simultaneously by particle image velocimetry. In addition, considering that the instantaneous velocity was needed in the SPOD analysis, LES was performed rather than solving the Reynolds-averaged Navier–Stokes equations. The calculation conditions of

LES were basically set according to the study by Okaze et al. (2017). In their study, they compared the results for the same building model using various computational conditions and provided some guidelines for LES. Figure 4.1 presents the simulation domain. The velocity input on the inlet boundary was obtained from an additional LES that simulated an urban boundary layer flow in a wind tunnel, which was the same as that of Kikumoto et al. (2018). The mean velocity profile was close to the $\alpha = 0.27$ power law with $U_H \approx 4.5$ m/s at the building height. The other simulation conditions are listed in Table 4.1. Although the obtained turbulence was spatially filtered on a small scale by LES (Versteeg and Malalasekera, 2007) so that it was not exactly equivalent to the real instantaneous velocity at each spatial point, the flow features to be identified were on a much larger scale compared to the filter scale. Therefore, we judged it to have little impact on the feature identification.

During the simulation, the vector wind speed data were sampled within the field below:

$$\Omega = \left\{ \mathbf{x} = (x, y, z)^T \mid -1.5b \leq x \leq 3.5b, \quad -2b \leq y \leq 2b, \quad 0 \leq z \leq 3.5b \right\}, \quad (4.9)$$

where b is the building width, which was 0.16 m in the simulation. This field was considered large enough to contain most of the main flow features around the building. The inflow mean velocity U_H (≈ 4.5 m/s) at the building height was considered as the reference wind speed, which was used to normalise the wind speed data. The sampling frequency was set to 1000 Hz.

The mean velocity and TKE are shown in Figures 4.2 and 4.3, respectively. The streamlines of the mean velocity show the flow separating at the leading edge on the roof and on both sides. The wake flow showed a downward trend and caused a vertical bubble in the time-average sense. The same situation was observed on the horizontal plane where the wake flow narrowed downstream and caused two symmetric bubbles in the time-average sense. The high values of TKE were mainly concentrated within the shear layers on the roof and on both sides of the building, and stretched downstream to the wake field. The streamwise mean velocity and TKE are compared with the results of the wind tunnel test provided by the AIJ guidebook and the original WTE results of Meng and Hibi (1998), in Figure 4.4. Most of the results are consistent, except that the LES tended to slightly underestimate the TKE on the sides of the building. The author considered the LES to be sufficiently accurate for the purposes of this study.

Table 4.1 CFD simulation conditions

Item	Content
Sub-grid scale model	Standard Smagorinsky model (Smagorinsky, 1963) with $C_s=0.12$ The length scale near the wall was modified using the Van Driest damping function (Van Driest, 1956).
Building size	$b(x) \times b(y) \times 2b(z)$ ($b = 0.16$ m)
Simulation domain	$x: 9.5b + b$ (building) + $14.5b$ $y: 6.375b + b$ (building) + $6.375b$ $z: 2b$ (building) + $11.75b$
Grid partitioning	$142(x) \times 122(y) \times 87(z)$ Total cells: 966,016 Minimum grid size: $b/32$ adjacent to building wall and tunnel floor ($y^+ \approx 100$) Stretching function: hyperbolic tangent function
Time step and marching	0.00025 s, Pressure-implicit with splitting order (PISO) (Issa, 1986)
Simulation period	Preparatory: 0~60 s, Sampling: 60~120 s
Inlet boundary conditions	Velocity inlet boundary condition: Inflow turbulence data was shared by Kikumoto et al. (2018), who did an additional LES that simulated an urban boundary layer flow in a wind tunnel. The mean velocity profile is close to the $\alpha = 0.27$ power law with $U_H \approx 4.5$ m/s at the building height and $U_0 \approx 6.5$ m/s at the tunnel height.
Outlet boundary conditions	Zero gradient pressure outlet boundary condition
Wall function	Surfaces of the tunnel floor: Spalding's law (Spalding, 1962) Building walls: Spalding's law Tunnel wall and ceiling: Spalding's law
Space discretisation	2 nd -order central difference
Time discretisation	Euler-implicit

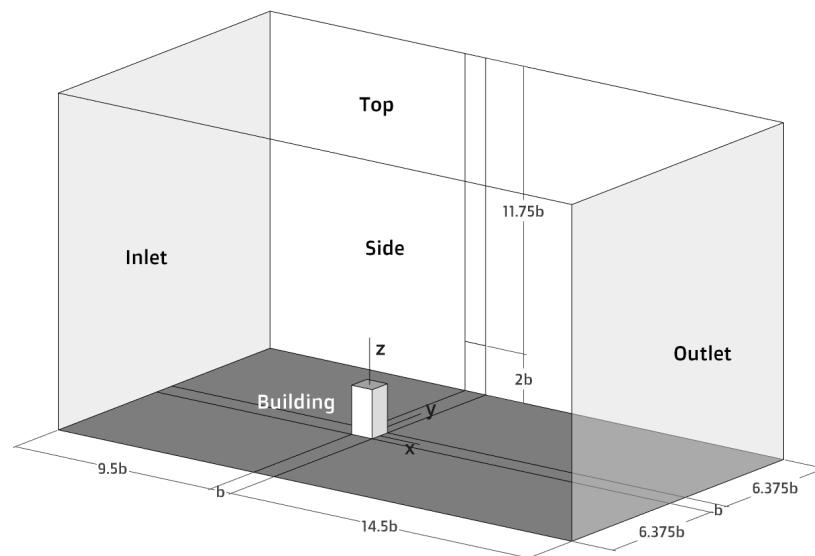


Figure 4.1 Simulation domain.

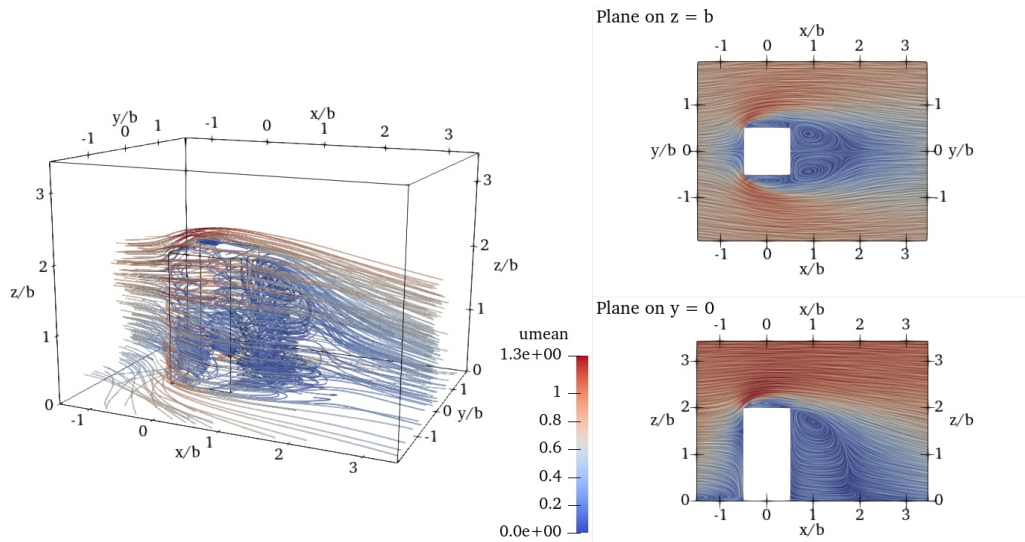


Figure 4.2 Mean velocity within the sampling domain. The left panel shows the streamlines seeding from the spatial points, where the vorticity magnitude was high.

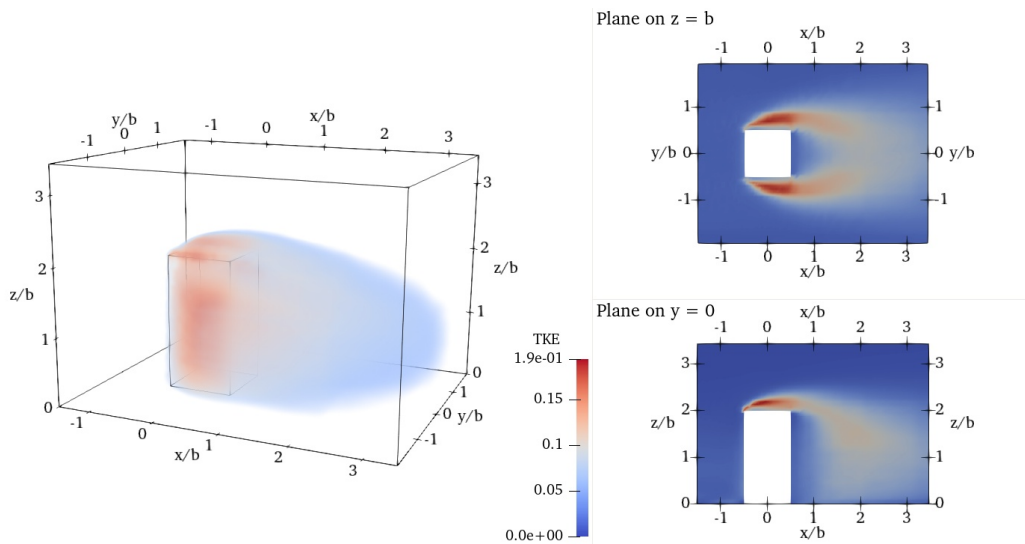


Figure 4.3 TKE within the sampling domain. The left panel only shows colour at the spatial points, where TKE is higher than 0.075, to provide a better view.

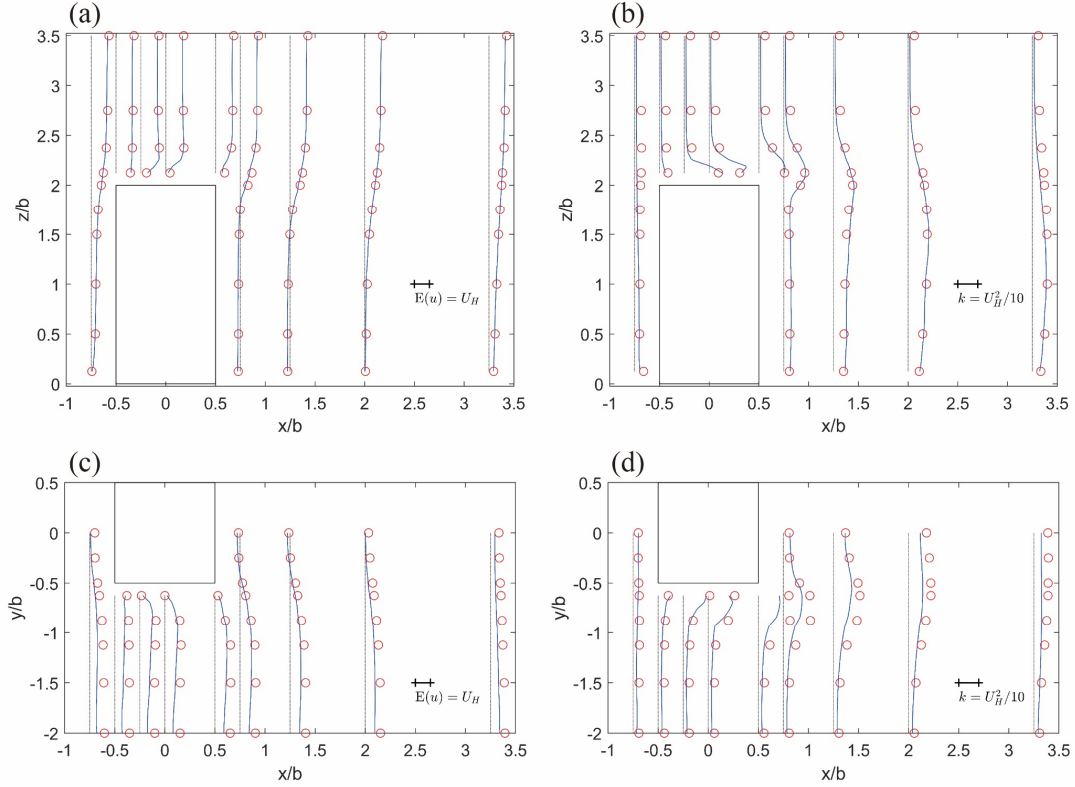


Figure 4.4 Comparison of the results between the LES (blue lines) and experiment (red circles). **(a)** Mean streamwise velocity on plane $y = 0$. **(b)** TKE on plane $y = 0$. **(c)** Mean streamwise velocity on plane $z = 1.25b$. **(d)** TKE on plane $z = 1.25b$.

4.4 SPOD analysis of the velocity field

4.4.1 Performing SPOD

The SPOD modes were calculated using the method proposed by Towne et al. (2018), which made good use of Welch's method (Welch, 1967). Welch's method for estimating power spectra is carried out by dividing the time signal into blocks, forming the periodogram for each block, and averaging. As previously suggested by Schmidt and Colonius (2020), a proper number of snapshots within each block need to be chosen to strike a balance between the resolvable frequency range and the uncertainty. In Welch's method, if the number of snapshots within each block is too small, the frequency resolution will be low, and aliasing errors will occur. If it is too large, the number of blocks will be insufficient because of the invariant amount of data, which will cause uncertainty in the energy estimation. In this study, this number was chosen to be 4,096 because the resolvable frequency range precisely covered the lowest frequency of the main vortex motion, and the number of blocks (28) was considered sufficient to obtain a

relatively precise result. Moreover, the overlap between the blocks was chosen to be 50% of the number of snapshots within each block, which is commonly accepted in the practise of Welch's method, and the Hamming window was applied to avoid spectral leakage.

4.4.2 SPOD spectrum

Figure 4.5 presents the SPOD spectrum, which shows the results of the largest 28 eigenvalues (single-sided spectrum) at all discrete frequencies. The eigenvalues and the frequencies are nondimensionalised and normalised, so that if one integrates these eigenvalues over a certain range, the area (or volume) obtained under the curve (or surface) will equal the proportion of the energy within that range in the total energy.

Note that the eigenvalue presented in Figure 4.5 corresponds to an SPOD mode. The modes can be understood by examining the real and imaginary parts of the eigenfunctions, or by watching the animation created by $\text{Re}(\psi_{f,n} e^{i2\pi ft})$. The animation process was approximately $\text{Re}(\psi_{f,n}) \rightarrow -\text{Im}(\psi_{f,n}) \rightarrow -\text{Re}(\psi_{f,n}) \rightarrow \text{Im}(\psi_{f,n}) \rightarrow \text{Re}(\psi_{f,n})$. Figures 4.6–4.13 provide several modes showing some characteristic flow phenomena, which will be introduced in detail in the latter subsections. Furthermore, the animations are shown in the multimedia views.

From the distribution of energy, the energy was primarily concentrated within the range of low frequency and low mode number. All the extracted modes accounted for nearly 100% of the total energy in this flow field. Almost all the basic flow features were captured by the SPOD modes with mode number $n = 1$ or 2, listed in Table 4.2, except for the horseshoe vortex. According to the study of Sau et al. (2003), the horseshoe vortex is located $x \approx -1.5b$ upstream of the building and extends to $y > 2b$ on both sides of the building, which is beyond the sampling domain of the present study. Fortunately, the horseshoe vortex does not join the vorticity interaction process with the near wake vortices (Sau et al., 2003), so it has little influence on other features.

For each of the other flow features, one or multiple typical modes, which were considered best depicting the flow features, were selected and are listed in Table 4.2. The primary frequency and intensity of each flow feature can be quantitatively estimated by the frequency of the typical modes listed in Table 4.2 and the energy percentage of the corresponding spatial pattern is shown in Figures 4.6–4.13. The following subsections describe these features in detail via SPOD modes.

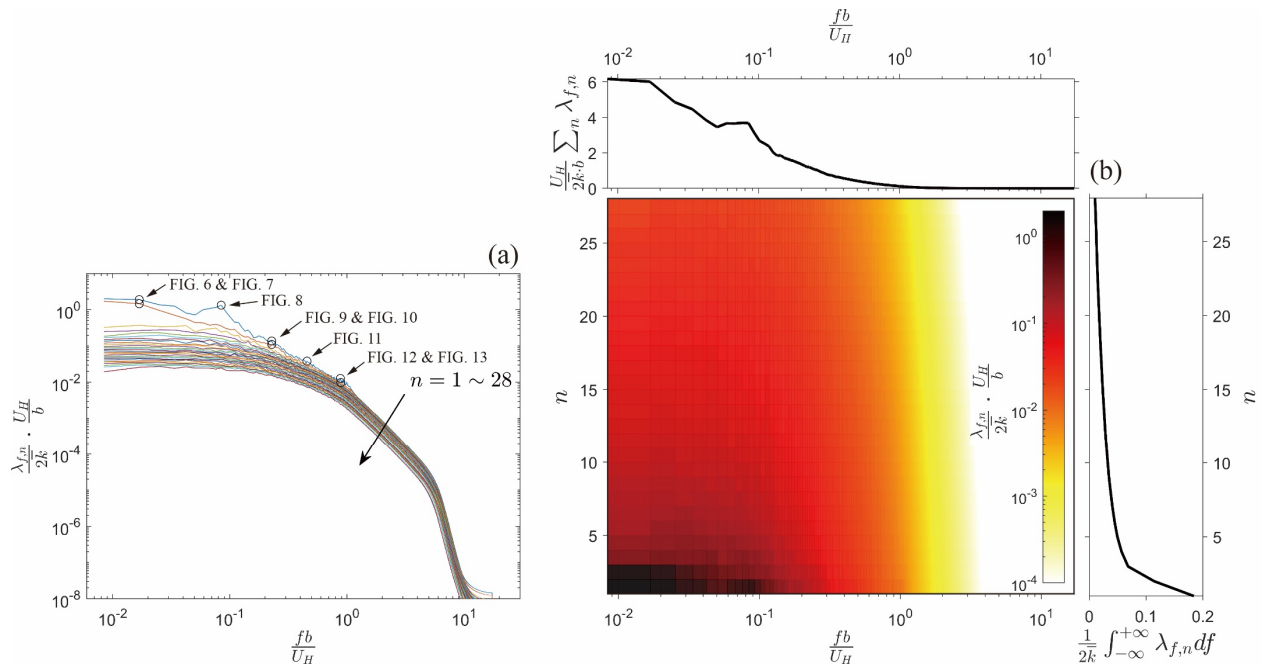


Figure 4.5 SPOD spectrum. **(a)** The nondimensional eigenvalues are plotted versus the nondimensional frequency. **(b)** The nondimensional eigenvalues (shown by colour) are plotted versus both the frequency and the spatial mode number. It also shows the summed or integrated eigenvalues along the frequency or the spatial mode number.

Table 4.2 Basic flow features and the corresponding typical SPOD modes.

Flow feature	Typical SPOD mode		
Low-frequency modes	Mode ($fb/U_H = 0.0169$, $n = 1$)	Figure 4.6	Antisymmetric mode
	Mode ($fb/U_H = 0.0169$, $n = 2$)	Figure 4.7	Symmetric mode
Primary wake vortex shedding	Mode ($fb/U_H = 0.0845$, $n = 1$)	Figure 4.8	Primary periodic vortices
Tip and base vortices	Mode ($fb/U_H = 0.2281$, $n = 1$)	Figure 4.9	A pair on one side
	Mode ($fb/U_H = 0.2281$, $n = 2$)	Figure 4.10	A pair on the other side
	Mode ($fb/U_H = 0.4562$, $n = 1$)	Figure 4.11	A pair on the roof
Primary side vortex shedding	Mode ($fb/U_H = 0.8786$, $n = 1$)	Figure 4.12	Vortices on the roof
	Mode ($fb/U_H = 0.8870$, $n = 2$)	Figure 4.13	Vortices on building side

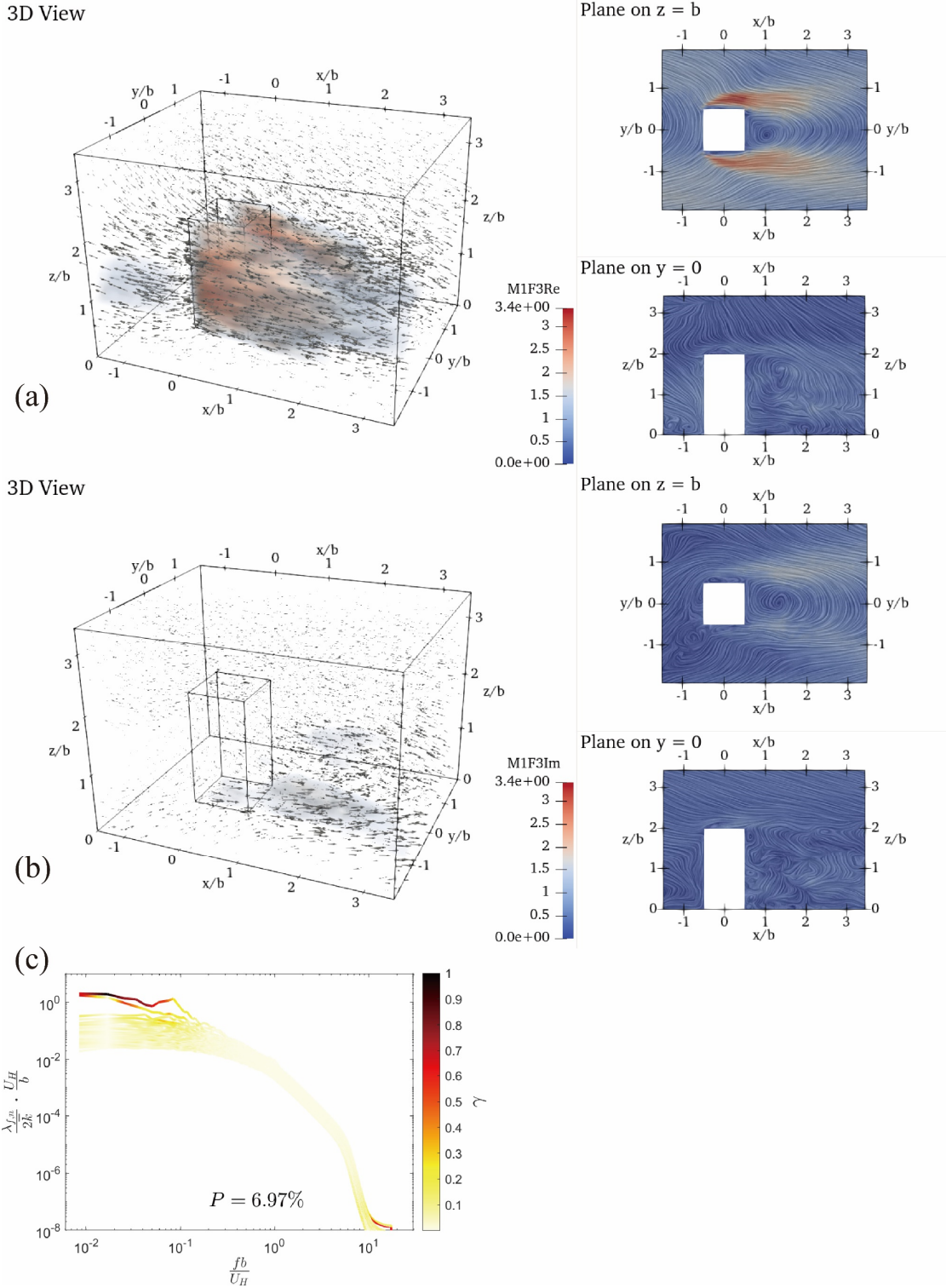


Figure 4.6 Mode ($f_b/U_H = 0.0169$, $n = 1$). **(a)** Real part of the eigenfunction. **(b)** Imaginary part of the eigenfunction. Each of **(a)** and **(b)** provides a 3D view (left), a characteristic horizontal plane (upper right) and a characteristic vertical plane (lower right). The real or imaginary part of the eigenfunction is displayed by the streamlines where the colour shows the magnitude. The colours in the 3D view are shown only at the spatial points, where the magnitude is relatively high, to provide a better view. **(c)** Spatial similarity coefficient shown by the colour and displayed based on the same panel of Figure 4.5 (a). The spatial similarity coefficient between the current mode and all other SPOD mode is given by Eq. (4.1), and the energy percentage value P is calculated by Eq. (4.3), where (f_i, n_i) is substituted by the index of the current mode.

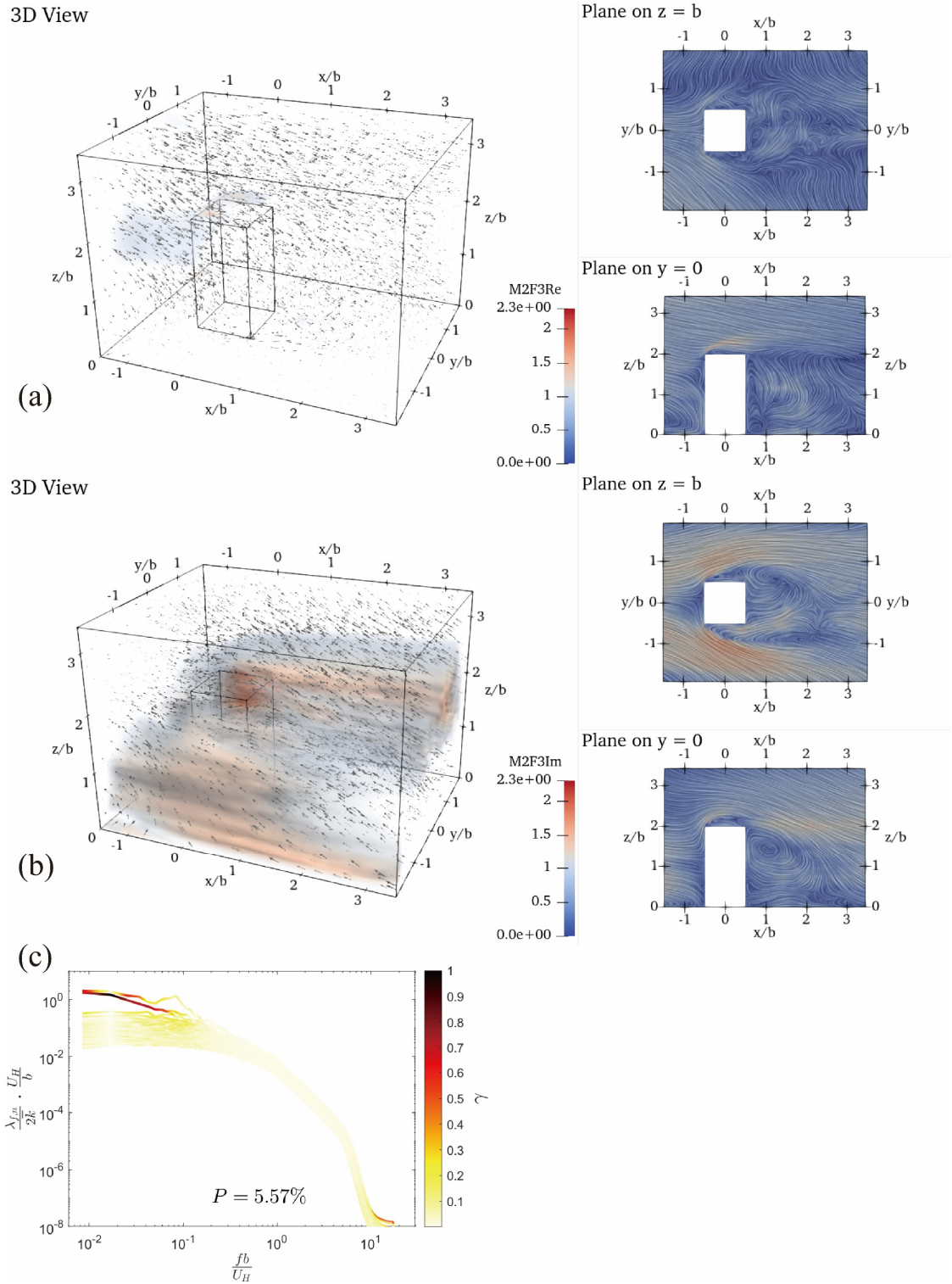


Figure 4.7 Mode ($fb/U_H = 0.0169$, $n = 2$). **(a)** Real part of the eigenfunction. **(b)** Imaginary part of the eigenfunction. **(c)** Spatial similarity coefficient. See the caption of Figure 4.6 for more details.

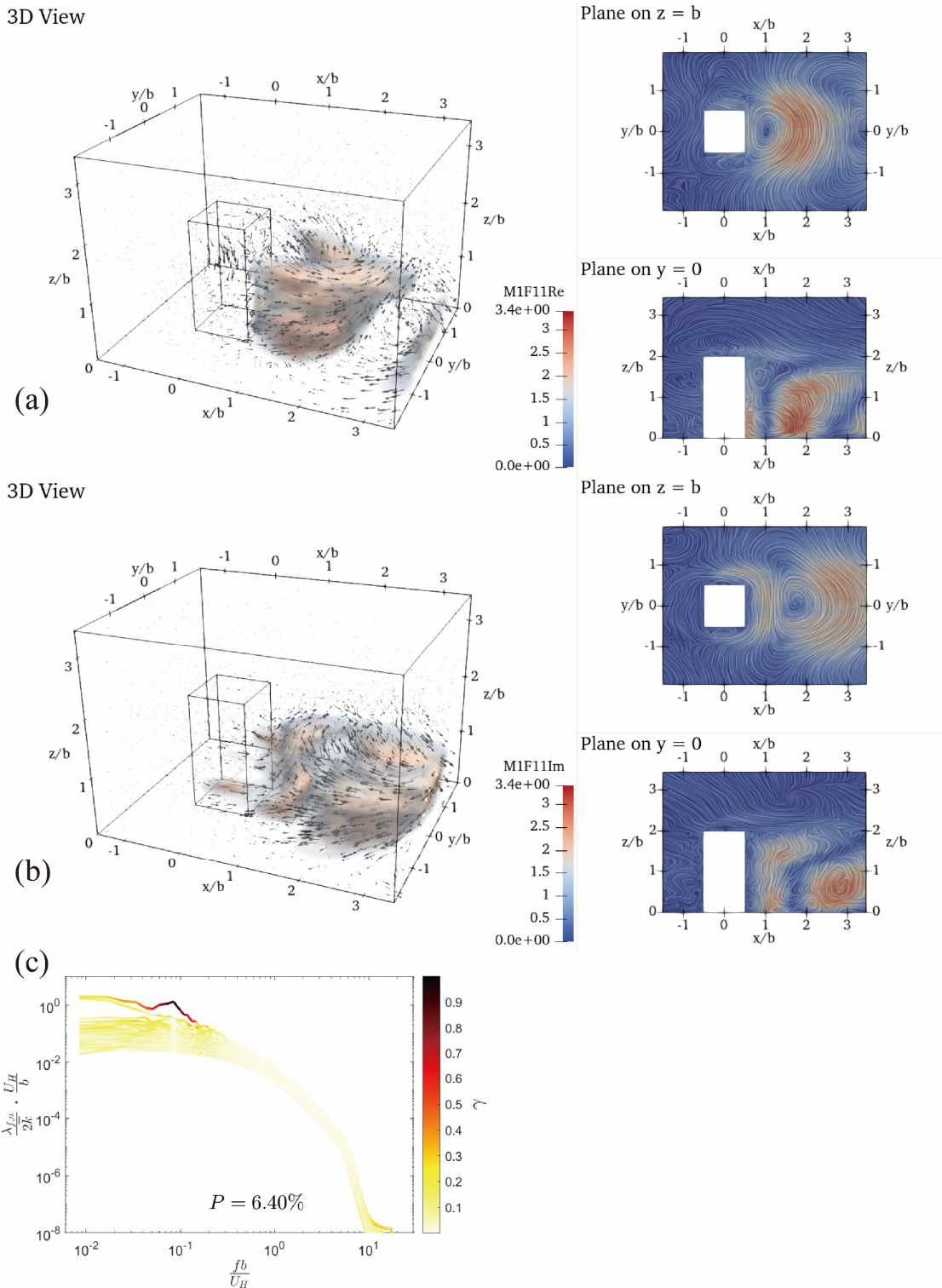


Figure 4.8 Mode ($fb/U_H = 0.0845$, $n = 1$). **(a)** Real part of the eigenfunction. **(b)** Imaginary part of the eigenfunction. **(c)** Spatial similarity coefficient. See the caption of Figure 4.6 for more details.

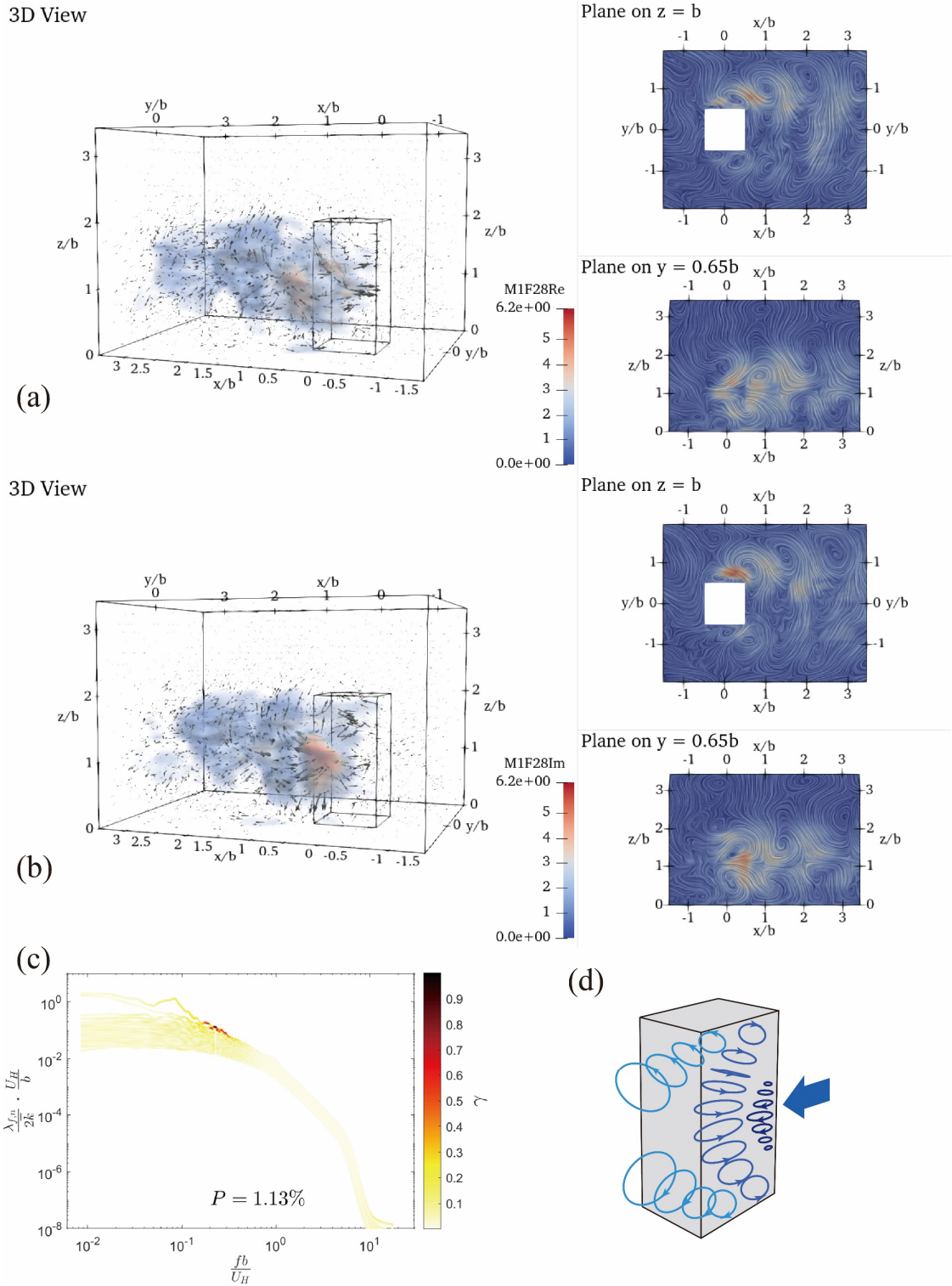
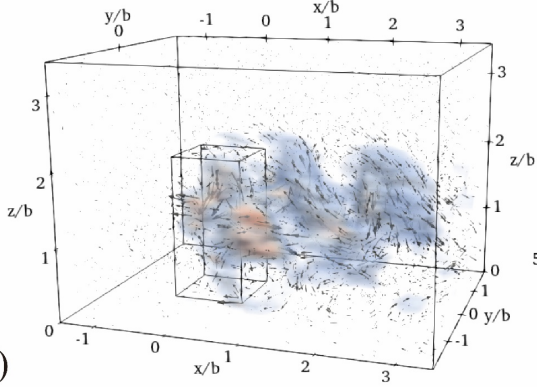


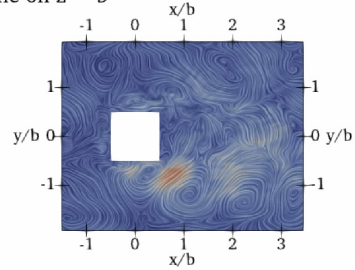
Figure 4.9 Mode ($fb/U_H = 0.2281$, $n = 1$). **(a)** Real part of the eigenfunction. **(b)** Imaginary part of the eigenfunction. **(c)** Spatial similarity coefficient. See the caption of Figure 4.6 for more details. **(d)** Schematic of the vortex structure.

3D View

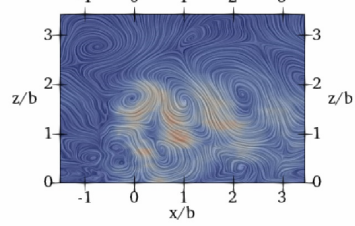


(a)

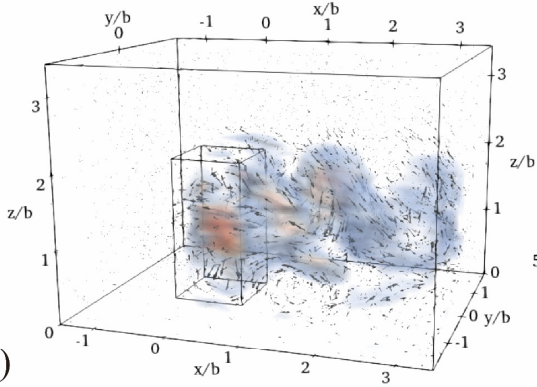
Plane on $z = b$



Plane on $y = -0.65b$

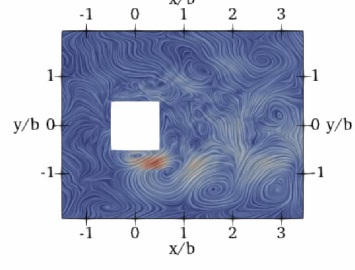


3D View

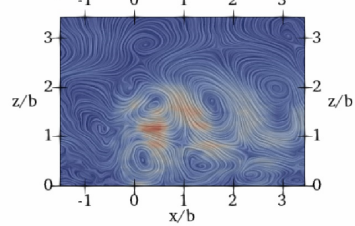


(b)

Plane on $z = b$



Plane on $y = -0.65b$



(c)

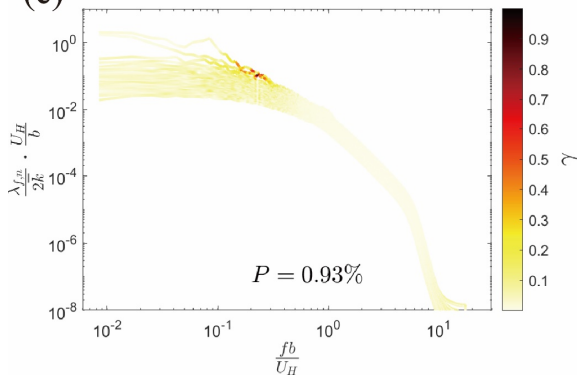


Figure 4.10 Mode ($fb/U_H = 0.2281$, $n = 2$). (a) Real part of the eigenfunction. (b) Imaginary part of the eigenfunction. (c) Spatial similarity coefficient. See the caption of Figure 4.6 for more details.

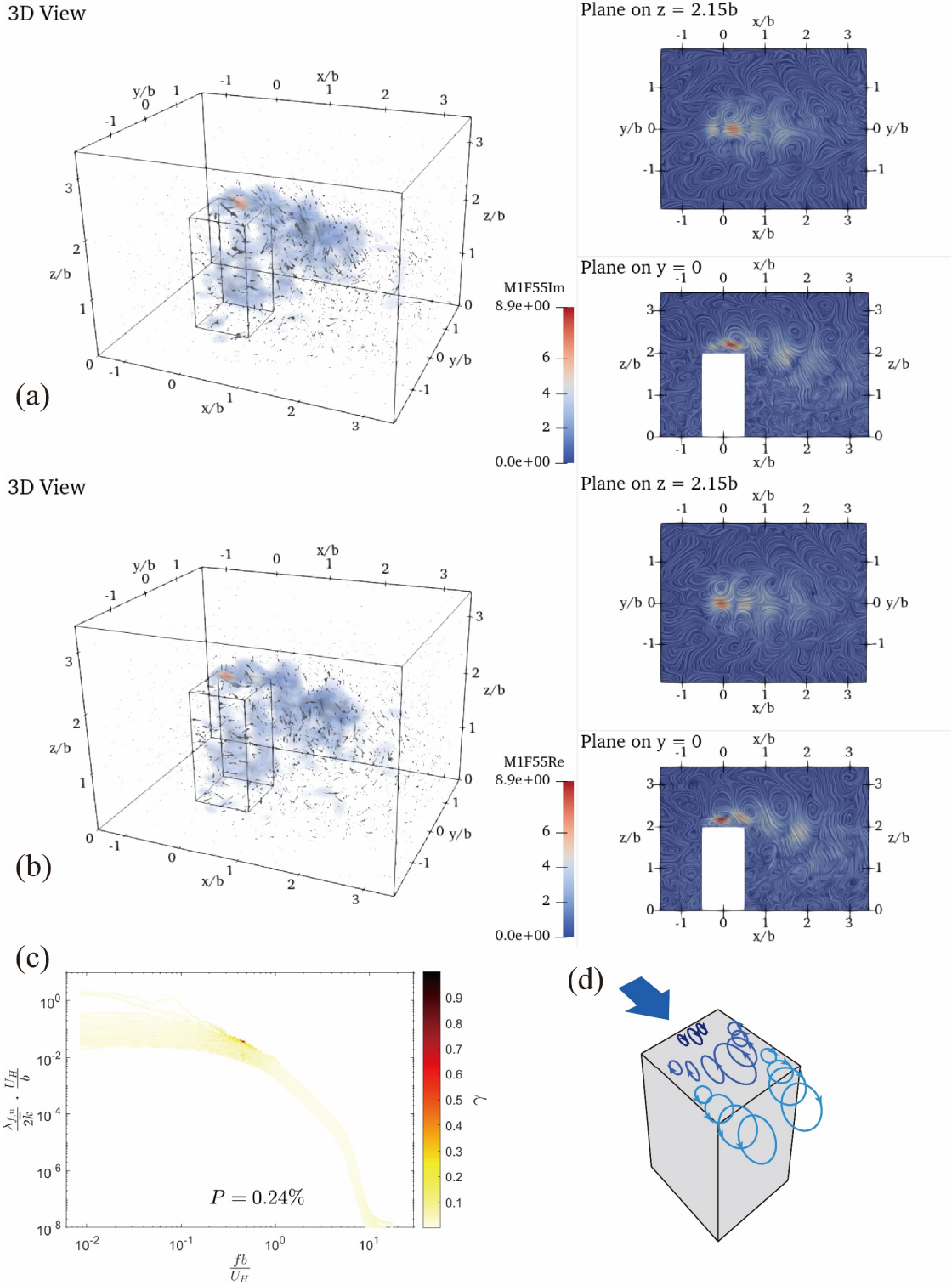


Figure 4.11 Mode ($fb/U_H = 0.4562$, $n = 1$). (a) Real part of the eigenfunction. (b) Imaginary part of the eigenfunction. (c) Spatial similarity coefficient. See the caption of Figure 4.6 for more details. (d) Schematic of the vortex structure.

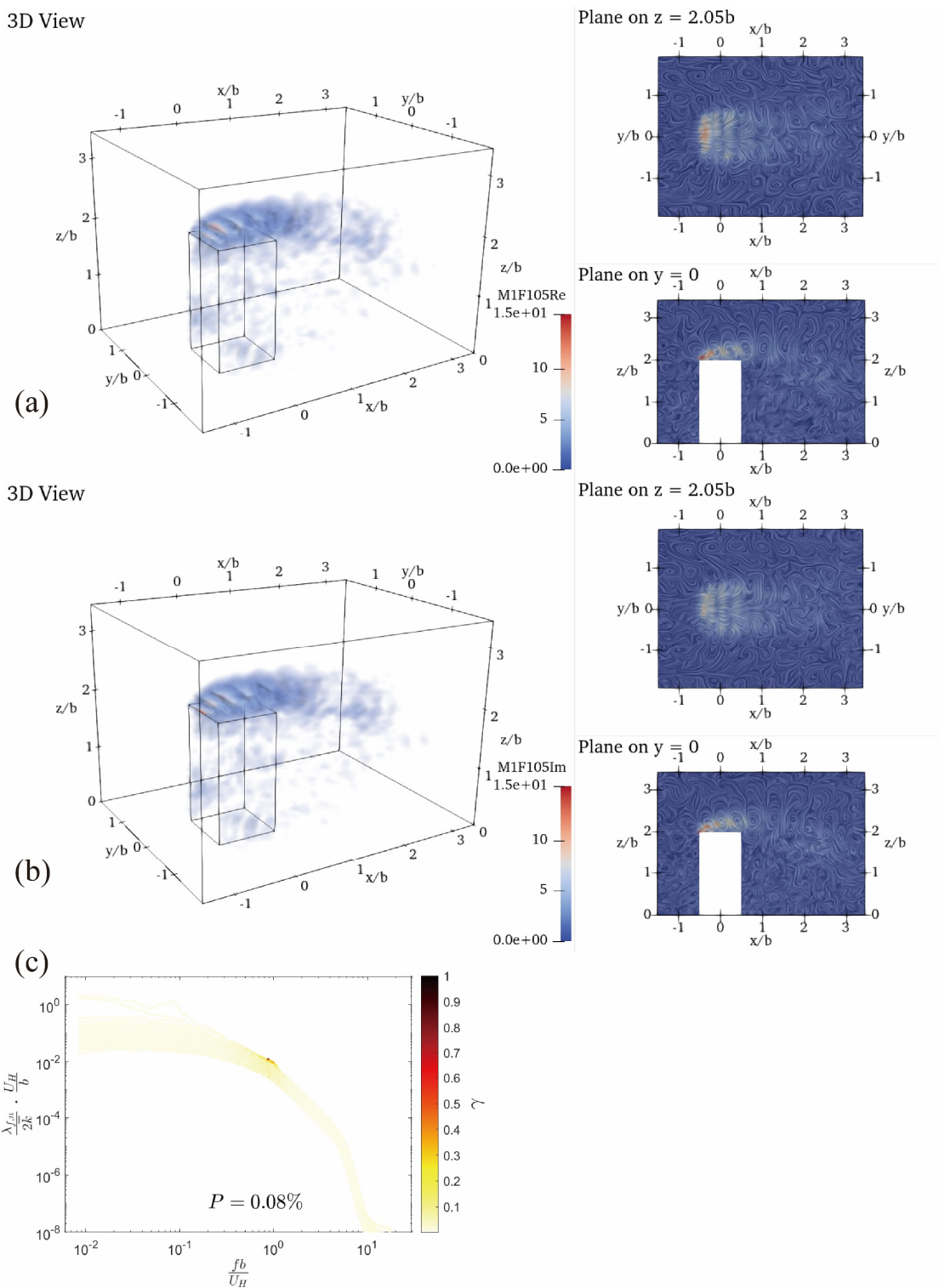


Figure 4.12 Mode ($fb/U_H = 0.8786$, $n = 1$). (a) Real part of the eigenfunction. (b) Imaginary part of the eigenfunction. (c) Spatial similarity coefficient. See the caption of Figure 4.6 for more details.

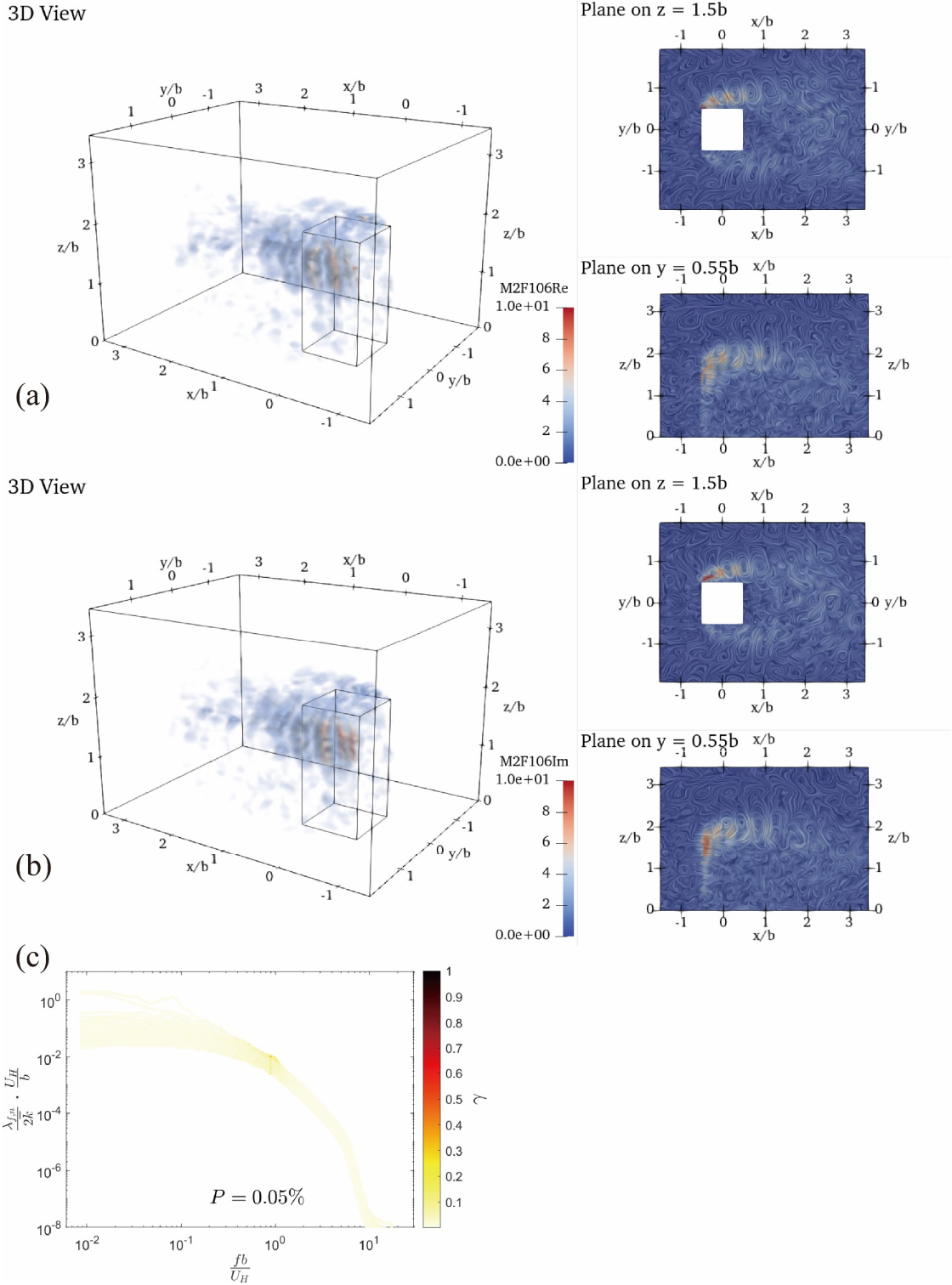


Figure 4.13 Mode ($fb/U_H = 0.8870$, $n = 2$). (a) Real part of the eigenfunction. (b) Imaginary part of the eigenfunction. (c) Spatial similarity coefficient. See the caption of Figure 4.6 for more details.

4.4.3 Low-frequency modes

The mode ($fb/U_H = 0.0169$, $n = 1$) (Figure 4.6) and mode ($fb/U_H = 0.0169$, $n = 2$) (Figure 4.7) were chosen to be the typical modes in the low-frequency region ($fb/U_H \approx 10^{-2}$). The spatial shape of the former mode is nearly antisymmetric, and the latter is nearly symmetric, where the notion of “antisymmetric” is defined as:

$$\begin{cases} \psi_{f,n}^{(1)}(x, -y, z) = -\psi_{f,n}^{(1)}(x, y, z) \\ \psi_{f,n}^{(2)}(x, -y, z) = \psi_{f,n}^{(2)}(x, y, z) \\ \psi_{f,n}^{(3)}(x, -y, z) = \psi_{f,n}^{(3)}(x, y, z) \end{cases}, \quad (4.10)$$

and the notion of “symmetric” is defined as:

$$\begin{cases} \psi_{f,n}^{(1)}(x, -y, z) = \psi_{f,n}^{(1)}(x, y, z) \\ \psi_{f,n}^{(2)}(x, -y, z) = -\psi_{f,n}^{(2)}(x, y, z) \\ \psi_{f,n}^{(3)}(x, -y, z) = \psi_{f,n}^{(3)}(x, y, z) \end{cases}, \quad (4.11)$$

where $\psi_{f,n}^{(1)}$, $\psi_{f,n}^{(2)}$, and $\psi_{f,n}^{(3)}$ are the three components of $\boldsymbol{\psi}_{f,n}$ along the x , y , and z directions, respectively. In Subsection 4.7, we show that the modes in the low-frequency region are directly related to the fluctuation of the incoming flow.

The eigenfunctions in Figures 4.6 (a) and (b) show that strong fluctuations concentrate on both sides of the building, and then extend to the wake. This provides an insight into the difference in the velocity on the building sides caused by the inflow fluctuation. In contrast, the eigenfunctions in Figures 4.7 (a) and (b) show that strong fluctuations almost fill up the whole sampling field, while no apparent fluctuations can be observed within the separation zone on the building sides or in the wake. It appears that a wind gust collided with the building, but few vortices were observed as a result.

Figures 4.6 (c) and 4.7 (c) display the spatial similarity coefficient of these two typical modes and all the other modes, which show that the modes related to these features are mostly concentrated in the low-frequency region ($fb/U_H \approx 10^{-2}$). In this region, note that these two spatial modes hold the largest dominant energy, which is far larger than the third.

The features in these two spatial patterns are 6.97% and 5.57%, respectively, of the total energy in this field (calculated by Eq. (4.3)), which are relatively large compared to most of the other spatial patterns extracted by SPOD.

4.4.4 *Primary wake vortex shedding*

The mode ($fb/U_H = 0.0845$, $n = 1$), as shown in (Figure 4.8), exhibits primary vortex shedding in the wake, which is usually termed as the Kármán vortex shedding in the two-dimensional flow.

This mode played an important role in periodic vortex shedding because it dominated the energy around the Strouhal frequency, which was $fb/U_H \approx 10^{-1}$ for the finite height square cylinder (Sakamoto and Arie, 1983; Wang and Lam, 2019). If the flow field is analysed by POD, a couple of POD modes depicting the same structure will be obtained, and an approximately $\pi/2$ phase difference can be observed between the mode pair (Bourgeois et al., 2013; Wang et al., 2019). While as a hybrid of POD and Fourier transformation, SPOD can better recognise this kind of travelling wave in a complex mode. Recently, Wang and Lam (2019) also extracted the antisymmetric low-frequency mode and periodic vortex shedding mode pairs via POD, and they applied a low-pass Gaussian filter to properly separate the two coherent structures. The filtered POD technique was also introduced by Sieber et al. (2016), also called SPOD, to obtain a better insight into the harmonic oscillator in the flow. However, these are unnecessary in the present study because the SPOD applied in this study already encompassed the Fourier analysis. The energy percentage for this mode was 6.40%. It contained the unignorable energy components in the Strouhal frequency region.

4.4.5 *Tip and base vortices*

Mode ($fb/U_H = 0.2281$, $n = 1$) (Figure 4.9) and mode ($fb/U_H = 0.2281$, $n = 2$) (Figure 4.10) exhibit the tip and base vortex pair on the two sides of the building, respectively. These two modes were almost symmetric, and were the two most energetic modes at the same frequency.

The tip and base vortices were observed in a number of bluff body studies (Kawamura et al., 1984; Sumner et al., 2004; Wang et al., 2009, 2004), while the present study provides proof of the relationship existence between the tip vortices and the base vortices. Because the vortices and their rotational directions are not well-shown by the vector plot in the 3D view, Figure 4.9 (d) provides a schematic of the vortex structure. The upper and lower parts of the vortices lag behind the driven part due to the obstruction of the upstream building corners, and they tear apart when leaving the building. This arch structure appears to be a large version of the hairpin vortices attached to the building walls. The fact that the pair of tip and base vortices were extracted in the same SPOD mode indicates that the correlation between them was detected by SPOD. Wang and Zhou (2009) also

discovered a similar arch-type structure, which was assumed to be the connection between the tip and base vortices. The results in the present study support their assumption; however, more evidence is needed for solid proof, because SPOD only proves their correlation and not the existence of their dynamic mechanism.

One deficiency of this SPOD analysis is that the rotation direction of the tip and base vortices cannot be determined. This is because the vortex structures are deemed as zero-mean sinusoidal functions by SPOD, which means that a vortex must be chronologically followed by another vortex whose direction is opposite to the former. However, although the real rotation direction of the tip and base was unknown in this study, the two modes indicated that the tip and base vortices always rotated in the opposite direction. Wang et al. (2009) indicated that the opposite rotation direction of the tip and base vortices induces a secondary flow around the centreline, which may influence the heat diffusion in the building wake.

Mode ($fb/U_H = 0.4562, n = 1$) (Figure 4.11) is another development of the tip vortices, which has usually been argued as the origin of the tip vortices in many studies (Wang et al., 2004; Zdravkovich et al., 1989). The schematic in Figure 4.11 (d) illustrates that the mechanism of this mode is the same as that of the aforementioned two modes, but occurs on the building roof.

Wang et al. (2004) illustrated two types of tip vortices rotating in different directions. Although the shapes were similar to the spatial patterns depicted by the SPOD modes, they cannot be directly compared. Because SPOD identifies waves or vortices travelling spatially, which results in a zero mean for each observed spatial point, while the tip and base vortices are examined in mean flow by Wang et al. (2004). However, imagine that the harmonically fluctuating spatial patterns are added onto the mean flow patterns in the same shape, then the vortices in the opposite rotation direction will be cancelled out. The tip and base vortices are shown as intermittent travelling vortices with a specific frequency.

The energy of these spatial patterns was estimated quantitatively. The spatial pattern of mode ($fb/U_H = 0.2281, n = 1$) and mode ($fb/U_H = 0.2281, n = 2$) were 1.13% and 0.93% of the total energy, respectively, while the spatial pattern of mode ($fb/U_H = 0.4562, n = 1$) was 0.24%.

4.4.6 *Primary side vortex shedding*

Mode ($fb/U_H = 0.8786$, $n = 1$) (Figure 4.12) and mode ($fb/U_H = 0.8870$, $n = 2$) (Figure 4.13) provides an insight into the primary vortices within the shear layer on the roof and on the sides, respectively. These vortices are hereafter called “primary side vortex shedding” to distinguish from “primary wake vortex shedding”.

These vortices have also been observed in several studies (Bruno et al., 2010; Joubert et al., 2015). Bruno et al. (2010) found that the primary vortex shedding period was approximately 0.75 non-dimensional time unit, which corresponds to a normalised frequency of 1.33. This roughly corresponded to the frequency ($fb/U_H \approx 1$), where we found this typical mode. The authors considered that two reasons may cause errors. First, the sampling length was only 4.25 non-dimensional time unit, as stated by Bruno et al. (2010), which might not be enough to reveal the long-term features. Second, the prism in our study was placed in a boundary layer, while Bruno et al. (2010) used an infinite-length 2D cylinder. The choice of the reference length and reference velocity can also affect the normalised frequency. Again, SPOD failed to provide information on the rotation direction of these vortices, but it was well illustrated by Bruno et al. (2010) via direct observation of the instantaneous flow field.

The energy percentage of the vortex pattern on the roof was 0.08%, which was much lower than that of the aforementioned patterns. In addition, although mode ($fb/U_H = 0.8870$, $n = 2$) was chosen as the typical mode for the same phenomenon occurring on the building side, this mode only showed the vortices on one side and the upper part of the building, while several modes around $fb/U_H \approx 1$ depicted the same type of vortices occurring on all parts of the building sides. This indicated that these vortices were not synchronised, so they could not be depicted by a single mode uniformly or a set of spatially similar modes. Considering the boundary layer set in this case, the impinging velocity was different at different heights, so the frequency of these vortices may be slightly different. This also caused the energy percentage of the spatial pattern of the typical mode to be only 0.05%, whereas the total energy for all the vortices in this type occurring on the building sides can be several times greater than that.

4.4.7 *Local-space spectrum*

In this subsection, the local-space SPOD spectrum defined in Section 2.4 is applied to examine some details for this sampling field, which varies in different spatial locations.

In the first application, the local space Γ was chosen as the inlet face of the sampling

field, to show which modes directly related to the inflow fluctuation. Figure 4.14 shows this local space spectrum. The energy is mainly concentrated in the low-frequency region ($fb/U_H \approx 10^{-2}$), where one each for symmetric mode and antisymmetric mode is found. This indicates that these two features are the direct results of the inflow fluctuation. In addition, note that this spectrum decreases much faster than the global SPOD spectrum in Figure 4.5 (a) in the high-frequency region ($fb/U_H > 1$), indicating that many small-scale features are generated by the prism when the flow passes it.

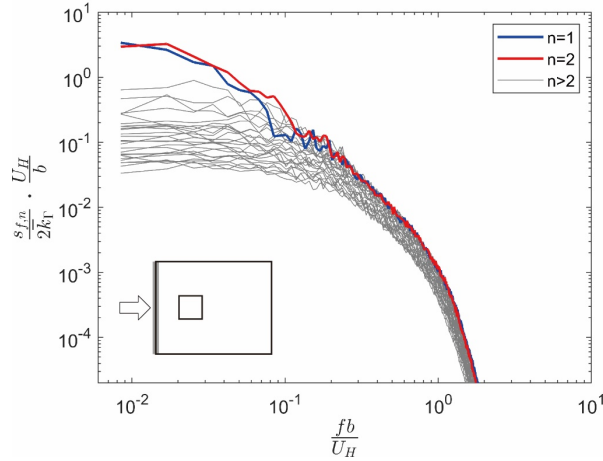


Figure 4.14. Local-space SPOD spectrum for the inlet face of the sampling domain.

Figures 4.15 (a–c) provide the local-space spectrum for three local spaces, as defined by the following:

Front: $-1.5b < x < -0.5b, -0.5b < y < 0.5b, 0 < z < 2b$

Side: $-0.5b < x < 0.5b, 0.5b < y < 1.5b, 0 < z < 2b$

Back: $0.5b < x < 1.5b, -0.5b < y < 0.5b, 0 < z < 2b$

where the original point was at the bottom centre of the prism. For a better comparison, the spectra of $n = 1$ and 2 are summed (i.e. $s_{f,1} + s_{f,2}$) and shown in Figure 4.15 (d). From these results, we see that different local spaces were influenced by different flow features. The modes in the low-frequency region dominated the flow fluctuation on the front of the prism, while the primary wake vortex shedding dominated the flow fluctuation in the back. The situation on the side of the prism was the most complicated. It was largely influenced by the low-frequency features, while most of the flow features caused by the prism have a certain proportion of the kinetic energy.

The above analysis technique is considered useful in real design work with regard to turbulent flow. Using SPOD, the global flow features can be well identified and provide general cognition for the whole field. Meanwhile, a local place of interest can be chosen to observe the details of the flow. It tells us which features are directly related to the fluctuation in this local space. This kind of reference benefits local modifications and

improvements.

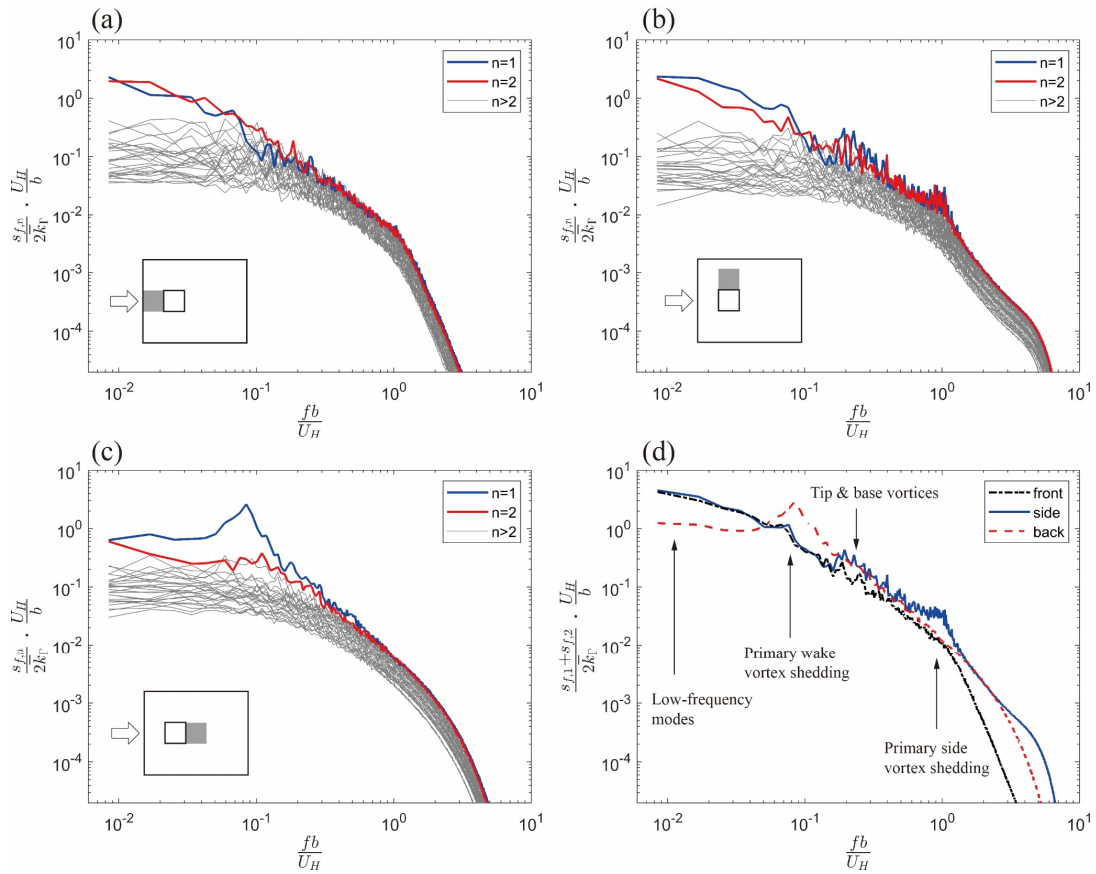


Figure 4.15. Local-space SPOD spectra for the front, side, and the back of the prism, respectively in (a–c). The spectra of $n = 1$ and 2 are summed and compared in (d).

4.5 Summary

This study reproduced the flow field around a square-section building model using LES, and performed SPOD analysis to identify the three-dimensional main flow features within the sampling field. The identified features, including the low-frequency modes related to the fluctuation of the incoming flow, primary wake vortex shedding, tip and base vortices, and primary side vortex shedding, were extracted from the single case at once. The primary frequency and the intensity of these features were revealed by studying the typical SPOD modes and estimating the energy percentage. In addition, the local-space SPOD spectrum was also defined to analyse the composition of the kinetic energy within some local parts of the sampling field.

The identified flow features and their details are summarised as follows: first, two energetic modes at low frequency were chosen as the typical modes to depict the symmetric and antisymmetric fluctuations around the building. They were found to be directly related to the inflow fluctuation by the local-space SPOD spectrum. The primary

wake vortex shedding was depicted using a complex mode at the Strouhal frequency, which exhibited periodic vortex shedding. The tip and base vortex pair on one side of the building appeared in one SPOD mode, which indicated their correlation. The mode also showed an arch structure by which the tip and base vortices were connected. The same structure was found on the roof of the building illustrated by another mode, which showed the other kind of development of the tip vortices. The primary side vortex shedding appeared on both the roof and sides of the building. However, the vortices at different heights on the sides were not synchronised. Finally, the local-space SPOD spectrum precisely showed the different compositions of the fluctuation patterns on the front, side, and back of the prism.

In general, the SPOD spectrum provided a comprehensive view of the turbulent structures in this flow field, which was an integration of all the above flow features. Unlike previous studies, where different flow features were studied by different physical quantities, this study revealed the primary frequency and intensity for all features, using a single mathematical process. To make this identification more quantitative, new quantities were defined (Sections 2.3 and 2.4). The spatial similarity in Section 2.3 was defined to classify the modes by similarity of the shapes, so that the energy percentage values for the flow features could be estimated. This made it possible to directly compare the intensity between features. The local-space spectrum in Section 2.4 was defined to reveal detailed information of the fluctuation pattern, so that the flow features responsible for the strong fluctuation at a local space could be precisely pinpointed. This was considered a good design tool with broad application prospects. The flow features were also animated using the animations for the SPOD eigenfunctions. The visualisations were more direct and intuitive than traditional methods, which facilitated the understanding of the turbulent structure.

This work may be the first study to apply SPOD for the identification of the three-dimensional flow features around a wall-mounted bluff body with a high Reynolds number. Although none of the flow features are new, the successful identification of these flow features proves that SPOD has the potential to become another effective tool for further research or design of bluff body aerodynamics.

Reference

- Architectural Institute of Japan, 2016. AIJ Benchmarks for Validation of CFD Simulations Applied to Pedestrian Wind Environment around Build. Architectural Institute of Japan, Tokyo.
- Bourgeois, J.A., Noack, B.R., Martinuzzi, R.J., 2013. Generalized phase average with applications to sensor-based flow estimation of the wall-mounted square cylinder

- wake. *J. Fluid Mech.* 736, 316–350. <https://doi.org/10.1017/jfm.2013.494>
- Bruno, L., Fransos, D., Coste, N., Bosco, A., 2010. 3D flow around a rectangular cylinder: A computational study. *J. Wind Eng. Ind. Aerodyn.* 98, 263–276. <https://doi.org/10.1016/j.jweia.2009.10.005>
- Carassale, L., Solari, G., Tubino, F., 2007. Proper orthogonal decomposition in wind engineering - Part 2: Theoretical aspects and some applications. *Wind Struct.* 10, 177–208. <https://doi.org/10.12989/was.2007.10.2.177>
- Flay, R.G.J., 2013. Bluff body aerodynamics, in: *Advanced Structural Wind Engineering*. Springer Japan, pp. 59–84. https://doi.org/10.1007/978-4-431-54337-4_3
- Irwin, P.A., 2008. Bluff body aerodynamics in wind engineering. *J. Wind Eng. Ind. Aerodyn.* 96, 701–712. <https://doi.org/10.1016/j.jweia.2007.06.008>
- Issa, R.I., 1986. Solution of the implicitly discretised fluid flow equations by operator-splitting. *J. Comput. Phys.* 62, 40–65. [https://doi.org/10.1016/0021-9991\(86\)90099-9](https://doi.org/10.1016/0021-9991(86)90099-9)
- Joubert, E.C., Harms, T.M., Venter, G., 2015. Computational simulation of the turbulent flow around a surface mounted rectangular prism. *J. Wind Eng. Ind. Aerodyn.* 142, 173–187. <https://doi.org/10.1016/j.jweia.2015.03.019>
- Kawamura, T., Hiwada, M., Hibino, T., Mabuchi, I., Kumada, M., 1984. Flow around a Finite Circular Cylinder on a Flat Plate : Cylinder height greater than turbulent boundary layer thickness. *Bull. JSME* 27, 2142–2151. <https://doi.org/10.1299/jsme1958.27.2142>
- Kikumoto, H., Ooka, R., Han, M., Nakajima, K., 2018. Consistency of mean wind speed in pedestrian wind environment analyses: Mathematical consideration and a case study using large-eddy simulation. *J. Wind Eng. Ind. Aerodyn.* 173. <https://doi.org/https://doi.org/10.1016/j.jweia.2017.11.021>
- Lumley, J.L., 1970. *Stochastic Tools in Turbulence*. Academic Press.
- Lumley, J.L., 1967. The structure of inhomogeneous turbulent flows. *Atmos. Turbul. wave Propag.* 166–178.
- Matsumoto, M., 1999. Vortex shedding of bluff bodies: a review. *J. Fluids Struct.* 13, 791–811. <https://doi.org/10.1006/jfls.1999.0249>
- Meng, Y., Hibi, K., 1998. Turbulent measurements of the flow field around a high-rise building. *Wind Eng. JAWE* 1998, 55–64. https://doi.org/10.5359/jawe.1998.76_55
- Okaze, T., Kikumoto, H., Ono, H., Imano, M., Hasama, T., Kishida, T., Nakao, K., Ikegaya, N., Tabata, Y., Tominaga, Y., 2017. Large-eddy simulations of flow around a high-rise building: validation and sensitivity analysis on turbulent statistics, in: *7th European and African Conference on Wind Engineering*. Liege, Belgium.
- Sakamoto, H., Arie, M., 1983. Vortex shedding from a rectangular prism and a circular cylinder placed vertically in a turbulent boundary layer. *J. Fluid Mech.* 126, 147–165. <https://doi.org/10.1017/S0022112083000087>
- Sau, A., Hwang, R.R., Sheu, T.W.H., Yang, W.C., 2003. Interaction of trailing vortices in the wake of a wall-mounted rectangular cylinder. *Phys. Rev. E - Stat. Physics, Plasmas, Fluids, Relat. Interdiscip. Top.* 68, 056303. <https://doi.org/10.1103/PhysRevE.68.056303>
- Schmidt, O.T., Colonius, T., 2020. Guide to Spectral Proper Orthogonal Decomposition. *AIAA J.* 58, 1023–1033. <https://doi.org/10.2514/1.J058809>
- Sieber, M., Paschereit, C.O., Oberleithner, K., 2016. Spectral proper orthogonal decomposition. *J. Fluid Mech.* 792, 798–828. <https://doi.org/10.1017/jfm.2016.103>
- Smagorinsky, J., 1963. General circulation experiments with the primitive equations. *Mon. Weather Rev.* 91, 99–164. [https://doi.org/10.1175/1520-0493\(1963\)091<0099:gcewtp>2.3.co;2](https://doi.org/10.1175/1520-0493(1963)091<0099:gcewtp>2.3.co;2)
- Solari, G., Carassale, L., Tubino, F., 2007. Proper orthogonal decomposition in wind engineering - Part 1: A state-of-the-art and some prospects. *Wind Struct.* 10, 153–176. <https://doi.org/10.12989/was.2007.10.2.153>
- Spalding, D.B., 1962. A new analytical expression for the drag of a flat plate valid for both the turbulent and laminar regimes. *Int. J. Heat Mass Transf.* 5, 1133–1138.

- [https://doi.org/10.1016/0017-9310\(62\)90189-8](https://doi.org/10.1016/0017-9310(62)90189-8)
 Sumner, D., Heseltine, J.L., Dansereau, O.J.P., 2004. Wake structure of a finite circular cylinder of small aspect ratio. *Exp. Fluids* 37, 720–730.
<https://doi.org/10.1007/s00348-004-0862-7>
- Taira, K., Brunton, S.L., Dawson, S.T.M., Rowley, C.W., Colonius, T., McKeon, B.J., Schmidt, O.T., Gordeyev, S., Theofilis, V., Ukeiley, L.S., 2017. Modal Analysis of Fluid Flows: An Overview. *AIAA J.* 55, 4013–4041.
<https://doi.org/10.2514/1.J056060>
- Tominaga, Y., Mochida, A., Yoshie, R., Kataoka, H., Nozu, T., Yoshikawa, M., Shirasawa, T., 2008. AIJ guidelines for practical applications of CFD to pedestrian wind environment around buildings. *J. Wind Eng. Ind. Aerodyn.* 96, 1749–1761.
<https://doi.org/10.1016/J.JWEIA.2008.02.058>
- Towne, A., Schmidt, O.T., Colonius, T., 2018. Spectral proper orthogonal decomposition and its relationship to dynamic mode decomposition and resolvent analysis. *J. Fluid Mech.* 847, 821–867. <https://doi.org/10.1017/jfm.2018.283>
- Träumner, K., Damian, T., Stawiarski, C., Wieser, A., 2015. Turbulent Structures and Coherence in the Atmospheric Surface Layer. *Boundary-Layer Meteorol.* 154.
<https://doi.org/10.1007/s10546-014-9967-6>
- Uffinger, T., Ali, I., Becker, S., 2013. Experimental and numerical investigations of the flow around three different wall-mounted cylinder geometries of finite length. *J. Wind Eng. Ind. Aerodyn.* 119, 13–27. <https://doi.org/10.1016/j.jweia.2013.05.006>
- Van Driest, E.R., 1956. On Turbulent Flow Near a Wall. *J. Aeronaut. Sci.* 23, 1007–1011. <https://doi.org/10.2514/8.3713>
- Versteeg, H.K., Malalasekera, W., 2007. *An Introduction to Computational Fluid Dynamics: The Finite Volume Method*, second. ed. Pearson Education Limited, Essex, England.
- Wang, F., Lam, K.M., 2019. Geometry effects on mean wake topology and large-scale coherent structures of wall-mounted prisms. *Phys. Fluids* 31, 125109.
<https://doi.org/10.1063/1.5126045>
- Wang, F., Lam, K.M., Zu, G.B., Cheng, L., 2019. Coherent structures and wind force generation of square-section building model. *J. Wind Eng. Ind. Aerodyn.* 188, 175–193. <https://doi.org/10.1016/j.jweia.2019.02.019>
- Wang, H., Zhou, Y., Chan, C., Zhou, T., 2009. Momentum and heat transport in a finite-length cylinder wake. *Exp. Fluids* 46, 1173–1185.
<https://doi.org/10.1007/s00348-009-0620-y>
- Wang, H.F., Zhou, Y., 2009. The finite-length square cylinder near wake. *J. Fluid Mech.* 638, 453–490. <https://doi.org/10.1017/S0022112009990693>
- Wang, H.F., Zhou, Y., Chan, C.K., Wong, W.O., Lam, K.S., 2004. Flow Structure Around A Finite-Length Square Prism, in: *15th Australasian Fluid Mechanics Conference*. Sydney, Australia.
- Welch, P.D., 1967. The Use of Fast Fourier Transform for the Estimation of Power Spectra: A Method Based on Time Averaging Over Short, Modified Periodograms. *IEEE Trans. Audio Electroacoust.* 15, 70–73.
<https://doi.org/10.1109/TAU.1967.1161901>
- Williamson, C.H.K., 1996. Three-dimensional vortex dynamics in bluff body wakes. *Exp. Therm. Fluid Sci.* 12, 150–168. [https://doi.org/10.1016/0894-1777\(95\)00085-2](https://doi.org/10.1016/0894-1777(95)00085-2)
- Yoshie, R., Mochida, A., Tominaga, Y., Kataoka, H., Harimoto, K., Nozu, T., Shirasawa, T., 2007. Cooperative project for CFD prediction of pedestrian wind environment in the Architectural Institute of Japan. *J. Wind Eng. Ind. Aerodyn.* 95, 1551–1578. <https://doi.org/10.1016/J.JWEIA.2007.02.023>
- Zdravkovich, M.M., 1990. Conceptual overview of laminar and turbulent flows past smooth and rough circular cylinders. *J. Wind Eng. Ind. Aerodyn.* 33, 53–62.
[https://doi.org/10.1016/0167-6105\(90\)90020-D](https://doi.org/10.1016/0167-6105(90)90020-D)
- Zdravkovich, M.M., Brand, V.P., Weston, A., Mathew, G., 1989. Flow past short circular cylinders with two free ends. *J. Fluid Mech.* 203, 557–575.
<https://doi.org/10.1017/S002211208900159X>
- Zhang, B., Ooka, R., Kikumoto, H., 2020. Analysis of turbulent structures around a

rectangular prism building model using spectral proper orthogonal decomposition.
J. Wind Eng. Ind. Aerodyn. 206, 104213.
<https://doi.org/10.1016/J.JWEIA.2020.104213>

Chapter 5

Analysis of the pedestrian-level wind around a square-section building model: the effect of inflow fluctuation on turbulent structures

5.1 Introduction

In recent years, technological progress on numerical calculations and WTEs has enabled the recording of detailed and large amounts of flow field data. However, extracting meaningful phenomena from a large amount of data using the conventional analysis method is often difficult. On this point, one may refer to the concept of coherent structures, which are characterized as correlated and concentrated dynamic systems lying in the complex multi-scale and chaotic motions of turbulent flow (Fiedler, 1988). Often, coherent structures can be clearly identified visually, but their quantitative assessment is still a challenge (Träumner et al., 2015) as the mechanism of turbulence is still not very clear. Therefore, in the field of wind environment analysis, observation-based empirical explanations are often preferred to mathematics-based analytical methods when elucidating the cause of maximum wind speeds within a complex urban area or planning countermeasures against them. For example, Blocken and Carmeliet (2004) reviewed a large number of case studies conducted by former researchers and summarized that corner streams and the frontal vortex are the most important causes of wind nuisance. A few recent reports of pedestrian-level wind studies for existing urban areas also conducted research in the same manner, and these are Zahid Iqbal and Chan (2016), Adamek et al. (2017), and Shui et al. (2018).

On another side, it is well known that inflow turbulence can greatly affect the flow field around buildings, and thus may further affect the fluctuation properties of the wind load on buildings. The simulations by Tamura and Ono (2003) shows that the size of the wake increases as the inflow turbulence increases, although there were no clear turbulence effects under vortex-induced oscillation. Mochida and Lun (2008) indicate that LES without inflow turbulence can reproduce the reattachment, but the reattachment length is

over-estimated, while the result of LES with inflow turbulence shows close agreement with the experiment. In Yan and Li (2015), four widely used inflow turbulence generation methods are adopted to generate inflow turbulence for numerical simulations of wind loadings, wind effects on the tall building was examined. Difference was found in the wind force and mean flow patterns. Especially, the difference of the latter was a significant one. Until now, studies on the influence of the inflow turbulence were based only on relatively superficial observation and comparison of the results. However, still no studies clearly explained the deep reasons behind these differences.

It is considered that studying on the differences of the turbulent structures can provide a deeper insight on this issue, and the SPOD technique is a good way to extract the turbulent structures. In this study, the effect of inflow fluctuation on turbulent structures around the building is focused on. The spatiotemporal structures of turbulent flow around a single building model (1:1:2 prism) are investigated using the SPOD technique. The vector velocity on the surface near the ground is decomposed to show and sort the main fluctuation patterns of the velocity by their frequencies, which provide a clear insight into the physical phenomena within the turbulence. The SPOD results for two simulation cases are compared, where the only difference is the existence of fluctuation at the inflow boundary, to show how the inflow fluctuation influenced the turbulent structures around the building. Additionally, the fluctuation energy of these fluctuation patterns is calculated, which is considered useful in attempting to improve pedestrian wind comfort.

5.2 Outline of the simulation of the flow field

The geometry and simulation settings in the current study were the LES in Chapter 4. Please refer to Section 4.3 for the details. In this study, two cases were calculated: the velocity inlet boundary condition was set as the wind speed, without fluctuation (Case 1) and with fluctuation (Case 2). In Case 1, the velocity input at the inlet boundary was kept constant as the mean velocity of the inflow turbulence data shared by Kikumoto et al. (2018), while in Case 2, the turbulence data was input normally.

During the simulation, the vector velocity data on a plane of $z = 0.125b$ (b : building width) height were sampled. The plane was chosen to be relatively close to the ground to represent pedestrian-level wind. The sampling frequency was set at 1000 Hz. The inflow mean velocity U_H (≈ 4.5 m/s) at the building height was taken as the reference velocity, with which the velocity data were made dimensionless.

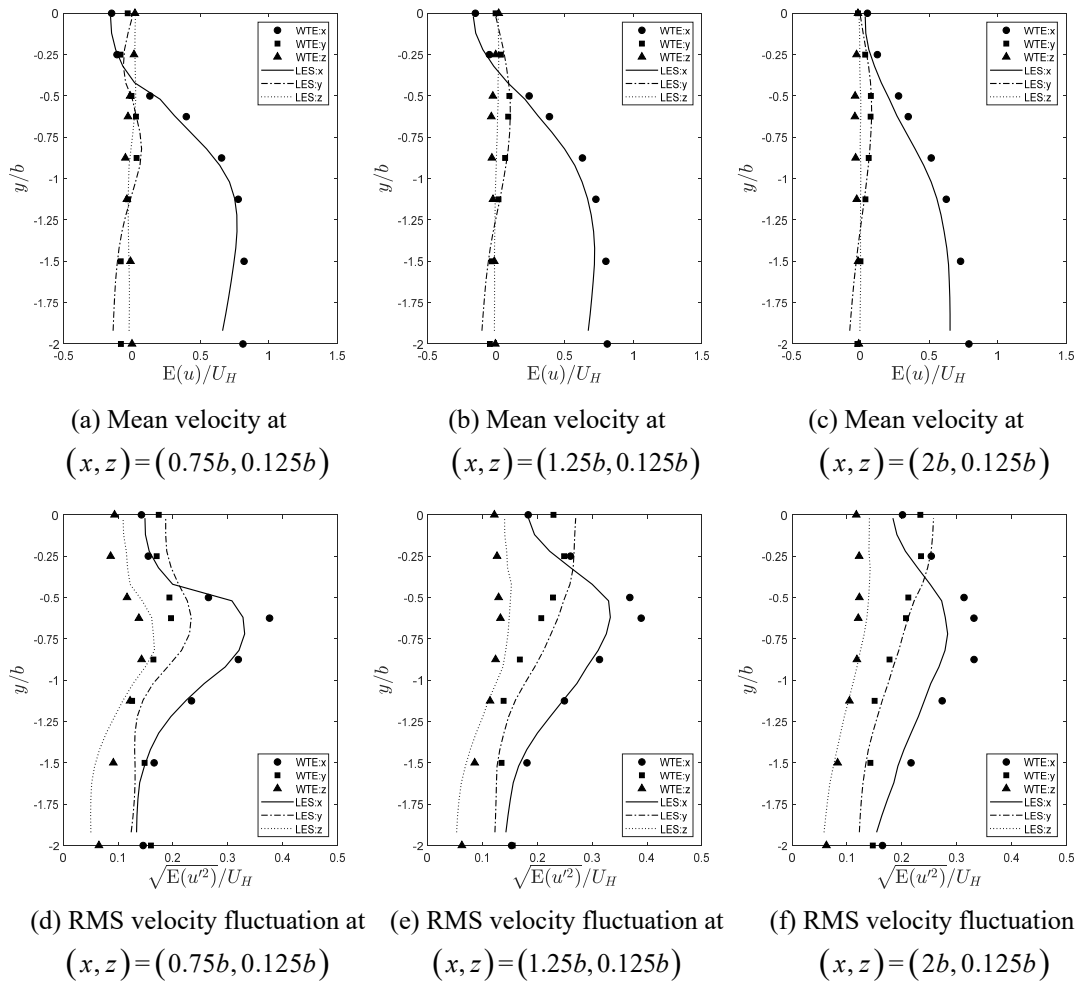


Figure 5.1 Comparison of mean velocity and RMS velocity fluctuation in the x, y, z directions between LES (Case 2) and the WTE database provided by AIJ.

As the case validation, Figure 5.1 compares the simulation results of Case 2 in this study with the WTE database of the guidebook proposed by the AIJ (Architectural Institute of Japan, 2016) in terms of mean velocity and RMS velocity fluctuation. The simulation results were in good agreement with the WTE, except that the LES tended to slightly underestimate the RMS velocity fluctuation in the x direction. However, the authors considered the LES to be sufficiently accurate for the purposes of this study. Furthermore, because performing a WTE using a correct profile of inflow without fluctuation is difficult and meaningless, no results validation was provided for Case 1. However, the authors considered that the accuracy of the result of Case 1 should be the same as that of Case 2 because the simulation conditions were the same with exception to the inlet boundary.

The mean velocity and TKE, for the two cases are shown in Figures 5.2 and 5.3. In Case 1, the width between the shear layers on the two sides of the building was narrower than that in Case 2, and the location of the maximum mean velocity was slightly different. In

Case 1, a large peak was observed in the value of TKE at the rear of the building, which was consistent with the results of the guideline mentioned above. In the following section, SPOD is performed to show the relationship between the turbulent energy distribution and vortex structure.

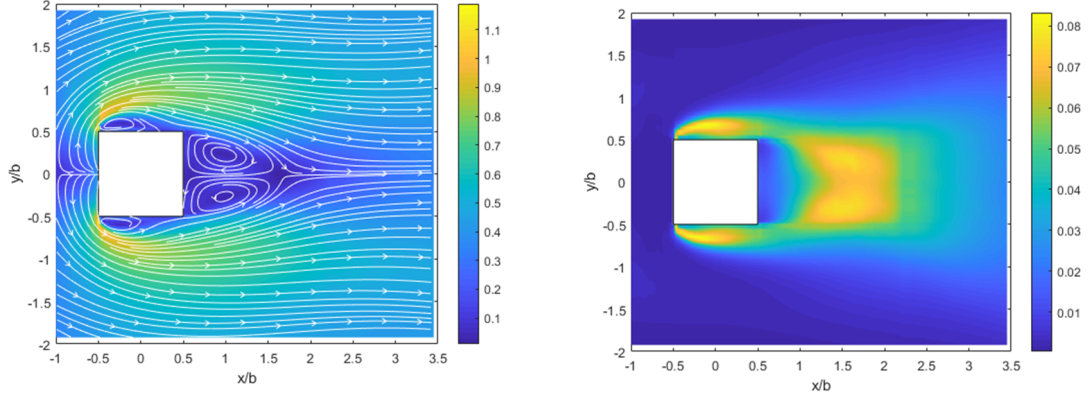


Figure 5.2 Mean velocity (left) and TKE (right) on $z = 0.125b$ plane (Case 1)

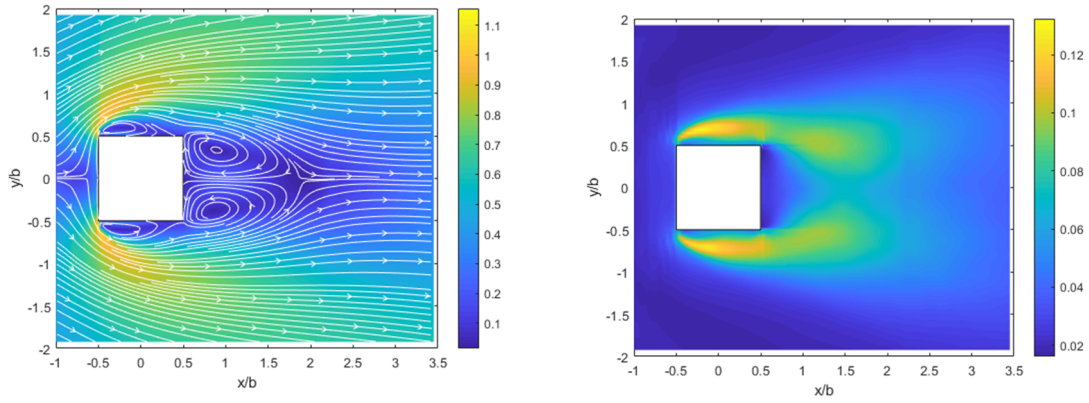


Figure 5.3 Mean velocity (left) and TKE (right) on $z = 0.125b$ plane (Case 2)

5.3 Analysis results

5.3.1 Analysis results for the whole flow field at the pedestrian level

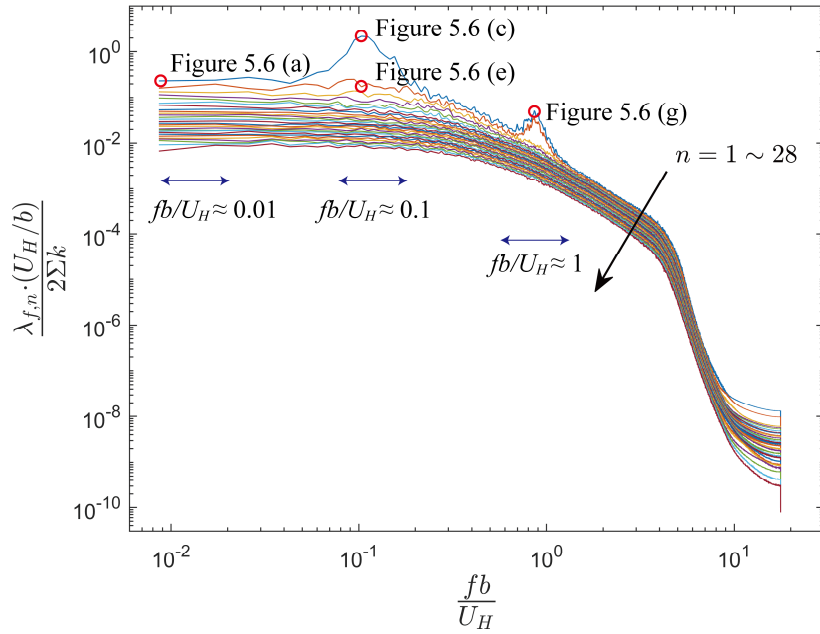
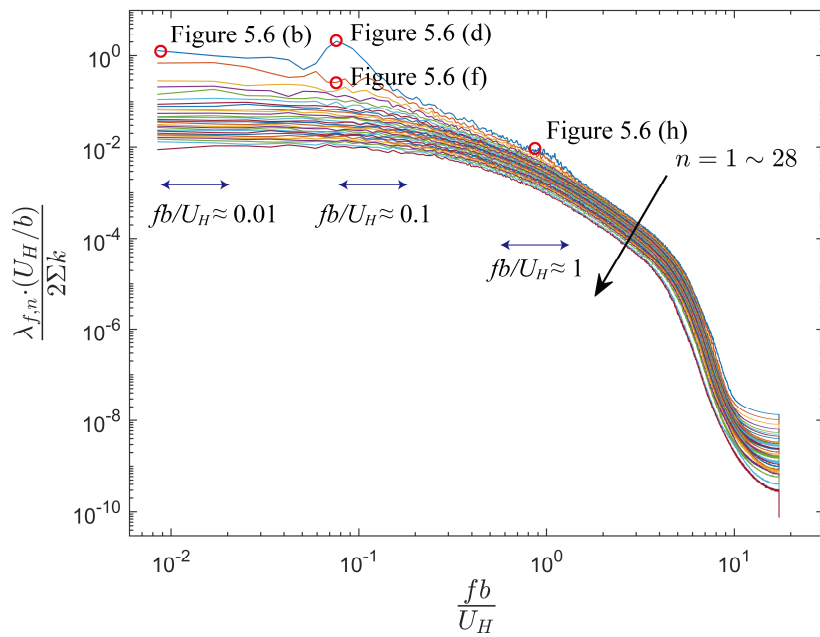
SPOD was implemented on the vector wind speed at all the cell centroids \mathbf{x} within the spatial interval Ω , defined by

$$\Omega = \left\{ \mathbf{x} = (x, y, z)^T \mid -b \leq x \leq 3.5b, \quad -2b \leq y \leq 2b, \quad z = 0.125b \right\}, \quad (5.1)$$

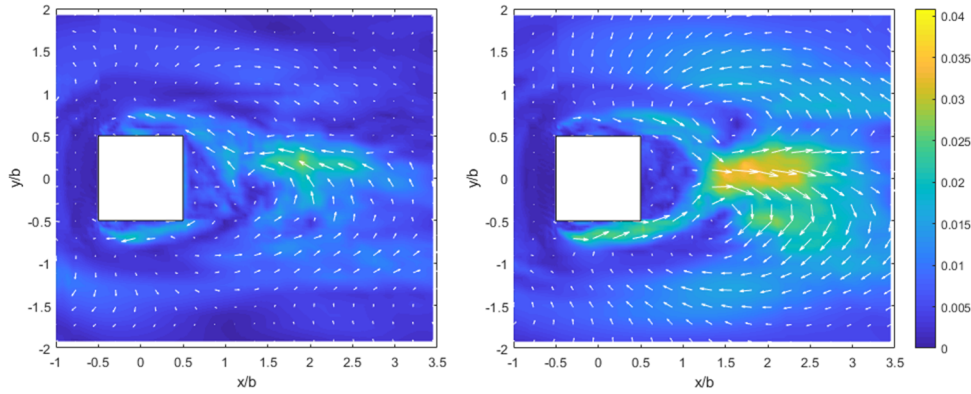
where 4697 spatial points existed within this field. The SPOD mode was calculated using the method proposed by Towne et al. (2018), along with other parameters listed in Table 5.1. Figures 5.4 and 5.5 show the results of the largest 28 $\lambda_{f,n}$ values (single-sided spectrum) at all the discrete frequencies f . The coordinates are normalised so that if one integrates these eigenvalues over a certain frequency range, the area obtained under the curve will equal the proportion of the energy within that range in the total TKE.

Table 5.1 Parameters used when performing SPOD, according to Towne et al. (2018)

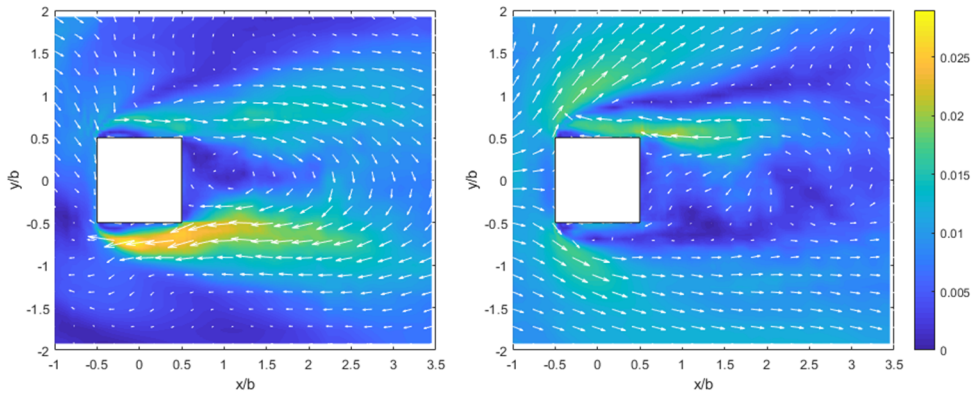
Total number of snapshots	60,000 snapshots
Window	Hamming window with a length of 4,096 snapshots
Blocks	28 blocks with a block length of 4,096 snapshots each
Overlap length	2,048 snapshots

**Figure 5.4** Result of the SPOD eigenvalues (Case 1)**Figure 5.5** Result of the SPOD eigenvalues (Case 2)

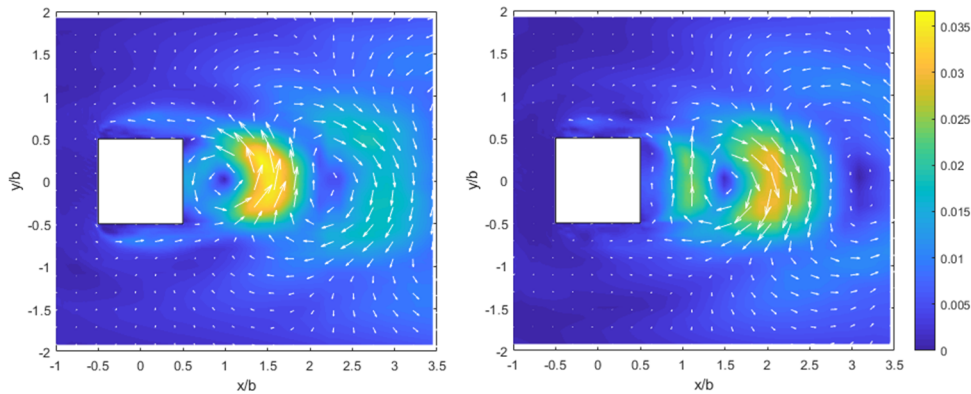
Each $\lambda_{f,n}$ value in Figures 5.4 and 5.5 corresponded to a fluctuation mode $\psi_{f,n}$. Here, although the output of periodic function $\psi_{f,n}(\mathbf{x})e^{i2\pi ft}$ was a complex number, it was understood by watching the animation of its real part, One cycle of which was approximately $\text{Re}(\psi_{f,n}) \rightarrow -\text{Im}(\psi_{f,n}) \rightarrow -\text{Re}(\psi_{f,n}) \rightarrow \text{Im}(\psi_{f,n}) \rightarrow \text{Re}(\psi_{f,n})$, where the eigenfunctions $\psi_{f,n}(\mathbf{x})$ corresponding to some main fluctuation modes are shown in Figure 5.6. The magnitude of $\lambda_{f,n}$ indicated the intensity of this fluctuation mode.



(a) $\psi_{f,n}$ at $n = 1$, $fb / U_H = 0.0086$ (Case 1)



(b) $\psi_{f,n}$ at $n = 1$, $fb / U_H = 0.0084$ (Case 2)



(c) $\psi_{f,n}$ at $n = 1$, $fb / U_H = 0.1034$ (Case 1)

Figure 5.6 (continued on next page)

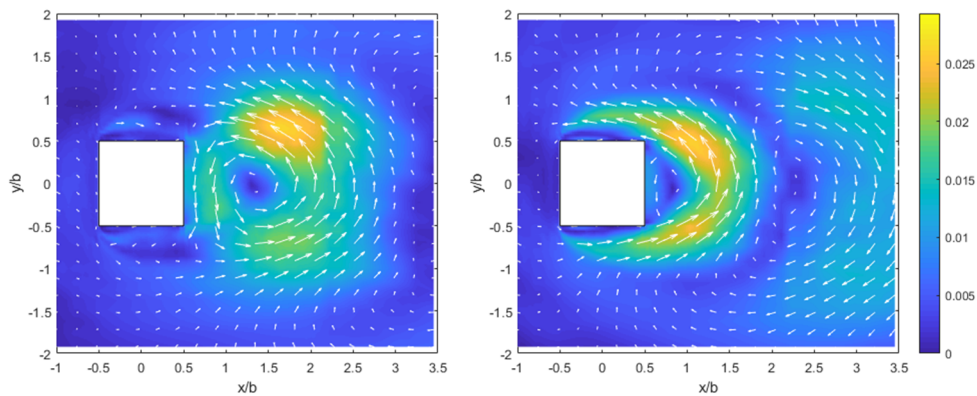
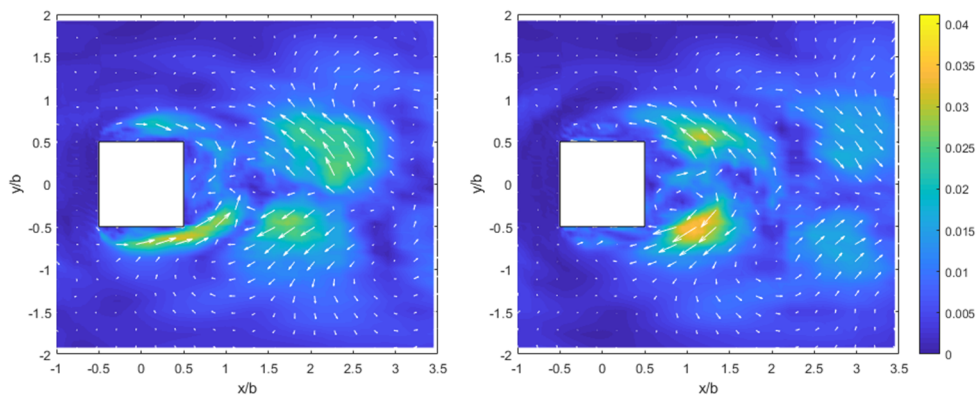
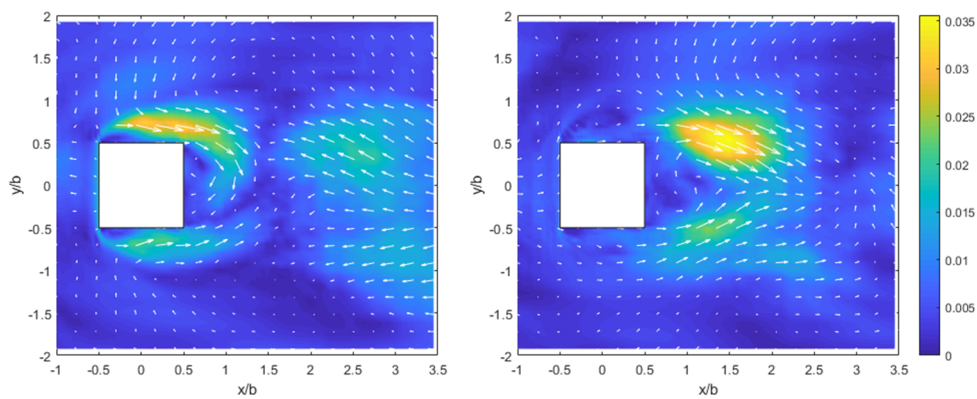
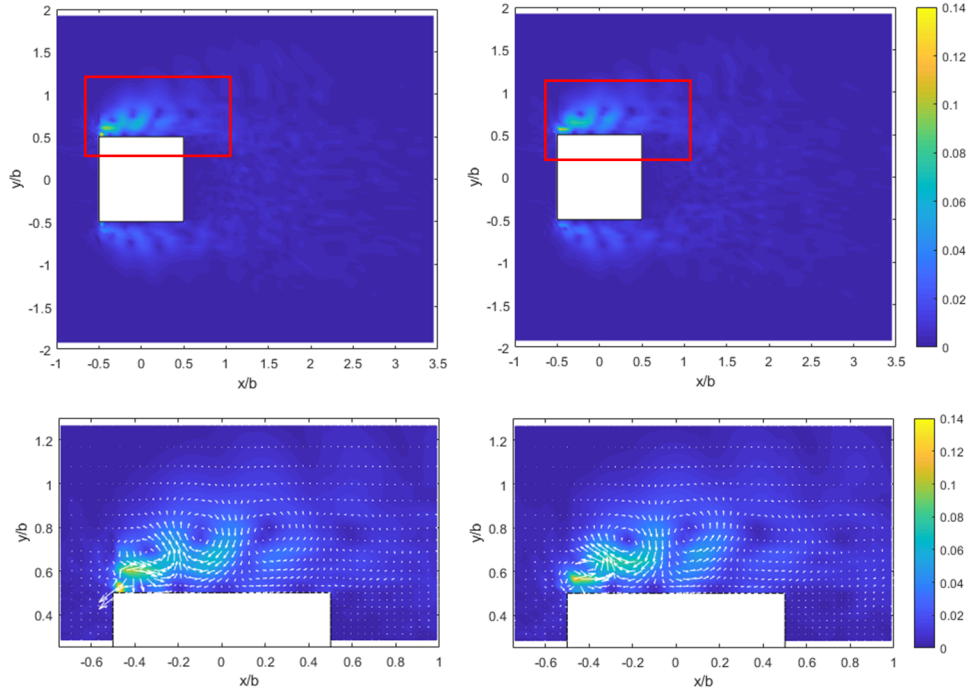
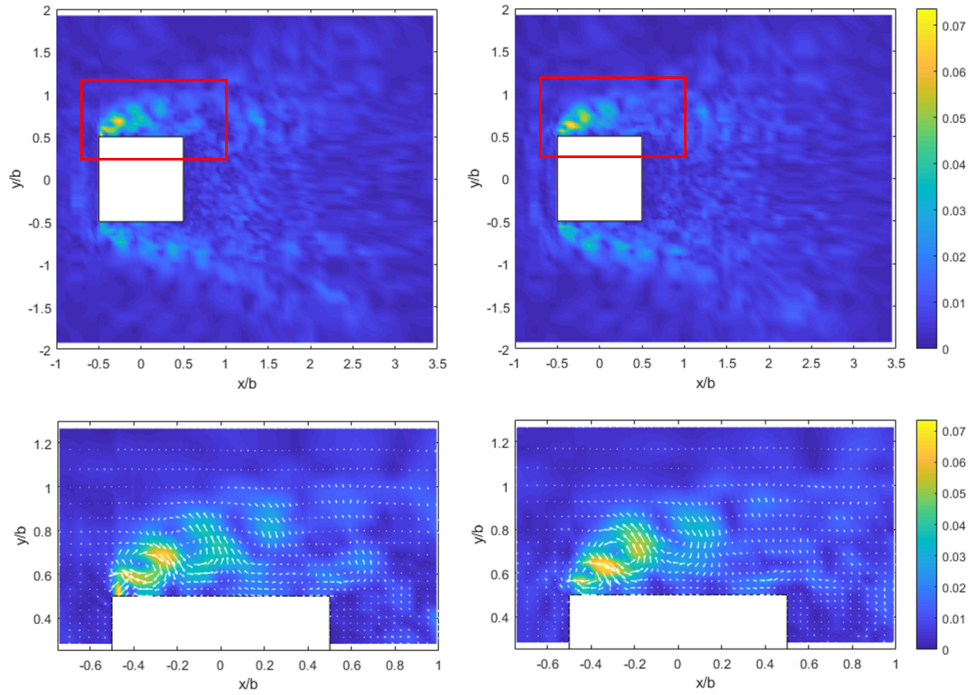
(d) $\psi_{f,n}$ at $n = 1$, $fb / U_H = 0.0760$ (Case 2)(e) $\psi_{f,n}$ at $n = 2$, $fb / U_H = 0.0947$ (Case 1)(f) $\psi_{f,n}$ at $n = 2$, $fb / U_H = 0.0591$ (Case 2)

Figure 5.6 (continued on next page)



(g) $\psi_{f,n}$ at $n = 1$, $fb / U_H = 0.8614$ (Case 1)

(The parts in the red boxes are magnified and shown at the bottom)



(h) $\psi_{f,n}$ at $n = 1$, $fb / U_H = 0.8448$ (Case 2)

(The parts in the red boxes are magnified and shown at the bottom)

Figure 5.6 Eigenfunctions corresponding to the SPOD modes at some specific frequencies. Left: $\text{Re}(\psi_{f,n})$, Right: $\text{Im}(\psi_{f,n})$. The colour shows the magnitude of the vector. The fluctuation mode $\psi_{f,n}(\mathbf{x})e^{i2\pi ft}$ is understood by watching the animation of its real part, $\text{Re}(\psi_{f,n})$, one cycle of which is approximately $\text{Re}(\psi_{f,n}) \rightarrow -\text{Im}(\psi_{f,n}) \rightarrow -\text{Re}(\psi_{f,n}) \rightarrow \text{Im}(\psi_{f,n}) \rightarrow \text{Re}(\psi_{f,n})$.

Furthermore, the SPOD theory indicates that, at a certain frequency, if the largest or several $\lambda_{f,n}$ values are significantly larger than the others, one or several physical coherent structures exist at that frequency, as these fluctuation modes hold most of the TKE at that frequency. In this study, main turbulent structures were observed at the following frequencies.

- $fb/U_H \approx 0.01$

The input of the inflow fluctuation on the inlet boundary had a significant influence on the fluctuation mode of the wind speed. As Figures 5.4 and 5.5 show, the energy of the first two modes in Case 2 was far higher than for other modes, while in Case 1, the superiority was not very clear. Therefore, the proportion of the energy around this frequency in Case 2 was much larger than that in Case 1. Figures 6 (a) and (b) show the respective first modes in the two cases, which were entirely different. In Case 1, the wind speed did not change significantly at the upstream side of the prism and generated two almost symmetrical vortices in the wake of the building. In Case 2, the wind fluctuated from the upstream side and separated from both sides because it collided with the building. However, the mode in Case 2 also exhibited an asymmetry due to the inevitable asymmetry of the inflow fluctuation wind.

- $fb/U_H \approx 0.1$

The Strouhal number $f_1 b/U_0$, where f_1 is the frequency value where the first peak of energy in Figures 5.4 and 5.5 was observed, was approximately 0.07, which roughly coincided with the value given by Sakamoto and Arie (1983), who measured the Kármán-type vortex shedding frequency behind a rectangular prism. Figures 6 (c) and (d) show the first mode. In the range of $0.06 < fb/U_H < 0.18$ (Case 1) or $0.04 < fb/U_H < 0.14$, the size of the vortex varied with frequency, but the fluctuation modes were qualitatively the same as that in Figure 5.6 (c) or (d). The total fluctuation energies in this range were 12% (Case 1) and 9% (Case 2), which can be seen as the strongest fluctuating patterns in this flow field. Additionally, the size of the Kármán-type vortex in Case 2 was slightly larger than that in Case 1. The wake fluctuation concentrated within the width of the building in Case 1, while it was much wider in Case 2, which explains the different wake widths indicated by the mean velocities shown in Figures 5.4 and 5.5. Also note that the large TKE peak in the wake of Case 1 corresponds well with the shape of the Kármán-type vortex identified by the SPOD mode.

Additionally, an arch-type vortex shedding was observed in the second modes in both

cases, shown in Figures 6 (e) and (f), although they appeared to be slightly asymmetrical, which was caused by a calculation error. Previous studies (Okamoto and Sunabashiri, 1992; Sakamoto and Arie, 1983) reported that when the aspect ratio H/b is under a critical value, vortex shedding changes from the anti-symmetrical Kármán-type to the symmetric arch-type and the critical value depends on the thickness of the boundary layer. However, recently, Wang et al.(2019) performed a POD on symmetrical and anti-symmetrical parts of the velocity field respectively and demonstrated that both types of vortex shedding occur in the wake of the building model. Referring to the decomposition results of SPOD, the authors of this article are inclined to agree with the latter. When one of the two vortex shedding phenomena contains more fluctuation energy than the other, it will be clear to observe.

- $fb/U_H \approx 1$

In the energy distribution of Case 1 (Figure 5.4), another peak was observed, while in Case 2 (Figure 5.5) this peak was unclear. This energy value corresponded to the flow separation phenomenon on both sides of the building. In the first mode of Case 1, as shown in Figure 5.6 (g), vortices were emitted mainly from one corner of the building. Although not shown, the second mode was symmetric with the first, which depicted the emitted vortices on the other side of the building. The total fluctuation energy of the two modes in this frequency area was approximately 3% of the total TKE. The first mode of Case 2 at the same frequency is also shown in Figure 5.6 (h), which was similar to that in Case 1, but the energy was quite significant. The reason was assumed to be that this phenomenon was more easily activated by the tidy inflow, such as the unfluctuating one in Case 1; thus, the vortices released from the corner of the building appeared clearly with a much higher energy than Case 2.

In summary, the result of SPOD depicted the difference between the two cases at all frequency levels, which provided an insight into how the inflow fluctuation influenced the turbulence around the building. Because the mechanism of turbulence was still not very clear, this result may provide some hints for further research on turbulence. From the perspective of pedestrian-level wind analysis, considering the inflow fluctuation would undoubtedly bring the result closer to reality. First, the inflow fluctuation would clearly increase both the TKE and instantaneous wind speed, which may harm the pedestrian. Furthermore, as shown above, some vortex shedding phenomena around the building would differ, which, for example, may change the place where a wind nuisance occurs.

5.3.2 Comparison of results with POD

In this section, a brief comparison of results between POD and SPOD is presented. While a detailed and theoretic comparison was discussed by Towne et al. (2018), the authors of this paper intuitively explain the advancement of SPOD over POD. Case 1 has been used as an example here.

Figure 5.7 (a) and (b) demonstrates the first two modes calculated using POD on the wind speed data from Case 1. The wake is similar to that of Kikitsu et al. (2008), who implemented POD on the wind speed data obtained using particle image velocimetry. Note that the appearance of these two modes is quite similar to the real and imaginary parts shown in Figure 5.6 (c). In addition, modes 3 and 4 (Figure (c) and (d)) correspond to the arch-type vortex, and modes 23 and 25 (Figure (e) and (f)) correspond to the flow separating on one side of the building. The corresponding relations between POD modes and SPOD modes are shown in Table 5.2. Figure 5.8 provides the power spectral density functions of the POD mode coefficients for all these modes, where power spectral density functions of each pair of modes exhibit almost the same trend. The peaks occur at the same frequency as observed in the results of SPOD. Further, the power spectral density functions demonstrate that the POD mode is composed of contributions from spatiotemporal coherent structures at many frequencies, which implies that certain flow phenomena would probably be buried. However, this is not the case of SPOD because it separates the flow phenomena in different time scales, as reported by Towne et al. (2018).

It is interesting to note that POD separated one classical flow dynamics into two modes with uncorrelated coefficients. This can be explained by a simple example. Consider two signals, $u_1(t) = \cos(t)$ and $u_2(t) = \sin(t)$. The covariance between them is 0, which makes the covariance matrix diagonal, so they will be regarded as uncorrelated in the eigenvalue problem raised by POD. However, the link between them is clear that $u_1^2 + u_2^2 = 1$. In mathematics, the covariance measures the linear correlation, and “linearly uncorrelated” is a necessary but not a sufficient condition for “independent”. Hence, beyond linear correlation (which POD can process), nonlinear correlation, such as $u_1^2 + u_2^2 = 1$, also exists and cannot be measured by the classical covariance matrix. Thus, POD does not recognize such a relationship. Actually, Wang et al. (2019) confirmed that an approximate $\pi/2$ phase difference existed between the first two anti-symmetric POD mode coefficients, which was similar to the relationship between $\cos(t)$ and $\sin(t)$, and between the each of the mode pairs in Case 1. However, each of the SPOD modes shows a simple harmonic motion within the data, such as the ones shown in Table 5.2.

In general, a simple harmonic motion will be decomposed by POD into two modes. This can be theoretically proved. First, let dataset $u'_m(t)$, $m=1,2,\dots,3M$ represent all the wind speed data in $\mathbf{u}'(\mathbf{x},t)$, where M denotes the number of the spatial points \mathbf{x} . A simple harmonic motion is usually defined as $u'_m(t) = A_m \cos(2\pi ft - \theta_m)$, where A_m is the amplitude and θ_m is the phase. $u'_m(t)$ can be further written as

$$u'_m(t) = A_m \cos(\theta_m) \cos(2\pi ft) + A_m \sin(\theta_m) \sin(2\pi ft), \quad (5.2)$$

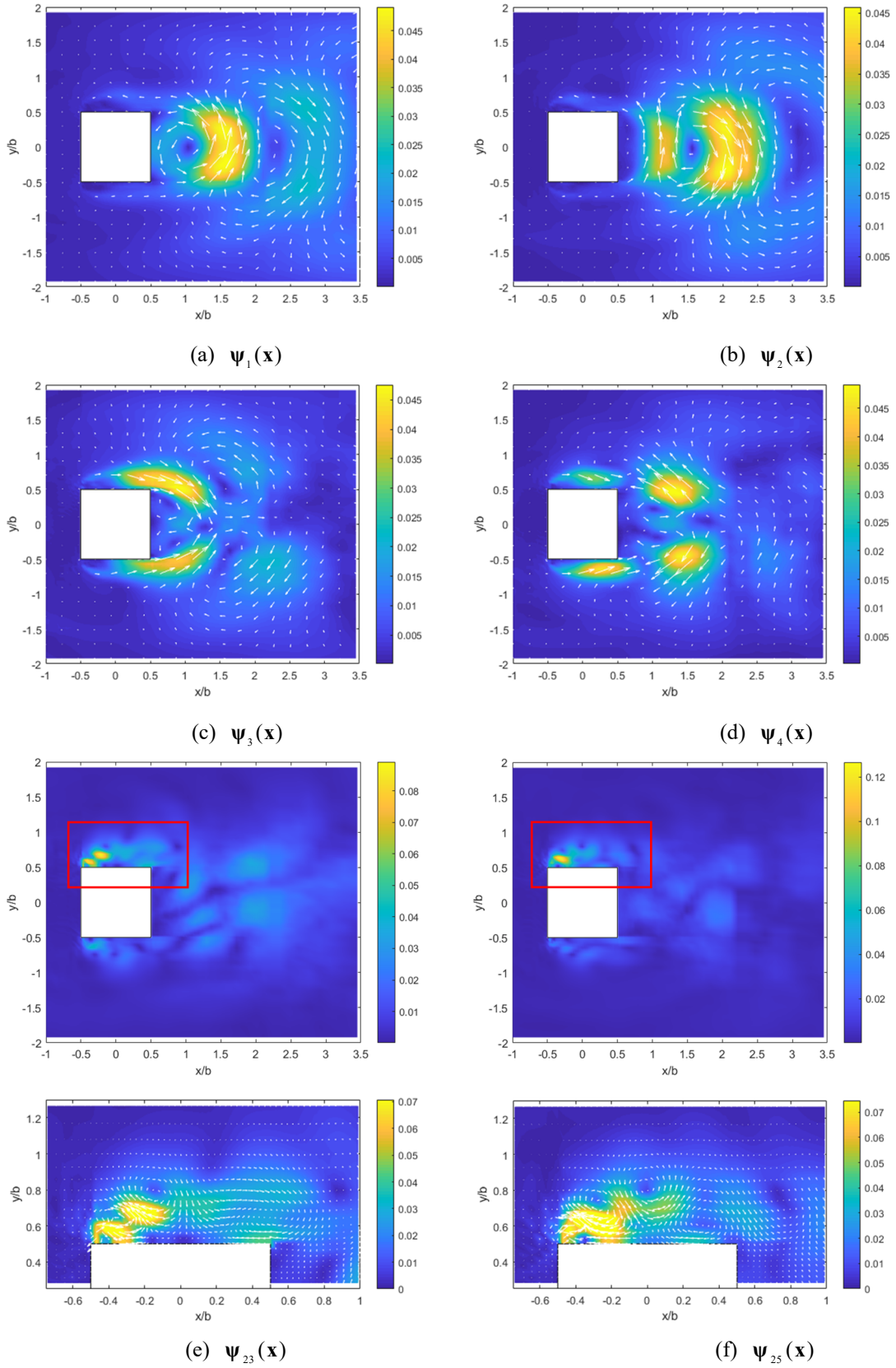
The vector form can be

$$[u'_m(t)]_{3M} = [A_m \cos(\theta_m)]_{3M} \cos(2\pi ft) + [A_m \sin(\theta_m)]_{3M} \sin(2\pi ft), \quad (5.3)$$

where $[\cdot]_{3M}$ denotes a vector, whose length is $3M$. Consider the general case that the vectors $[A_m \cos(\theta_m)]_{3M}$ and $[A_m \sin(\theta_m)]_{3M}$ are not along the same line. This indicates that all the data can be plotted on a two-dimensional plane in the $3M$ -dimensional space, so the true dimension of the dataset $u'_m(t)$ is 2. Consequently, POD will also need two orthogonal modes to depict a two-dimensional dataset with two non-zero eigenvalues.

Table 5.2. Corresponding relations between POD modes and SPOD modes. In each row, the appearance of the two POD modes is similar to the real and imaginary parts of the SPOD eigenfunction.

Physical phenomenon	POD	SPOD
Karman type vortex	Modes 1 and 2 (Figure 9 (a) and (b))	Mode $n = 1$, $fb / U_H = 0.1034$ (Figure 8 (c))
Arch type vortex	Modes 3 and 4 (Figure 9 (c) and (d))	Mode $n = 2$, $fb / U_H = 0.0947$ (Figure 8 (e))
Flow separation on one side of building	Modes 23 and 25 (Figure 9 (e) and (f))	Mode $n = 1$, $fb / U_H = 0.8614$ (Figure 8 (g))



(The parts in the red boxes are magnified and shown at the bottom)

Figure 5.7 POD modes (Case 1)

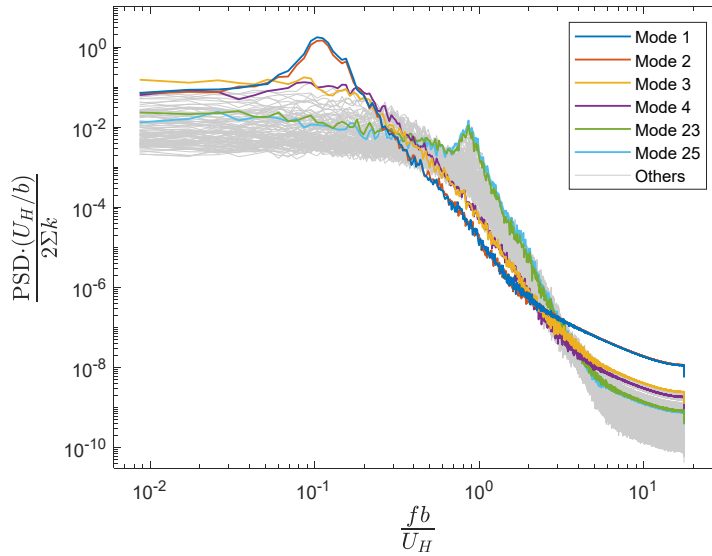


Figure 5.8 Power spectral density functions of the POD mode coefficients (Case 1)

As a hybrid decomposition skill of POD and discrete Fourier transform (DFT), SPOD is no doubt a better solution to deal with such simple harmonic motion in the flow field. However, in addition to the SPOD applied in this study, other DFT-POD hybrid approaches were also developed recently. The decomposition proposed by Sieber et al. (2016), which was also called SPOD, applied a low-pass filter along the diagonals of POD correlation matrix to force POD to resemble DFT. The multi-scale proper orthogonal decomposition (mPOD) proposed by Mendez et al. (2019) combined the ideas from Sieber's SPOD and the SPOD in Towne et al. (2018) to integrate their advantages. Additionally, the dynamic mode decomposition (DMD) was developed as an alternative to POD (Rowley et al., 2009; Schmid, 2010) and was proved to be related to DFT (Chen et al., 2012). However, none of the aforementioned methods preserve the orthogonality property. Thus, the spatial modes are not mutually orthogonal. The orthogonality property of POD or SPOD makes it easy to compute the mode energy and provides comprehensible physical meaning to mode energy. It directly connects mode energy to TKE, or RMS velocity fluctuation, which is considered convenient in the applications of wind engineering and wind environment assessment. Further, this leads to the idea introduced in the next section.

5.3.3 Energy distribution at a certain point

The above introduced SPOD as a mathematic tool to analyse the whole flow field, while in this section SPOD will be applied to resolve the fluctuation energy of wind speed at a certain point, \mathbf{x} . This can be done by realise Γ in Eq. (4.7) as a single spatial point \mathbf{x} ,

and the volume of Γ can be omitted. After such manipulation, we get

$$s_{f,n}(\mathbf{x}) = \lambda_{f,n} \Psi_{f,n}^\dagger(\mathbf{x}) \Psi_{f,n}(\mathbf{x}), \quad (5.4)$$

In this case, $s_{f,n}(\mathbf{x})$ can be considered as the contribution of each SPOD mode to the TKE at point \mathbf{x} , because the relationship between the TKE at point \mathbf{x} and $s_{f,n}(\mathbf{x})$ can be represented as

$$2k(\mathbf{x}) = \int_{-\infty}^{+\infty} \sum_n s_{f,n}(\mathbf{x}) df, \quad (5.5)$$

which indicates that the TKE at point \mathbf{x} is divided by both spatial mode and frequency. $s_{f,n}(\mathbf{x})$ can be considered as the extent to which the fluctuating wind speed at the point \mathbf{x} is influenced by the n th mode at frequency f .

Taking Case 2 as a calculation example, the results of $s_{f,n}(\mathbf{x})$ at two points, \mathbf{x}_A and \mathbf{x}_B , are shown in Figures 5.9 and 5.10, and the three modes with the largest $s_{f,n}(\mathbf{x})$ values are marked by \bigcirc . Assuming that one is analysing the wind environment around this building, and is not satisfied with the instantaneous wind speed at points \mathbf{x}_A and \mathbf{x}_B , then restraining the physical phenomena indicated by the three modes in Figures 5.9 and 5.10 is the most effective action because they form the larger part of TKE at these two points. Among the three marked modes, two are low-frequency modes and are the same for the two points. This shows that the wind speed at the two points is affected by the low-frequency modes due to the inflow fluctuating wind. By observing the other mode which is different for the two points, the mode corresponding to the first peak at point B represents the Kármán-type vortex, while it is different at point A with low energy, which means the Kármán-type vortex has a greater effect on point B.

The above analysis provides a method to recognize the most influential fluctuation modes, which contributes to the planning of countermeasures against a too-large TKE at a certain point, and further against the wind nuisance caused by the fluctuating wind speed. However, neither POD nor SPOD provides a hint on the cause of the too-large mean wind speed, because the mean value has already been deducted before the implementing of POD or SPOD. In practice, the target point of the analysis should not be restricted to the places where the strongest winds occur, because the standards of wind nuisance differ for the places with different functions. For the places such as parks and public squares where the pedestrians tend to concentrate and stay for a relatively long time, the standards for the wind environment are usually more strict. Such places might not be the places where the strongest winds occur, but the probability of wind nuisance is larger because of the strict standard. Therefore, the target of the analysis can be anywhere, which depends on the cases.

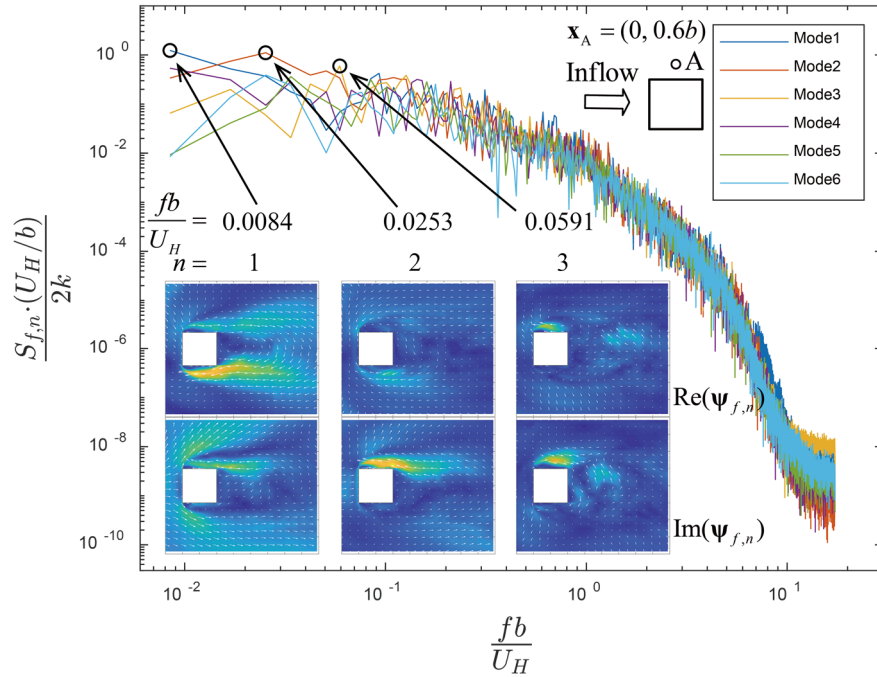


Figure 5.9 Result of $s_{f,n}(\mathbf{x})$ at observation point $\mathbf{x}_A = (0, 0.6b)$ in Case 2

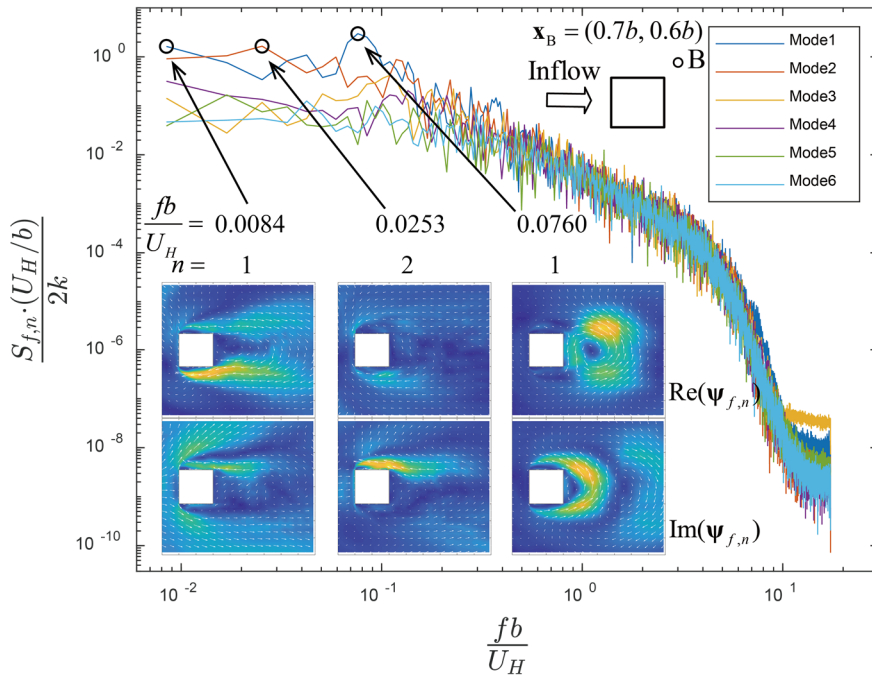


Figure 5.10. Result of $s_{f,n}(\mathbf{x})$ at observation point $\mathbf{x}_B = (0.7b, 0.6b)$ in Case 2

5.4 Summary

In this study, turbulent structures around a rectangular prism building model are analysed using the SPOD technique, with which one can decompose the fluctuation energy of wind velocity based on the spatiotemporal correlation and obtain an insight into the fluctuation pattern of the flow. Two cases of wind speed time series data (with and without the fluctuation at the inflow boundary) were analysed using SPOD. By observing the results, some conclusions can be obtained, as follows:

(1) The input of the inflow fluctuation on the inlet boundary had a significant influence on the turbulent structures at a low frequency because the fluctuation modes and energy differed between the two cases.

(2) In both cases, the strongest fluctuation mode corresponded to the Kármán-type vortex shedding, while the frequency was slightly larger when no fluctuation was input at the inflow boundary. The difference in the shapes of the Kármán-type vortex shedding was considered related to the difference in the mean velocity and TKE fields of the two cases.

(3) The arch-type vortex shedding was observed in the second modes of both cases. The results of this study correspond with those of the former study (Wang et al., 2019). Both the Kármán-type and arch-type vortices occurred in any case regardless of the aspect ratio. However, the clarity required to observe either of them depends on their fluctuation energy.

(4) At a high frequency, flow separation phenomenon occurred on both sides of the building. In the case where no fluctuation was input at the inflow boundary, this phenomenon exhibited a peak on the distribution of energy, while it was not quite significant in the other case.

(5) Considering the inflow fluctuation will undoubtedly bring the results closer to reality when performing pedestrian-level wind analysis, because the inflow fluctuation will increase both the TKE and instantaneous wind speed, and some vortex shedding phenomena will be different such that the place where the wind nuisance occurs will change.

(6) For each of the physical phenomena investigated in this manuscript, the two modes calculated using POD was quite similar to the real and imaginary parts of the eigenfunction calculated using SPOD. This indicated that SPOD successfully detected the simple harmonic motions from the turbulence data, while the original POD needed two modes with uncorrelated coefficients to depict each of these simple harmonic motions.

(7) SPOD can be used to decompose the TKE at a certain point and display the extent to which the fluctuating wind speed at the point is influenced by each mode. This is considered useful in finding the main reason of large fluctuation and the improvement of pedestrian-level wind.

Grasping the factors that compose the flow field is important to improving the wind environment in an urban area. However, because flows of various scales are mixed, the flow field around a building can be so intricate that capturing the characteristic turbulent structures from it is not always easy. In this study, SPOD has been proved to be an effective tool to analyse turbulent structures.

Reference

- Adamek, K., Vasan, N., Elshaer, A., English, E., Bitsuamlak, G., 2017. Pedestrian level wind assessment through city development: A study of the financial district in Toronto. *Sustain. Cities Soc.* 35, 178–190. <https://doi.org/10.1016/J.SCS.2017.06.004>
- Architectural Institute of Japan, 2016. AIJ Benchmarks for Validation of CFD Simulations Applied to Pedestrian Wind Environment around Build. Architectural Institute of Japan, Tokyo.
- Blocken, B., Carmeliet, J., 2004. Pedestrian Wind Environment around Buildings: Literature Review and Practical Examples. *J. Therm. Envel. Build. Sci.* 28, 107–159. <https://doi.org/10.1177/1097196304044396>
- Chen, K.K., Tu, J.H., Rowley, C.W., 2012. Variants of dynamic mode decomposition: Boundary condition, Koopman, and fourier analyses. *J. Nonlinear Sci.* 22, 887–915. <https://doi.org/10.1007/s00332-012-9130-9>
- Fiedler, H.E., 1988. Coherent structures in turbulent flows. *Prog. Aerosp. Sci.* [https://doi.org/10.1016/0376-0421\(88\)90001-2](https://doi.org/10.1016/0376-0421(88)90001-2)
- Kikitsu, H., Okuda, Y., Ohashi, M., Kanda, J., 2008. POD analysis of wind velocity field in the wake region behind vibrating three-dimensional square prism. *J. Wind Eng. Ind. Aerodyn.* 96, 2093–2103. <https://doi.org/10.1016/J.JWEIA.2008.02.057>
- Kikumoto, H., Ooka, R., Han, M., Nakajima, K., 2018. Consistency of mean wind speed in pedestrian wind environment analyses: Mathematical consideration and a case study using large-eddy simulation. *J. Wind Eng. Ind. Aerodyn.* 173. <https://doi.org/https://doi.org/10.1016/j.jweia.2017.11.021>
- Mendez, M.A., Balabane, M., Buchlin, J.M., 2019. Multi-scale proper orthogonal decomposition of complex fluid flows. *J. Fluid Mech.* 870, 988–1036. <https://doi.org/10.1017/jfm.2019.212>
- Mochida, A., Lun, I.Y.F., 2008. Prediction of wind environment and thermal comfort at pedestrian level in urban area. *J. Wind Eng. Ind. Aerodyn.* 96, 1498–1527. <https://doi.org/10.1016/j.jweia.2008.02.033>
- Okamoto, S., Sunabashiri, Y., 1992. Vortex Shedding From a Circular Cylinder of Finite Length Placed on a Ground Plane. *J. Fluids Eng.* 114, 512–521. <https://doi.org/10.1115/1.2910062>
- Rowley, C.W., Mezi, I., Bagheri, S., Schlatter, P., Henningson, D.S., 2009. Spectral analysis of nonlinear flows. *J. Fluid Mech.* 641, 115–127. <https://doi.org/10.1017/S0022112009992059>
- Sakamoto, H., Arie, M., 1983. Vortex shedding from a rectangular prism and a circular cylinder placed vertically in a turbulent boundary layer. *J. Fluid Mech.* 126, 147–

-
165. <https://doi.org/10.1017/S0022112083000087>
- Schmid, P.J., 2010. Dynamic mode decomposition of numerical and experimental data. *J. Fluid Mech.* 656, 5–28. <https://doi.org/10.1017/S0022112010001217>
- Shui, T., Liu, J., Yuan, Q., Qu, Y., Jin, H., Cao, J., Liu, L., Chen, X., 2018. Assessment of pedestrian-level wind conditions in severe cold regions of China. *Build. Environ.* 135, 53–67. <https://doi.org/10.1016/J.BUILDENV.2018.03.006>
- Sieber, M., Paschereit, C.O., Oberleithner, K., 2016. Spectral proper orthogonal decomposition. *J. Fluid Mech.* 792, 798–828. <https://doi.org/10.1017/jfm.2016.103>
- Tamura, T., Ono, Y., 2003. LES analysis on aeroelastic instability of prisms in turbulent flow. *J. Wind Eng. Ind. Aerodyn.* 91, 1827–1846. <https://doi.org/10.1016/j.jweia.2003.09.032>
- Towne, A., Schmidt, O.T., Colonius, T., 2018. Spectral proper orthogonal decomposition and its relationship to dynamic mode decomposition and resolvent analysis. *J. Fluid Mech.* 847, 821–867. <https://doi.org/10.1017/jfm.2018.283>
- Träumner, K., Damian, T., Stawiarski, C., Wieser, A., 2015. Turbulent Structures and Coherence in the Atmospheric Surface Layer. *Boundary-Layer Meteorol.* 154. <https://doi.org/10.1007/s10546-014-9967-6>
- Wang, F., Lam, K.M., Zu, G.B., Cheng, L., 2019. Coherent structures and wind force generation of square-section building model. *J. Wind Eng. Ind. Aerodyn.* 188, 175–193. <https://doi.org/10.1016/j.jweia.2019.02.019>
- Yan, B.W., Li, Q.S., 2015. Inflow turbulence generation methods with large eddy simulation for wind effects on tall buildings. *Comput. Fluids* 116, 158–175. <https://doi.org/10.1016/j.compfluid.2015.04.020>
- Zahid Iqbal, Q.M., Chan, A.L.S., 2016. Pedestrian level wind environment assessment around group of high-rise cross-shaped buildings: Effect of building shape, separation and orientation. *Build. Environ.* 101, 45–63. <https://doi.org/10.1016/J.BUILDENV.2016.02.015>

Chapter 6

Spectral analysis of turbulent flow in a two-dimensional street canyon and its role in pollutant removal

6.1 Introduction

Modern construction of urban areas has led to the development of semi-enclosed spaces surrounded by buildings and a rapidly growing residential population. Within these spaces, which are often termed as street canyons, air pollutants, including gases and particulate material that harm the microclimate and air quality, are frequently emitted. A street canyon with an aspect ratio (i.e., the ratio between building height and street width) larger than 0.65 is common in a high-density urban area. According to Oke (1987), the flow in such a canyon is classified as a skimming flow, within which the lower part is a weak wind area. The efficiency of pollutant dispersion is relatively low, which may lead to deterioration of air quality. In a common situation where the temperature difference is insignificant, inertial convection outweighs buoyancy. In this case, the transfer of pollutants is determined by the flow pattern within and near the canyon. Therefore, understanding the characteristics of canyon flows is vital for urban planning.

The mechanism of pollutant removal by pure inertial processes has been investigated in many studies. Although the efficiency of pollutant removal varies with the geometry of the canyon and surrounding buildings, such as the aspect ratio of the canyon (Park et al., 2015) and the roof geometries of surrounding buildings (Cintolesi et al., 2021; Kastner-Klein et al., 2004), it is usually assumed that turbulence, rather than mean wind, plays a major role in pollutant removal from the canyon. The RANS simulation by Cheng et al. (2008) revealed that ventilation (pollutant removal) by turbulence exhibits a broad maximum covering the entire roof of the street canyon, while mean flow-induced ventilation mainly occurs on the windward side. This was supported by an LES conducted by Michioka et al. (2011). By contrast, the inward and outward pollutant transport driven by the mean wind is almost balanced, which results in an insignificant

net pollutant exchange (Liu and Wong, 2014). Quadrant analysis has shown that strong ejection events carried by turbulent fluctuations are highly correlated with pollutant removal at the rooftop (Cheng and Liu, 2011; Di Bernardino et al., 2018; Michioka et al., 2011).

It was found that the exchange process at the interface between the canyon and external flow is driven by the momentum flux in the shear layer (Barbano et al., 2021; Solazzo and Britter, 2007). The shear layer is shed from the upstream roof and becomes unstable through Kelvin–Helmholtz instabilities (Louka et al., 2000). Cui et al. (2004) showed that the streamwise and vertical fluctuation velocities at the roof level were highly intermittent, and the time scale of the ejection events fit well with that of the Kelvin–Helmholtz instabilities. Letzel et al. (2008) also concluded that the shedding of Kelvin–Helmholtz waves causes unsteadiness of the shear layer and renders the canyon recirculation highly intermittent.

However, Salizzoni et al. (2009) demonstrated that external turbulence directly influences the flow and dispersion within the canyon. Zhang et al. (2011) claimed that the turbulence affecting the pollutant transport at the roof level might not be due to Kelvin–Helmholtz instabilities; instead, it might be a result of the evolution of the resolved scale velocities caused by the changes in the time series of upper boundary wind conditions. Michioka et al. (2011) and Michioka and Sato (2012) indicated that large amounts of pollutants are removed from the canyon by ejection because of the large-scale coherent structure. This was supported by the observations reported by Han et al. (2018). Indeed, large-scale low- and high-momentum fluids have also been confirmed to cause strong ejection and sweep events (Coceal et al., 2007; Inagaki and Kanda, 2010; Kanda, 2006).

This may not be an either-or problem. A reasonable explanation is that the shear layer dynamics at the interface are modified by external turbulence. Salizzoni et al. (2011) revealed that turbulent transfer is caused by the coupling between the instabilities of the shear layer and turbulent structures in the external flow; thus, no single velocity scale exists that characterises all aspects of the flow. The results obtained by Klein and Galvez (2015) agree with these findings. These authors collected data from a real street canyon located in suburban terrain and found that the turbulence properties inside the canyon varied with external flows in two cases where the wind directions were perpendicular to the street. Blackman and Perret (2016) found nonlinear interactions between large- and small-scale structures, where small-scale structures can be amplified or suppressed by high- or low-momentum fluids carried by large-scale structures. A low but unneglectable

correlation was detected between the fluctuations of the two structures. A similar analysis was conducted by Jaroslowski et al. (2020), who found that sweep and ejection events were mainly caused by the dynamic contribution of small-scale structures. However, although large-scale structures may not contribute directly to pollutant removal, they contribute indirectly by promoting small-scale turbulence.

To gain deeper insights into turbulent structures and mass transfer mechanisms, decomposition of the turbulence should be performed before fluid mechanisms and their relationships with pollutant transport are discussed. Several attempts have been made in previous studies. Such approaches include POD (Perret and Rivet, 2013), linear stochastic estimation decomposition (Blackman et al., 2018; Blackman and Perret, 2016), and the use of a spanwise filter to distinguish large- and small-scale structures (Jaroslowski et al., 2020). However, to the best of our knowledge, an approach that can accurately decompose canyon flow into various fluctuation patterns according to the scales and can concretely illustrate these fluctuation patterns, which are directly related to already known physical mechanisms in street canyon flow, has not been developed yet. For this purpose, SPOD (Schmidt and Colonius, 2020; Towne et al., 2018) is considered a more suitable tool.

This study aims to apply SPOD to extract turbulent structures from a two-dimensional street canyon flow and provide vivid flow visualisations for observing the flow fluctuations at various scales in detail, which have already been related with known physical mechanisms in street canyon flow. Based on these results, the pollutant removal mechanisms are unveiled by quantitatively computing the amount of ejection events and turbulent mass flux at the roof level contributed by various turbulent structures.

In this study, we first describe reproduction of the LES for a two-dimensional street canyon with reference to the simulation and wind tunnel experiment conducted by Michioka et al. (2011). The LES models, simulation conditions, and basic statistical results are reported in Section 6.2. In Section 6.3, the newly defined SPOD co-spectrum are briefly introduced. The application of these tools is described in Sections 6.4 and 6.5. Section 6.4 provides the decomposition results of the velocity field and discusses the sweep and ejection events provided by the decomposed structures. Section 6.5 uses the SPOD co-spectrum to link the turbulent structures to pollutant removal and discusses the pollutant removal mechanism.

6.2 Large-eddy simulation

6.2.1 Physical Models and Equations

The flow field was calculated via LES using open-source computational fluid dynamics (CFD) software, OpenFOAM v8 (The OpenFOAM Foundation Ltd, 2020). The standard Smagorinsky model (Smagorinsky, 1963) was employed to evaluate the eddy viscosity ν_T at the sub-grid scale. The Smagorinsky constant C_s was set to 0.12 (Tominaga and Stathopoulos, 2011). The length scale near the wall was modified using the van Driest damping function (Van Driest, 1956).

The transport equation of the filtered concentration c (ppm) of the tracer gas can be written as:

$$\frac{\partial c}{\partial t} + \nabla \cdot (\mathbf{u}c) = \nabla \cdot \left(\left(\frac{\nu}{Sc} + \frac{\nu_T}{Sc_T} \right) \nabla c \right) + P_c, \quad (6.1)$$

where \mathbf{u} (m/s) is the filtered velocity vector, Sc is the Schmidt number ($= 1$), Sc_T is the SGS turbulence Schmidt number ($= 0.5$), ν is the kinematic viscosity of air ($= 1.5 \times 10^{-5} \text{ m}^2/\text{s}$), and P_c (ppm/s) is the source term of the tracer gas.

6.2.2 Simulation design

The geometry of the simulated domain (Figure 6.1) was mainly set with reference to the wind tunnel experiment conducted by Michioka et al. (2011). The size of the roughness bars was $H(x) \times H(z)$, where $H = 0.12$ m. A continuous line source was placed on the ground at the centre of the target canyon to represent pollutant emissions. Periodic boundary conditions were imposed on streamwise (x) and spanwise (y) directions. The streamwise pressure gradient was adjusted during the simulation to maintain the volume-average streamwise velocity in the entire computational domain at 1 m/s. The Reynolds number based on the bar height and free-stream velocity (≈ 1.4 m/s) was approximately 11,200. The inlet boundary concentration was adjusted to 0 to prevent the tracer gas from returning to the simulation domain through the inlet. The slip and no-slip boundary conditions were imposed on the upper and lower boundaries, respectively. The total variation diminishing (TVD) scheme (Roe, 1986) for the advection term of pollutant concentration was employed to avoid unphysical concentration fluctuations caused by its steep spatial gradient. Other details of the simulation conditions are presented in Table 6.1.

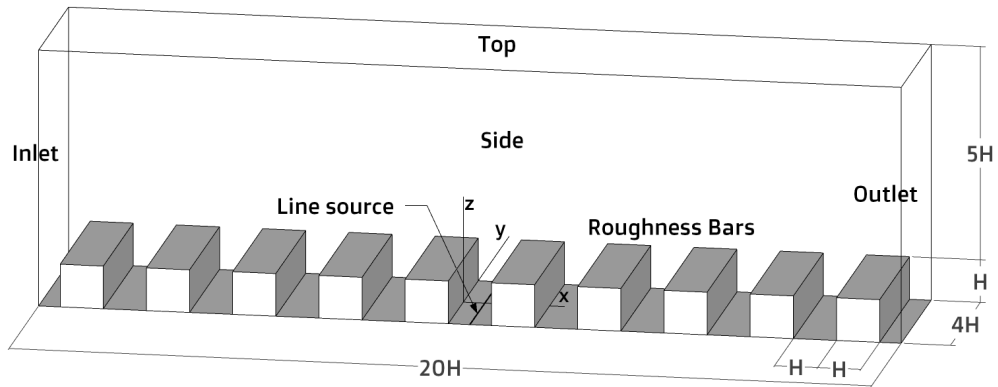


Figure 6.1 Simulation domain

Table 6.1 CFD simulation conditions

Item	Content
Simulation domain	$20H (x) \times 4H (y) \times 6H (z)$ x : streamwise; y : spanwise; z : vertical
Roughness bar size	$H (x) \times H (z)$ ($H = 0.12$ m)
Grid partitioning (Case 1)	$448 (x) \times 160 (y) \times 100 (z)$ Total cells: 5,233,920 In target canyon: $40 (x) \times 160 (y) \times 40 (z)$ Minimum grid size in target canyon: $H/60$ (adjacent to the wall and roof)
Time marching	Pressure-implicit with splitting order (PISO) (Issa, 1986)
Simulation period	Preparatory: 0–120 s, Sampling: 120–240 s
Time-step	During preparatory: 0.0013–0.002 s, (adjusted automatically to keep the maximum Courant's number equal to 1) During sampling: 0.00125 s Sampling time step: 0.0025 s (Sampling frequency: 400 Hz)
Inlet and outlet B.C.	Periodic The concentration on the inlet boundary was adjusted to 0.
Side B.C.	Periodic
Ground and wall B.C.	Velocity: no-slip; Pressure and concentration: zero-Gradient
Top B.C.	Velocity: slip; Pressure and concentration: zero-Gradient
Momentum source	The volume average streamwise velocity in the whole computational domain was kept constant 1 m/s by adjusting the streamwise pressure gradient.
Tracer gas source	Total emission rate $Q = 100$ ppm·m ³ /s at the line source
Wall function	Wall and ground: the Spalding's law (Spalding, 1962)
Space discretisation	2 nd -order central difference TVD scheme for advection terms in scalar transport equations
Time discretisation	Euler-implicit

To confirm the grid-independent, three cases with different grid resolution were computed. In the case where the grid is the finest (Case 1), the simulation domain was partitioned into 448 (x) \times 160 (y) \times 100 (z) grids, and the target canyon was partitioned into 40 (x) \times 40 (z) grids. The total number of cells was 5,233,920. The minimum grid size in the target canyon, which was adjacent to the wall and roof, was $H/60$. The grid was stretched using a hyperbolic tangent function. The grid independence was tested by comparing the results with those of the other two cases with coarser grids. Case 2 used a mesh with 30 (x) \times 30 (z) grids within the target canyon with a minimum size of $H/40$, and Case 3 used a mesh with 20 (x) \times 20 (z) grids with a minimum size of $H/30$. Only the information of Case 1 is presented in Table 6.1, because we will show in the latter section that the grid resolution of Case 1 was sufficient, and all further statistics and post-processing presented in this study were calculated based on the results of Case 1.

During the simulation, the velocity and concentration data were sampled within the following domain:

$$\Omega = \left\{ \mathbf{x} = (x, y, z)^T \mid -0.5H \leq x \leq 1.5H, \quad y = 0, \quad 0 \leq z \leq 2H \right\}, \quad (6.2)$$

which contained 3450 cells. The time signals of the velocity and concentration at all the cell centres were recorded. The sampling frequency was set at 400 Hz. The time-average velocity at $z/H = 2$ was chosen as the reference velocity $U_{\text{ref}} (\approx 0.96 \text{ m/s})$, which was used to normalise the velocity samples. The concentration samples were normalised by the reference concentration C_{ref} , defined by

$$C_{\text{ref}} = \frac{Q}{U_{\text{ref}} H L_y}, \quad (6.3)$$

where Q is the total emission rate ($= 100 \text{ ppm} \cdot \text{m}^3/\text{s}$), and L_y is the length of the line source ($= 4H$). All statistics and post-processing presented in this paper were calculated based on the time signals lasting for 120 s, which was approximately $1000 H/U_{\text{ref}}$.

6.2.3 Statistics and validation

Figures 6.2 and 6.3 show the profiles of the mean streamwise velocity and root mean square of the streamwise fluctuating velocity at $x/H = 0.25, 0.50$, and 0.75 . Figure 6.4 shows the profiles of the mean concentrations at $x/H = 0, 0.50$, and 1 . The results of all three cases with different grids are consistent with the wind tunnel experimental results of Michioka et al. (2011) and Pavageau and Schatzmann (1999), with the only exception being that the mean concentration on the windward wall computed in Case 3 (the coarsest grid), which was considerably different from the results computed in Cases 1 and 2. Because both Cases 1 and 2 can produce grid-independent results, all further statistics

and post-processing presented in this paper were calculated based on the results of Case 1, where the finest grid was used.

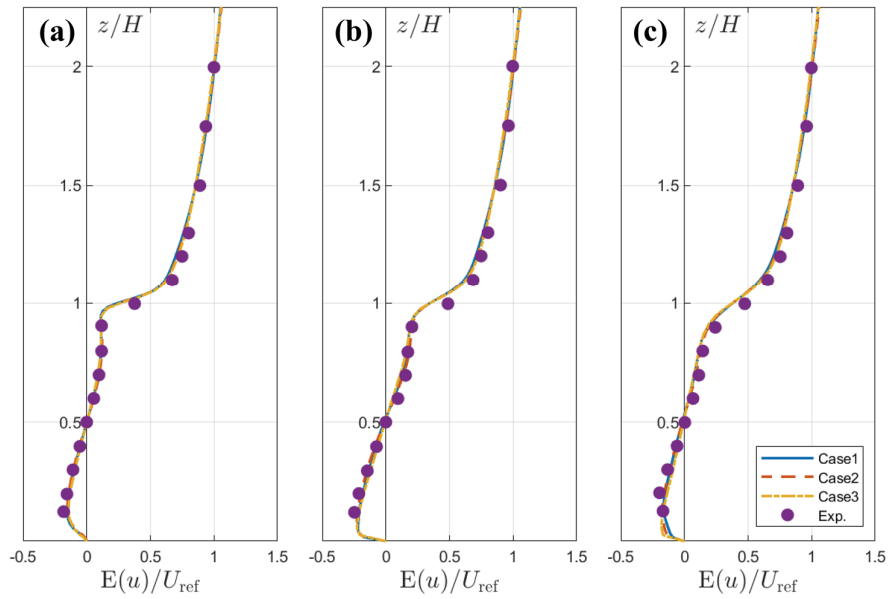


Figure 6.2 Profiles of the mean streamwise velocity at (a) $x/H = 0.25$, (b) $x/H = 0.5$ and (c) $x/H = 0.75$. Filled circles are the results of the wind tunnel experiment conducted by Michioka et al. (2011).

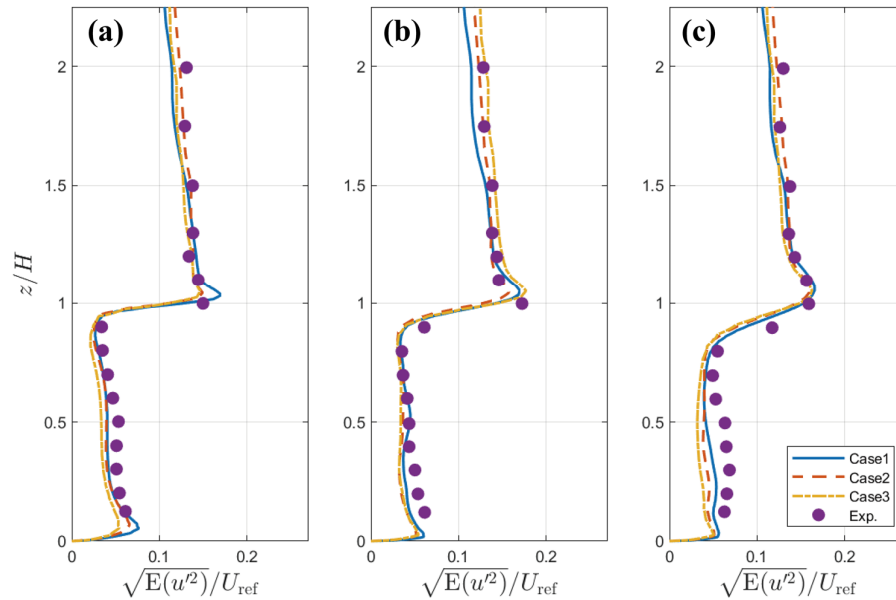


Figure 6.3 Profiles of the root mean square of the streamwise fluctuating velocity at (a) $x/H = 0.25$, (b) $x/H = 0.5$ and (c) $x/H = 0.75$. Filled circles are the results of the wind tunnel experiment conducted by Michioka et al. (2011).

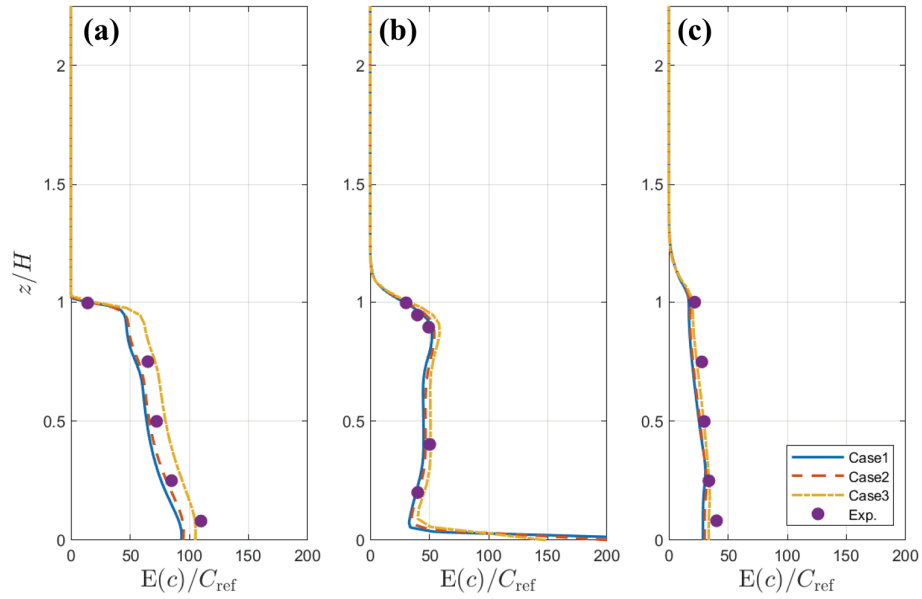


Figure 6.4 Profiles of the mean concentration at (a) $x/H = 0$, (b) $x/H = 0.5$ and (c) $x/H = 1$. Filled circles are the results of the wind tunnel experiment conducted by Pavageau and Schatzmann (1999).

The mean flow within the canyon was characterised by a principal recirculating cell with smaller counter-rotating vortices in the corners, as shown by the streamlines plotted in Figure 6.5 (a); however, the TKE within the canyon was much lower than that in the external flow, as shown in Figure 6.5 (b). The maximum TKE was generated at the junction between the canyon and external flow, where the TKE plume collided on the upper corner of the downstream bar before dividing into two bundles. One bundle continued flowing downstream with the external flow, while the other entered the canyon along the windward wall, resulting in the left–right asymmetric distribution of the TKE in the canyon. These results are consistent with the results of the wind tunnel experiment by Cheng et al. (2008) and the CFD results reported by Walton and Cheng (2002). The mean concentration, plotted in Figure 6.5 (c), also showed a left–right asymmetric distribution. The concentration plume followed the principal recirculation and travelled along the leeward wall. However, most of the concentration plume re-entered the canyon on reaching the roof level rather than travel with the external flow.

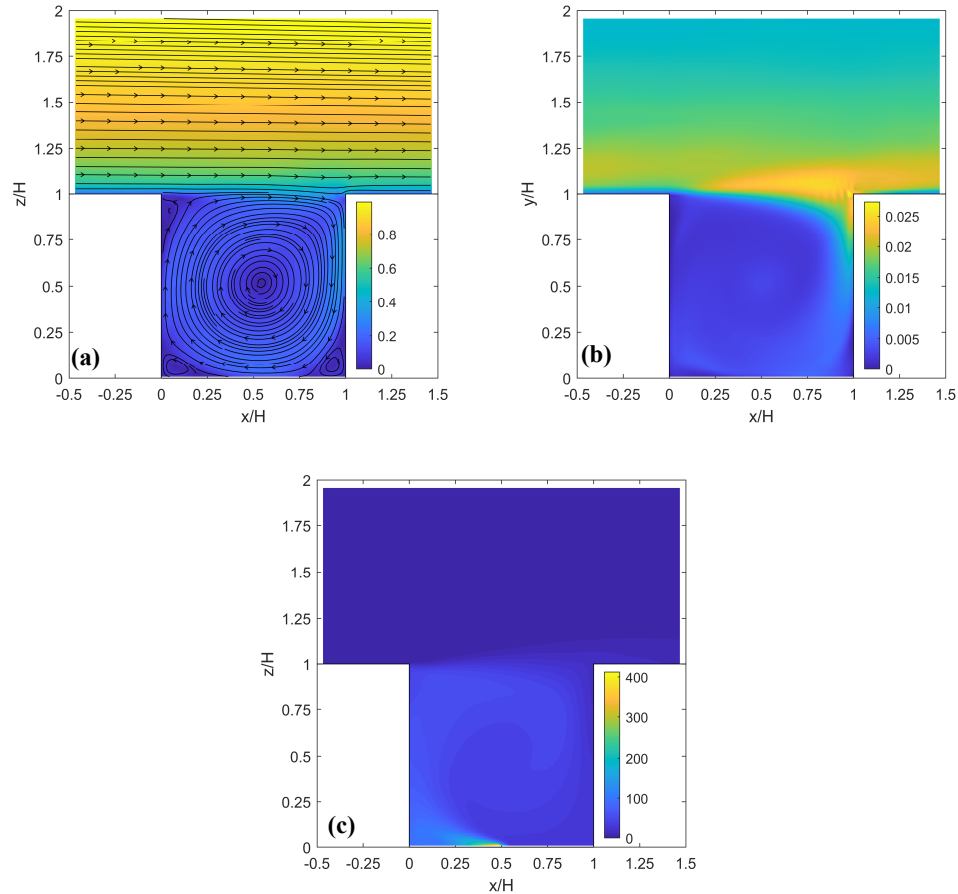


Figure 6.5 Cross-sections of (a) mean velocity with streamlines on the x - z plane, (b) TKE and (c) mean concentration.

Figure 6.6 shows the streamwise distributions of the vertical advective, turbulent, and total mass fluxes at $z/H = 1$, which is similar to the results of Michioka et al. (2011). Generally, these results match very well, although there is a slight difference in the gradient near the windward wall. This is considered as due to the different strategies applied to the mesh, discretisation, and wall function in the LES simulation, which have no significant influence on further analyses. The advective mass fluxes are close to zero or even negative, indicating that its contribution to pollutant removal from the canyon was small. The peak of the advective mass fluxes near $x/H = 1$ is considered unrelated to the pollutant removal, judging by the streamline passing through the point of $(x/H = 1, z/H = 1)$ in Figure 6.5 (a). However, the turbulent mass fluxes were much larger than the advective mass fluxes, indicating that turbulent fluctuations mainly affect pollutant removal from the canyon (Michioka et al., 2011).

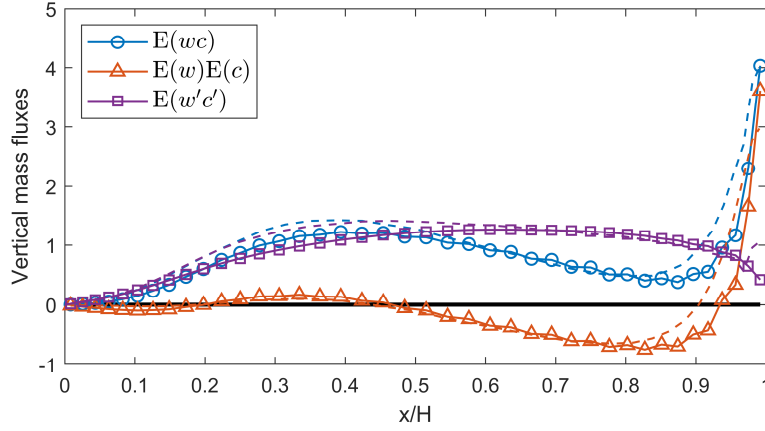


Figure 6.6 Streamwise distributions of advective, turbulent and total vertical mass fluxes at $z/H = 1$. A similar result can also be found in Michioka et al. (2011) and Michioka and Sato (2012).

Turbulent fluctuation contains complex multiscale and chaotic motions, and the type of turbulent motion mainly responsible for pollutant removal remains unclear based on basic statistics. In the next section, SPOD serves as a post-processing tool for decomposing the flow and extracting the turbulent structures.

6.3 Definition of SPOD co-spectrum

To better apply the SPOD technique to the current study, the SPOD co-spectrum is newly defined in this section, where the properties and algorithm are also discussed.

Besides the SPOD spectrum, the SPOD co-spectrum can be defined to illustrate the relationship between the velocities in different directions or even between the velocity and another scalar field. For elucidating the mechanism of pollutant removal in the canyon case described in Section 6.2, the turbulent structure and vertical mass flux at the roof level should be understood. Considering these issues, the two co-spectra are defined as follows:

- (1) The SPOD cross-spectrum between the streamwise fluctuation velocity $u'(\mathbf{x}, t)$ and vertical fluctuation velocity $w'(\mathbf{x}, t)$ is defined as

$$\tilde{S}_{f,n}^{(uw)}(\mathbf{x}) = \lambda_{f,n} \psi_{f,n}^{(u)}(\mathbf{x}) \psi_{f,n}^{(w)*}(\mathbf{x}). \quad (6.4)$$

Then, the SPOD co-spectrum is the real part of the SPOD cross-spectrum

$$S_{f,n}^{(uw)}(\mathbf{x}) = \text{Re} \left(\lambda_{f,n} \psi_{f,n}^{(u)}(\mathbf{x}) \psi_{f,n}^{(w)*}(\mathbf{x}) \right), \quad (6.5)$$

where $\psi_{f,n}^{(u)}$ and $\psi_{f,n}^{(w)}$ denote the u and w components of the vector $\Psi_{f,n}$, respectively. Similar to the relationship between SPOD spectrum and TKE, the Reynolds shear stress

at the spatial point \mathbf{x} will be obtained if the SPOD cross-spectrum is integrated over all frequencies f and summed over all the mode numbers n as

$$E(u'(\mathbf{x}, t)w'(\mathbf{x}, t)) = \int_{-\infty}^{+\infty} \sum_n S_{f,n}^{(uw)}(\mathbf{x}) df. \quad (6.6)$$

When summed over all the mode numbers n , the result equals the usual Fourier co-spectrum between u' and w' at the spatial point \mathbf{x} ,

$$S^{(uw)}(\mathbf{x}, f) = \text{Re} \left(\frac{1}{T} \hat{u}'(\mathbf{x}, f) \hat{w}'^*(\mathbf{x}, f) \right) = \sum_n S_{f,n}^{(uw)}(\mathbf{x}). \quad (6.7)$$

(2) Similarly, the SPOD cross-spectrum between the vertical fluctuation velocity $w'(\mathbf{x}, t)$ and fluctuation concentration $c'(\mathbf{x}, t) = c(\mathbf{x}, t) - E(c(\mathbf{x}, t))$ is defined as

$$\tilde{S}_{f,n}^{(wc)}(\mathbf{x}) = \frac{1}{T} a_{f,n} \psi_{f,n}^{(w)}(\mathbf{x}) \hat{c}'^*(\mathbf{x}, f). \quad (6.8)$$

where $\hat{c}'(\mathbf{x}, f)$ denotes the Fourier transformation of $c'(\mathbf{x}, t)$. Then, the SPOD co-spectrum is the real part of the SPOD cross-spectrum

$$S_{f,n}^{(wc)}(\mathbf{x}) = \text{Re} \left(\frac{1}{T} a_{f,n} \psi_{f,n}^{(w)}(\mathbf{x}) \hat{c}'^*(\mathbf{x}, f) \right). \quad (6.9)$$

Similar to the relationship between SPOD spectrum and TKE, the vertical turbulent mass flux at the spatial point \mathbf{x} will be obtained if the SPOD cross-spectrum is integrated over all frequencies f and summed over all the mode numbers n as

$$E(w'(\mathbf{x}, t)c'(\mathbf{x}, t)) = \int_{-\infty}^{+\infty} \sum_n S_{f,n}^{(wc)}(\mathbf{x}) df. \quad (6.10)$$

When summed over all the mode numbers n , the result equals the usual Fourier co-spectrum between w' and c' at the spatial point \mathbf{x} ,

$$S^{(wc)}(\mathbf{x}, f) = \text{Re} \left(\frac{1}{T} \hat{w}'(\mathbf{x}, f) \hat{c}'^*(\mathbf{x}, f) \right) = \sum_n S_{f,n}^{(wc)}(\mathbf{x}). \quad (6.11)$$

If the SPOD for the velocity is performed according to the algorithm proposed by Towne et al. (2018), the mode coefficient $a_{f,n}$ is not explicitly available. Although the mode coefficient can be calculated using the Fourier coefficients in each block, the values differ for different blocks because of the phase differences. Therefore, when estimating the SPOD co-spectrum $S_{f,n}^{(wc)}$, Welch's method (Welch, 1967) was followed again. The concentration should also be divided into blocks, whose number should be the same as that of the blocks of the velocity. Then, the $S_{f,n}^{(wc)}$ value was calculated independently for each block, according to Eq. (6.9). The final estimation of $S_{f,n}^{(wc)}$ for the whole signal was obtained by averaging the values from all blocks.

6.4 Decomposition of the velocity field

The SPOD analysis results of the velocity field within the sampling field are presented in this section.

6.4.1 Performing SPOD

The SPOD modes were calculated using the method proposed by Towne et al. (2018). In this study, the sampled time signal data consisted of 48,000 snapshots of the velocity field. They were divided into 19 blocks with 50% overlap, and each block consisted of 4,800 snapshots. The Hamming window was imposed on each block when performing a discrete Fourier transform to reduce the impact of spectral leakage. In this case, where the sampling frequency is 400 Hz, the resolution frequency is $400/4800 \text{ Hz} = 0.0833 \text{ Hz}$ ($\approx 0.01 U_{\text{ref}}/H$), and the Nyquist frequency was $400/2 \text{ Hz} = 200 \text{ Hz}$ ($\approx 25 U_{\text{ref}}/H$). These are also the minimum and maximum resolved frequency values in the SPOD spectrum. These parameters are also listed in Table 6.2.

Given that the total signal length is fixed, a proper block length should be chosen. On the one hand, each block should have a sufficient length to prevent the occurrence of a bias error and so that a good frequency resolution can be obtained. On the other hand, the block number should be sufficient so that a relatively precise and converged energy estimation with low uncertainty can be obtained. This is ultimately a trade-off when Welch's method is used (Schmidt and Colonius, 2020). In the current study, we trialled several schemes to divide the time signals when computing the SPOD spectrum and modes. The block number was chosen from a minimum of nine (with 9,600 snapshots in each block) up to a maximum of 79 (with 1,200 snapshots in each block). The analysis results revealed no substantial difference, and the results of 19 blocks are provided in this paper for further analysis. The case with fewer blocks gave relatively vague mode visualisations owing to its relatively poor convergence, although the turbulent structures can still be recognised. The cases with more blocks provided relatively clear mode visualisations, but the frequency resolution of the spectrum was not as good as that provided in this study.

These parameters are not newly proposed in the SPOD algorithm but are directly inherited from Welch's method (Welch, 1967). They are also necessary when a usual Fourier spectrum analysis is performed. Therefore, to understand the relationship between the fluctuation velocity and another scalar field, it is better to take the same block number and block length when performing the Fourier transform for the scalar field,

as is reported in Section 6.5 when dealing with the concentration field.

Table 6.2 Parameters used when performing SPOD according to the algorithm proposed by Towne et al. (2018)

Item	Content
Total number of snapshots	48,000
Sampling frequency	400 Hz
Window (block length)	Hamming window with a length of 4,096 snapshots
Blocks	19 blocks with a block length of 4,800 snapshots each
Overlap length	2,400 snapshots (50% overlap)
Resolution frequency	$400 \text{ Hz} / 4800 = 0.0833 \text{ Hz} = 0.01 U_{\text{ref}} / H$
Nyquist frequency	$400 \text{ Hz} / 2 = 200 \text{ Hz} = 25 U_{\text{ref}} / H$

6.4.2 SPOD spectrum and turbulent fluctuation patterns

Figure 6.7 presents the SPOD spectrum, showing the results of 19 eigenvalues (single-sided spectrum) at all discrete frequencies. Each eigenvalue (point) in the figure corresponds to an SPOD mode. The modes can be understood by examining the real and imaginary parts of the eigenfunctions or by watching the animation created by $\text{Re}(\boldsymbol{\psi}_{f,n} e^{i2\pi ft})$. The animation process is approximately $\text{Re}(\boldsymbol{\psi}_{f,n}) \rightarrow -\text{Im}(\boldsymbol{\psi}_{f,n}) \rightarrow -\text{Re}(\boldsymbol{\psi}_{f,n}) \rightarrow \text{Im}(\boldsymbol{\psi}_{f,n}) \rightarrow \text{Re}(\boldsymbol{\psi}_{f,n})$. For example, Figure 6.8 provides the streamlines for the seven selected modes, which correspond to the seven boxed eigenvalues in Figure 6.7. Modes A–B2 are chosen because they show large energy in Figure 6.7, while modes C–D3 are chosen according to their importance to pollutant removal at the roof level, as confirmed by the SPOD co-spectrum in Figures 6.10 and 6.11, which will be explained later. These modes are chosen according to their importance to pollutant removal at the roof level, as confirmed by the SPOD co-spectrum, which will be explained later. Please note that the modes, especially at high frequencies, change gradually with the frequency, so many modes show similar shapes. In this study, only several representative modes are visualised and analysed, as observing modes with similar energy at similar frequencies will not qualitatively change the conclusions.

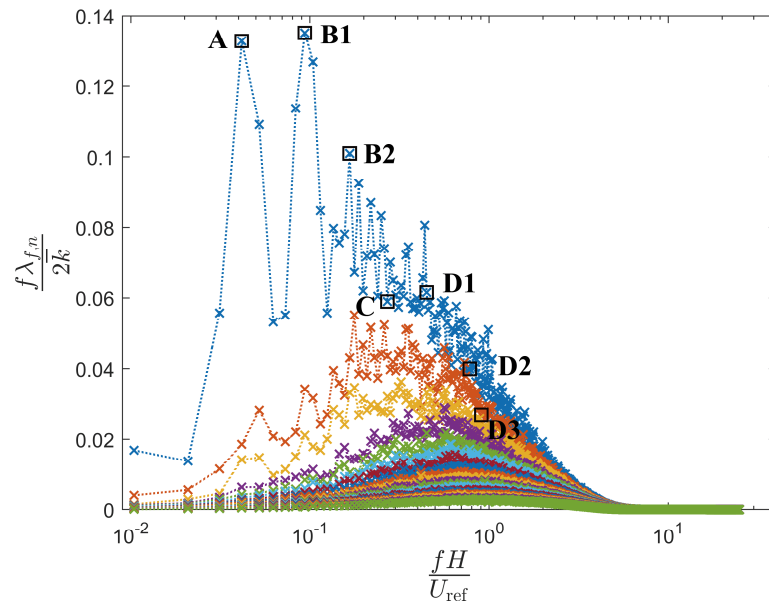
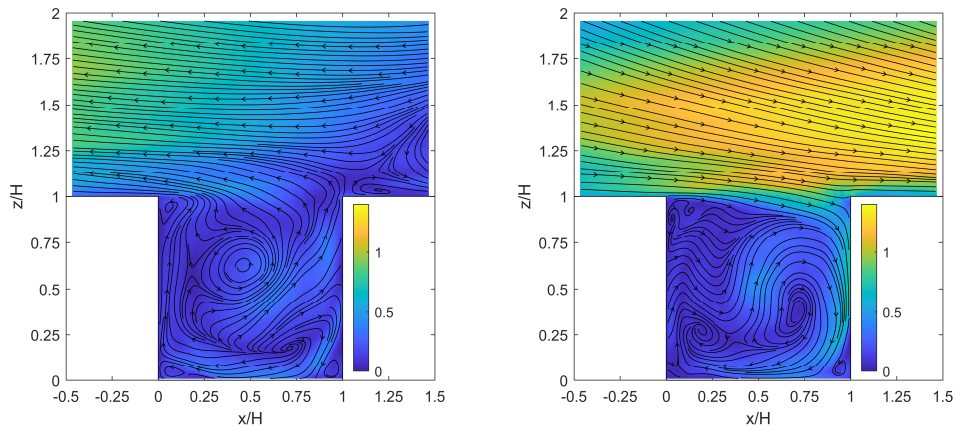
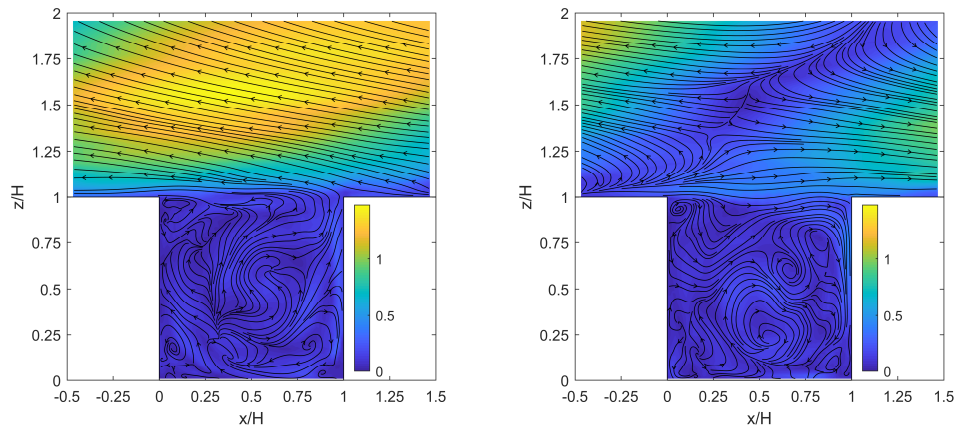


Figure 6.7 SPOD spectrum (single-sided). The nondimensional eigenvalues are plotted versus the nondimensional frequency. At each discrete frequency, 19 eigenvalues are numbered from largest to smallest as $n = 1, 2, \dots, 19$, distinguished by colours. Each eigenvalue corresponds to a complex eigenfunction, depicting a certain spatial distribution of the velocity. For instance, the eigenfunctions of the seven selected modes, whose eigenvalues are boxed, are shown in Figure 6.8.

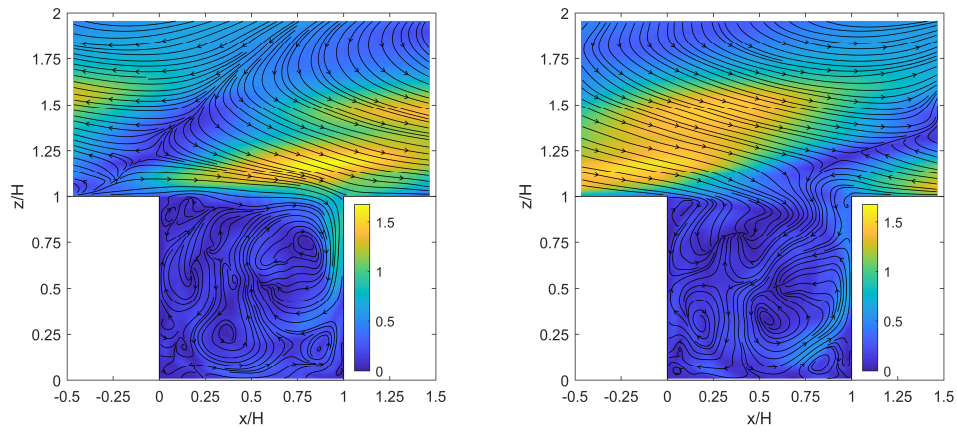


(a) Real (left) and imaginary (right) parts of the eigenfunction of mode A ($fH/U_{\text{ref}} = 0.0417$, $n = 1$)

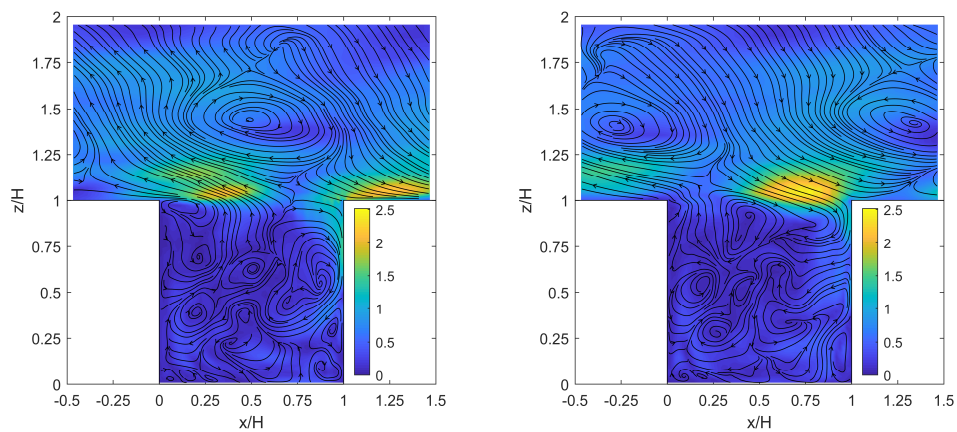
Figure 6.8 (continued on the next page)



(b) Real (left) and imaginary (right) parts of the eigenfunction of mode B1 ($fH/U_{\text{ref}} = 0.0938$, $n = 1$)

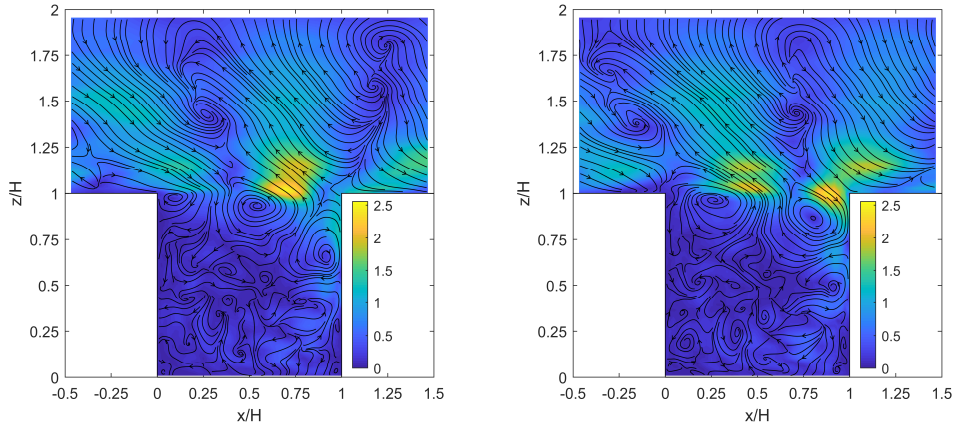


(c) Real (left) and imaginary (right) parts of the eigenfunction of mode B2 ($fH/U_{\text{ref}} = 0.1667$, $n = 1$)

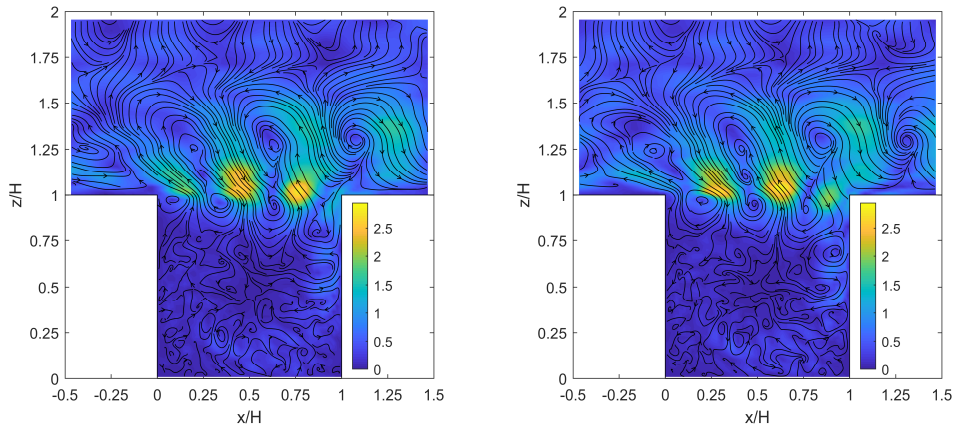


(d) Real (left) and imaginary (right) parts of the eigenfunction of mode C ($fH/U_{\text{ref}} = 0.2708$, $n = 1$)

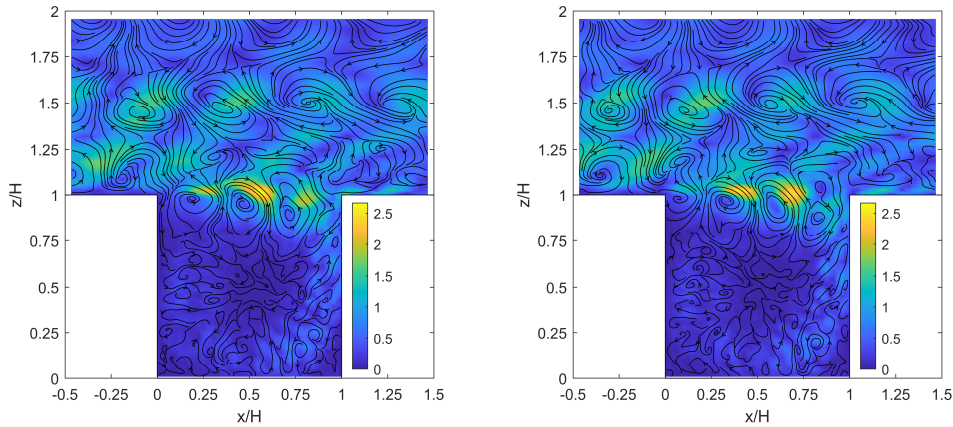
Figure 6.8 (continued on the next page)



(e) Real (left) and imaginary (right) parts of the eigenfunction of mode D1 ($fH/U_{\text{ref}} = 0.4479$, $n = 1$)



(f) Real (left) and imaginary (right) parts of the eigenfunction of mode D2 ($fH/U_{\text{ref}} = 0.7813$, $n = 1$)



(g) Real (left) and imaginary (right) parts of the eigenfunction of mode D3 ($fH/U_{\text{ref}} = 0.9062$, $n = 2$)

Figure 6.8 Eigenfunctions for the seven selected modes. The colour shows the magnitude of the vector. The fluctuation pattern is understood by watching the animation of $\text{Re}(\boldsymbol{\psi}_{f,n} e^{i2\pi ft})$, one cycle of which is approximately $\text{Re}(\boldsymbol{\psi}_{f,n}) \rightarrow -\text{Im}(\boldsymbol{\psi}_{f,n}) \rightarrow -\text{Re}(\boldsymbol{\psi}_{f,n}) \rightarrow \text{Im}(\boldsymbol{\psi}_{f,n}) \rightarrow \text{Re}(\boldsymbol{\psi}_{f,n})$.

Previous studies (Lee et al., 2011; Michioka et al., 2011; Takimoto et al., 2013) have measured the length scale of the coherent structures over a two-dimensional canyon using the two-point correlation coefficient calculated from the streamwise fluctuation velocity. The streamwise length scale was measured by the maximum streamwise distance between the two points where the chosen threshold (0.3 or 0.4) of the two-point correlation coefficient occurred. The results of the streamwise length scale at $z \approx 2H$ were approximately $9H$ (Lee et al., 2011), $7H$ (Michioka et al., 2011), and $6H$ (Takimoto et al., 2013). Therefore, the time scale of the coherent structures can be estimated as 6–9 H/U_{ref} , which roughly corresponds to the normalised frequency of modes B1 and B2 in Figure 6.7, with high mode energy. These large-scale coherent structures have been found to strongly affect pollutant removal (Han et al., 2018; Michioka et al., 2011; Michioka and Sato, 2012). Judging by the figures in Kanda (2006) and Michioka et al. (2011), the instantaneous coherent structures of low-momentum fluid have a streaky shape along the streamwise direction. As an illustration, mode B2 shows a large-scale coherent structure that is sufficiently low near the roof level, as illustrated in Figure 6.8 (c). When this large-scale pattern passes over the canyon, the fluctuation enters the canyon along the windward wall, strengthening or weakening the principal recirculation within the canyon. However, according to Michioka et al. (2011), if the coherent structures in the external flow do not expand to the roof level, they have little influence on the pollutant within the canyon, which is the case for mode B1 in Figure 6.8 (b).

Another large-scale structure detected by SPOD was named mode A. In this simulation, periodic boundary conditions were imposed on the inlet and outlet, which resulted in an inevitable periodic fluctuation, whose period could be estimated by the streamwise length of the simulation domain ($= 20H$) divided by the prevailing velocity ($\approx U_{\text{ref}}$). This period corresponds to the frequency of mode A ($\approx U_{\text{ref}}/20H$). Therefore, unlike modes B1 or B2, mode A is not the physical consequence of the flow passing through the canyon but is due to the artificial simulation setting. However, it can be regarded as a representation of the slow change in the approaching flow due to external conditions, such as meteorological variations. Although the variation in the approaching flow is an artifact, the induced flow around the target canyon is not. The eigenfunction of mode A in Figure 6.8 (a) shows that this pattern affects the flow similar to mode B2 by strengthening or weakening the principal recirculation within the canyon.

As shown in Figures 6.8 (e), (f), and (g), modes D1, D2, and D3 in the frequency range from $U_{\text{ref}}/2H$ to U_{ref}/H are considered to represent the Kelvin–Helmholtz instabilities, because they illustrate vortices in the shear layer. The frequencies also fit well with the time-scale of the Kelvin–Helmholtz instabilities indicated by Cui et al. (2004). These

vortices generated at the roof level move downstream and enter the canyon following the principal recirculation within the canyon. Previous studies have indicated that Kelvin–Helmholtz instabilities render intermittent pollutant dispersion (Cui et al., 2004; Letzel et al., 2008). These three modes show similar Kelvin–Helmholtz vortices of different sizes.

It is also interesting to note that all the modes D1–D3 also show some vortices in the external flow upon the canyon, with a similar scale as the Kelvin–Helmholtz vortices. One possible interpretation is that these outside vortices are generated by the free ends of the roughness bars in the upstream because they appear to be generated upstream outside the sampling domain. These external vortices in the same scale in the region called roughness sublayer. Castro et al. (2006) showed that the dominant length scales in the roughness sublayer are of the same order as the canyon length scale. Because they share the same time scale with the Kelvin–Helmholtz vortices, they are captured by the same modes with the Kelvin–Helmholtz vortices. In the next chapter, we will show that the spanwise scales of these external vortices are highly different from the Kelvin–Helmholtz vortices, which gives a way to separate these two types of vortices in different modes.

If the information provided by the two types of modes are combined, we can see that the Kelvin–Helmholtz vortices travel with the principal recirculation, while the fluctuation caused by the external large-scale coherent structures directly strengthens or weakens the principal recirculation. This implies the existence of nonlinear interactions between the large- and small-scale structures, which was detected statistically by Blackman and Perret (2016), and that the external large-scale coherent structures may play a role in triggering and transporting the Kelvin–Helmholtz vortices at the roof level. The modes in the current study show such a process more intuitively rather than in an abstract manner.

In addition, mode C illustrated in Figure 6.8 (d) shows both features of the large-scale coherent structures and the Kelvin–Helmholtz instabilities, which can be regarded as a smooth transition between these two physical mechanisms. The frequency of mode C is also shown in Figure 6.7. This frequency is regarded as the boundary between the large-scale coherent structures and Kelvin–Helmholtz instabilities. At frequencies larger than U_{ref}/H , that is, the right side of mode D3, the energy quickly fades.

In this spectral analysis, only the leading modes with $n = 1$ or 2 were observed. Theoretically, the higher modes with higher n can show minor fluctuation patterns at each frequency, which are different from the leading modes. However, observations of

the higher modes are not suggested. As a common weakness of POD-based methods, POD is based on second-order correlation, and higher-order correlations are ignored (Taira et al., 2017). The higher-order relationships provided by the fluid dynamics were not detected by POD and were excessively decomposed into multiple modes. The higher modes are bounded considerably by spatial orthogonality with the modes ahead. Note that the spatial orthogonality of POD modes is a mathematical requirement rather than a physical one; therefore, the fluctuation patterns depicted by the higher modes may be unphysical. They are, therefore, difficult to explain unless the higher-order relationships are known beforehand. Although POD-based methods are now widely used in many fields, owing to their effectiveness in detecting the most characteristic features of turbulence, few studies have made good use of the higher modes.

6.4.3 *Ejection and sweep events at the roof level*

Quadrant analysis, employed to inspect the momentum exchange mechanism in many studies (Cheng and Liu, 2011; Cui et al., 2004; Kikumoto and Ooka, 2012), is also feasible for SPOD modes. Figure 6.9 shows the Lissajous curves between the streamwise and vertical components of the seven selected modes at the roof-height centre point of the target canyon ($x/H = 0.5$, $z/H = 1$); that is, the streamwise components are plotted versus the vertical components. The streamwise or vertical component of a mode refers to the streamwise or vertical component of the periodic vector function $a_{f,n} \boldsymbol{\Psi}_{f,n}(\mathbf{x}) e^{i2\pi ft}$, which is a part of the fluctuation velocity (see the decomposition form of SPOD). With the exception of mode B1, Figure 6.9 illustrates six harmonic motions oscillating between ejection and sweep. The shapes of these Lissajous curves indicate a $\pi/2$ – $3\pi/2$ phase difference between the streamwise and vertical components, resulting in a negative correlation and negative Reynolds shear stress. It should be noted that the inclination angles of these shapes differed. The ejection and sweep events caused by the Kelvin–Helmholtz instabilities (modes D1–D3) have relatively strong vertical components and weak streamwise components, whereas those caused by the large-scale coherent structures (modes A and B2) have relatively strong streamwise components and weak vertical components. The performance of mode C appears between them. This difference may affect pollutant removal efficiency. For the same intensity, the ejection events with stronger vertical components are expected to boost pollutant removal.

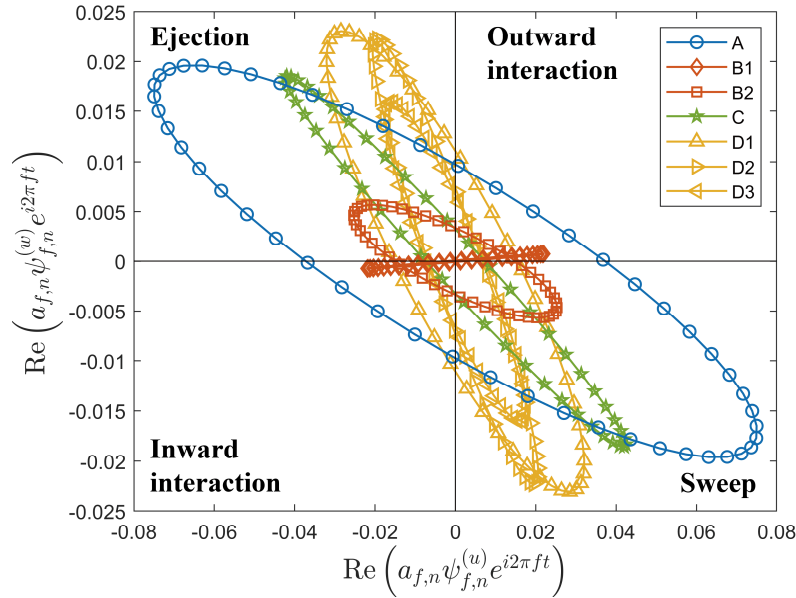


Figure 6.9 Lissajous curves between the streamwise and vertical components of the seven selected modes at the roof-height centre point ($x/H = 0.5$, $z/H = 1$).

Similar to mode B1, the ejection-sweep circle is not apparent for all modes. This can be examined using the SPOD co-spectrum, defined by Eq. (6.5). In Fourier analysis, the co-spectrum denotes the in-phase component of the cross spectrum. A large positive value in the co-spectrum indicates high signal amplitudes and a phase difference near 0, implying strong outward and inward interaction events. In contrast, a large negative value indicates high signal amplitudes and phase difference near π , implying strong ejection and sweep events.

Figure 6.10 (a) shows the single-sided SPOD co-spectrum between the streamwise and vertical fluctuation velocities at the roof-height centre point ($x/H = 0.5$, $z/H = 1$). Most of the modes show negative values in the SPOD co-spectrum, implying that they all contribute to the ejection and sweep events at this point, but the extent differs. The ejection and sweep events are caused by both the large-scale coherent structures and Kelvin–Helmholtz instabilities, while the latter seems to be more important. A similar co-spectrum shape can also be found in Michioka and Sato (2012). However, using SPOD, the specific fluctuation patterns corresponding to the energy values in the co-spectrum can be observed. This finding is also supported by Jaroslowski et al. (2020), who found that sweep and ejection events are mainly due to the dynamical contribution of small-scale coherent structures using a spatial filter to distinguish the large- and small-scale coherent structures. Moreover, within the range of the large-scale coherent

structures, mode A causes stronger ejection and sweep events than modes B1 and B2, indicating that the effect of the large-scale structures caused by the canyon roughness is quite limited, whereas the change in the approaching flow caused by the external conditions plays a relatively larger role. Similar results can also be found in Figure 6.10 (b), where the SPOD co-spectrum is spatially integrated along the roof-height line ($0 < x/H < 1, z/H = 1$). This provides a more comprehensive understanding of the ejection and sweep events occurring at the roof level.

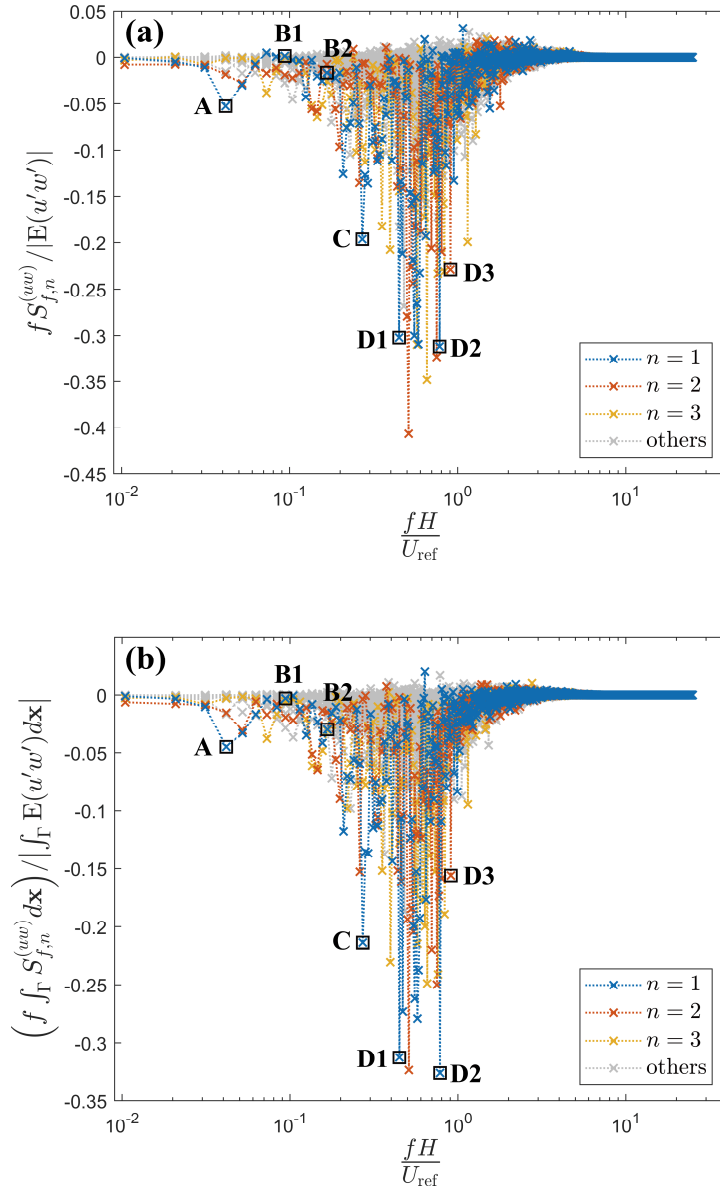


Figure 6.10 SPOD co-spectrum (single-sided) between the streamwise and vertical fluctuation velocity (a) at the roof-height centre point ($x/H = 0.5, z/H = 1$), (b) integrated spatially along the roof-height line Γ ($0 < x/H < 1, z/H = 1$).

Although ejection and sweep events strongly affect pollutant removal, velocity decomposition alone does not explain the pollutant removal mechanism because the direction of the fluctuation velocity is undetermined. The fluctuation patterns are deemed zero-mean sinusoidal functions by SPOD, indicating that a sweep will chronologically follow an ejection. The discussion of pollutant removal is invalid without discussing the phase consistency between the fluctuation pattern and the concentration, which is the target of the next section.

6.5 Spectral analysis for the pollutant removal

In this section, the SPOD co-spectrum defined in Eq. (6.9) is applied in the canyon case to elucidate the relationship between turbulent fluctuation and pollutant removal. Similar to velocity discussed in Section 3.3, the concentration signals were initially divided into blocks with the identical parameters, listed in Table 6.2. Then, Fourier transformation was performed on the concentration signals, and SPOD co-spectrum was calculated within each block. The SPOD co-spectrum for the whole-length signal was then estimated by averaging the co-spectra over all blocks.

Figure 6.11 (a) shows the single-sided SPOD co-spectrum between the vertical fluctuating velocity and concentration at the roof-height centre point ($x/H = 0.5, z/H = 1$). This co-spectrum is again analysed as the velocity spectrum. The positive values in this SPOD co-spectrum indicate that the phase difference between the vertical components and concentration ranges from $-\pi/2$ to $\pi/2$. Thus, the vertical components and concentration are positively correlated, which is consistent with previous studies (Cheng and Liu, 2011; Cui et al., 2004; Kikumoto and Ooka, 2012). If the magnitude of these values is observed, the SPOD co-spectrum shows a highly similar shape to that in Figure 6.10(a). A similar shape of the co-spectrum can also be found in Michioka and Sato (2012). Given the positive correlation between the vertical components and concentration, it can be concluded that the ejections caused by both the large-scale coherent structures and Kelvin–Helmholtz instabilities are highly correlated to pollutant removal. The spatially integrated SPOD co-spectrum in Figure 6.11 (b) also supports the same conclusion.

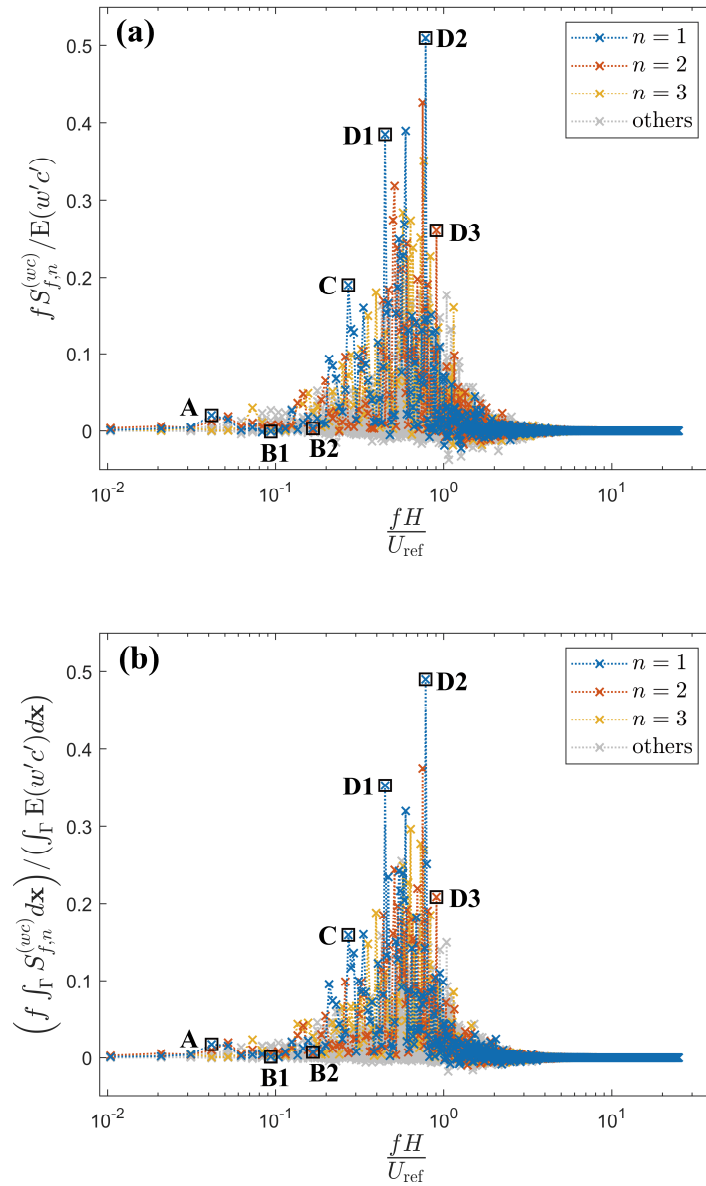


Figure 6.11 SPOD co-spectrum (single-sided) between the vertical fluctuating velocity and concentration (a) at the roof-height centre point ($x/H = 0.5, z/H = 1$), (b) integrated spatially along the roof-height line Γ ($0 < x/H < 1, z/H = 1$).

As shown in Eq. (6.10), the SPOD co-spectrum can also be considered as a decomposition of the vertical turbulent mass flux. Reconstructing the parts of interest will approximate the amount of pollutants removed by large-scale coherent structures or Kelvin–Helmholtz instabilities. This can also be compared with the reconstruction of the TKE. The percentage values are provided in Table 6.3, where the SPOD co-spectrum in Figure 6.11 (b) and SPOD spectrum in Figure 6.7 are the integrands. The frequency of mode C was used as the boundary of the frequency range, and all modes within the frequency range were considered for the integrations. Within the frequency range of $0 <$

$fH/U_{\text{ref}} < 0.27$, which contains large-scale coherent structures, the modes accounted for 51% of the TKE, while they only contributed 27% of the vertical turbulent mass flux at the roof level. In contrast, the modes within the frequency range of $0.27 < fH/U_{\text{ref}} < 1$ containing the Kelvin–Helmholtz instabilities only account for 33% of the TKE, but they contribute 63% of the vertical turbulent mass flux at the roof level. The large TKE of the large-scale coherent structures indicates that they can be easily observed on the instantaneous snapshots of the velocity field (Michioka et al., 2011; Michioka and Sato, 2012), while the waves of the Kelvin–Helmholtz instabilities and their contribution to pollutant removal require closer observation over a certain period (Cui et al., 2004). Note that, in this rough estimation of TKE and pollutant removal, the modes are classified according to the frequency only but not to the mode number; therefore, irrelevant modes may be involved in the integrations. However, the modes of large-scale coherent structures account for the vast majority of TKE at low frequencies, judging by the SPOD spectrum, and the modes of Kelvin–Helmholtz instabilities account for the majority of pollutant removal at high frequencies, judging by the SPOD co-spectra. This conclusion will not qualitatively change, even if irrelevant modes are involved. However, the current analysis does not take the nonlinear interactions (Blackman and Perret, 2016) into account. Based on the shapes of the fluctuations of the modes, the external large-scale coherent structures play a role in triggering and transporting the small-scale turbulence at the roof level, which may indirectly help with the pollutant removal.

Table 6.3 Percentage of vertical turbulent mass flux at the roof level and whole-field TKE. These percentage values are calculated by integrating the SPOD co-spectrum in Figure 6.11 (b) or the SPOD spectrum in Figure 6.7 within a specific frequency range.

Frequency range	Percentage of the vertical turbulent mass flux at the roof level	Percentage of the whole-field TKE
$0 < fH/U_{\text{ref}} < 0.27$	27%	51%
$0.27 < fH/U_{\text{ref}} < 1$	63%	33%
$fH/U_{\text{ref}} > 1$	10%	16%

More intuitively, Figure 6.12 shows the spatial-temporal variation in the normalised concentration and vertical components of the selected modes on the roof-height line ($0 < x/H < 1$, $z/H = 1$). This intermittent distribution of the concentration in Figure 6.12 (a), reported in previous studies (Cui et al., 2004; Walton and Cheng, 2002), agrees well with the shapes of the vertical components of modes D1 and D2 in Figures 6.12 (d) and (e), respectively, which represent the Kelvin–Helmholtz instabilities, while its relationship with modes A and B2 in Figures 6.12 (b) and (c), respectively, representing large-scale coherent structures, is ambiguous. The performance of mode C in Figure 6.12 (d) appears to fall between the performances these two groups of modes.

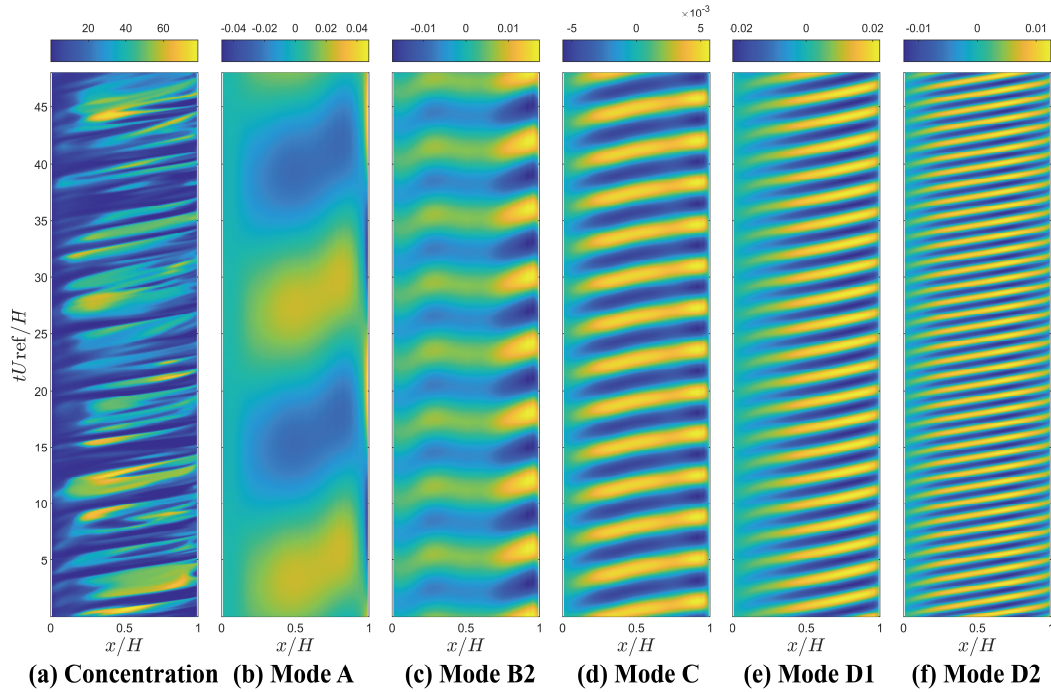


Figure 6.12 Spatial-temporal variation in (a) normalised concentration, (b) vertical component of mode A, (c) vertical component of mode B2, (d) vertical component of mode D1, (e) vertical component of mode D2 on the roof-height line ($0 < x/H < 1, z/H = 1$) from nondimensional time $tU_{ref}/H = 0$ to $tU_{ref}/H = 48$.

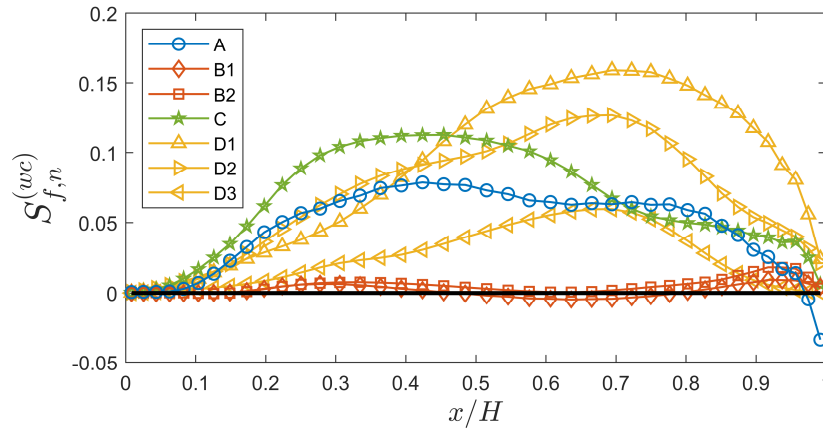


Figure 6.13 Spatial variation of the SPOD co-spectrum values for the seven selected modes along the roof-height line ($0 < x/H < 1, z/H = 1$). These results indicate that different flow patterns provide pollutant removal at different spatial positions. The co-spectrum values integrated over all the frequencies and summed over all the mode numbers will equal to the vertical turbulent mass flux shown in Figure 6.6.

Finally, note that the oblique stripes in Figure 6.12 (e) are more skewed towards $x/H > 0.5$, than those in Figure 6.12 (f), indicating that different modes may contribute differently to pollutant removal at different spatial locations. This can be examined by the spatial variation of the SPOD co-spectrum values shown in Figure 6.13. Although the modes D1 to D3 correspond to the Kelvin–Helmholtz instabilities, the spatial distributions of the pollutant removal amount slightly differ, which might be attributed to their different vortex shapes. Mode A facilitates pollutant removal, but a small amount of the pollutant returns into the canyon near the windward wall. Although modes B1 and B2 show poor performance in pollutant removal at the canyon centre, it plays a role near the windward wall, although it is very limited. It is natural that the turbulent structures at close frequencies exhibit basically the same shape but different details. The details captured in this study show the effectiveness of SPOD in identifying turbulent structures and analysing the mass transfer mechanism. Further studies are suggested on the differences between the modes to obtain deeper insights.

6.6 Summary

In this study, the SPOD technique was applied to decompose the velocity field of a two-dimensional street canyon. The SPOD modes depicting the large-scale coherent structures and Kelvin–Helmholtz instabilities were extracted and visualised. The Kelvin–Helmholtz instabilities were depicted as a series of vortices, which were generated at the roof level, and entered the canyon following the principal recirculation, while the fluctuation caused by the external large-scale coherent structures directly strengthened or weakened the principal recirculation. These results also suggest the presence of nonlinear interactions between the large- and small-scale structures (Blackman and Perret, 2016), and that the external large-scale coherent structures may play a role in triggering and transporting the Kelvin–Helmholtz vortices at the roof level.

The ejection events and pollutant removal were quantitatively analysed using the newly defined SPOD co-spectra to understand their relationships with the turbulent fluctuation patterns. Both the Kelvin–Helmholtz instabilities and large-scale coherent structures can cause ejection and sweep events at the roof level, thus contributing to pollutant removal. However, the former contributed to stronger ejection and sweep events with stronger vertical components. As Michioka et al. (2011) stated, not all large-scale coherent structures contribute to the ejection and sweep events if they do not expand down to the roof level. Therefore, not all modes depicting large-scale coherent structures were found providing obvious ejection and sweep events at the roof level. In addition, the results also revealed that large-scale structures caused by external conditions contribute to stronger

ejection and sweep events than those caused by canyon roughness.

The reconstruction provides quantitative estimations of ejection events and pollutant removal due to various flow mechanisms. The results revealed that the Kelvin–Helmholtz instabilities accounted for a small percentage of TKE, but they contributed most to the vertical turbulent mass flux at the roof level. In contrast, the large-scale coherent structures occupied a large proportion of the TKE, while they contributed less to the vertical turbulent mass flux. The intermittent concentration fluctuation fits better with the time scale of the Kelvin–Helmholtz instabilities. Therefore, the exchange process is dominated by the Kelvin–Helmholtz vortices in the shear layer. Although large-scale coherent structures provide less pollutant removal numerically, they may indirectly contribute to pollutant removal by intensifying the turbulence and transporting the Kelvin–Helmholtz vortices, judging by the appearance of the modes.

Finally, we showed that the fluctuations illustrated by different modes may contribute differently to pollutant removal at different spatial locations. This depends on the nature of turbulent structures. Even for the modes that were classified as the same type, a slight difference was observed in the SPOD analysis. Further studies are suggested on the detailed differences between the modes to obtain deeper insights.

This study might be the first to extract turbulent structures from instantaneous fields with vivid animations that can be directly related to already known physical mechanisms in street canyon flow. This makes it possible to quantitatively estimate and compare the pollutant removal contributed by each mechanism. Our findings offer insights that could improve our understanding of fluid mechanisms and inertially driven pollutant removal from street canyons. Furthermore, more quantitative analyses can be performed based on our results.

A potential weakness of the present study is that the time signal was only sampled from a two-dimensional plane. However, coherent structures also exist along the spanwise direction (Kanda et al., 2004; Lee et al., 2011), contributing to pollutant removal (Michioka and Sato, 2012). The problem that the spanwise fluctuations were not considered also causes the incomplete extracting of the Kelvin–Helmholtz vortices. As shown in Figures 6.8 (e–g), the external vortices in the roughness sublayer were also captured in the same modes with the Kelvin–Helmholtz vortices. They share similar time scales but may largely vary in spanwise scales. Although the computation cost might be considerable, the discrete Fourier transformation along the homogeneous spanwise direction during SPOD is considered feasible and will be discussed in the future.

Reference

- Barbano, F., Brattich, E., Di Sabatino, S., 2021. Characteristic Scales for Turbulent Exchange Processes in a Real Urban Canopy. *Boundary-Layer Meteorol.* 178, 119–142. <https://doi.org/10.1007/s10546-020-00554-5>
- Blackman, K., Perret, L., 2016. Non-linear interactions in a boundary layer developing over an array of cubes using stochastic estimation. *Phys. Fluids* 28, 095108. <https://doi.org/10.1063/1.4962938>
- Blackman, K., Perret, L., Savory, E., 2018. Effects of the Upstream-Flow Regime and Canyon Aspect Ratio on Non-linear Interactions Between a Street-Canyon Flow and the Overlying Boundary Layer. *Boundary-Layer Meteorol.* 169, 537–558. <https://doi.org/10.1007/s10546-018-0378-y>
- Castro, I.P., Cheng, H., Reynolds, R., 2006. Turbulence over urban-type roughness: Deductions from wind-tunnel measurements. *Boundary-Layer Meteorol.* 118, 109–131. <https://doi.org/10.1007/s10546-005-5747-7>
- Cheng, W.C., Liu, C.H., 2011. Large-Eddy Simulation of Flow and Pollutant Transports in and Above Two-Dimensional Idealized Street Canyons. *Boundary-Layer Meteorol.* 139, 411–437. <https://doi.org/10.1007/s10546-010-9584-y>
- Cheng, W.C., Liu, C.H., Leung, D.Y.C., 2008. Computational formulation for the evaluation of street canyon ventilation and pollutant removal performance. *Atmos. Environ.* 42, 9041–9051. <https://doi.org/10.1016/j.atmosenv.2008.09.045>
- Cintolesi, C., Pulvirenti, B., Sabatino, S. Di, 2021. Large-Eddy Simulations of Pollutant Removal Enhancement from Urban Canyons. *Boundary-Layer Meteorol.* 1–26. <https://doi.org/10.1007/s10546-021-00610-8>
- Coceal, O., Dobre, A., Thomas, T.G., Belcher, S.E., 2007. Structure of turbulent flow over regular arrays of cubical roughness. *J. Fluid Mech.* 589, 375–409. <https://doi.org/10.1017/S002211200700794X>
- Cui, Z., Cai, X., J. Baker, C., 2004. Large-eddy simulation of turbulent flow in a street canyon. *Q. J. R. Meteorol. Soc.* 130, 1373–1394. <https://doi.org/10.1256/qj.02.150>
- Di Bernardino, A., Monti, P., Leuzzi, G., Querzoli, G., 2018. Pollutant fluxes in two-dimensional street canyons. *Urban Clim.* 24, 80–93. <https://doi.org/10.1016/j.uclim.2018.02.002>
- Han, B.S., Baik, J.J., Kwak, K.H., Park, S.B., 2018. Large-eddy simulation of reactive pollutant exchange at the top of a street canyon. *Atmos. Environ.* 187, 381–389. <https://doi.org/10.1016/j.atmosenv.2018.06.012>
- Inagaki, A., Kanda, M., 2010. Organized structure of active turbulence over an array of cubes within the logarithmic layer of atmospheric flow. *Boundary-Layer Meteorol.* 135, 209–228. <https://doi.org/10.1007/s10546-010-9477-0>
- Issa, R.I., 1986. Solution of the implicitly discretised fluid flow equations by operator-splitting. *J. Comput. Phys.* 62, 40–65. [https://doi.org/10.1016/0021-9991\(86\)90099-9](https://doi.org/10.1016/0021-9991(86)90099-9)
- Jaroslawski, T., Savory, E., Perret, L., 2020. Roof-level large- and small-scale coherent structures in a street canyon flow. *Environ. Fluid Mech.* 20, 739–763. <https://doi.org/10.1007/s10652-019-09721-w>
- Kanda, M., 2006. Large-eddy simulations on the effects of surface geometry of building arrays on turbulent organized structures. *Boundary-Layer Meteorol.* 118, 151–168. <https://doi.org/10.1007/s10546-005-5294-2>
- Kanda, M., Moriwaki, R., Kasamatsu, F., 2004. Large-eddy simulation of turbulent organized structures within and above explicitly resolved cube arrays. *Boundary-Layer Meteorol.* 112, 343–368. <https://doi.org/10.1023/B:BOUN.0000027909.40439.7c>
- Kastner-Klein, P., Berkowicz, R., Britter, R., 2004. The influence of street architecture on flow and dispersion in street canyons. *Meteorol. Atmos. Phys.* 87, 121–131. <https://doi.org/10.1007/s00703-003-0065-4>
- Kikumoto, H., Ooka, R., 2012. A numerical study of air pollutant dispersion with

- bimolecular chemical reactions in an urban street canyon using large-eddy simulation. *Atmos. Environ.* 54, 456–464. <https://doi.org/10.1016/j.atmosenv.2012.02.039>
- Klein, P.M., Galvez, J.M., 2015. Flow and turbulence characteristics in a suburban street canyon. *Environ. Fluid Mech.* 15, 419–438. <https://doi.org/10.1007/s10652-014-9352-5>
- Lee, J.H., Sung, H.J., Krogstad, P.Å., 2011. Direct numerical simulation of the turbulent boundary layer over a cube-roughened wall. *J. Fluid Mech.* 669, 397–431. <https://doi.org/10.1017/S0022112010005082>
- Letzel, M.O., Krane, M., Raasch, S., 2008. High resolution urban large-eddy simulation studies from street canyon to neighbourhood scale. *Atmos. Environ.* 42, 8770–8784. <https://doi.org/10.1016/j.atmosenv.2008.08.001>
- Liu, C.H., Wong, C.C.C., 2014. On the pollutant removal, dispersion, and entrainment over two-dimensional idealized street canyons. *Atmos. Res.* 135–136, 128–142. <https://doi.org/10.1016/j.atmosres.2013.08.006>
- Louka, P., Belcher, S.E., Harrison, R.G., 2000. Coupling between air flow in streets and the well-developed boundary layer aloft. *Atmos. Environ.* 34, 2613–2621. [https://doi.org/10.1016/S1352-2310\(99\)00477-X](https://doi.org/10.1016/S1352-2310(99)00477-X)
- Michioka, T., Sato, A., 2012. Effect of Incoming Turbulent Structure on Pollutant Removal from Two-Dimensional Street Canyon. *Boundary-Layer Meteorol.* 145, 469–484. <https://doi.org/10.1007/s10546-012-9733-6>
- Michioka, T., Sato, A., Takimoto, H., Kanda, M., 2011. Large-Eddy Simulation for the Mechanism of Pollutant Removal from a Two-Dimensional Street Canyon. *Boundary-Layer Meteorol.* 138, 195–213. <https://doi.org/10.1007/s10546-010-9556-2>
- Oke, T.R., 1987. *Boundary Layer Climates*, 2nd Editio. ed, Boundary Layer Climates. Routledge, London. <https://doi.org/10.4324/9780203407219>
- Park, S.J., Kim, J.J., Kim, M.J., Park, R.J., Cheong, H. Bin, 2015. Characteristics of flow and reactive pollutant dispersion in urban street canyons. *Atmos. Environ.* 108, 20–31. <https://doi.org/10.1016/j.atmosenv.2015.02.065>
- Pavageau, M., Schatzmann, M., 1999. Wind tunnel measurements of concentration fluctuations in an urban street canyon, in: *Atmospheric Environment*. Pergamon, pp. 3961–3971. [https://doi.org/10.1016/S1352-2310\(99\)00138-7](https://doi.org/10.1016/S1352-2310(99)00138-7)
- Perret, L., Rivet, C., 2013. Dynamics of a turbulent boundary layer over cubical roughness elements: Insight from PIV measurements and POD analysis, in: *Proceedings of Eighth International Symposium on Turbulence and Shear Flow Phenomena*. Poitiers, France.
- Roe, P.L., 1986. Characteristic-Based Schemes for the Euler Equations. *Annu. Rev. Fluid Mech.* 18, 337–365. <https://doi.org/10.1146/annurev.fl.18.010186.002005>
- Salizzoni, P., Soulhac, L., Mejean, P., 2009. Street canyon ventilation and atmospheric turbulence. *Atmos. Environ.* 43, 5056–5067. <https://doi.org/10.1016/j.atmosenv.2009.06.045>
- Schmidt, O.T., Colonius, T., 2020. Guide to Spectral Proper Orthogonal Decomposition. *AIAA J.* 58, 1023–1033. <https://doi.org/10.2514/1.J058809>
- Smagorinsky, J., 1963. General circulation experiments with the primitive equations. *Mon. Weather Rev.* 91, 99–164. [https://doi.org/10.1175/1520-0493\(1963\)091<0099:gcewtp>2.3.co;2](https://doi.org/10.1175/1520-0493(1963)091<0099:gcewtp>2.3.co;2)
- Solazzo, E., Britter, R.E., 2007. Transfer processes in a simulated urban street canyon. *Boundary-Layer Meteorol.* 124, 43–60. <https://doi.org/10.1007/s10546-007-9176-7>
- Spalding, D.B., 1962. A new analytical expression for the drag of a flat plate valid for both the turbulent and laminar regimes. *Int. J. Heat Mass Transf.* 5, 1133–1138. [https://doi.org/10.1016/0017-9310\(62\)90189-8](https://doi.org/10.1016/0017-9310(62)90189-8)
- Taira, K., Brunton, S.L., Dawson, S.T.M., Rowley, C.W., Colonius, T., McKeon, B.J., Schmidt, O.T., Gordeyev, S., Theofilis, V., Ukeiley, L.S., 2017. Modal Analysis of Fluid Flows: An Overview. *AIAA J.* 55, 4013–4041. <https://doi.org/10.2514/1.J056060>
- Takimoto, H., Inagaki, A., Kanda, M., Sato, A., Michioka, T., 2013. Length-Scale

- Similarity of Turbulent Organized Structures over Surfaces with Different Roughness Types. *Boundary-Layer Meteorol.* 147, 217–236. <https://doi.org/10.1007/s10546-012-9790-x>
- The OpenFOAM Foundation Ltd, 2020. OpenFOAM | Free CFD Software | The OpenFOAM Foundation [WWW Document]. URL <https://openfoam.org/> (accessed 1.16.21).
- Tominaga, Y., Stathopoulos, T., 2011. CFD modeling of pollution dispersion in a street canyon: Comparison between LES and RANS. *J. Wind Eng. Ind. Aerodyn.* 99, 340–348. <https://doi.org/10.1016/j.jweia.2010.12.005>
- Towne, A., Schmidt, O.T., Colonius, T., 2018. Spectral proper orthogonal decomposition and its relationship to dynamic mode decomposition and resolvent analysis. *J. Fluid Mech.* 847, 821–867. <https://doi.org/10.1017/jfm.2018.283>
- Van Driest, E.R., 1956. On Turbulent Flow Near a Wall. *J. Aeronaut. Sci.* 23, 1007–1011. <https://doi.org/10.2514/8.3713>
- Walton, A., Cheng, A.Y.S., 2002. Large-eddy simulation of pollution dispersion in an urban street canyon - Part II: Idealised canyon simulation. *Atmos. Environ.* 36, 3615–3627. [https://doi.org/10.1016/S1352-2310\(02\)00260-1](https://doi.org/10.1016/S1352-2310(02)00260-1)
- Welch, P.D., 1967. The Use of Fast Fourier Transform for the Estimation of Power Spectra: A Method Based on Time Averaging Over Short, Modified Periodograms. *IEEE Trans. Audio Electroacoust.* 15, 70–73. <https://doi.org/10.1109/TAU.1967.1161901>
- Zhang, Y.W., Gu, Z.L., Cheng, Y., Lee, S.C., 2011. Effect of real-time boundary wind conditions on the air flow and pollutant dispersion in an urban street canyon-Large eddy simulations. *Atmos. Environ.* 45, 3352–3359. <https://doi.org/10.1016/j.atmosenv.2011.03.055>

Chapter 7

Analysis of a two-dimensional street canyon flow and mechanism of pollutant removal via SPOD with 2DFT

7.1 Introduction

At the end of Chapter 6, a limitation is pointed out, which inspires us to further consider the spanwise fluctuations in the two-dimensional street canyon. Therefore, this chapter continues the study on the turbulent structures and their relationship to pollutant removal. The research target and objective are the same as those in Chapter 6, but the spanwise performance of the structures are additionally considered, aiming for better decomposition and visualisation.

In the case of the two-dimensional street canyon, coherent structures also exist along the spanwise direction (Jaroslowski et al., 2020; Lee et al., 2011; Volino et al., 2009), and may contribute to pollutant removal. However, the studies are still few. The existing studies mainly focused on general statistics indicators to describe the turbulent structures, e.g., the Reynolds shear stress, fluctuating velocity correlations and integral length scales. Volino et al. (2009) and Lee et al. (2011) calculated the streamwise and spanwise length scales of the turbulence in a boundary layer over a two-dimensional roughness array and compared with those over a smooth wall and over a three-dimensional roughness. The results show that the streamwise length scale was 3–4 times the spanwise length. Michioka and Sato (2012) showed that the spanwise size of the coherent structures of the low-momentum fluid depends on the upwind block configuration. The amount of pollutant removal is also directly related to the size of this coherent structure. Jaroslowski et al. (2019) made a systematic study on how the oncoming boundary-layer flow influences the flow in a horizontal plane at canyon rooftop level. The variation of the two-point correlations and integral length scales in the streamwise and spanwise directions were investigated. It was found that these quantities were strongly affected by the upstream roughness. However, to the best of our knowledge, there has not been a

study that provides specific and intuitive insights for the characteristic spanwise structures.

In the classical POD theory, if the flow field is homogeneous in one or more directions, the spectrum of the eigenvalues becomes continuous and the eigenfunctions become Fourier modes (Aubry et al., 1988). Therefore, combining Fourier transformation with POD may be a better application. Here, the notion of “homogeneous direction” can be either spatial direction or time. The stationary in time is a quite often assumption for the flow process with a sufficient length in time, which provides a relatively broader application scope for combining Fourier transformation in time and POD in space. This kind of spatial and frequency decomposition, termed as SPOD later by Towne et al. (2018), was applied in some fields such as boundary layers (Tutkun and George, 2017), the wake of a wind turbine (Araya et al., 2017), and turbulent jets (Schmidt et al., 2017). In contrast, the assumption of spatial homogeneity is suitable for only a few cases, one of which is the wall layer of a turbulent channel flow, where the two directions horizontal to the wall are usually simulated as periodic and stationary. Derebail Muralidhar et al. (2019) extended POD using Fourier transformation in both the two horizontal directions and time, and applied it to the channel flow as a data reduction technique.

Because there is clear evidence of homogeneous turbulent statistics over the spanwise direction of the two-dimensional street canyon (Bright et al., 2013), decomposing the turbulent field on the spanwise direction by the Fourier modes, the same manner in which the temporal fluctuation is dealt with in SPOD, is considered worth trying. The non-homogeneous streamwise and vertical directions are decomposed classically by POD. This combination, called SPOD with the two-dimensional Fourier transformation (2DFT) in this paper, is applied to elucidate the spatiotemporal structures of the flow within the two-dimensional street canyon. The insights are provided not only for the fluctuation patterns on the streamwise-vertical plane, but also on the spanwise direction.

The simulation and wind tunnel experiment conducted by Michioka et al. (2011) is again referred to in this study when performing the LES for a two-dimensional street canyon. The LES models, simulation conditions, and basic statistical results are reported in Section 7.2. In Section 7.3, the theory and algorithm of SPOD with 2DFT is introduced. The SPOD co-spectrum defined in our previous study is also modified to a 2DFT version. These tools are applied to the street canyon case as the post-processing methods in Sections 7.4 to reveal the relationship between the turbulent fluctuation patterns and pollutant removal. Finally, based on these results, the nonlinear interactions between the large- and small-scale structures are discussed in Section 7.5.

7.2 Large-eddy simulation

7.2.1 Physical models and simulation design

The physical models used in the simulation were identical to the LES in Chapter 6. Please refer to Section 6.2.1 for the details.

The simulation case was also the same as the one in Chapter 6 (see Section 6.2.2), which was mainly set according to the wind tunnel experiment conducted by Michioka et al. (2011), with the only exception of the spanwise size. The spanwise size of the current case was increased to $8H$, where $H = 0.12$ m is the size of the roughness bars, to provide more realisations for the flow on the spanwise direction so that the later Fourier analysis can catch large-scale periodic fluctuations on the spanwise direction. The geometry of the simulated domain is shown in Figure 7.1. The mesh of the simulation was also adjusted accordingly. Other details of the simulation conditions are presented in Table 7.1, which are the same as those in Chapter 6.

During the simulation, the velocity and concentration data were sampled within the following domain:

$$\Omega = \left\{ (x, y, z)^T \mid -0.5H \leq x \leq 1.5H, \quad -4H \leq y \leq 4H, \quad 0 \leq z \leq 2H \right\}, \quad (7.1)$$

which contained 1,104,000 cells. This number equals to the cell number on a x - z plane (3450) multiplied by the partitioning number on the y -direction (320). The sampling wavenumber on the spanwise direction was set at $20 H^{-1}$, so the total number of the sampled cells are $3450 \times 160 = 552,000$. The time signals of the velocity and concentration at these cell centres were recorded. The sampling frequency was set at 400 Hz. The sampling wavenumber/frequency was chosen so that the range between the resolution and Nyquist wavenumber/frequency can cover the wavenumber/frequency of interest in the later Fourier analysis.

The volume average streamwise velocity in the whole computational domain was chosen as the reference velocity $U_{\text{ref}} (\approx 1 \text{ m/s})$, which was used to normalise the velocity samples. The concentration samples were normalised by the reference concentration C_{ref} , defined by

$$C_{\text{ref}} = \frac{Q}{U_{\text{ref}} H L_y}, \quad (7.2)$$

where Q is the total emission rate ($=100 \text{ ppm} \cdot \text{m}^3/\text{s}$), and L_y is the length of the line source

($= 8H$). All statistics and post-processing presented in this paper were calculated based on the time signals lasting for 120 s, which was approximately $1000 H/U_{ref}$.

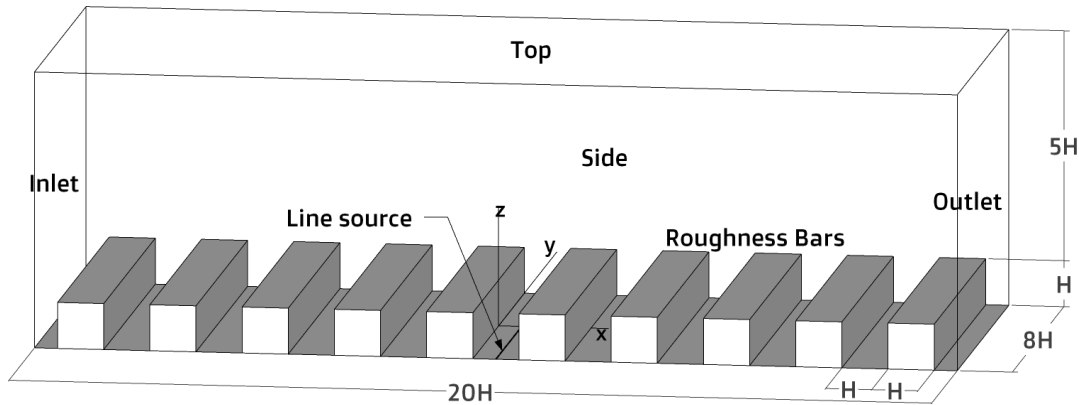


Figure 7.1 Simulation domain

Table 7.1 CFD simulation conditions

Item	Content
Simulation domain	$20H (x) \times 8H (y) \times 6H (z)$ x : streamwise; y : spanwise; z : vertical
Roughness bar size	$H (x) \times H (z)$ ($H = 0.12$ m)
Grid partitioning	$448 (x) \times 320 (y) \times 100 (z)$ Total cells: 10,467,840 In target canyon: $40 (x) \times 320 (y) \times 40 (z)$ Minimum grid size in target canyon: $H/60$ (adjacent to the wall and roof)
Time marching	Pressure-implicit with splitting order (PISO) (Issa, 1986)
Simulation period	Preparatory: 0–120 s, Sampling: 120–240 s
Time-step	During preparatory: 0.0013–0.002 s, (adjusted automatically to keep the maximum Courant's number equal to 1) During sampling: 0.00125 s Sampling time step: 0.0025 s (Sampling frequency: 400 Hz)
Inlet and outlet B.C.	Periodic The concentration on the inlet boundary was adjusted to 0.
Side B.C.	Periodic
Ground and wall B.C.	Velocity: no-slip; Pressure and concentration: zero-Gradient
Top B.C.	Velocity: slip; Pressure and concentration: zero-Gradient
Momentum source	The volume average streamwise velocity in the whole computational domain was kept constant 1 m/s by adjusting the streamwise pressure gradient.
Tracer gas source	Total emission rate $Q = 100 \text{ ppm} \cdot \text{m}^3/\text{s}$ at the line source
Wall function	Wall and ground: the Spalding's law (Spalding, 1962)
Space discretisation	2^{nd} -order central difference TVD scheme for advection terms in scalar transport equations
Time discretisation	Euler-implicit

7.2.2 *Statistics and validation*

Before the general statistic, it needs to clarify that the velocity and concentration fields are regarded as stochastic and homogeneous over both the time and spanwise (y -) coordinate in this study. Therefore, the expectation is redefined which should remove the fluctuation along both the time and y -direction. For a general stochastic quantity $\Phi(x, y, z, t)$, the expectation is estimated by temporal average over time and spatial average over the y -direction, that is,

$$E(\Phi) = \frac{1}{TL_y} \int_0^{L_y} dy \int_0^T \Phi(x, y, z, t) dt, \quad (7.3)$$

where T is the length of the time signal, and L_y is the spanwise length.

Figures 7.2 and 7.3 show the profiles of the mean streamwise velocity and root mean square of the streamwise fluctuating velocity at $x/H = 0.25, 0.50,$ and 0.75 . Figure 7.4 shows the profiles of the mean concentrations at $x/H = 0, 0.50,$ and 1 . These results are consistent with the wind-tunnel experiment results of Michioka et al. (2011) and Pavageau and Schatzmann (1999). The mean flow in Figure 7.5 (a), TKE in Figure 7.5 (b) and mean concentration in Figure 7.5 (c) show almost the same shape with those in Chapter 6. Note the principal recirculation shown in the mean flow, following which the TKE generated at the roof level was brought into the canyon along the windward wall and the concentration was driven onto the roof level along the leeward wall. A large amount of concentration re-entered the canyon on reaching the roof level rather than travel with the external flow. Previous researches show that turbulence plays a major role in pollutant removal from the canyon (Cheng et al., 2008; Cheng and Liu, 2011), while the mean wind carries pollutants into and out of a street canyon simultaneously (Liu and Wong, 2014). Therefore, turbulent structures are focus on in the following study, and their relationship to pollutant removal is also the aim.

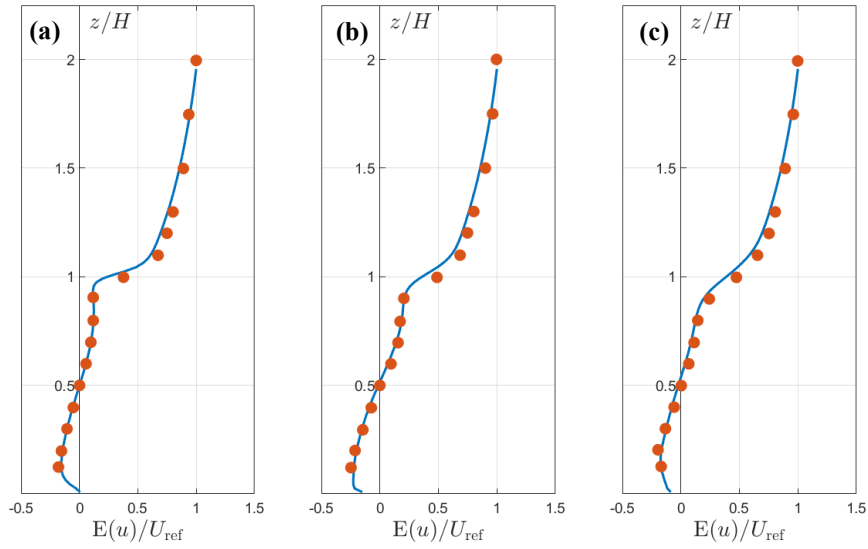


Figure 7.2 Profiles of the mean streamwise velocity at (a) $x/H = 0.25$, (b) $x/H = 0.5$ and (c) $x/H = 0.75$. Filled circles are the results of the wind tunnel experiment conducted by Michioka et al. (2011).

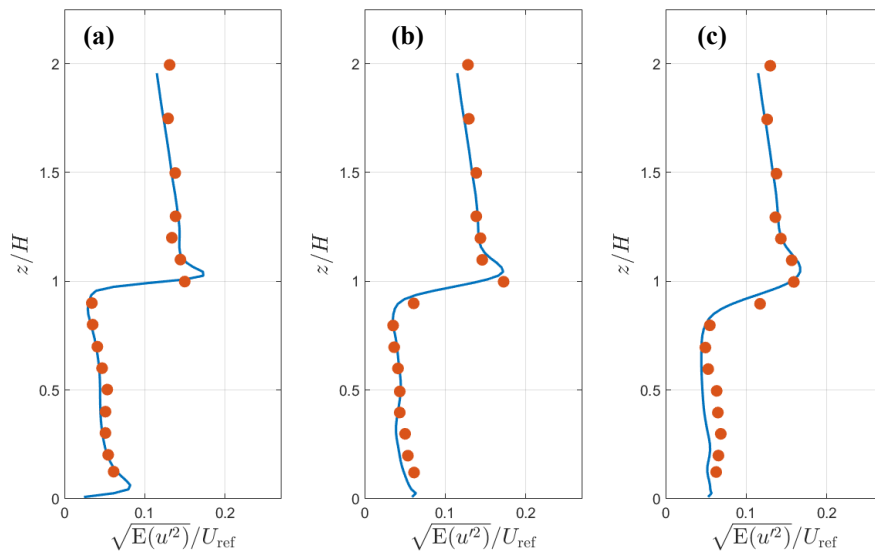


Figure 7.3 Profiles of the root mean square of the streamwise fluctuating velocity at (a) $x/H = 0.25$, (b) $x/H = 0.5$ and (c) $x/H = 0.75$. Filled circles are the results of the wind tunnel experiment conducted by Michioka et al. (2011).

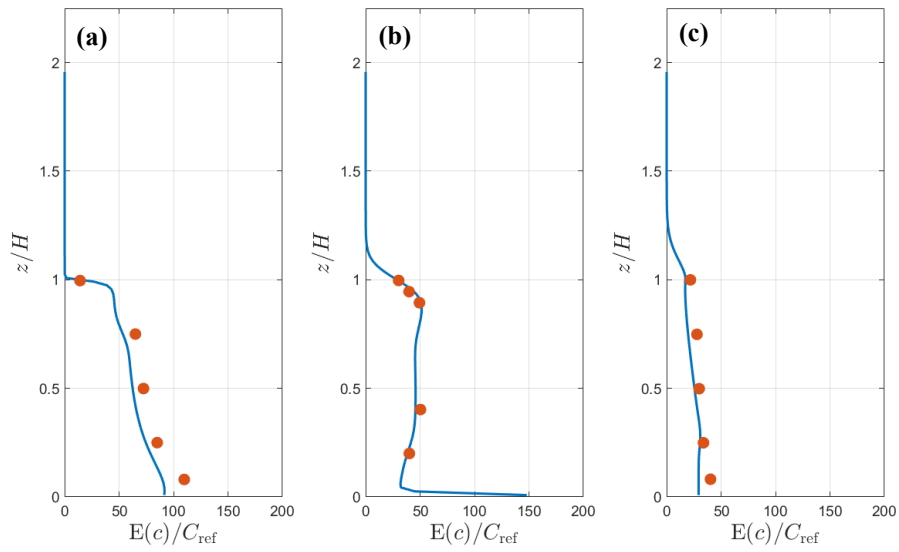


Figure 7.4 Profiles of the mean concentration at (a) $x/H = 0$, (b) $x/H = 0.5$ and (c) $x/H = 1$. Filled circles are the results of the wind tunnel experiment conducted by Pavageau and Schatzmann (1999).

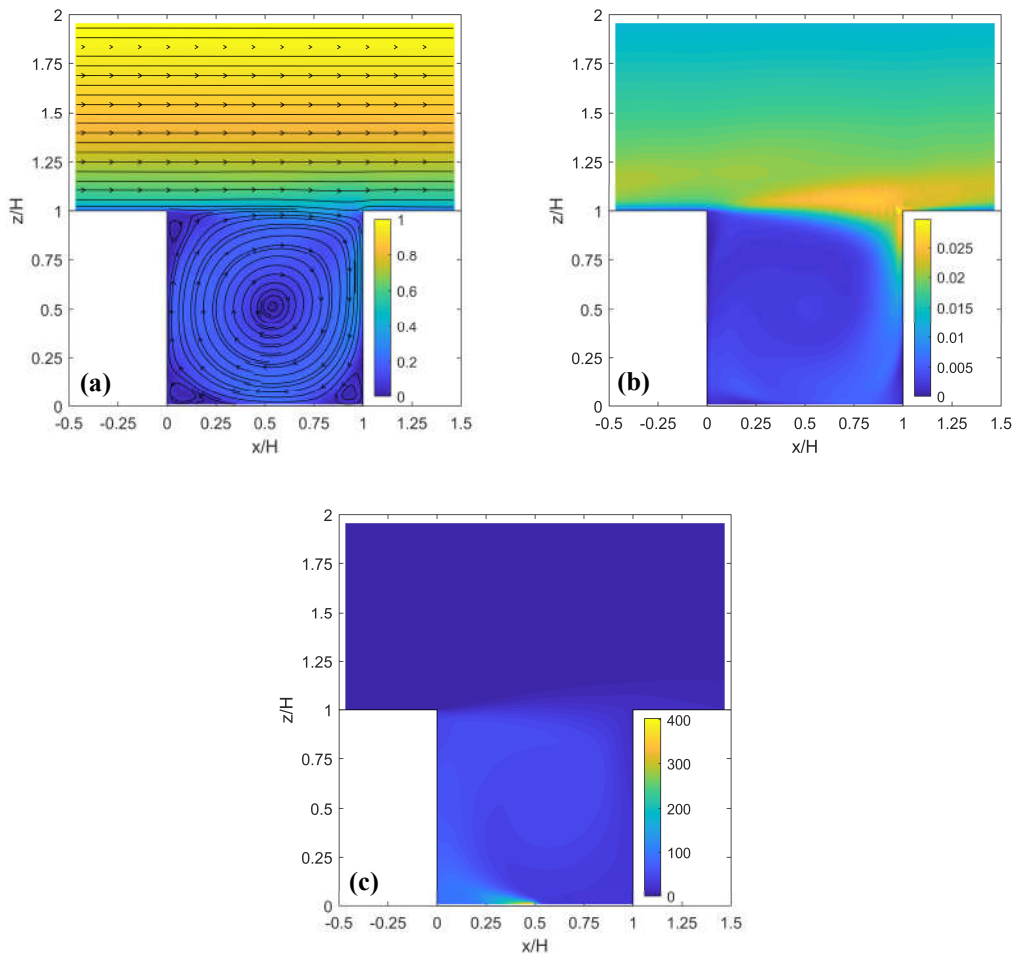


Figure 7.5 Cross-sections of (a) mean velocity with streamlines on the x - z plane, (b) TKE and (c) mean concentration.

7.3 SPOD with 2DFT

As we have noted, both the velocity and concentration field are regarded as stochastic with both the time and spanwise coordinate. The Fourier transformation in SPOD is extended to a two-dimensional one to elucidate the periodic properties of the turbulent structures and pollutant removal, especially on the spanwise direction. The basic theory and algorithm of SPOD with 2DFT, are introduced in Sections 7.3.1 and 7.3.2. The SPOD co-spectrum defined in our previous study is also modified to a 2DFT version, which is introduced in Section 7.3.3.

7.3.1 Theory

The velocity vector is denoted by

$$\mathbf{u}(x, y, z, t) = \begin{bmatrix} u(x, y, z, t) \\ v(x, y, z, t) \\ w(x, y, z, t) \end{bmatrix}, \quad (7.4)$$

For briefness, the independent variables in the brackets are omitted hereafter. For example, the velocity $\mathbf{u}(x, y, z, t)$ is simply written as \mathbf{u} after its first appearance. The fluctuation velocity targeted in the POD based analysis can be written as

$$\mathbf{u}'(x, y, z, t) = \mathbf{u} - E(\mathbf{u}), \quad (7.5)$$

which is the target of the current analysis. Please refer to Eq. (7.3) for the definition of the expectation operator $E(\cdot)$.

Because of the homogeneity and stationarity of the statistics in the spatial y -direction and in time, the exact solutions of POD modes are identical to Fourier series in these directions (Berkooz et al., 1993; Carassale et al., 2007). Therefore, Fourier transformation over these directions is a more direct process. In this study, the 2DFT is performed over the time t and y -coordinate, which is written as

$$\hat{\mathbf{u}}'(x, z; \eta, f) = \int_0^{L_y} dy \int_0^T \mathbf{u}' e^{-i2\pi(ft+\eta y)} dt, \quad (7.6)$$

where $\hat{\mathbf{u}}'$ denotes the 2DFT of \mathbf{u}' , i is the imaginary unit, f is the frequency, and η is the wavenumber along the y -direction which has the unit of m^{-1} . The following symmetry property can easily be obtained:

$$\hat{\mathbf{u}}'(x, z; -\eta, -f) = \hat{\mathbf{u}}'^*(x, z; \eta, f), \quad (7.7)$$

where $\hat{\mathbf{u}}'^*$ denotes the conjugate of $\hat{\mathbf{u}}'$. Such a symmetry property is termed as ‘‘conjugate symmetry’’ hereafter. In addition, the inverse transformation is represented as

$$\mathbf{u}' = \int_{-\infty}^{+\infty} d\eta \int_{-\infty}^{+\infty} \hat{\mathbf{u}}' e^{i2\pi(ft+\eta y)} df. \quad (7.8)$$

The Fourier transformation over the time and y -coordinate can be performed separately to reach the 2DFT. For example, one can first take the Fourier transformation over the y -coordinate, and then take the Fourier transformation of the results over the time.

The above 2DFT is applied to SPOD, and the decomposition form can be written as

$$\hat{\mathbf{u}}' = \sum_n a_n(\eta, f) \Psi_n(x, z; \eta, f), \quad (7.9)$$

where $\Psi_n(x, z; \eta, f)$ and $a_n(\eta, f)$ is the mode and mode coefficient, respectively, with the index of n . Both the mode and mode coefficient are conjugate symmetric functions of η and f , so three indexes (n , η and f) are needed to specify a certain mode. The decomposition form can also be written into a similar form with the inverse 2DFT as

$$\mathbf{u}' = \int_{-\infty}^{+\infty} d\eta \int_{-\infty}^{+\infty} \sum_n a_n \Psi_n e^{i2\pi(ft+\eta y)} df. \quad (7.10)$$

This brings the direct connection to the modes and fluctuation velocity.

The decomposition form is not unique, if the following orthogonal conditions are not given. Similar to POD, both the modes and mode coefficients hold the orthogonal conditions. For the modes, the orthogonal condition is written as

$$\langle \Psi_n, \Psi_m \rangle = \delta_{nm} = \begin{cases} 0 & n \neq m \\ 1 & n = m \end{cases}, \quad (7.11)$$

where the inner product is defined as

$$\langle \Phi_1, \Phi_2 \rangle = \frac{1}{A_{xz}} \iint_{\Omega_{xz}} \Phi_2^\dagger \Phi_1 dx dz. \quad (7.12)$$

\cdot^\dagger denotes Hermitian transpose. Ω_{xz} is the sampling interval on the x - z plane, which is invariant with the time and the y -coordinate. A_{xz} is the area of this interval, which equals to $\iint_{\Omega_{xz}} dx dz$. Next, the orthogonal condition for the mode coefficients is written as

$$\frac{1}{TL_y} a_n a_m^* = \lambda_n(\eta, f) \delta_{nm}, \quad (7.13)$$

where $\lambda_n(\eta, f)$ is termed as ‘‘mode energy’’, which represents the intensity of the mode. The mode energy is a symmetric function of η and f , that is

$$\lambda_n(-\eta, -f) = \lambda_n(\eta, f). \quad (7.14)$$

The above orthogonal conditions can bring an important property that constructs the relationship between the mode energy and spatial average TKE, \bar{k} , that

$$2\bar{k} = \int_{-\infty}^{+\infty} d\eta \int_{-\infty}^{+\infty} \sum_n \lambda_n df, \quad (7.15)$$

which is deduced as follows:

$$\begin{aligned} 2\bar{k} &= \frac{2}{TA_{xz}L_y} \iint_{\Omega_{xz}} dx dz \int_0^{L_y} dy \int_0^T \frac{1}{2} \mathbf{u}'^\dagger \mathbf{u}' dt = \frac{1}{TA_{xz}L_y} \iint_{\Omega_{xz}} dx dz \int_{-\infty}^{+\infty} d\eta \int_{-\infty}^{+\infty} \hat{\mathbf{u}}'^\dagger \hat{\mathbf{u}}' df \\ &= \int_{-\infty}^{+\infty} d\eta \int_{-\infty}^{+\infty} \sum_n \left(\frac{1}{TL_y} a_n^* a_n \right) \langle \Psi_n, \Psi_n \rangle df = \int_{-\infty}^{+\infty} d\eta \int_{-\infty}^{+\infty} \sum_n \lambda_n df. \end{aligned} \quad (7.16)$$

The second equation in Eq. (7.16) is an application of Parseval's theorem, and the third used the decomposition form, Eq. (7.9), along with the orthogonality conditions, Eqs. (7.11) and (7.13). As a function of wave number and frequency, λ_n is also called ‘‘SPOD spectrum’’, which denotes the energy density on the f - η plane.

7.3.2 Algorithm

Theoretically, the modes and mode energies are the eigenfunctions and eigenvalues of the two-point spectrum tensor. To enhance the convergence and enforceability of the estimation of the modes and energies from the discrete velocity data, an algorithm was proposed by Towne et al. (2018), which combined the Welch's method for spectral estimation and the snapshot POD algorithm (Sirovich, 1987). This algorithm, introduced in Chapter 3, is still applicable to estimate the modes Ψ_n and mode energies λ_n in SPOD with 2DFT, although some complement needs to be made.

If the Fourier transformation over the y -coordinate is performed on both sides of Eq. (7.10), it becomes

$$\int_0^{L_y} \mathbf{u}' e^{-i2\pi\eta y} dy = \int_{-\infty}^{+\infty} \sum_n a_n \Psi_n e^{i2\pi\eta t} df. \quad (7.17)$$

The right side shows the form of the original SPOD, and the Ψ_n and λ_n can be estimated directly by the algorithm proposed by Towne et al. (2018) if the term on left side is given in advance. Note that the term on the left side is just the one-dimensional Fourier transformation of \mathbf{u}' , so one can simply discretise the y -coordinate into $y_j, j = 1, 2, \dots, N_y$, and perform the discrete Fourier transformation over y -coordinate.

The algorithm for SPOD with 2DFT is as follows:

(1) Calculate the one-dimensional discrete Fourier transformation of the fluctuation velocity \mathbf{u}' over the y -coordinate. For a specified wavenumber η_j , we get

$$\tilde{\mathbf{u}}'(x, z, t; \eta_j) = \int_0^{L_y} \mathbf{u}' e^{-i2\pi\eta_j y} dy, \quad j = 1, 2, \dots, N_y. \quad (7.18)$$

(2) Replace the \mathbf{u}' in the original SPOD algorithm by the above $\tilde{\mathbf{u}}'(x, z, t; \eta_j)$, and

calculate the mode $\boldsymbol{\psi}_n(x, z; \eta_j, f)$ and mode energy $\lambda_n(\eta_j, f)$.

(3) Repeat until the modes and mode energies at all the discrete wavenumbers are obtained.

Note that the SPOD algorithm is processed independently for each discrete wavenumber, so the parallel processing can be applied here to accelerate the computing. Also note that $\tilde{\mathbf{u}}'(x, z, t; \eta_j)$ usually consists of complex numbers, so the modes are not symmetric with respect to $f=0$. One may need to compute for both positive and negative f with the same wavenumber. However, because the mode energy is symmetric, and the mode and mode coefficient are conjugate symmetric with respect to the original point on the f - η plane, the results in only two quadrants need to be computed.

7.3.3 SPOD co-spectrum

Similar to that introduced in Chapter 6, the SPOD co-spectrum based on the SPOD with 2DFT can be also defined.

The SPOD co-spectrum between the streamwise fluctuation velocity $u'(x, y, z, t)$ and vertical fluctuation velocity $w'(x, y, z, t)$ is defined as

$$S_n^{(uw)}(x, z; \eta, f) = \text{Re}(\lambda_n \boldsymbol{\psi}_n^{(u)} \boldsymbol{\psi}_n^{(w)*}), \quad (7.19)$$

where $\boldsymbol{\psi}_n^{(u)}$ and $\boldsymbol{\psi}_n^{(w)}$ denote the u and w components of the vector $\boldsymbol{\psi}_n$, respectively. This co-spectrum shows the planar density of the Reynolds shear stress on the f - η plane, and its integral equals to the Reynolds shear stress at the spatial position (x, z) , that is

$$E(u'w') = \int_{-\infty}^{+\infty} d\eta \int_{-\infty}^{+\infty} \sum_n S_n^{(uw)} df. \quad (7.20)$$

The SPOD co-spectrum between the vertical fluctuation velocity $w'(x, y, z, t)$ and fluctuation concentration $c'(x, y, z, t) = c(x, y, z, t) - E(c)$ is defined as

$$S_n^{(wc)}(x, z; \eta, f) = \text{Re} \left(\frac{1}{TL_y} a_n \boldsymbol{\psi}_n^{(w)} \hat{c}'^* \right), \quad (7.21)$$

where \hat{c}' is the 2DFT of the c' whose spatial and temporal discretisation should be the same with the velocity. This co-spectrum shows the planar density of the vertical turbulent mass flux on the f - η plane, and its integral equals to the vertical turbulent mass flux at the spatial position (x, z) , that is

$$E(w'c') = \int_{-\infty}^{+\infty} d\eta \int_{-\infty}^{+\infty} \sum_n S_n^{(wc)} df. \quad (7.22)$$

The SPOD spectrum is estimated by the Welch's method (Welch, 1967), in which the

time signal is first divided into blocks, and the energy of the entire signal is estimated by averaging the energy values over all the blocks. In this case, the mode coefficient a_n is not the same value in different blocks. Therefore, the values of $S_n^{(wc)}$ need to be estimated by the same Welch's method, i.e., dividing then averaging, where the block dividing and window function (if used) should be kept the same with the velocity when performing SPOD.

In application, because both $S_n^{(uw)}$ and $S_n^{(wc)}$ are symmetric with respect to the original point on the f - η plane, the results in only two quadrants need to be computed.

Table 7.2 Parameters used in the energy and mode estimation when performing SPOD with 2DFT

Item	Fourier transformation along time	Fourier transformation along spanwise direction
Total number of snapshots	48,000	160
Sampling frequency/wavenumber	400 Hz = 48 U_{ref}/H	167 m^{-1} = 20 H^{-1}
Window (block length)	Hamming window with a length of 4,800 snapshots	None
Block dividing	19 blocks with a block length of 4,800 snapshots each	1 block (undivided)
Overlap length	2,400 snapshots (50% overlap)	None
Resolution frequency/wavenumber	400 Hz / 4800 = 0.0833 Hz = 0.01 U_{ref}/H	167 m^{-1} / 160 = 1.04 m^{-1} = 0.125 H^{-1}
Nyquist frequency/wavenumber	400 Hz / 2 = 200 Hz =24 U_{ref}/H	167 m^{-1} / 2 = 83 m^{-1} =10 H^{-1}

7.4 Results and discussion

7.4.1 Performing SPOD with 2DFT on the velocity field

The modes were calculated using the algorithm provided in Section 7.3.2. The parameters used in the estimation of modes and energies are listed in Table 7.2. Appropriate block length was chosen so that the block number was considered sufficient to obtain a relatively precise energy estimation with low uncertainty, and the resolvable frequency range can also cover the lowest frequency of interest. Because the snapshots along the spanwise direction were not as many as those along time, the process was not divided into blocks along the spanwise direction. This will not cause any convergence problem, because there were still sufficient realisations of the flow in different time periods so that the energies can be estimated by averaging. In addition, the Hamming window was

applied before the Fourier transformation over time to prevent the spectral leakage caused by the non-periodicity at the boundaries of each block, while window function is unnecessary for the spanwise direction, because the process along the spanwise direction was periodic due to the periodic boundary condition in LES. The same manner of 2DFT was also applied on the concentration data.

7.4.2 SPOD spectrum and turbulent fluctuation patterns

Figure 7.6 presents the SPOD spectrum, showing the largest of the computed 19 eigenvalues at all discrete frequencies. The eigenvalues are nondimensionalised as

$$\underline{\lambda}_n(\eta, f) = \frac{f\eta\lambda_n}{2k}. \quad (7.23)$$

Because the purpose of the current study is to perform data analysis but not dimension reduction, where the energy completeness is not required, observation only on the modes with the largest energy in on the f - η plane is considered sufficient for understanding the turbulent flow. Therefore, only the eigenvalues with $n = 1$ and 2 are provided in Figures 7.6 and 7.7, respectively. All the following analysis is focused on the modes with $n = 1$, which depicts the most characteristic fluctuation patterns in this turbulent flow, along with some inspection on the eigenvalues with $n = 2$, which provide additional remarks for better understanding. Note that the mode energy is theoretically symmetric with respect to the original point on the f - η plane, only two quadrants, ($f > 0, \eta > 0$) and ($f > 0, \eta < 0$), are shown in Figures 7.6 and 7.7. Also note that the SPOD spectrum is almost symmetric with respect to $\eta = 0$, indicating the statistical symmetry of the flow along the spanwise direction.

Each eigenvalue at the resolved (f, η) point in the figures corresponds to a SPOD mode. The modes can be understood by examining the real and imaginary parts of the eigenfunctions, or by watching the animation created by the function $\text{Re}(\boldsymbol{\psi}_n e^{i2\pi(ft+\eta y)})$, which is both time-periodic and y -periodic. With the increasing of t or y , the animation process is approximately $\text{Re}(\boldsymbol{\psi}_n) \rightarrow -\text{Im}(\boldsymbol{\psi}_n) \rightarrow -\text{Re}(\boldsymbol{\psi}_n) \rightarrow \text{Im}(\boldsymbol{\psi}_n) \rightarrow \text{Re}(\boldsymbol{\psi}_n)$. For example, Figure 7.8 provides the streamlines for the eight selected modes, which correspond to the eight circled eigenvalues in Figure 7.6. Compared to the modes provided in Chapter 6, the modes in the current study show clearer shapes of flow patterns, especially inside the target canyon where the fluctuation is relatively weak. This is because the samples are increased by extending the coordinates on the spanwise direction, which is equivalent to provide more flow realisations. In addition to the real and imaginary parts of the eigenfunctions, the spanwise variation on the y - z planes with $x/H = 0.5$ and 0.9 are also provided in Figure 7.8 for the eight selected modes, which are also created by the function $\text{Re}(\boldsymbol{\psi}_n e^{i2\pi(ft+\eta y)})$ but with $t = 0$. With the increasing of t , the

spanwise variation will show translational motions that move left for ($f > 0, \eta > 0$) or move right for ($f > 0, \eta < 0$).

Before taking a closer look at the spectrum and modes, we first divided the f - η plane into four zones, named A, B, C, and D, for the convenience of description and further study. The chosen modes are also named corresponding to the zone name they are in. Please see Table 7.3 for the range of frequency and wavenumber for each zone. The zones are mainly divided according to the key characteristics of the modes in them, and the eigenvalues with $n = 2$ in Figure 7.7 was also taken as reference. To better explain why the eigenvalues with $n = 2$ are examined in this case, Figure 7.9 provides a schematic to illustrate how the SPOD spectrum deal with multiple physical structures. Because the POD process is performed separately at various frequencies/wavenumbers, SPOD will recognise the largest energy as the eigenvalue with $n = 1$ and the second-largest energy as the eigenvalue with $n = 2$ regardless of which physical structure they belong to. Therefore, at the junction of the two spectra of the physical structures, circled in Figure 7.9, the eigenvalue with $n = 2$ will reach its maximum. In addition, the modes at the junction will mix with each other due to the numerical issues, e.g., the mode with $n = 1$ may present both characteristics of the two physical structures. For the same reason, the boundaries of the zones are chosen at the frequency/wavenumber where the eigenvalues with $n = 2$ in Figure 7.7 are large. However, please note that the modes change gradually along the frequency and wavenumber, so the boundaries of the zones are actually not so obvious as shown by the white dash lines in Figures 7.6 and 7.7. The division in this study is rough and qualitative.

Table 7.3 Zone division and percentages of whole-field TKE and vertical turbulent mass flux at the roof level within the zones. These percentage values are calculated by integrating the SPOD spectrum in Figure 7.6 by Eq. (7.5) or the SPOD co-spectrum in Figure 7.11 (b) by Eq. (7.22) within a specific frequency/wavenumber range.

Zone	Range of frequency and wavenumber	Percentage of the whole-field TKE	Percentage of the vertical turbulent mass flux at the roof level
A	$0 < fH/U_{\text{ref}} < 0.3$ and $0 < \eta H < 0.9$	39%	8%
B	$0.3 < fH/U_{\text{ref}} < 3$ and $0.9 < \eta H < 9$	24%	40%
C	$0 < fH/U_{\text{ref}} < 0.3$ and $0.9 < \eta H < 9$	12%	22%
D	$0.3 < fH/U_{\text{ref}} < 3$ and $0 < \eta H < 0.9$	22%	29%
Other	$ fH/U_{\text{ref}} > 3$ or $ \eta H > 9$	3%	1%

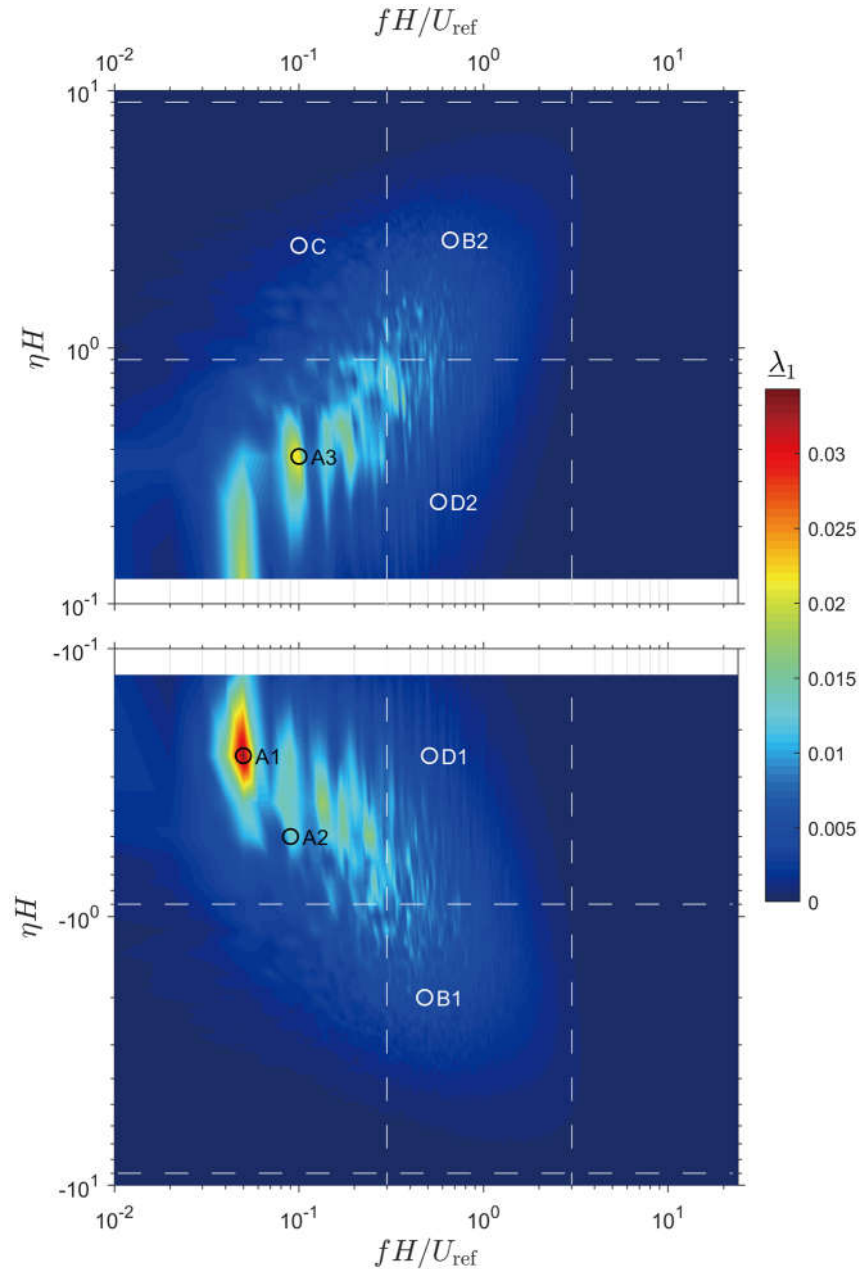


Figure 7.6 SPOD spectrum showing the largest nondimensional eigenvalues ($n = 1$) plotted versus the nondimensional frequency and wavenumber. This spectrum is theoretically symmetric with respect to the original point on the f - η plane, so only two quadrants are shown. At each resolved (f, η) point, the colour shows the eigenvalue with the index of $n = 1$. Each eigenvalue corresponds to a complex eigenfunction, depicting a certain spatial distribution and fluctuation pattern of the velocity. For instance, the eigenfunctions of the eight selected modes, whose eigenvalues are circled, are shown in Figure 7.8. The f - η plane is divided into zones bounded by the white dash lines to classify the modes by the key characteristics. See Table 7.3 for the range of frequency and wavenumber for each zone.

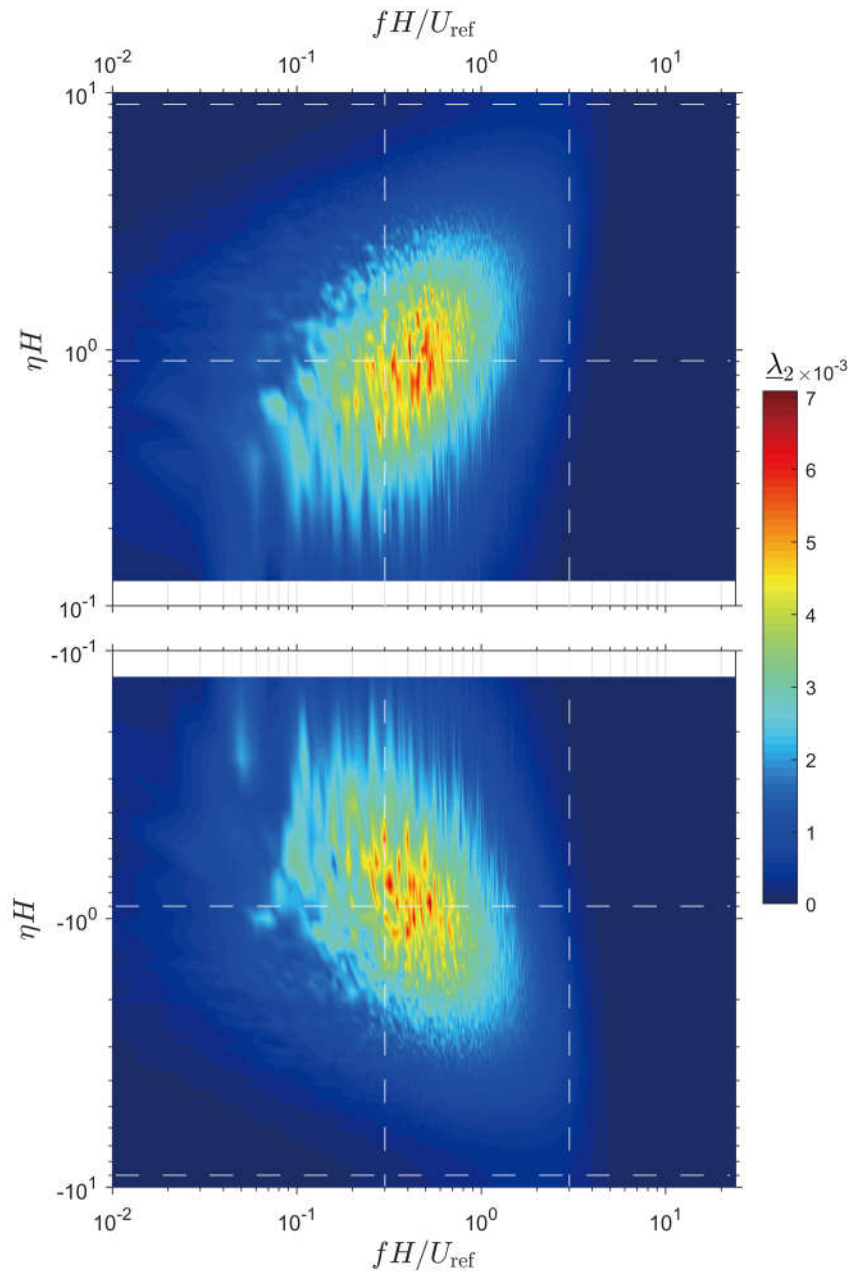
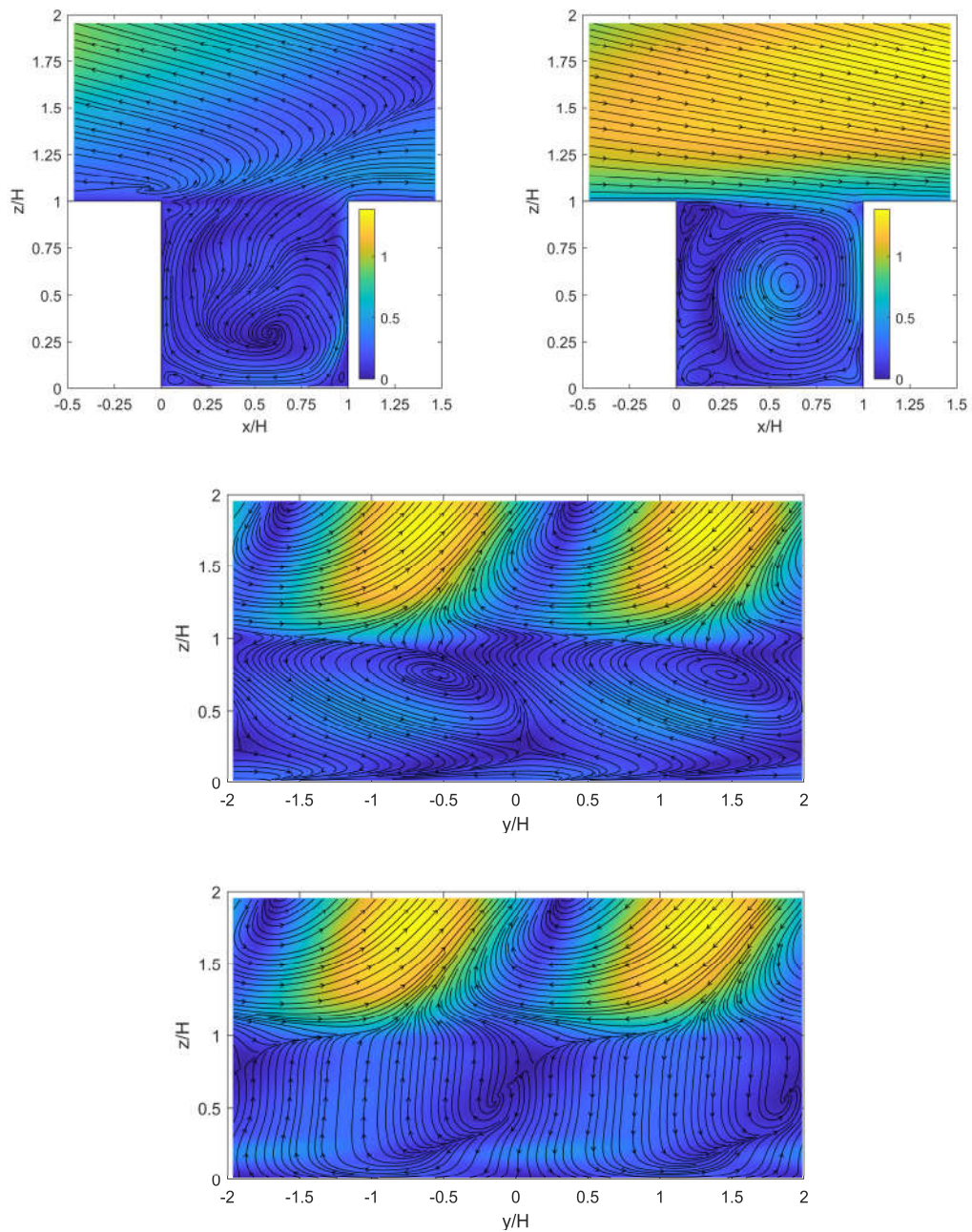
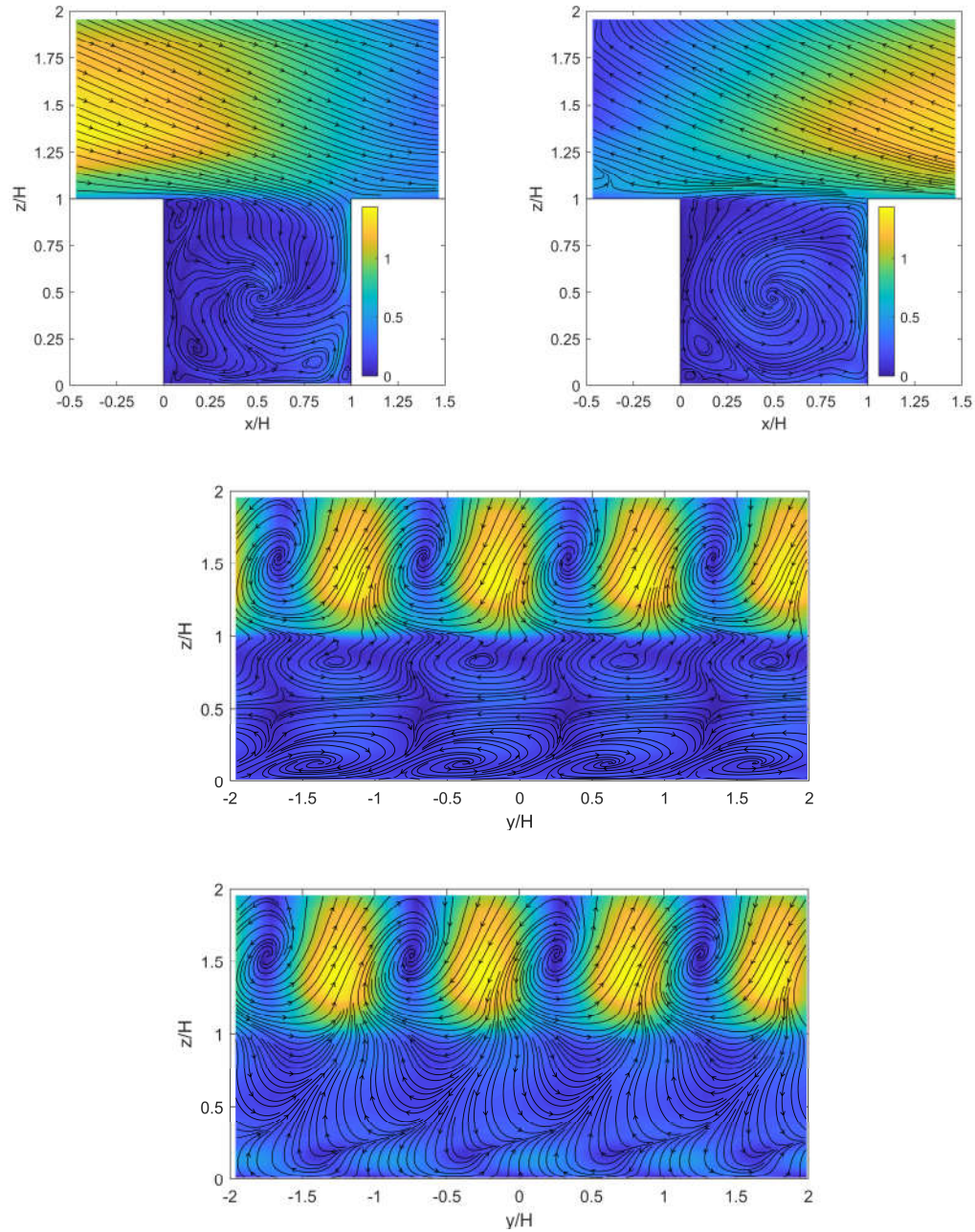


Figure 7.7 SPOD spectrum showing the second largest nondimensional eigenvalues ($n = 2$) plotted versus the nondimensional frequency and wavenumber. Please see the capture of Figure 7.6 for more description.



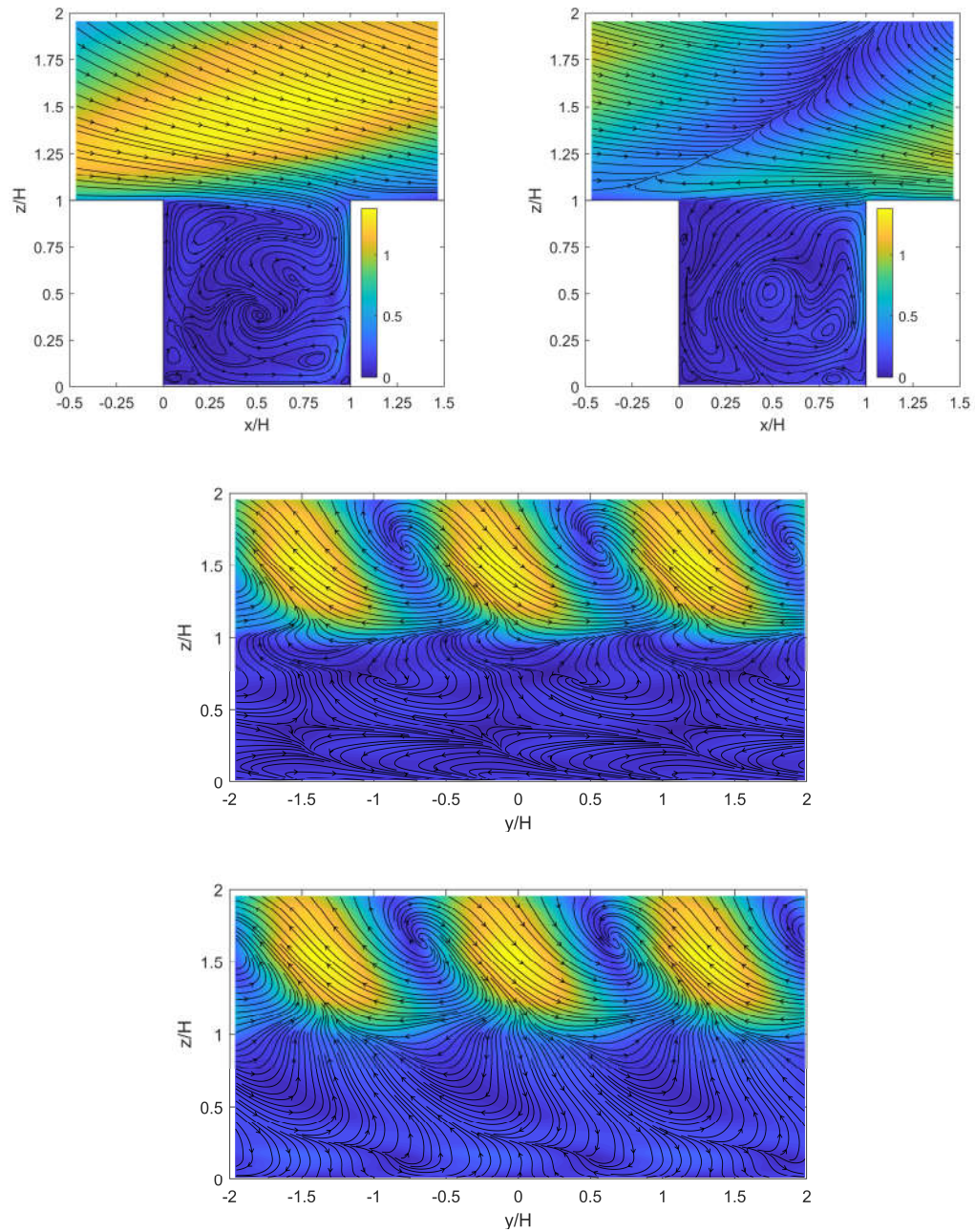
(a) Real (top-left) and imaginary (top-right) parts of the eigenfunction of mode A1 ($fH/U_{\text{ref}} = 0.05$, $\eta H = -0.250$, $n = 1$), and spanwise variation on the y - z planes with $x/H = 0.5$ (middle) and 0.9 (bottom).

Figure 7.8 (continued on next page)



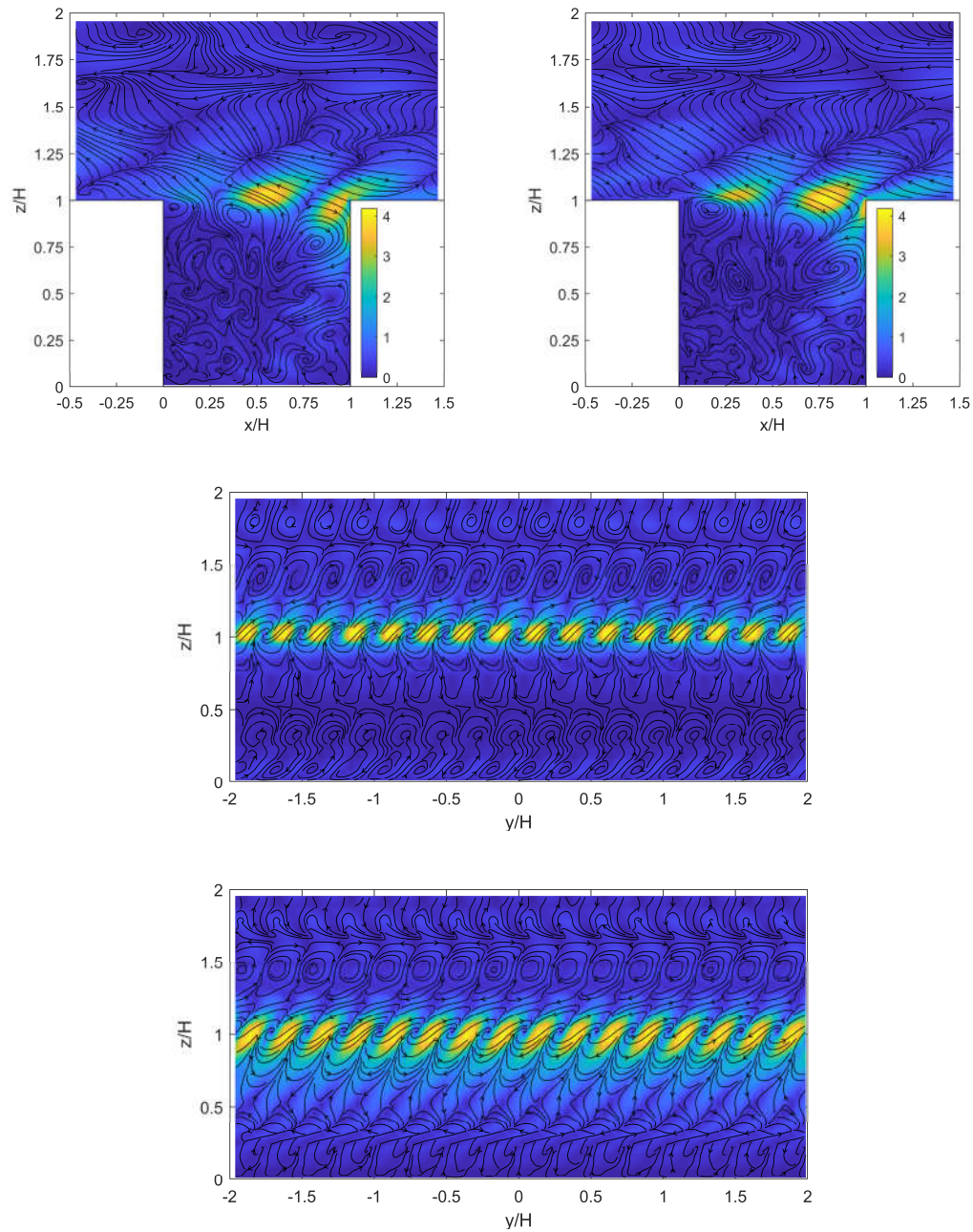
(b) Real (top-left) and imaginary (top-right) parts of the eigenfunction of mode A2 ($fH/U_{\text{ref}} = 0.09$, $\eta H = -0.50$, $n = 1$), and spanwise variation on the y - z planes with $x/H = 0.5$ (middle) and 0.9 (bottom).

Figure 7.8 (continued on next page)



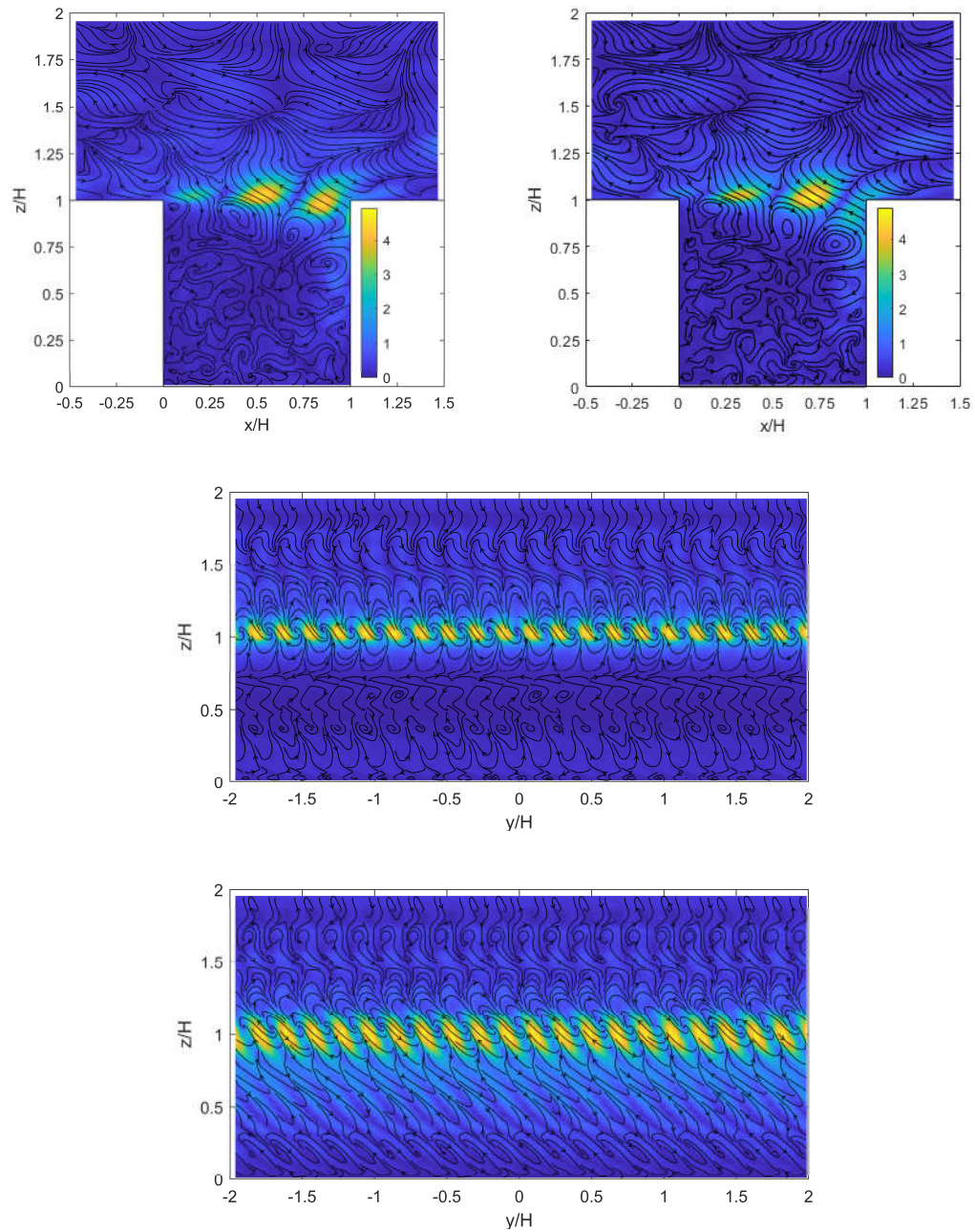
(c) Real (top-left) and imaginary (top-right) parts of the eigenfunction of mode A3 ($fH/U_{\text{ref}} = 0.10$, $\eta H = 0.375$, $n = 1$), and spanwise variation on the y - z planes with $x/H = 0.5$ (middle) and 0.9 (bottom).

Figure 7.8 (continued on next page)



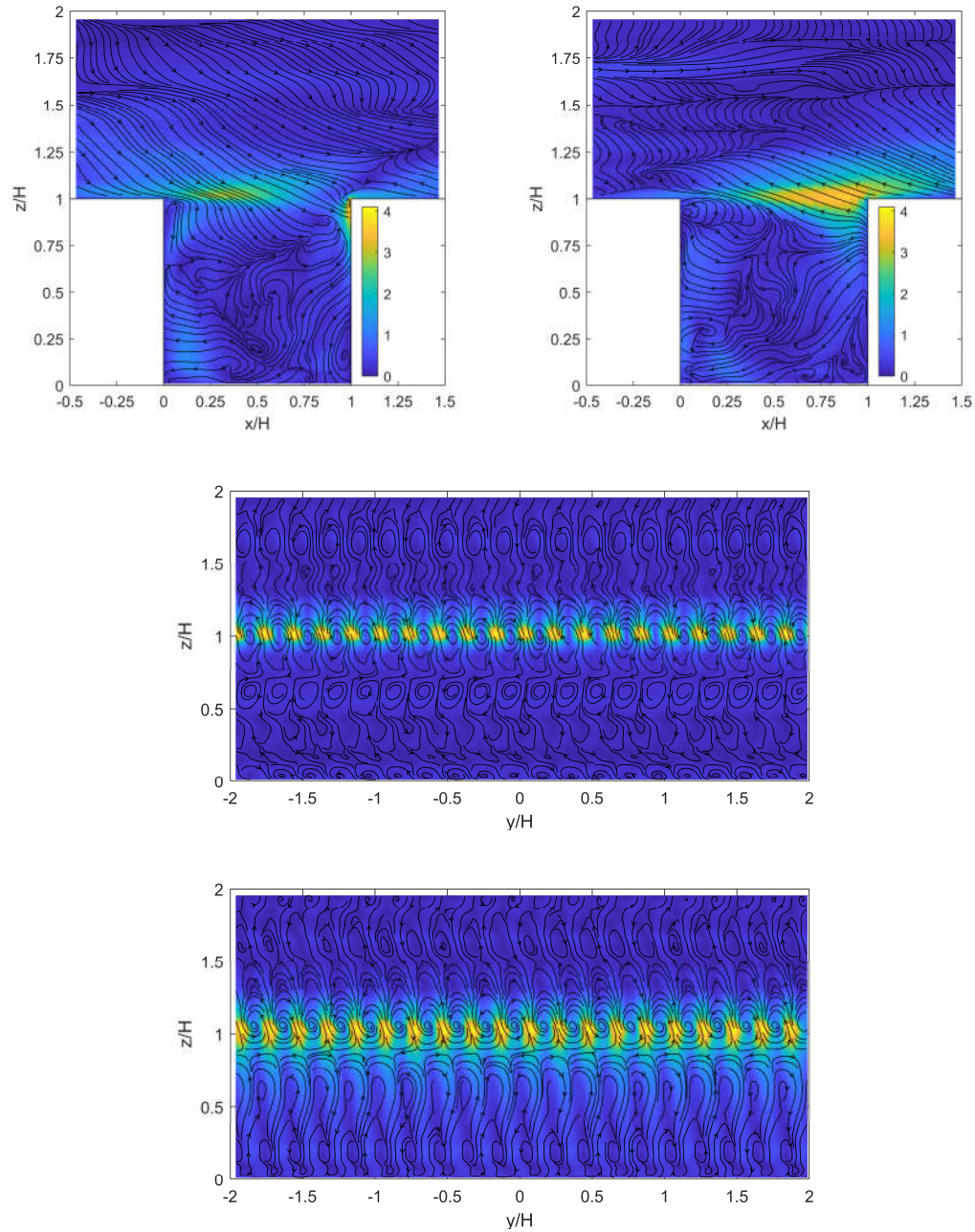
(d) Real (top-left) and imaginary (top-right) parts of the eigenfunction of mode B1 ($fH/U_{\text{ref}} = 0.48$, $\eta H = -2.000$, $n = 1$), and spanwise variation on the y - z planes with $x/H = 0.5$ (middle) and 0.9 (bottom).

Figure 7.8 (continued on next page)



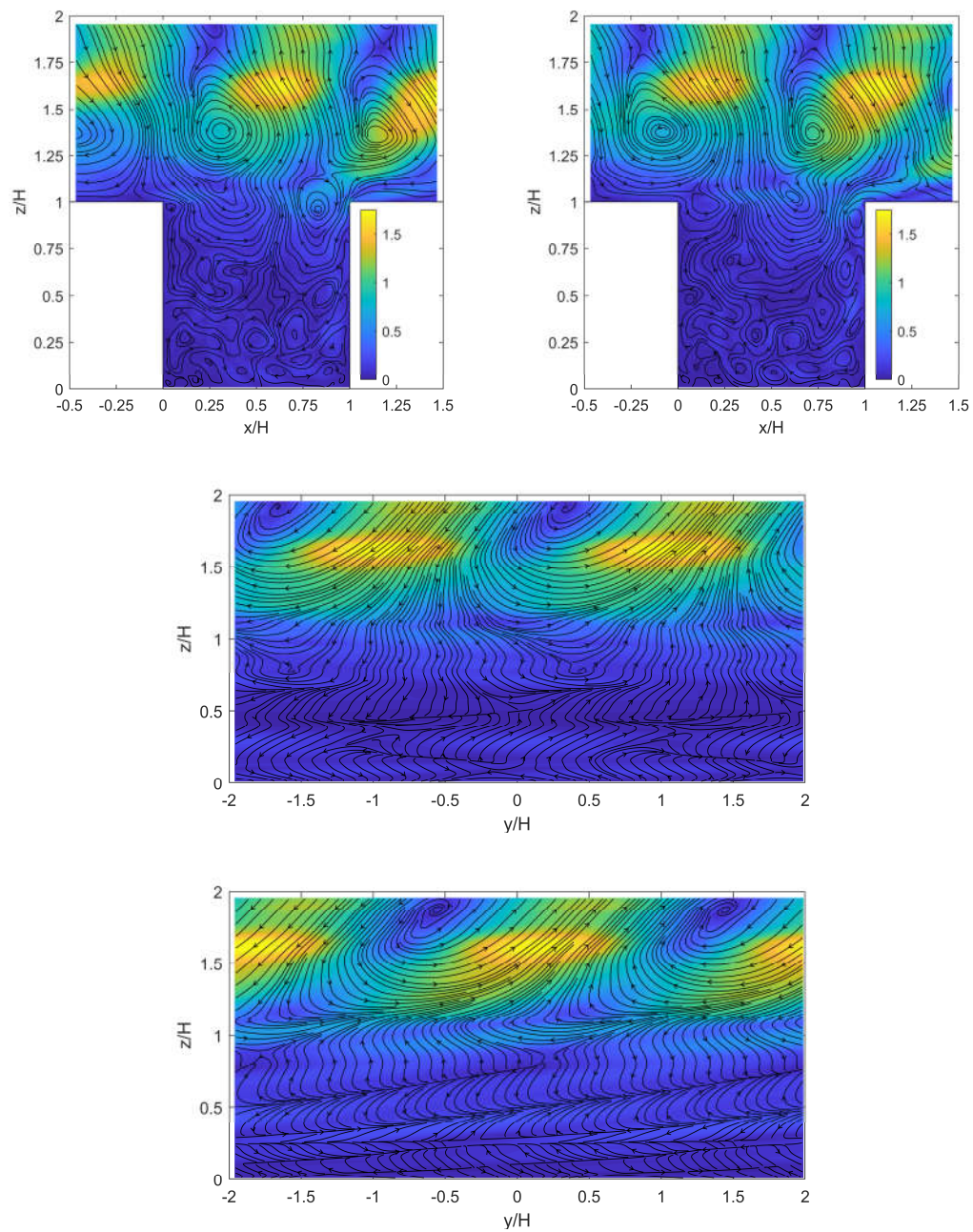
(e) Real (top-left) and imaginary (top-right) parts of the eigenfunction of mode B2 ($fH/U_{\text{ref}} = 0.66$, $\eta H = 2.625$, $n = 1$), and spanwise variation on the y - z planes with $x/H = 0.5$ (middle) and 0.9 (bottom).

Figure 7.8 (continued on next page)



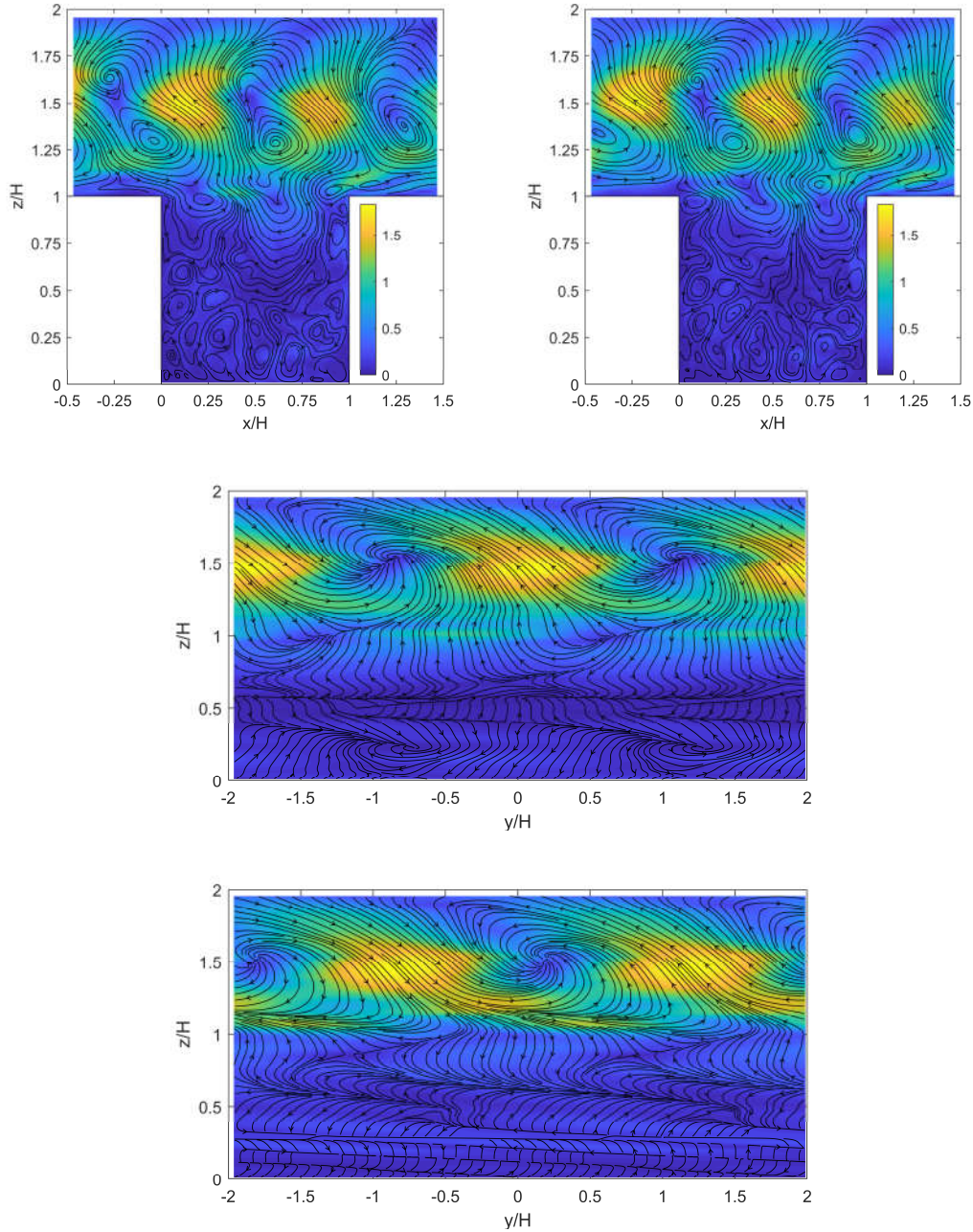
(f) Real (top-left) and imaginary (top-right) parts of the eigenfunction of mode C ($fH/U_{\text{ref}} = 0.10$, $\eta H = 2.500$, $n = 1$), and spanwise variation on the y - z planes with $x/H = 0.5$ (middle) and 0.9 (bottom).

Figure 7.8 (continued on next page)



(g) Real (top-left) and imaginary (top-right) parts of the eigenfunction of mode D1 ($fH/U_{\text{ref}} = 0.51$, $\eta H = -0.250$, $n = 1$), and spanwise variation on the y - z planes with $x/H = 0.5$ (middle) and 0.9 (bottom).

Figure 7.8 (continued on next page)



(h) Real (top-left) and imaginary (top-right) parts of the eigenfunction of mode D2

($fH/U_{\text{ref}} = 0.57$, $\eta H = 0.250$, $n = 1$), and spanwise variation on the y - z planes with $x/H = 0.5$ (middle) and 0.9 (bottom).

Figure 7.8 Eigenfunctions for the eight selected modes. The corresponding eigenvalues are shown in Figure 7.6. The colour shows the magnitude of the vector. The fluctuation pattern is understood by watching the animation of the time-periodic and y -periodic function $\text{Re}(\psi_n e^{i2\pi(f+\eta y)})$, one cycle of which is approximately $\text{Re}(\psi_n) \rightarrow -\text{Im}(\psi_n) \rightarrow -\text{Re}(\psi_n) \rightarrow \text{Im}(\psi_n) \rightarrow \text{Re}(\psi_n)$. The spanwise variation on the y - z planes with $x/H = 0.5$ and 0.9 are also made by the same function with $t = 0$. With the increasing of t , the spatial variation will show travelling waves moving left for ($f > 0$, $\eta > 0$) or moving right for ($f > 0$, $\eta < 0$).

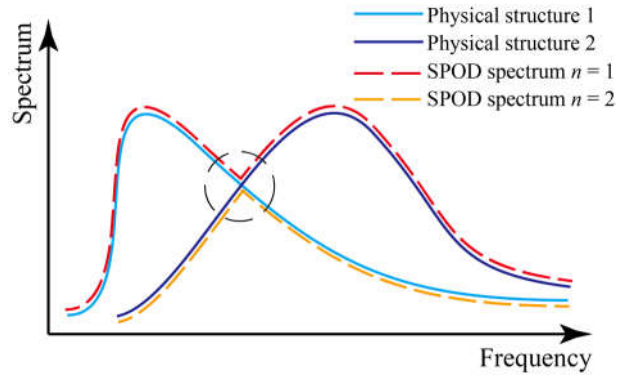


Figure 7.9 Schematic of the manner by which SPOD spectrum shows multiple physical structures.

In the SPOD spectrum of Figures 7.6 and 7.7, it can be noted that the large energy values with the bright colours exhibit the shapes with a 45-degree inclination, indicating the spanwise wavenumber is always roughly proportion to the frequency when large energy values are obtained, regardless of the scales of the structures. The ratio of the nondimensional wavenumber and frequency ($= |\eta U_{\text{ref}}/f|$) is approximately 3 if the central lines of the shapes are taken. Similar linear relation between the streamwise and spanwise length scales was also found in high-Reynolds-number turbulent boundary layer by Chandran et al. (2017). They indicated that this linear relation is a necessary condition for self-similarity, i.e., the range of scales with an equal energetic contribution to the streamwise velocity maintain a constant aspect ratio. This self-similarity theory is valid only for high-Reynolds-number turbulence. According to the aforementioned mode division, the modes in zones A and B are close to the lines of $|\eta U_{\text{ref}}/f| = 3$, so they are the main turbulent structures in this case. The modes in zones A and B correspond to the large- and small-scale structures, respectively. Because most of the modes in zones C and D are not adjacent to the lines of $|\eta U_{\text{ref}}/f| = 3$, these structures are relatively unstable and statistically less common.

In zone A, the modes mainly show the large-scale coherent structures outside the canyon. These modes have the highest eigenvalues, indicating that the fluctuation in these patterns is in strong intensity, and holds a large amount of TKE. The low- and high-momentum fluid caused by the large-scale coherent structures can strongly affect pollutant removal (Han et al., 2018; Michioka et al., 2011; Michioka and Sato, 2012). Modes A1–A3 are examples. The eigenfunctions illustrated in Figure 7.8 (a)–(c) well depict the low- and high-momentum fluid with large streamwise length scales passing through the canyon. The fluctuation enters the canyon along the windward wall, directly strengthening or weakening the principal recirculation within the canyon. The energy distribution shows that the nondimensional time scales are 1–5 times of the nondimensional spanwise length scales, indicating that the streamwise length scales are much larger than the spanwise length scales, which is consistent with previous studies

(Jaroslowski et al., 2019; Volino et al., 2009). In the figures of spanwise variations, the external coherent structures exhibit large-scale vortices on the y - z planes, which are identical on the planes of $x/H = 0.5$ and 0.9 because of the large streamwise scale of these structures. However, the pattern within the canyon differs for $x/H = 0.5$ and 0.9 . On the plane of $x/H = 0.5$, which is the middle of the canyon, the flow is divided clear at the roof level so that the external fluid can hardly be brought into the canyon, while on the plane of $x/H = 0.9$, the fluid is exchanged near the windward wall, which may contribute to the ventilation of the canyon.

In these three modes, mode A1 differs from the other two. Previous studies (Lee et al., 2011; Michioka et al., 2011; Takimoto et al., 2013) measured the streamwise length scale of the coherent structures at $z \approx 2H$, which are approximately $6\text{--}9H$. This roughly corresponds to the frequency of modes A2 and A3. However, the frequency of mode A1 ($\approx U_{\text{ref}}/20H$) corresponds to the period in which the flow needs to pass the simulation domain through the inlet and outlet periodically. This fluctuation pattern is not caused by the roughness of the canyon, and is thus unphysical but inevitable in LES simulation. It can be regarded as the slow change in the approaching flow due to external conditions such as meteorological variation. Its effect on the flow around the canyon is almost the same with the fluctuation caused by the canyon roughness.

The modes in zone B are characterised by the wave caused by the Kelvin–Helmholtz instabilities at the interface of the canyon and external flow. The eigenfunctions of modes B1 and B2 in Figure 7.8 (d) and (e) are considered good visualisation of the Kelvin–Helmholtz instabilities. Previous studies have indicated that Kelvin–Helmholtz instabilities render intermittent pollutant dispersion (Cui et al., 2004; Letzel et al., 2008). On the x - z plane, the vortices generated at the roof level move downstream and enter the canyon following the principal recirculation within the canyon. On the y - z plane, it can be seen that the array of waves provides high-rate ejection and sweep events, which enhance the exchanging of the fluid on the roof level. The fact that vortices enter the canyon along the windward wall is also embodied in the figures of the spanwise variation on the plane of $x/H = 0.9$ by the slanting stripes.

Most of the modes in zones C and D does not satisfy the self-similarity. As a representation, mode C in Figure 7.8 (f) shows the vortices along the streamwise direction occurring at the interface of the canyon and external flow. These vortices have relatively large scales on the streamwise direction, and small scales on the spanwise direction. These vortices separate when they reach the free end of the downstream building. A part of them enters the canyon and travels with the principal recirculation,

similar to the structures of the Kelvin–Helmholtz vortices. The high-rate air exchanging can be also observed in the spanwise direction.

The modes in zone D mainly depict the external vortices. Complex and various structures are observed in these modes, and finding a common character in shapes is difficult. For example, both modes D1 and D2 illustrated in Figure 7.8 (g) and (f) show the external vortices travelling upon the canyon, but their shapes vary largely. Castro et al. (2006) showed that the dominant length scales in the roughness sublayer (the region within which the flow remains spatially inhomogeneous) are of the same order as the canyon length scale. This length scale is close to those of the Kelvin–Helmholtz instabilities depicted by the modes in zone B. Therefore, the modes in zones B and D share the same frequencies. However, the spanwise wavenumbers largely differ, indicating different spanwise scales between them. Our previous study in Chapter 6 did not separate these two structures well, because the spanwise fluctuation was not considered, while the decomposition in this study gives a better visualisation.

The percentage of the whole-field TKE in each zone is also listed in Table 7.3. In the gross, most of the whole-field TKE is held by the external fluctuation out of the canyon (zones A and D), which can also be confirmed by Figure 7.5 (b), due to its large spatial scale. Especially, zone A, where the modes mainly show the very large-scale external coherent structures, holds the largest percentage of TKE. The fluctuation caused by the Kelvin–Helmholtz instabilities at the roof level, shown in the modes in zone B, also accounts for a considerable part of TKE, because the TKE shows maximum values at the roof level.

7.4.3 Results of SPOD co-spectrum

The two SPOD co-spectra defined in Section 7.3.3 are applied to evaluate the performance of turbulent structures on the pollutant removal at the roof level. The two SPOD co-spectra are integrated over the line at the roof level and nondimensionalised by the following equations:

$$\underline{S}_n^{(uw)}(\eta, f) = \frac{f\eta \int_{\Gamma} S_n^{(uw)} d\Gamma}{\left| \int_{\Gamma} E(u'w') d\Gamma \right|}, \quad (7.24)$$

$$\underline{S}_n^{(wc)}(\eta, f) = \frac{f\eta \int_{\Gamma} S_n^{(wc)} d\Gamma}{\int_{\Gamma} E(w'c') d\Gamma}. \quad (7.25)$$

The integral domain Γ is defined as

$$\Gamma = \{(x, z) | 0 \leq x \leq H, \quad z = H\}, \quad (7.26)$$

which denotes the line at the roof level. The absolute operator is applied on the denominator in Eq. (7.24), because the Reynolds shear stress $E(u'w')$ is negative at the roof level.

The nondimensionalised SPOD co-spectrum between the streamwise and vertical fluctuation velocity, $\underline{S}_n^{(uw)}$, and the nondimensionalised SPOD co-spectrum between the vertical fluctuation velocity and concentration, $\underline{S}_n^{(wc)}$, are presented in Figures 7.10 and 7.11, respectively. The $\underline{S}_n^{(uw)}$ and $\underline{S}_n^{(wc)}$ are examined at each resolved (f, η) point only for the modes with $n = 1$, which is considered sufficient for analytical purposes. Note that $\underline{S}_n^{(uw)}$ and $\underline{S}_n^{(wc)}$ are theoretically symmetric with respect to the original point on the f - η plane, so only two quadrants, $(f > 0, \eta > 0)$ and $(f > 0, \eta < 0)$, are shown. Also note that $\underline{S}_n^{(uw)}$ and $\underline{S}_n^{(wc)}$ is almost symmetric with respect to $\eta = 0$, indicating the statistical symmetry of both the velocity and concentration along the spanwise direction.

The distributions of $\underline{S}_1^{(uw)}$ and $\underline{S}_1^{(wc)}$ in the figures show high similarity, although the former is negative and the latter is positive. According to the theory of Fourier analysis, the co-spectrum denotes the in-phase component of the cross-spectrum. A positive value in the co-spectrum indicates a phase difference near 0, and a large negative value indicates a phase difference near π . The magnitude denotes the amplitude of the two signals at the specified frequency/wavenumber. In the current case, the negative values of $\underline{S}_1^{(uw)}$ indicate the negative correlation between the streamwise and vertical velocity, which implies the ejection ($u' < 0, w' > 0$) and sweep ($u' > 0, w' < 0$) events at the roof level. The positive values of $\underline{S}_1^{(wc)}$ indicate the positive correlation between the vertical velocity and concentration. Because the pollutant removal events are denoted by the positive values of the vertical mass flux ($w'c' > 0$), also given by the similar shape of $\underline{S}_1^{(uw)}$ and $\underline{S}_1^{(wc)}$, it can be concluded that the ejection events are highly related to the pollutant removal at the roof level. The same results can also be obtained by quadrant analysis performed in many studies (Cheng and Liu, 2011; Cui et al., 2004; Kikumoto and Ooka, 2012). The current study shows that the ejection and sweep events and the pollutant removal mainly occur at the wavenumber of $|\eta H| \approx 1-4$ and frequency of $|fH/U_{\text{ref}}| \approx 0.2-0.8$. A similar frequency range was also given by Michioka and Sato (2012), while the range of the spanwise wavenumber is revealed by the current study.

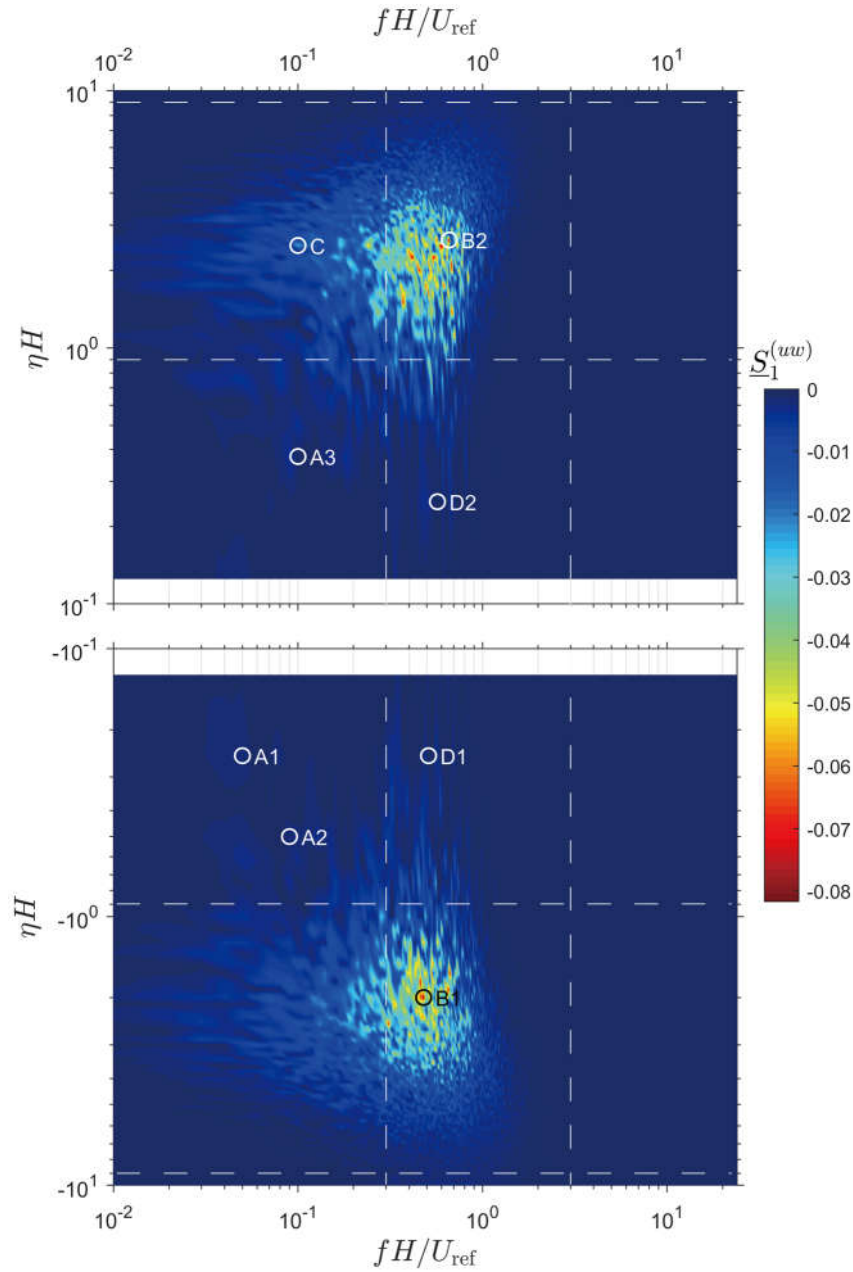


Figure 7.10 SPOD co-spectrum between the streamwise and vertical fluctuation velocity integrated spatially along the line at the roof level line ($0 \leq x/H \leq 1, z/H = 1$) computed based on the leading mode ($n = 1$). This co-spectrum is theoretically symmetric with respect to the original point on the f - η plane, so only two quadrants are shown. At each resolved (f, η) point, the co-spectrum value denotes the density of the Reynolds shear stress $E(u'w')$ contributed by the corresponding SPOD mode.

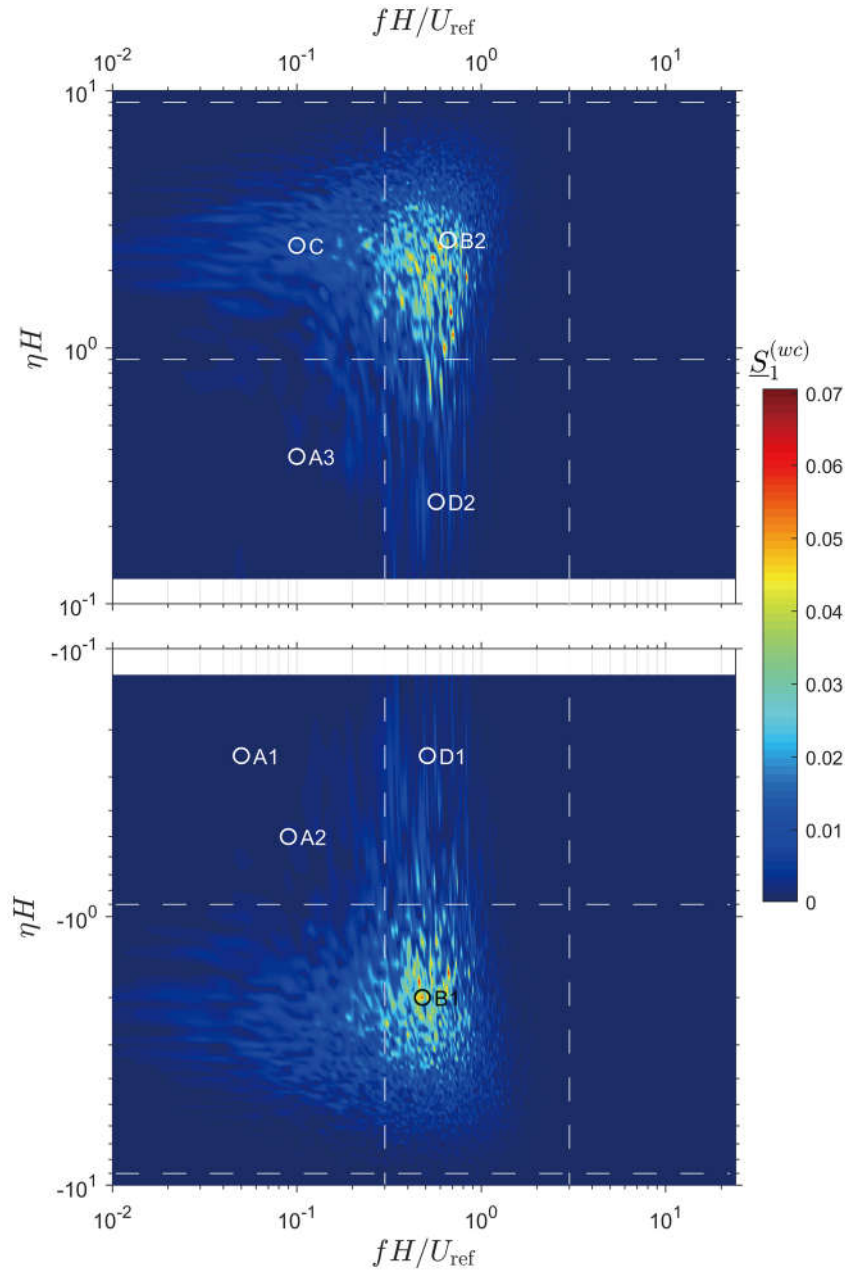


Figure 7.11 SPOD co-spectrum between the vertical fluctuating velocity and concentration integrated spatially along the line at the roof level line ($0 \leq x/H \leq 1, z/H = 1$) computed based on the leading mode ($n = 1$). This co-spectrum is theoretically symmetric with respect to the original point on the f - η plane, so only two quadrants are shown. At each resolved (f, η) point, the co-spectrum value denotes the density of the vertical turbulent mass flux $E(w'c')$ contributed by the corresponding SPOD mode.

Another advantage of SPOD is that the fluctuation patterns corresponding to the energy values in the co-spectrum can be easily specified, so that the ejection and sweep events and the effect of the pollutant removal can be directly linked to the turbulent structures depicted by the SPOD modes. The modes in zone B fall in both the ranges of wavenumber and frequency, and the modes in zone C and D fall in either of the ranges. These structures are considered related to pollutant removal at the roof level.

To quantify the pollutant removal contributed by the modes in each zone, the percentage of the vertical turbulent mass flux at the roof level that the modes in each zone contribute is listed in Table 7.3. These values are calculated by integrating the SPOD co-spectrum within a specific range of frequency/wavenumber by Eq. (7.22) and then dividing the total vertical turbulent mass flux at the roof level. Although the modes in zone A accounted for the largest percentage of the TKE, they only contributed 8% of the vertical turbulent mass flux at the roof level, indicating that the pollutant provided by the large-scale coherent structures is very limited. For the small-scale structures, 40% of the vertical turbulent mass flux is contributed by the modes in zone B, which denote the Kelvin–Helmholtz instabilities. The modes in zones C and D also show good performance in pollutant removal, by contributing 22% and 29% of the vertical turbulent mass flux.

Although the pollutant removal contributed by the modes in zone A is little in the gross, they still have their roles in pollutant removal near the windward wall. This can be confirmed by the spatial variation of the SPOD co-spectrum $S_n^{(wc)}$, provided in Figure 7.12. The peaks can be observed near $x/H = 0.9$ for modes A1–A3, which corresponds to the air exchanging illustrated in the spanwise structures in Figure 7.8 (a)–(c). For the modes in zones B and C, one can see from Figure 7.12 that the pollutant removal mainly occurs in the middle of the target canyon, which indicates a trend that the fluctuation caused by these vortices grows to be the strongest near the centre, then becomes weaker in moving downstream, and finally collides the windward wall and enters the canyon. For the modes in zone D, it is difficult to find a common pattern on the air exchanging, because the shapes of the external vortices vary significantly depending on the chosen modes.

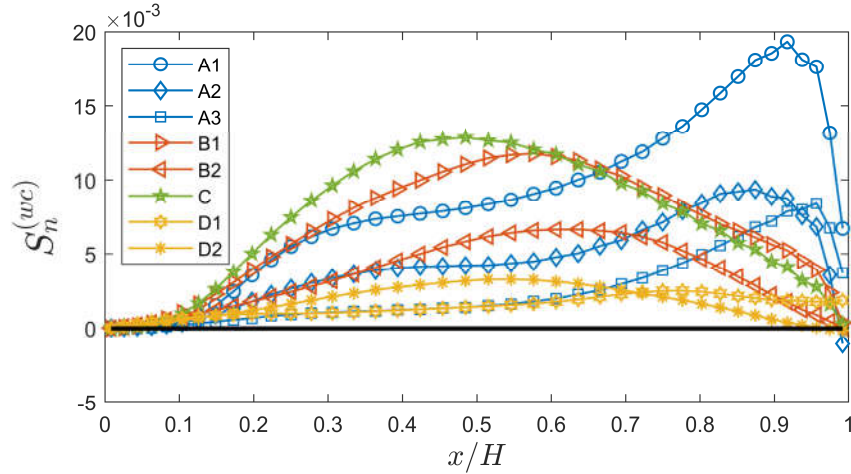


Figure 7.12 Spatial variation of the SPOD co-spectrum values for the eight selected modes along the line at the roof level line ($0 \leq x/H \leq 1$, $z/H = 1$). These results indicate that different flow patterns provide pollutant removal at different spatial positions.

7.5 Nonlinear interactions between large- and small-scale structures

The nonlinear interactions between the large- and small-scale structures in street canyon were first investigated by Blackman and Perret (2016) by the skewness decomposition and correlation analysis. They found that, as the high- or low-momentum fluids carried by the large-scale structures pass over the canyon, the small-scale structures are amplified or suppressed. Therefore, the large-scale structures may indirectly contribute to the turbulent removal. Please refer to Figure 17 in Blackman and Perret (2016) for a more intuitive view. The effects of the upstream-flow regime and canyon aspect ratio on these nonlinear interactions is further investigated in Blackman et al. (2018). The same interactions are also confirmed by Jaroslowski et al. (2020) using a different filtering process. Although these findings are quite attractive, the correlation coefficients are only around 0.2 and no larger than 0.5, which, in our opinion, is too low to be considered as solid evidence. Because there still does not exist a strict physical or mathematical definition of the large- or small-scale structures, the computed correlation coefficients highly depend on the different mathematical assumptions made in the decomposition process. This gives difficulty in quantitative analysis on this problem.

Because the current study provides specific spatial fluctuation patterns that can directly link to the already-known mechanisms of large- or small-scale structures, the nonlinear interactions between them can be further investigated based on the obtained SPOD modes to provide more intuitive and quantitative insights via the joint probability distributions of the states of the fluctuation patterns.

7.5.1 Definition of the mode state

We start by computing the state of the fluctuation patterns of interest, which can be defined as the projection of the fluctuation velocity on the corresponding mode. For a certain mode X indexed by (f, η, n) , the state at (y, t) can be written as

$$\zeta_X(y, t) = \langle \mathbf{u}', \boldsymbol{\psi}_n \rangle. \quad (7.27)$$

The state ζ_X is a two-dimensional complex-valued stochastic process. For a better understanding of the concept of the state, please recall the periodic fluctuation pattern depicted by mode X , the animation of which provides the variation of the field on x - z plane with the phase changing from 0 to 2π with the unit intensity. The realisation of the flow at (y, t) is constructed by the modes, so a part of it can be denoted by a snapshot of the periodic fluctuation indicated by mode X at a certain phase and multiplied by a certain intensity value. Both the phase and intensity values are stochastic processes over y and t . The phase is denoted by the argument of the complex state, and the intensity is denoted by the modulus of the complex state.

7.5.2 Correlation analysis between the states of large- and small-scale structures

We first study statistics on this state process performed base on the samples over both time and spanwise direction without distinguishment. The probability distribution of such a process shows different shapes for large- and small-scale structures represented by, e.g., modes A1 and B1. The probability density functions are provided in Figure 7.13 (a) and (b). The distribution for a large-scale structure (mode A1) shows a stretched shape along a certain direction on the complex plane, while that for a small-scale structure (mode B1) shows a nearly isotropic shape. This difference is directly related to the spatial scale of the structure. Note that the width of the sampling domain in this study is two times of the canyon length scales, which is much larger than that of small-scale structures, and much smaller than that of large-scale structures. Therefore, for the small-scale structures, the spatial periodic motions occur totally within the sampling domain, so the kinetic energy within the entire sampling domain does not change much with the phase of the fluctuation. However, it is not the case for large-scale structures. The sampling domain is periodically filled by the low- or high-momentum fluids, which causes a significant change in the kinetic energy. These reflect well on the magnitude of the fluctuation states.

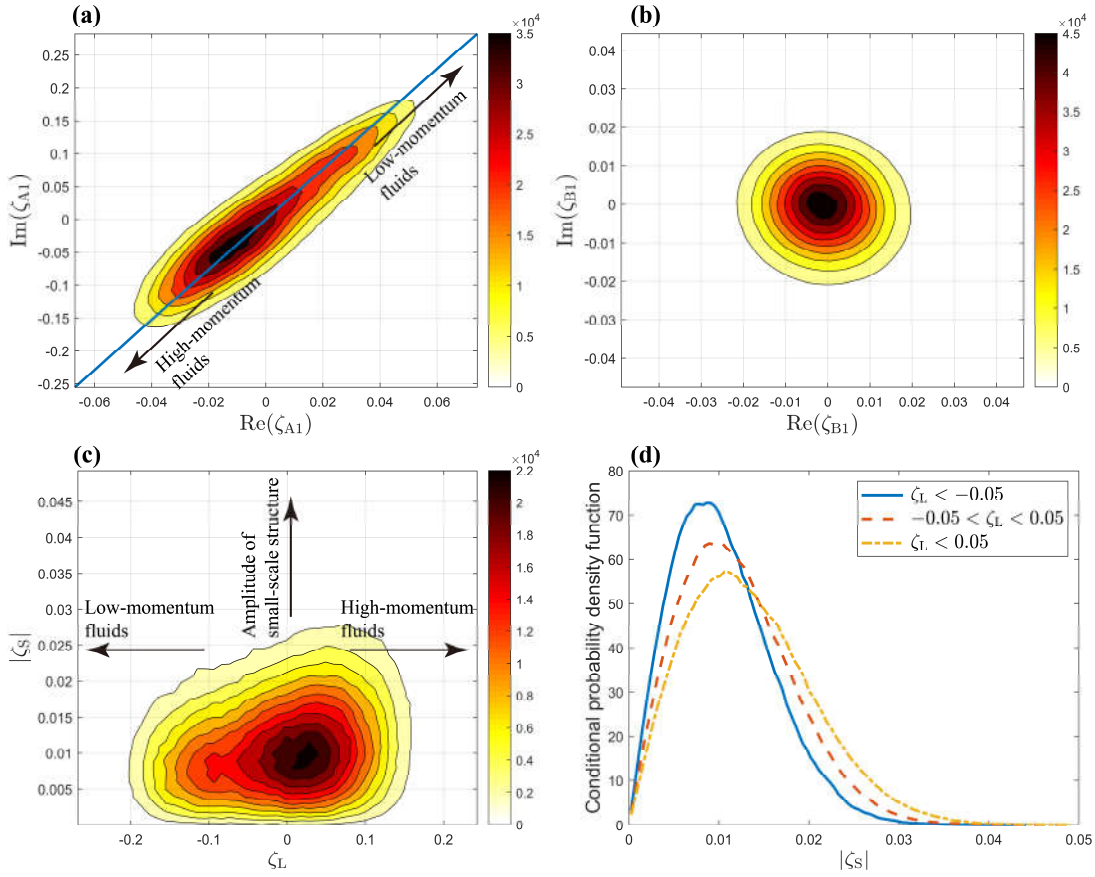


Figure 7.13 Probability density functions of the fluctuation states. **(a)** Mode A1, representing the large-scale structure. **(b)** Mode B1, representing the small-scale structure. **(c)** Joint probability density function between the state of the large-scale structure and the amplitude of the small-scale structure. **(d)** Conditional probability density functions of the amplitude of the small-scale structure under different state intervals of the large-scale structure. Please see the text for the definition and details of the fluctuation states.

Therefore, the target of the next step is to identify the phase denoting the appearance of the low- or high-momentum fluids, i.e., the main stretching direction in Figure 7.13 (a). This can be easily realised by solving the eigenvector (the one corresponding to the larger eigenvalue) of the following matrix:

$$\begin{bmatrix} E(\operatorname{Re}(\zeta_{A1})\operatorname{Re}(\zeta_{A1})) & E(\operatorname{Re}(\zeta_{A1})\operatorname{Im}(\zeta_{A1})) \\ E(\operatorname{Im}(\zeta_{A1})\operatorname{Re}(\zeta_{A1})) & E(\operatorname{Im}(\zeta_{A1})\operatorname{Im}(\zeta_{A1})) \end{bmatrix}. \quad (7.28)$$

Alternatively, one can also perform a line fitting for the state samples, which was also tried in this study and the result will show little difference. In this study, the eigenvector is adopted, the direction of which is shown by the blue line in Figure 7.13 (a). One can refer to the shape of the corresponding mode to judge which of the two opposite directions of that line is for the high-momentum fluids. For example, the imaginary part of the mode ψ_n shown in Figure 7.8 (a) presents the external fluctuation velocities which have the same direction of the mean wind. This indicates the high-momentum fluids. Therefore, if \mathbf{u}' also presents the same shape as the high-momentum fluids, the

inner product in Eq. (7.27) will result in a complex value with a relatively large negative imaginary part.

The fluctuation state for the large-scale structure, ζ_L , is defined as the projection of ζ_{A1} on the blue line in Figure 7.13 (a), and the fluctuation state for the small-scale structure, ζ_S , is defined as equal to ζ_{B1} . At this stage, the relationship between ζ_L and $|\zeta_S|$ is studied, where $|\cdot|$ denotes the modulus of a complex number. The correlation coefficient between them is defined as

$$R = \frac{\sum_{y_j, t_j} \zeta_L |\zeta_S| - \frac{1}{M} \sum_{y_j, t_j} \zeta_L \sum_{y_j, t_j} |\zeta_S|}{\sqrt{\left(\sum_{y_j, t_j} \zeta_L^2 - \frac{1}{M} \left(\sum_{y_j, t_j} \zeta_L \right)^2 \right) \left(\sum_{y_j, t_j} |\zeta_S|^2 - \frac{1}{M} \left(\sum_{y_j, t_j} |\zeta_S| \right)^2 \right)}}, \quad (7.29)$$

where y_l and t_j are the resolved y -coordinates and time, $l = 1, 2, \dots, 160, j = 1, 2, \dots, 48000$, M is the number of the samples which equals the product between the numbers of the resolved y -coordinates (160) and time (48,000). In this case, the correlation coefficient is found approximately 0.19. To confirm the universality, the same procedure was repeated for choosing modes A1–A3 as the large-scale structure and B1–B2 as the small-scale structure in turn. The resulted correlation coefficients are listed in Table 7.4, which are all around 0.2. The results are roughly consistent with those in Blackman and Perret (2016), although totally different filtering methods are applied. The correlation coefficients may imply the weak correlation between the motion of the large-scale structures and the amplitude of the small-scale structures.

Table 7.4 Correlation coefficients between the state of the large-scale structure and the amplitude of the small-scale structure when choosing various modes as the large- and small-scale structure.

Correlation coefficients		Mode chosen as the large-scale structure		
		A1	A2	A3
Mode chosen as the small-scale structure	B1	0.1936	0.1958	0.1949
	B2	0.2134	0.2184	0.2163

However, because such low correlation coefficients may be attributed to statistical uncertainties rather than correlation, the joint probability density function is further examined. Figure 7.13 (c) provides the joint probability density function between ζ_L and $|\zeta_S|$ when choosing modes A1 as the large-scale structure and B1 as the small-scale structure. The results are similar if other modes are chosen. The figure shows that, with the increase of ζ_L , $|\zeta_S|$ has the larger probability to become large. Although it is not a

necessary outcome, the small-scale structure has a good chance to be amplified or suppressed by the high- or low-momentum fluids. The conditional probability density functions of $|\zeta_s|$ under the conditions of $\zeta_L < -0.05$, $-0.05 < \zeta_L < 0.05$, and $\zeta_L > 0.05$, are plotted in Figure 7.13 (d). These distributions also show the same tendency. Quantitatively, the amplitude of the small-scale structure under a strong high-momentum fluid is approximately 29% larger than that under a strong low-momentum fluid, and 13% larger than that when the large-scale structures are absent. These values are computed based on the comparisons of the expectations of the three conditional probability distributions.

Finally, the statistics were performed base on the samples over the time and spanwise direction separately, to confirm that the nonlinear interactions occur along both the directions. The correlation coefficient over either direction is calculated as follow:

$$R_t(y_l) = \frac{\sum_{t_j} \zeta_L |\zeta_s| - \frac{1}{48000} \sum_{t_j} \zeta_L \sum_{t_j} |\zeta_s|}{\sqrt{\left(\sum_{t_j} \zeta_L^2 - \frac{1}{M} \left(\sum_{t_j} \zeta_L \right)^2 \right) \left(\sum_{t_j} |\zeta_s|^2 - \frac{1}{48000} \left(\sum_{t_j} |\zeta_s| \right)^2 \right)}}, \quad l = 1, 2, \dots, 160, \quad (7.30)$$

$$R_y(t_j) = \frac{\sum_{y_l} \zeta_L |\zeta_s| - \frac{1}{160} \sum_{y_l} \zeta_L \sum_{y_l} |\zeta_s|}{\sqrt{\left(\sum_{y_l} \zeta_L^2 - \frac{1}{M} \left(\sum_{y_l} \zeta_L \right)^2 \right) \left(\sum_{y_l} |\zeta_s|^2 - \frac{1}{160} \left(\sum_{y_l} |\zeta_s| \right)^2 \right)}}, \quad j = 1, 2, \dots, 48000. \quad (7.31)$$

R_t denotes the correlation coefficient over the time, which varies with y and has 160 samples. R_y denotes the correlation coefficient over the spanwise direction, which varies with t and has 48,000 samples. Again, the example of choosing modes A1 as the large-scale structure and B1 as the small-scale structure is given, but the results are similar if other modes are chosen. The results are provided in Figure 7.14 by presenting the probability density function of the correlation coefficients. The majority of the samples of both correlation coefficients show positive values, which indicates the nonlinear interactions between the large- and small-scale structures occurs along both the time and spanwise direction.

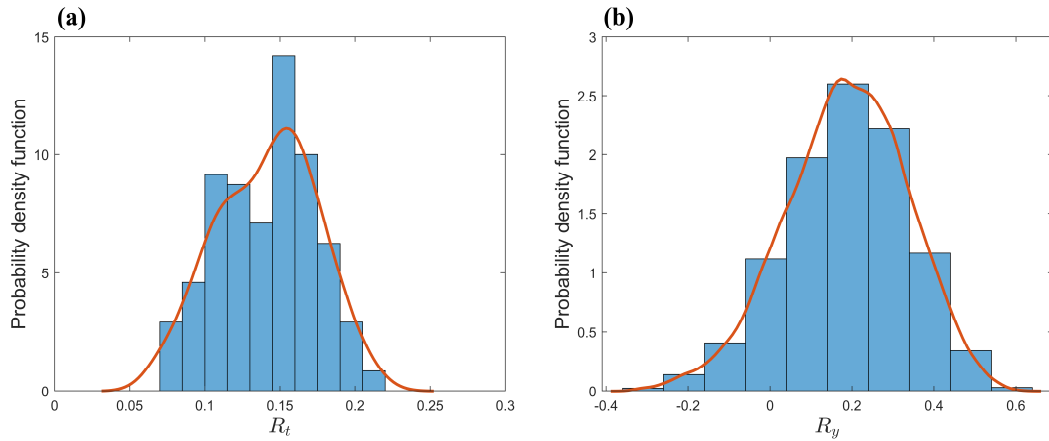


Figure 7.14 Probability density functions of the correlation coefficient over (a) the time and (b) spanwise direction. Please see the text for more information.

7.6 Summary

This chapter continued the study of Chapter 6 on elucidating the turbulent structures within a two-dimensional street canyon, and seeking their contributes to the pollutant removal. To extract the turbulent structures over the spanwise direction, this study applied a technique named SPOD with 2DFT, which combines the spatial modal decomposition of POD along the streamwise and vertical directions and the Fourier modal decomposition along the time and the spanwise direction. The SPOD spectrum and co-spectra were all modified based on this technique. The modes showing the various fluctuation patterns were better visualised than Chapter 6, and their intensities and contributions to the pollutant removal were quantitatively analysed via the SPOD spectrum and co-spectra. In addition, based on these results, the nonlinear interactions between the large- and small-scale structures were discussed. The following was observed.

(1) Because of the increase of the flow realisations, clearer shapes of turbulent structures were illustrated by the modes than the previous study. The large-scale structures mainly directly strengthen or weaken the principal recirculation within the canyon, and provide the air exchange mainly near the windward wall. The small-scale coherent structures provide the air exchange via the vortices induced by the Kelvin–Helmholtz instabilities. Not like the previous study where the Kelvin–Helmholtz vortices and the external vortices were presented in the same mode, the Kelvin–Helmholtz vortices was decomposed completely this time. These periodic fluctuation patterns are detected along both time and spanwise direction with specific frequencies and wavenumbers.

(2) The nondimensional spanwise length scales were found approximately 1–5 times of

the nondimensional time scales for both large- and small-scale structures, although the mechanisms of these structures differ. This can be explained by the self-similarity of the high-Reynolds-number turbulence, i.e., a constant aspect ratio of the length scale is maintained.

(3) On the SPOD co-spectra, the sweep and ejection events at the roof level mainly occurred at the spanwise wavenumber of $|\eta H| \approx 1-4$ and frequency of $|fH/U_{\text{ref}}| \approx 0.2-0.8$. This range coincided with that of the small-scale structures caused by the Kelvin–Helmholtz instabilities at the roof level. The same range of wavenumber and frequency were found for pollutant removal, indicating that the small-scale structures at the roof level contribute the most to the pollutant removal.

(4) Although the large-scale structures contributed less to the pollutant removal than the small-scale structures, they still had a good chance to enhance the pollutant removal indirectly by amplifying the small-scale structures. The correlation coefficient between the amplitude of the small-scale structures and the state of the large-scale structures was found approximately 0.2. The joint probability distribution indicated that the high- and low-momentum fluids passing through the canyon were related to the amplifying and suppressing of the small-scale structures. This phenomenon occurred stochastically along both the time and spanwise direction. Quantitatively, the amplitude of the small-scale structure under a strong high-momentum fluid is approximately 29% larger than that under a strong low-momentum fluid, and 13% larger than that when the large-scale structures are absent.

This study has provided significant insights into the turbulent structures and pollutant removal mechanism of a two-dimensional street canyon. However, we have restricted ourselves to the single geometry of the canyon, while previous studies have shown that the upstream-flow regime and aspect ratio can largely affect the turbulent structures (Blackman et al., 2018; Liu et al., 2005; Michioka and Sato, 2012), and thus may change the nature of pollutant removal. Further work may focus on discovering the variation of the turbulent structures when these factors are changed.

Reference

- Araya, D.B., Colonius, T., Dabiri, J.O., 2017. Transition to bluff-body dynamics in the wake of vertical-axis wind turbines. *J. Fluid Mech.* 813, 346–381.
<https://doi.org/10.1017/jfm.2016.862>
- Aubry, N., Holmestil, P., John, L., Stone, E., 1988. The dynamics of coherent structures in the wall region of a turbulent boundary layer. *J. Fluid Mech.* 192, 115–173.
<https://doi.org/10.1017/S0022112088001818>

- Berkooz, G., Holmes, P., Lumley, J.L., 1993. The Proper Orthogonal Decomposition in the Analysis of Turbulent Flows. *Annu. Rev. Fluid Mech.* 25, 539–575. <https://doi.org/10.1146/annurev.fl.25.010193.002543>
- Blackman, K., Perret, L., 2016. Non-linear interactions in a boundary layer developing over an array of cubes using stochastic estimation. *Phys. Fluids* 28, 095108. <https://doi.org/10.1063/1.4962938>
- Blackman, K., Perret, L., Savory, E., 2018. Effects of the Upstream-Flow Regime and Canyon Aspect Ratio on Non-linear Interactions Between a Street-Canyon Flow and the Overlying Boundary Layer. *Boundary-Layer Meteorol.* 169, 537–558. <https://doi.org/10.1007/s10546-018-0378-y>
- Bright, V.B., Bloss, W.J., Cai, X., 2013. Urban street canyons: Coupling dynamics, chemistry and within-canyon chemical processing of emissions. *Atmos. Environ.* 68, 127–142. <https://doi.org/10.1016/j.atmosenv.2012.10.056>
- Carassale, L., Solari, G., Tubino, F., 2007. Proper orthogonal decomposition in wind engineering - Part 2: Theoretical aspects and some applications. *Wind Struct.* 10, 177–208. <https://doi.org/10.12989/was.2007.10.2.177>
- Castro, I.P., Cheng, H., Reynolds, R., 2006. Turbulence over urban-type roughness: Deductions from wind-tunnel measurements. *Boundary-Layer Meteorol.* 118, 109–131. <https://doi.org/10.1007/s10546-005-5747-7>
- Chandran, D., Baidya, R., Monty, J.P., Marusic, I., 2017. Two-dimensional energy spectra in high-Reynolds-number turbulent boundary layers. *J. Fluid Mech.* 826, R1. <https://doi.org/10.1017/jfm.2017.359>
- Cheng, W.C., Liu, C.H., 2011. Large-Eddy Simulation of Flow and Pollutant Transports in and Above Two-Dimensional Idealized Street Canyons. *Boundary-Layer Meteorol.* 139, 411–437. <https://doi.org/10.1007/s10546-010-9584-y>
- Cheng, W.C., Liu, C.H., Leung, D.Y.C., 2008. Computational formulation for the evaluation of street canyon ventilation and pollutant removal performance. *Atmos. Environ.* 42, 9041–9051. <https://doi.org/10.1016/j.atmosenv.2008.09.045>
- Cui, Z., Cai, X., J. Baker, C., 2004. Large-eddy simulation of turbulent flow in a street canyon. *Q. J. R. Meteorol. Soc.* 130, 1373–1394. <https://doi.org/10.1256/qj.02.150>
- Derebail Muralidhar, S., Podvin, B., Mathelin, L., Fraigneau, Y., 2019. Spatio-temporal proper orthogonal decomposition of turbulent channel flow. *J. Fluid Mech.* 864, 614–639. <https://doi.org/10.1017/jfm.2019.48>
- Han, B.S., Baik, J.J., Kwak, K.H., Park, S.B., 2018. Large-eddy simulation of reactive pollutant exchange at the top of a street canyon. *Atmos. Environ.* 187, 381–389. <https://doi.org/10.1016/j.atmosenv.2018.06.012>
- Issa, R.I., 1986. Solution of the implicitly discretised fluid flow equations by operator-splitting. *J. Comput. Phys.* 62, 40–65. [https://doi.org/10.1016/0021-9991\(86\)90099-9](https://doi.org/10.1016/0021-9991(86)90099-9)
- Jaroslowski, T., Perret, L., Blackman, K., Savory, E., 2019. The Spanwise Variation of Roof-Level Turbulence in a Street-Canyon Flow. *Boundary-Layer Meteorol.* 170, 373–394. <https://doi.org/10.1007/s10546-018-0405-z>
- Jaroslowski, T., Savory, E., Perret, L., 2020. Roof-level large- and small-scale coherent structures in a street canyon flow. *Environ. Fluid Mech.* 20, 739–763. <https://doi.org/10.1007/s10652-019-09721-w>
- Kikumoto, H., Ooka, R., 2012. A numerical study of air pollutant dispersion with bimolecular chemical reactions in an urban street canyon using large-eddy simulation. *Atmos. Environ.* 54, 456–464. <https://doi.org/10.1016/j.atmosenv.2012.02.039>
- Lee, J.H., Sung, H.J., Krogstad, P.Å., 2011. Direct numerical simulation of the turbulent boundary layer over a cube-roughened wall. *J. Fluid Mech.* 669, 397–431. <https://doi.org/10.1017/S0022112010005082>
- Letzel, M.O., Krane, M., Raasch, S., 2008. High resolution urban large-eddy simulation studies from street canyon to neighbourhood scale. *Atmos. Environ.* 42, 8770–8784. <https://doi.org/10.1016/j.atmosenv.2008.08.001>
- Liu, C.H., Leung, D.Y.C., Barth, M.C., 2005. On the prediction of air and pollutant exchange rates in street canyons of different aspect ratios using large-eddy simulation. *Atmos. Environ.* 39, 1567–1574.

- <https://doi.org/10.1016/j.atmosenv.2004.08.036>
- Liu, C.H., Wong, C.C.C., 2014. On the pollutant removal, dispersion, and entrainment over two-dimensional idealized street canyons. *Atmos. Res.* 135–136, 128–142. <https://doi.org/10.1016/j.atmosres.2013.08.006>
- Michioka, T., Sato, A., 2012. Effect of Incoming Turbulent Structure on Pollutant Removal from Two-Dimensional Street Canyon. *Boundary-Layer Meteorol.* 145, 469–484. <https://doi.org/10.1007/s10546-012-9733-6>
- Michioka, T., Sato, A., Takimoto, H., Kanda, M., 2011. Large-Eddy Simulation for the Mechanism of Pollutant Removal from a Two-Dimensional Street Canyon. *Boundary-Layer Meteorol.* 138, 195–213. <https://doi.org/10.1007/s10546-010-9556-2>
- Pavageau, M., Schatzmann, M., 1999. Wind tunnel measurements of concentration fluctuations in an urban street canyon, in: *Atmospheric Environment*. Pergamon, pp. 3961–3971. [https://doi.org/10.1016/S1352-2310\(99\)00138-7](https://doi.org/10.1016/S1352-2310(99)00138-7)
- Schmidt, O.T., Towne, A., Colonius, T., Cavalieri, A.V.G., Jordan, P., Brès, G.A., 2017. Wavepackets and trapped acoustic modes in a turbulent jet: Coherent structure eduction and global stability. *J. Fluid Mech.* 825, 1153–1181. <https://doi.org/10.1017/jfm.2017.407>
- Sirovich, L., 1987. Turbulence and the dynamics of coherent structures. I. Coherent structures. *Q. Appl. Math.* 45, 561–571.
- Spalding, D.B., 1962. A new analytical expression for the drag of a flat plate valid for both the turbulent and laminar regimes. *Int. J. Heat Mass Transf.* 5, 1133–1138. [https://doi.org/10.1016/0017-9310\(62\)90189-8](https://doi.org/10.1016/0017-9310(62)90189-8)
- Takimoto, H., Inagaki, A., Kanda, M., Sato, A., Michioka, T., 2013. Length-Scale Similarity of Turbulent Organized Structures over Surfaces with Different Roughness Types. *Boundary-Layer Meteorol.* 147, 217–236. <https://doi.org/10.1007/s10546-012-9790-x>
- Towne, A., Schmidt, O.T., Colonius, T., 2018. Spectral proper orthogonal decomposition and its relationship to dynamic mode decomposition and resolvent analysis. *J. Fluid Mech.* 847, 821–867. <https://doi.org/10.1017/jfm.2018.283>
- Tutkun, M., George, W.K., 2017. Lumley decomposition of turbulent boundary layer at high Reynolds numbers. *Phys. Fluids* 29. <https://doi.org/10.1063/1.4974746>
- Volino, R.J., Schultz, M.P., Flack, K.A., 2009. Turbulence structure in a boundary layer with two-dimensional roughness. *J. Fluid Mech.* 635, 75–101. <https://doi.org/10.1017/S0022112009007617>
- Welch, P.D., 1967. The Use of Fast Fourier Transform for the Estimation of Power Spectra: A Method Based on Time Averaging Over Short, Modified Periodograms. *IEEE Trans. Audio Electroacoust.* 15, 70–73. <https://doi.org/10.1109/TAU.1967.1161901>

Chapter 8

Conclusions and prospective

8.1 Conclusions

This study pioneers the applications of SPOD in wind environment fields. The applications in the following two classical cases were introduced: the flow field around single square-section building model and the two-dimensional street canyon flow. The effectivity of SPOD in identification of characteristic flow structures was well proved, even for the cases with very high Reynolds numbers. In addition, mathematical tools for evaluating the pedestrian-level wind environment and outdoor air exchanging are also developed in this study. The main findings of this study are listed as follow.

In Chapter 4, SPOD analysis was performed on the flow field around a square-section building model calculated by LES to identify the three-dimensional main flow features within the sampling field. The identified features, including the low-frequency modes related to the fluctuation of the incoming flow, primary wake vortex shedding (Kármán-type vortex shedding), tip and base vortices, and primary side vortex shedding (flow separation), were extracted from the single case at once. The primary frequency and the intensity of these features were revealed by studying the typical SPOD modes and estimating the energy percentage. In addition, the local-space SPOD spectrum was also defined to analyse the composition of the kinetic energy within some local parts of the sampling domain.

The identified flow features and their details are summarised as follows: first, two energetic modes at low frequency were chosen as the typical modes to depict the symmetric and antisymmetric fluctuations around the building. They were found to be directly related to the inflow fluctuation by the local-space SPOD spectrum. The primary wake vortex shedding was depicted using a complex mode at the Strouhal frequency, which exhibited periodic vortex shedding. The tip and base vortex pair on one side of the building appeared in one SPOD mode, which indicated their correlation. The mode also showed an arch structure by which the tip and base vortices were connected. The same

structure was found on the roof of the building illustrated by another mode, which showed the other kind of development of the tip vortices. The primary side vortex shedding caused by the strong shear force and separation appeared on both the roof and sides of the building. However, the vortices at different heights on the sides were not synchronised. Finally, the local-space SPOD spectrum precisely showed the different compositions of the fluctuation patterns on the front, side, and back of the prism. In general, the SPOD spectrum provided a comprehensive view of the turbulent structures in this flow field, which was an integration of all the above flow features. Unlike previous studies, where different flow features were studied by different physical quantities, this study revealed the primary frequency and intensity for all features, using a single mathematical process.

In Chapter 5, the target was focused on the pedestrian-level wind of the same case. The SPOD results for two simulation cases were compared, where the only difference was the existence of fluctuation at the inflow boundary, to show how the inflow fluctuation influenced the turbulent structures around the building. The results showed that the input of the inflow fluctuation on the inlet boundary had a significant influence on the turbulent structures at a low frequency because the modes and energy significantly differed. In both cases, the strongest modes corresponded to the Kármán-type vortex shedding, while the frequency was slightly larger when no fluctuation was input at the inflow boundary. The difference in the shapes of the Kármán-type vortex shedding was considered related to the difference in the mean velocity and TKE fields of the two cases. At a high frequency, flow separation phenomenon occurred on both sides of the building. In the case where no fluctuation was input at the inflow boundary, this phenomenon exhibited a peak on the distribution of energy, while it was not quite significant in the other case. A method was developed to decompose the TKE at a certain point and display the extent to which the fluctuating wind speed at the point is influenced by each mode. This is considered useful in the finding the main reason of large fluctuation and improvement of pedestrian-level wind.

In Chapter 6, the SPOD technique was applied to decompose the velocity field of a two-dimensional street canyon. The SPOD modes, depicting the large-scale coherent structures and Kelvin–Helmholtz instabilities, were well extracted and visualised. The SPOD modes depicted the Kelvin–Helmholtz instabilities as a series of vortices, which are generated at the roof level, and enter the canyon following the principal recirculation, while the fluctuation caused by the external large-scale coherent structures directly strengthens or weakens the principal recirculation. In addition, the ejection events and pollutant removal were quantitatively analysed using the newly defined SPOD co-spectra

to understand their relationships with the turbulent fluctuation patterns. The results showed that both Kelvin–Helmholtz instabilities and large-scale coherent structures can cause ejection and sweep events at the roof level, thus contributing to pollutant removal. However, the former contributed to stronger ejection and sweep events with stronger vertical components. The Kelvin–Helmholtz instabilities accounted for a small percentage of TKE, but they contributed most to the vertical turbulent mass flux at the roof level. In contrast, the large-scale coherent structures occupied a large proportion of the TKE, while they contributed less towards vertical turbulent mass flux. The intermittent concentration fluctuation fit better with the time scale of the Kelvin–Helmholtz instabilities.

In Chapter 7, the study on the two-dimensional street canyon flow is continued, but the spanwise performance and nonlinear interactions of the turbulent structures were mainly focused on. This was done by modifying the original SPOD to the one combining 2DFT. The SPOD co-spectrum defined in our previous study was also modified to a 2DFT version. As the result, the modes extracted by SPOD with 2DFT showed clearer shapes of turbulent structures than the previous study because of the increase of the flow realisations. These turbulent structures were depicted by periodic fluctuation patterns detected along both the time and spanwise direction with specific frequencies and wavenumbers. The nondimensional time scales were found approximately 1–5 times of the nondimensional spanwise length scales for both large- and small-scale structures, although the mechanisms of these structures differ. This can be explained by the self-similarity of the high-Reynolds-number turbulence, i.e., a constant aspect ratio of the length scale is maintained. The SPOD co-spectra showed that the sweep and ejection events at the roof level mainly occurred at the spanwise nondimensional wavenumber of 1–4 and frequency of 0.2–0.8. This range coincided with that of the small-scale structures caused by the Kelvin–Helmholtz instabilities at the roof level. The same range of wavenumber and frequency were found for pollutant removal. Although the large-scale structures contributed less to the pollutant removal than the small-scale structures, they still had a good chance to enhance the pollutant removal indirectly by amplifying the small-scale structures. The amplitude of the small-scale structures showed a weak but non-negligible correlation with the state of the large-scale structures. The joint probability distribution indicated that the high- and low-momentum fluids passing through the canyon were related to the amplifying and suppressing of the small-scale structures. This phenomenon appeared stochastically along both the time and spanwise direction.

8.2 Prospective for further work

As previously mentioned in the conclusions, this study is just the very beginning of the applications of SPOD in the wind environment field. As SPOD has shown its effectiveness and efficiency in the analysis of high-Reynolds-number turbulence, it has the potential to become another useful tool for further research or design in the field of wind environment. Further studies and applications for the following objectives are suggested.

(1) The studies in this thesis were restricted on the geometry and setting of building or canyon, while the studies can be extended on the following aspects:

- a. The flow around the square-section buildings with different aspect ratios (Sakamoto and Arie, 1983; Wang et al., 2009);
- b. Changing the attack angle of the flow in the single building case (Kawai, 1995);
- c. The wind-induced interference effects on multiple buildings (Khanduri et al., 1998; Kim et al., 2018);
- d. The canyons with different aspect ratios (Di Bernardino et al., 2018; Liu et al., 2005);
- e. The influence of the upstream-flow regime (Blackman et al., 2018; Jaroslawski et al., 2019; Michioka and Sato, 2012);
- f. The turbulent structures within three-dimensional street canyon flow (Inagaki and Kanda, 2010; Kanda, 2006; Michioka et al., 2014).

(2) Some new elements can also be added into the analysis of SPOD, listed as follow:

- a. Studies on wind-induced forces on buildings and the aerodynamically modifying the buildings. This is a new trend in building design. The aerodynamic characteristics of the building are highly related to the outer shapes (Sharma et al., 2019). It can be tried to modify the building shape according to the identified turbulent structure around it.
- b. The chemical reactions of the pollutant. Some reactive pollutants can still be considered as passive scalar quantities, because their chemical oxidation time scale is much longer than the canyon dynamical time scale. However, it is not the case for the relatively short-lived traffic-related pollutants (Zhong et al., 2016). Some studies (Han et al., 2018; Kikumoto and Ooka, 2012) have been conducted for the transport of these pollutants. It is considered interesting to study the relationship between turbulent structures and the reaction rates
- c. Techniques for improving the pollutant removal of pollution from urban canyons. For example, a modification of roof infrastructures was suggested by Cintolesi et al. (2021). SPOD might have the potential ability to provide a deeper insight on its mechanism and attempt to optimise the design.

- d. Study on the in-canyon flow or turbulence. These might accelerate or decelerate the pollutant travelling from the bottom to the top of the canyon, and the fresh air entering the canyon and mixing. Additional quantities can be defined to quantify these speeds, such as the time scale (Barbano et al., 2021) or exchanging velocity (Solazzo and Britter, 2007). The study can be performed on different SPOD modes separately.
- (3) In the current study, several defects of SPOD were also found that might limit its applications in some cases. The defects are listed as follow, and further studies are suggested to make some improvement on these aspects:
- a. In Chapter 5, a local SPOD spectrum was used to decompose the TKE at a certain point, which identifies the most influential fluctuation pattern on this point, and contributes to the planning of countermeasures against a too-large TKE. However, neither POD nor SPOD provides a hint on the cause of the too-large mean wind speed, because the mean value has already been deducted before the implementing of POD or SPOD, while the too-large mean wind is also an important cause of wind nuisance.
 - b. SPOD technique is based on the spatial and temporal correlation relationships, so it only provides correlation information. However, correlation only give hints on the relevance of two issues, but it does not confirm the causality. Therefore, in the applications of SPOD, remember to stay prudent when giving conclusions such as “A is found caused by B”, and provide more solid evidence.

Reference

- Barbano, F., Brattich, E., Di Sabatino, S., 2021. Characteristic Scales for Turbulent Exchange Processes in a Real Urban Canopy. *Boundary-Layer Meteorol.* 178, 119–142. <https://doi.org/10.1007/s10546-020-00554-5>
- Blackman, K., Perret, L., Savory, E., 2018. Effects of the Upstream-Flow Regime and Canyon Aspect Ratio on Non-linear Interactions Between a Street-Canyon Flow and the Overlying Boundary Layer. *Boundary-Layer Meteorol.* 169, 537–558. <https://doi.org/10.1007/s10546-018-0378-y>
- Cintolesi, C., Pulvirenti, B., Sabatino, S. Di, 2021. Large-Eddy Simulations of Pollutant Removal Enhancement from Urban Canyons. *Boundary-Layer Meteorol.* 1–26. <https://doi.org/10.1007/s10546-021-00610-8>
- Di Bernardino, A., Monti, P., Leuzzi, G., Querzoli, G., 2018. Pollutant fluxes in two-dimensional street canyons. *Urban Clim.* 24, 80–93. <https://doi.org/10.1016/j.uclim.2018.02.002>
- Han, B.S., Baik, J.J., Kwak, K.H., Park, S.B., 2018. Large-eddy simulation of reactive pollutant exchange at the top of a street canyon. *Atmos. Environ.* 187, 381–389. <https://doi.org/10.1016/j.atmosenv.2018.06.012>
- Inagaki, A., Kanda, M., 2010. Organized structure of active turbulence over an array of cubes within the logarithmic layer of atmospheric flow. *Boundary-Layer Meteorol.* 135, 209–228. <https://doi.org/10.1007/s10546-010-9477-0>
- Jaroslawski, T., Perret, L., Blackman, K., Savory, E., 2019. The Spanwise Variation of Roof-Level Turbulence in a Street-Canyon Flow. *Boundary-Layer Meteorol.* 170, 373–394. <https://doi.org/10.1007/s10546-018-0405-z>
- Kanda, M., 2006. Large-eddy simulations on the effects of surface geometry of

- building arrays on turbulent organized structures. *Boundary-Layer Meteorol.* 118, 151–168. <https://doi.org/10.1007/s10546-005-5294-2>
- Kawai, H., 1995. Effects of angle of attack on vortex induced vibration and galloping of tall buildings in smooth and turbulent boundary layer flows. *J. Wind Eng. Ind. Aerodyn.* 54–55, 125–132. [https://doi.org/10.1016/0167-6105\(94\)00035-C](https://doi.org/10.1016/0167-6105(94)00035-C)
- Khanduri, A.C., Stathopoulos, T., Bédard, C., 1998. Wind-induced interference effects on buildings - A review of the state-of-the-art. *Eng. Struct.* 20, 617–630. [https://doi.org/10.1016/S0141-0296\(97\)00066-7](https://doi.org/10.1016/S0141-0296(97)00066-7)
- Kikumoto, H., Ooka, R., 2012. A numerical study of air pollutant dispersion with bimolecular chemical reactions in an urban street canyon using large-eddy simulation. *Atmos. Environ.* 54, 456–464. <https://doi.org/10.1016/j.atmosenv.2012.02.039>
- Kim, W., Tamura, Y., Yoshida, A., Yi, J.-H., 2018. Interference effects of an adjacent tall building with various sizes on local wind forces acting on a tall building. *Adv. Struct. Eng.* 21, 1469–1481. <https://doi.org/10.1177/1369433217750170>
- Liu, C.H., Leung, D.Y.C., Barth, M.C., 2005. On the prediction of air and pollutant exchange rates in street canyons of different aspect ratios using large-eddy simulation. *Atmos. Environ.* 39, 1567–1574. <https://doi.org/10.1016/j.atmosenv.2004.08.036>
- Michioka, T., Sato, A., 2012. Effect of Incoming Turbulent Structure on Pollutant Removal from Two-Dimensional Street Canyon. *Boundary-Layer Meteorol.* 145, 469–484. <https://doi.org/10.1007/s10546-012-9733-6>
- Michioka, T., Takimoto, H., Sato, A., 2014. Large-Eddy Simulation of Pollutant Removal from a Three-Dimensional Street Canyon. *Boundary-Layer Meteorol.* 150, 259–275. <https://doi.org/10.1007/s10546-013-9870-6>
- Sakamoto, H., Arie, M., 1983. Vortex shedding from a rectangular prism and a circular cylinder placed vertically in a turbulent boundary layer. *J. Fluid Mech.* 126, 147–165. <https://doi.org/10.1017/S0022112083000087>
- Sharma, A., Mittal, H., Gairola, A., 2019. Wind-induced forces and flow field of aerodynamically modified buildings. *Environ. Fluid Mech.* 19, 1599–1623. <https://doi.org/10.1007/s10652-019-09687-9>
- Solazzo, E., Britter, R.E., 2007. Transfer processes in a simulated urban street canyon. *Boundary-Layer Meteorol.* 124, 43–60. <https://doi.org/10.1007/s10546-007-9176-7>
- Wang, H., Zhou, Y., Chan, C., Zhou, T., 2009. Momentum and heat transport in a finite-length cylinder wake. *Exp. Fluids* 46, 1173–1185. <https://doi.org/10.1007/s00348-009-0620-y>
- Zhong, J., Cai, X.M., Bloss, W.J., 2016. Coupling dynamics and chemistry in the air pollution modelling of street canyons: A review. *Environ. Pollut.* <https://doi.org/10.1016/j.envpol.2016.04.052>

Publications

Bingchao Zhang, Ryoza Ooka, Hideki Kikumoto. (2020). Analysis of turbulent structures around a rectangular prism building model using spectral proper orthogonal decomposition. *Journal of Wind Engineering and Industrial Aerodynamics*, 206, 104213.

<https://doi.org/10.1016/J.JWEIA.2020.104213>

Bingchao Zhang, Ryoza Ooka, Hideki Kikumoto. (2021). Identification of three-dimensional flow features around a square-section building model via spectral proper orthogonal decomposition. *Physics of Fluids*, 33(3), 35151.

<https://doi.org/10.1063/5.0041395>

Bingchao Zhang, Ryoza Ooka, Hideki Kikumoto. Spectral proper orthogonal decomposition analysis of turbulent flow in a two-dimensional street canyon and its role in pollutant removal. *Boundary-Layer Meteorology*. (Under review)

Acknowledgements

In April 2018, I quit my job, flew to Tokyo, seeking for something that can fill me, fundamentally and lastingly. Luckily, the time of three years has become so short, since I always find myself being surrounded by everything so interesting in this lab. Even within the pandemic of COVID-19, staying at home does not mean relaxation, but constant day and night efforts. With so such fullness and excitement, I finally realise that it nearly ends, although still hungry. Here, it is the time for expressing gratitude for all the suggestions and help I have received.

First and foremost, I wish to thank my advisor, Professor Ryozo Ooka. Although there are few opportunities to discuss with you, great insights and suggestions are received in each weekly meeting. As a great researcher and the leader of the lab, I see your mastering of solid knowledge, as well as the ability of economically and educationally operating the lab. You have set a shining example for us.

I also want to thank Associate Professor Hideki Kikumoto for all the help and constructive comments on my studies. You are always kind to every student who seeks for your help. From you I learnt that, the ability of doing profound work is of course one of the required qualities to be a good researcher, while the ability of giving a clear and easy-to-understand explanation is another.

I extend my appreciation to my advising committee members, Prof. Fujihiro Hamba, Associate Professor Yosuke Hasegawa, and Associate Professor Tsubasa Okaze for their precious time and constructive comments and suggestions.

And thanks to colleagues and staff in this lab. Working and living with you guys are happy and memorable.

I would also like to say a heartfelt thank you to my parents for always believing in me and supporting me to persuade my dreams. And finally to my love, because of whom I am encouraged a lot, and no longer afraid of being accompanied. Even, unconsciously,

life becomes good, and a good end is expected.



Bingchao Zhang

May 2021